

**“A Comprehensive Computational Model for Coupled Fluid
Flow, Mass Transfer and Light Supply in Photobioreactors
with Lattice Boltzmann Methods”**

Zur Erlangung des akademischen Grades eines
DOKTORS DER INGENIEURWISSENSCHAFTEN

von der KIT-Fakultät für Chemieingenieurwesen und Verfahrenstechnik des
Karlsruher Instituts für Technologie (KIT)
genehmigte

DISSERTATION

von

Albert Mink

Tag der mündlichen Prüfung: 27. September 2021

Referent : Prof. Dr.-Ing. habil. Hermann Nirschl

Zweitgutachter: Prof. Dr.-Ing. Clemens Posten

Zweitgutachter: Dr. rer. Nat. Mathias J. Krause

Acknowledgments

I would like to begin by expressing my gratitude to my advisor Mathias J. Krause for giving me the chance to do a PhD thesis in the Lattice Boltzmann Research Group, founded during this time. I am very grateful for his guidance and advice throughout every stage of the PhD thesis.

I would also like to express my deepest thanks to my supervisors Hermann Nirschl for his support and Clemens Posten for refereeing my PhD thesis. Both provided valuable feedback for the application part and support whenever needed.

I enjoyed many hours of fruitful discussions with Christopher McHardy, whose enthusiasm and differing viewpoint was valuable in fleshing out new ideas and writing papers. Since 2017 your inspirations brought the development of radiative transport Lattice Boltzmann Methods to another level.

My special thanks go to the people whom I had the opportunity and pleasure to work with at the Institute of Mechanical Process Engineering and Mechanics. This dissertation would not have been possible if not for their stimulating environment and happiness in the difficult times. Special thanks to the society 'circle of trust', for the lively dedication to triathlon and other needed distraction.

I am very grateful for the students with whom I worked together, notably Sebastian Biehl, Marc Haussmann, David Herrmann and Lea Willmann. Furthermore, I enjoyed the time in Tunis where Eziddine Sediki and Mahdi Tekitek demonstrated an impressive hospitality and kindness, besides organizing the first *Lattice Boltzmann Methods with OpenLB Software Lab* spring school in 2017.

I would also like to say a heartfelt thank you to my family for always believing in me as the person I am. I thank my wonderful Mar for the great deal of love, support and patience she has afforded to me over the many years. And to Arthur and Hugo for being such lovely childs. Family made the completion of this thesis something to truly look forward to.

Abstract

The growing demand for energy, while the fossil-based resources deplete, is considered as one of the major challenges for science and society in the 21st century. As part of the bio-economy strategy of the federal and state governments of Germany, the supply by fossil-based materials and energy sources is being increasingly converted to bio-based products. For this purpose, the residual biomass from agriculture is not enough. Microalgae are considered to be a promising alternative for biomass production, that neither competes with areas for which already other options are planned nor negatively impacts the environment. In precisely controlled technical environments, referred to as Photobioreactors (PBR), microalgae convert solar energy to biomass and other desirable products.

Since the early 2000s, the commercial production of microalgae have undergone continuous development, not only driven by experience but goal-oriented engineering. But still, many engineering implementations of PBR suffer from photo-limitation effects, due to steep light gradients in algae cultures. For a better understanding of the light supply and its interplay to hydrodynamic mixing and mass transfer, researchers start to implement complex multi-physics simulation models. Such computational studies are proposed to quantitatively predict the PBR performance and facilitates the process scale-up to large industrial applications.

The objective of this work is the development of a consistent simulation framework for the prediction of light supply, hydrodynamic mixing and biomass growth kinetics to assess the PBR performance. All submodels are implemented in the framework of Lattice Boltzmann Methods (LBM), best known for their parallel performance and multi-physics models, and the coupling benefits from the consistent modeling scope. For this background, it is derived and validated a new mesoscopic submodel to simulate the light supply, inside participating media such as microalgae suspensions, by solving the radiative transport equation (RTE). Additionally, existing LBM for the fluid flow, mass transport and microalgae tracking are implemented to gain insights in complex flow patterns and to better understand the mixing. Due to the consistent scope of model equation and numerical algorithm of the submodels, the comprehensive coupling is

achieved through biomass growth kinetic models in a numerical efficient way and does not contribute to the model complexity. All conducted simulations are implemented in the open-source LBM library OpenLB and available to the public from release version 1.3 and newer. Implementation details of the new light LBM models are presented and referenced whenever possible.

The developed mesoscopic simulation framework is applied to three PBR to quantitatively analyze and propose design improvements of the reactors. Special focus is put on complex reactor geometries and light settings, for which sophisticated simulation models are needed, due to the absence of known analytical solutions (e.g. Lambert–Beer for flat plate PBR) or correlations of mass transport and hydrodynamics (e.g. tubular PBR). Additionally, the robustness and numerical efficiency of the simulation framework is emphasized on a complex sponge-structured tubular PBR with internal illumination. Its complex flow patterns and light setup stresses the need of a consistent and yet highly efficient algorithm to solve and predict real 3D PBR. This survey suggests that the proposed computational framework is also suitable for the support of process scale-up of PBR, that requires efficient 3D predictions.

Zusammenfassung

Der wachsende Bedarf an Energie bei gleichzeitiger Erschöpfung der fossilen Ressourcen gilt als eine der großen Herausforderungen für Wissenschaft und Gesellschaft im 21. Jahrhundert. Im Rahmen der Bioökonomie-Strategie von Bund und Ländern wird die Versorgung durch fossile Brennstoffe und Energieträger zunehmend auf biobasierte Produkte umgestellt. Hierfür reicht die Restbiomasse aus der Landwirtschaft nicht aus. Mikroalgen gelten als vielversprechende Alternative zur Biomasseproduktion, die weder mit Flächen konkurriert für die bereits andere Optionen geplant sind, noch die Umwelt negativ beeinflusst. In genau kontrollierten technischen Umgebungen, den so genannten Photobioreaktoren (PBR), wandeln Mikroalgen Sonnenenergie in Biomasse und andere erwünschte Produkte um.

Seit den frühen 2000er Jahren hat die kommerzielle Mikroalgenproduktion eine kontinuierliche Entwicklung durchlaufen. Diese Entwicklung basiert in zunehmenden Massen auf zielorientiertes Engineering. Nach wie vor unterliegen viele PBR der Photo-Limitierung, die durch steile Lichtgradienten in der Algenkultur verursacht werden. Für ein besseres Verständnis der Lichtführung und deren Wechselwirkung mit der hydrodynamischen Durchmischung und dem Stofftransport beginnen Forscher, komplexe Multiphysik-Simulationsmodelle zu implementieren. Solche computergestützten Studien sollen die PBR-Leistung quantitativ vorhersagen und gleichzeitig, das Scale-up des Prozesses für große industrielle Anwendungen beschleunigen.

Das Ziel dieser Arbeit ist die Entwicklung eines konsistenten Simulationswerkzeugs für die Vorhersage des Lichteintrages, der hydrodynamischen Durchmischung und der Biomassewachstumskinetik, zur Bewertung der PBR-Leistung. Alle drei Modelle werden mit Lattice-Boltzmann-Methoden (LBM) realisiert, die für ihre gute Parallelisierbarkeit auf Hochleistungsrechnern und Multiphysik-Modelle bekannt sind. Darüber hinaus profitiert die Kopplung der Modelle von der konsistenten Formulierung. Vor diesem Hintergrund wird eine neue LBM abgeleitet und validiert, welche den Lichttransport in partizipierenden Medien, wie zum Beispiel Mikroalgen-Suspensionen, durch Lösung der Strahlungstransportgleichung (RTE) berechnet. Zusätzlich werden bestehende LBM für die Fluidströmung, den Stofftransport und der Mikroalgentrajektorien implemen-

tiert, um Einblicke in komplexe Strömungsmuster zu gewinnen und die Durchmischung besser zu verstehen. Aufgrund der einheitlichen Formulierung der Modellgleichungen und des numerischen Algorithmus der Teilmodelle, wird die Kopplung durch Biomasse-Wachstumskinetik-Modelle auf numerisch effiziente Weise erreicht und trägt im geringen Maße zur Modellkomplexität bei. Sämtliche durchgeführten Simulationen sind in der open-source LBM-Bibliothek OpenLB implementiert und ab Version 1.3 öffentlich verfügbar. Im Rahmen der vorliegenden Dissertation wird, wann immer möglich, auf Implementierungsdetails des neuen LBM-Modells verwiesen bzw. diese vorgestellt.

Das entwickelte Simulationswerkzeug, basierend auf LBM, wird auf drei PBR angewendet, um die Reaktoren quantitativ zu analysieren und Designverbesserungen vorzuschlagen. Besonderes Augenmerk wird auf komplexe Reaktorgeometrien und Lichtführung gelegt, für die aufgrund des Fehlens bekannter analytischer Lösungen (z. B. Lambert-Beer für Flachplatten-PBR) oder Korrelationen von Stofftransport und Hydrodynamik (z. B. röhrenförmige PBR) anspruchsvolle Simulationsmodelle erforderlich sind. Zusätzlich wird die Robustheit und numerische Effizienz des Simulationsframeworks an einem komplexen, schwammartig strukturierten, röhrenförmigen PBR mit interner Beleuchtung herausgestellt. Die komplexen Strömungsmuster und aufwendige Beleuchtung unterstreichen die Notwendigkeit eines konsistenten und dennoch hocheffizienten Algorithmus zur Lösung und Vorhersage realer 3D-PBR. Diese Untersuchung legt nahe, dass das vorgeschlagene Berechnungsframework auch für die Unterstützung des Prozess-Scale-up von PBR geeignet ist, welches im besonderen Maße effiziente Algorithmen für 3D Modelle erfordert.

Contents

1. Introduction and Objective	1
1.1. Introduction	1
1.2. Objective and Work Program	3
1.2.1. Objective	3
1.2.2. Work program	5
2. Radiative Transport Modeling	7
2.1. Basic Radiation Characteristics	7
2.2. The Law of Lambert–Beer	9
2.3. The Equation of Radiative Transfer in Participating Media	9
2.3.1. Radiative transport regimes	12
2.3.2. Scattering events and phase functions	12
2.4. Optical Characteristics of Algae Suspensions	16
2.5. Diffusion Approximation	17
2.6. Approximated Solutions of Radiative Transfer in Volume	19
2.7. Boundary Conditions for the Radiative Transfer Equation	21
2.8. Existing Numerical Methods	24
2.8.1. Monte–Carlo Methods	25
2.8.2. Discrete Ordinate Method	25
3. Lattice Boltzmann Methods	27
3.1. Kinetic Theory	28
3.2. Boltzmann Equation	31
3.3. Lattice Boltzmann Method Algorithm	32
3.3.1. Collision operators in LBM	34
3.3.2. Equilibrium functions in LBM	35
3.3.3. LBM and target equations	36
3.4. From Lattice Boltzmann Methods to Macroscopic Equations	37
4. Radiative Transport with LBM	39
4.1. Discrete Radiative Transport Lattice Boltzmann Equation	41
4.2. Radiative Transport Lattice Boltzmann Methods	42
4.2.1. Macroscopic RTLBM	43
4.2.2. Mesoscopic RTLBM	44
4.2.3. P1-RTLBM	46
4.2.4. Discussion of the RTLBM	48

4.3. Boundary Models for RTLBM	49
4.3.1. Source models	50
4.3.2. Bounce-back wall	51
4.3.3. Partial bounce-back wall	52
4.3.4. Specular wall	55
5. Numerical Validation Against Analytical Solutions	57
5.1. Validation of Macroscopic RTLBM	57
5.1.1. Simulation setup and analytical solution	58
5.1.2. Convergence study and discussion	59
5.2. Validation of Fresnel Boundaries	62
5.2.1. Simulation setup	62
5.2.2. Convergence study	62
5.2.3. Application to multiple LED spots	64
6. Numerical Validation Against Monte-Carlo	67
6.1. Benchmark Design and Transport Regimes	68
6.1.1. Benchmark design	68
6.1.2. Transport regimes and optical parameter set	70
6.2. Numerical Experiments for Mesoscopic RTLBM	71
6.2.1. Angular discretization and grid independence	71
6.2.2. Infinite radiative source	73
6.2.3. Finite radiative source	74
6.3. Numerical Experiments for P1-RTLBM	77
6.3.1. Angular discretization and grid independence	78
6.3.2. Infinite radiative source	78
6.3.3. Finite radiative source	80
6.4. Numerical Experiments for Macroscopic RTLBM	83
6.4.1. Angular discretization and grid independence	83
6.4.2. Infinite radiative source	84
6.4.3. Finite radiative source	86
6.5. Performance of RTLBM	88
6.5.1. Validity range of RTLBM	88
6.5.2. Comparison of computation time	89
6.5.3. The choice of suitable RTLBM	91
6.6. Future Model Extensions	92
7. Comprehensive Kinetic Model of PBR	95
7.1. Fluid, Particle and Gas Transport Models	96
7.1.1. State-of-the-art	96
7.1.2. Fluid flow equation and Lagrangian particle tracking	97
7.1.3. Gaseous transport equation	98
7.2. Light Model	99
7.2.1. State-of-the-art	100

7.2.2. Light model equation	102
7.2.3. Optical characteristic of microalgae suspension	103
7.2.4. Boundary treatment	104
7.3. Algal Growth Models	105
7.4. Application to Flat Plate PBR	107
7.4.1. Modeling of the reactor dynamics	108
7.4.2. Simulation results	109
7.5. Application to Algine – An internally-illuminated PBR	112
7.5.1. Reactor dimensions	112
7.5.2. Simulation results	114
7.6. Application to Sponge-Structured PBR	116
7.6.1. Modeling of reactor dynamics	118
7.6.2. Simulation results	119
8. Conclusion and Outlook	125
8.1. Conclusion	125
8.2. Outlook	128
Bibliography	131
Publications and Contributions	149
Articles	149
Congress proceedings	149
Conference talks and posters	150
Curriculum Vitae	151
Acronyms	153
A. Chapman–Enskog Analysis of the RTLBM in Volume	155
B. Chapman–Enskog Analysis of the RTLBM on Boundaries	157
C. Parallel Efficient Data Output in OpenLB	159
C.1. VTK-Data Format	159
C.2. Data Size	160
C.3. Sequential Data Output	161
C.4. Parallel Data Output	162
D. Functors in OpenLB	165
D.1. Calculations with Functors	165
D.2. Application to Data Processing	166
D.3. Facilitate Geometry Creation	167
D.4. Functor Design	168
D.4.1. Expression templates	168

Contents

D.4.2. Class hierarchy	169
E. Radiative Transport LBM Implementation in OpenLB	171
E.1. Conversion Factors and Refraction Parameter C_R	171
E.2. Collision Kernels and Integration Stencils	172
E.3. Discrete Phase Function	173
E.4. Boundary Conditions	173
F. Factory Functions for XML-based Geometry Creation in OpenLB	175
F.1. Showcase: Algine	176

1. Introduction and Objective

1.1. Introduction

As part of the bio-economy strategy of the federal and state governments of Germany, the supply of oil-based materials and energy sources is being increasingly converted to bio-based products. For this purpose, the residual biomass from agriculture is not enough. Microalgae are considered to be a promising alternative for biomass production without competing with areas for which already other options are planned. In precisely controlled environments, referred to as Photobioreactors (PBR), microalgae convert solar energy to biomass and many other desirable products. Beginning with Borowitzka [20], the commercial production of microalgae have undergone continuous development towards biorefineries of microalgae, not only driven by experience but goal-oriented engineering [73].

To cope with high areal productivity, the biomass concentration in PBR is typically increased, which comes with a critical illumination and undesired photo-limitation effects. As reported by Posten [147], the high absorption and scattering behavior of algae results in a light penetration depth of only 0.02 m for a *Porphyridium* concentration of 2.0 gL⁻¹. Algae beyond that distance are subjected to photo-limitation and contribute rather to the costs than biomass production. This dilemma leads straight to the all-dominant question in general PBR design, that is driven by the great desire of establishing PBR as a cost neutral alternative in industry [82]. Can the productivity of PBR be enhanced when increasing microalgal concentration by implementing a clever illumination and mixing strategy?

From an engineering perspective, the demand of a homogeneous illumination can be met in particular by closed PBR due to their hardly limited light setups, ranging from internal illumination installations including light guides to external illuminations including photo-conductive reactor elements, as recently assessed by Nwoba et al. [138]. In modern approaches, photo-conductive reactor elements are used as part of the reactor wall [90] or explicitly introduced structure [34, 43], to increase the surface to volume ratio and implement a homogeneous reactor illumination. This constructional effort

1. Introduction and Objective

pays off by attaining a proper mixing, while maintaining or even reducing the fluid velocity, as reported for tubular reactors with passive elements [65, 204]. The controlled mixing additionally improves the light supply on a metabolic level by implementing light/dark cycles (LD-cycles). One strategy is based on wall turbulence promoters, that were investigated by computational fluid dynamics (CFD) simulations and found to establish better mixing behaviour, compared to tubular reactors, at much fewer flow velocities yielding a reduced energy uptake of 60–80 % [65]. Adopting the principle of static mixers, the cultivation efficiency in flat plate PBR has been increased by optimizing the arrangement of the meander through CFD accompanied by experiments [81]. Both strategies achieve the reduction of energy costs and at the same time improve the performance of known reactor designs, by attaining a homogeneous light supply. A third approach is the cultivation in novel reactor designs, e. g. the Taylor vortex PBR, that show complex flow pattern and algae trajectories leading to promising mixing behaviour [55].

Other innovative concepts that reinvent the PBR design are porous substrate and biofilm PBR. Both approaches aim to overcome the volume-related limitations of suspension through a cultivation process of immobilized algae [162, 203, 144]. The authors suggest, that the almost complete separation of algal biomass from the bulk of the liquid culture medium, is likely to improve the cost-effectiveness of the cultivation process. Similar techniques are known for bioreactors, that lack the aspect of illumination by shared structural aspects. For instance, the monolithic reactor design consisting of a uniform structure of parallel channels with diameter 1–5 mm attains a very high surface to volume ratio and increases gas-liquid mass transfer through a Taylor flow [155, 96]. An illumination strategy might be based on light installations between the small capillaries.

The many cultivation strategies and reactor designs outline the great potential and equally the desire and urgency of finding a suitable process engineering answer, to the increased demand of bio-based energy sources. Comprehensive simulation tools can play an important role in the optimization of existing reactor designs and simultaneously the acquisition and assessment of numerous innovative concepts from other process engineering disciplines, through analyzing the interplay of flow field, light supply and mass transfer, to predict biomass growth kinetics. Among the many existing numerical models and algorithms for the above phenomena, the comprehensive coupling towards an efficient PBR model, that allows studying the interplay in real 3D geometries, remains an open topic [59, 17]. Consistent numerical frameworks that model the multi-physics at a persistent scope are needed in order to study the complex coupling in a comprehensive way, besides keeping the algorithmic efforts of data structures and complex interfaces at a minimum.

1.2. Objective and Work Program

First, the objective and goal of the work is presented. Then, the work program along with the structure of the doctoral thesis is given.

1.2.1. Objective

Until today, there remains a lack of reliable simulation models, not only for the prediction of 3D light distribution in general PBR but for the comprehensive description of the complex interplay in PBR. For instance, existing light simulations in PBR literature, are still often based on Lambert–Beer’s law instead of implementing the scattering properties described by the radiative transport equation (RTE). Needless to say, that the many hydrodynamic PBR models have to be coupled to proper light models, in order to provide a robust and efficient predicting of the biomass growth kinetic. It is not enough to model light transport by Lambert–Beer and consider hydrodynamics separately, when providing a feature rich simulation framework.

The main objective of the thesis is to overcome this fundamental limitation, by developing an efficient 3D simulation tool for general radiative (light) transport problems in volume. Besides novel isotropic radiative transport (RT) models in participating media, here algae suspension, it has been proposed and equally validated a new anisotropic RT model based on Lattice Boltzmann Methods (LBM). By solving the light distribution in the framework of LBM, a common fluid flow solver, the subsequently coupling, to existing hydrodynamic and mass transfer LBM models, shares the same modeling scope and numerical method. In addition, this strategy adopts the competence of LBM in the discipline of hydrodynamics and the effort is concentrated to the methodical development and validation of a general Radiative Transport Lattice Boltzmann Methods (RTLBM), and the study of the interplay of the multi-physics. For instance, once the fluid flow is computed, numerous algae particles are placed inside the flow field and their trajectory is obtained by an Euler–Lagrange method implemented in the framework of LBM. Also the mass transfer benefits from existing LBM models. Based on an Euler–Euler approach, the gas phase is transported in the flow field and dissolved by a diffusion mechanism. Finally, the flow field, algae trajectories, gas transport and light supply, are coupled to predict the biomass growth kinetic, as depicted in Figure 1.1.

In recent years LBM has been established as a numerical tool for multi-physics phenomena related to fluid flows, that benefit from a highly parallel algorithm and very intuitive modeling in the mesoscopic scale. Except for RT, there are LBM simulation submodels for gas transport and hydrodynamic known in literature. Hence, a major effort is dedi-

1. Introduction and Objective

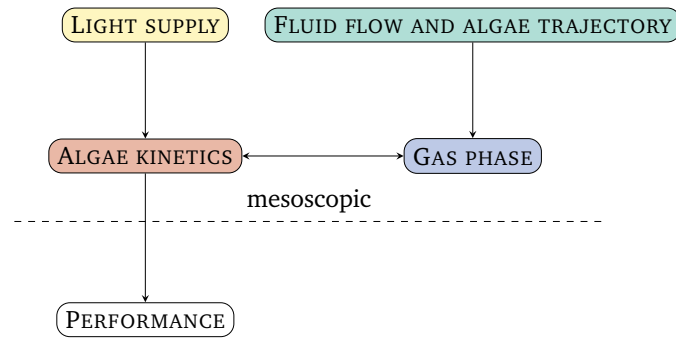


Figure 1.1.: Interplay between radiation, fluid flow, gas transport and algae kinetics. The arrows indicate the implemented coupling in the present work.

cated to the methodical development of RTLBM, to establish a coherent and consistent modeling scope of PBR. This task is based upon three parts and is related to the author's publications as indicated: The development of novel reflection boundary conditions for outgoing radiation on surfaces in Mink et al. [123], the modeling of radiative sources and a proper numerical validation against analytical and Monte-Carlo Methods (MC) solutions in Mink et al. [125, 123].

The validation of the developed numerical framework for the comprehensive simulation of PBR is conducted on simple test scenarios, such as classical reactor geometries in Section 7.4, but also on new and innovative internally-illuminated and sponge-structured tubular designs, see Sections 7.5 and 7.6. The comprehensive computational framework is designed to answer the following PBR design relevant questions:

1. Can we predict the spacial light distribution inside general PBR geometries?
2. What is the impact of the coupled process parameters such as light intensity, flow rate and CO₂ concentration in a reactor?
3. What recommendations can be derived for PBR operating parameters, with respect to existing reactor and also novel reactor types?

The main outcome of the work is the establishment of RTLBM for the simulation of RT in participating media, achieved by comprehensive modeling and proper numerical validation, and is prepared to be published in Mink et al. [124]. Followed by a multi-physics coupling as presented in Figure 1.1, the hydrodynamics are incorporated, yielding a robust and accurate numerical tool to predict algae growth kinetics. In particular, the mesoscopic modeling and simulation superiors traditional macroscopic based methods with respect to parallel-efficiency, but also covering the complex coupling of multi-physics

in a consistent and hence very intuitive way. Finally, it is expected a reliable and robust simulation tool for algae growth in arbitrary and complex PBR geometries and new insights in the interplay of light and fluid dynamics in PBR design. The generic derivation of RTLBM allows reusing or extend the developed numerical tool to many engineering problems, as the comprehensive validation and the application guidelines, presented in [121], shows.

1.2.2. Work program

The development of the mesoscopic simulation model for PBR can be broken down into three tasks. Key parts of the tasks have been published by the author as the references show. Publication [121] stands out, as it is a result of a collaboration with Christopher McHardy. Its implementation and validation in OpenLB has been contributed by the author together with the discussion of the macroscopic RTLBM.

- **Predict light supply with RTLBM.** First, the modeling and simulation of light distribution in participating volume is investigated in the framework of LBM. The results are published in Mink et al. [125] and form the basis of Chapter 5. In order to solve the RTE, it is developed, implemented and validated a novel RTLBM model, including boundary models, see Chapter 4. The results have been submitted and are currently under review [123]. The author implemented not only isotropic RTLBM but the anisotropic RTLBM proposed in McHardy et al. [115]. Both authors then collaborated and presented the first validation paper of RTLBM in Mink et al. [121] where improvements of both models have been applied. This work forms the basis of Chapter 6 and shows that RTLBM is accurate for a wide range of optical parameters beyond algae suspensions. Finally, the Chapman–Enskog expansions are given in Appendix A and B. All implementation, testing and validation is executed in the software OpenLB.
- **Compute algae trajectories and mass transport in the flow field with LBM.** Second, the flow field inside a PBR is computed by LBM. Together with an Euler–Lagrange particle simulation the algae trajectories and more generally, the time evolution of the algae suspension is retrieved. By the trajectories it is clearly seen, whether there are dead zones or in other words, it is detected the quality of mixing. From the numerical perspective, it is applied an Euler–Lagrange scheme based on LBM literature as presented in Section 7.1.2. Furthermore, the gas component is modeled in the flow field by an Euler–Euler model, where the transport by the fluid regime is modeled by an advective term and the natural diffusion by a diffusion

1. Introduction and Objective

process. The applied numerical algorithm is based on the existing LBM literature for diffusion-advection problems shown in Section 7.1.

- **Design a comprehensive LBM based model for PBR.** The coupling of the above light supply, mass transport and algae trajectories models yields in a comprehensive and consistent simulation tool. The photo-conversion of the transported gas has been coupled to the local light supply, via a sink term in the advection-diffusion equation. A qualitative study inside a tubular PBR equipped with glass sponges has been prepared for publication and can be found in the Appendix.

The work starts with the introduction to RT modeling, its characteristic quantities and the RTE in Chapter 2. Then, the numerical framework LBM is introduced from scratch in Chapter 3 with the required steps to outline the novel RTLBM in Chapter 4. Its validation against analytical solution extends over Chapter 5, whereas the validation against MC is provided in Chapter 6. Finally, the developed light simulation is coupled with hydrodynamic and gas supply models, to provide a simulation model for PBR shown in Chapter 7. The Appendix covers the contributions to the software OpenLB and technical parts of the LBM development such as the Chapman–Enskog analysis. In addition, the Appendix provides a short vitae, published and unpublished articles along an overview of the many conference contributions.

2. Radiative Transport Modeling

The RT in volume is the study of photon propagation in volume that interacts and one of its applications is the modeling of photon distribution in such volumes. A photon interacts by getting absorbed or scattered by the volume, not by photon-photon interaction. For instance, light entering fog or clouds interacts with small water droplets. This three dimensional transport phenomena is modeled by the RTE, the central equation in the present chapter.

2.1. Basic Radiation Characteristics

The present work models radiation as small, virtual particles that propagate on trajectories through space. Depending on the wavelength λ , these particles carry the *photon energy* or radiant energy

$$E(\lambda) = \frac{\hbar c}{\lambda} \quad \text{in J,}$$

with Planck constant \hbar given in Js, constant speed of light in vacuum c in ms^{-1} and specific wavelength λ in m. Associating the photon energy to a certain time interval the *photon power* is derived by $P(t, \mathbf{x}) = dE/dt$ at position \mathbf{x} . The photon power is measured in Js^{-1} .

By taking the propagation direction into account, the radiance is defined, as the photon power per unit normal area and per unit solid angle

$$L(t, \mathbf{x}, \mathbf{s}) = \frac{d^2 P(t, \mathbf{x})}{dA d\Omega} \quad \text{in } \text{Js}^{-1} \times \frac{1}{\text{m}^2} \times \frac{1}{\text{sr}},$$

with respect to time t , position \mathbf{x} and into direction \mathbf{s} . The abstract quantity radiance can be thought of, as the amount of photons that pass a small surface element dA arriving from directions $d\Omega$, see Figure 2.1a.

The radiance on the particle level can then be linked to macroscopic observable

2. Radiative Transport Modeling

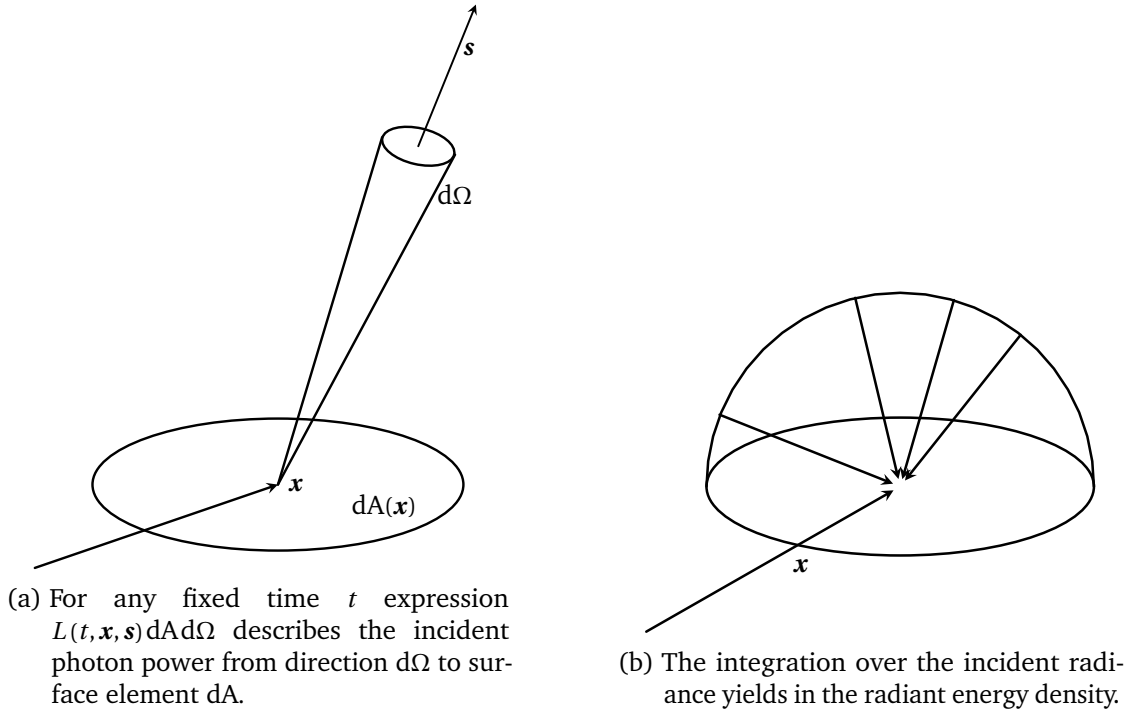


Figure 2.1.: The left side illustrates the radiance. The right side illustrates the radiant energy density on a surface.

quantities by integration. This retrieves the radiant energy density¹ by

$$\Phi(t, \mathbf{x}) = \frac{1}{c} \int_{\Omega} L(t, \mathbf{x}, \mathbf{s}) d\Omega \quad \text{in } \text{Jm}^{-3}, \quad (2.1)$$

for the speed of radiation c . This formula can be interpreted as the brightness or photon density of a volume element at position \mathbf{x} . An illustration of the radiant energy density on a semi-hemisphere is shown in Figure 2.1b.

Besides the radiant energy density, there is a further important macroscopic quantity the radiant flux defined by

$$\mathbf{J}(t, \mathbf{x}) = \int_{\Omega} \mathbf{s} L(t, \mathbf{x}, \mathbf{s}) d\Omega \quad \text{in } \text{Js}^{-1} \times \frac{1}{\text{m}^2},$$

which expresses the averaged propagation direction of the radiance. Both macroscopic expressions help to understand the modeling quantity radiance L in terms of macroscopic observables.

¹Note that the integral is stated in spherical coordinates and reads $\int_{\Omega} L(t, \mathbf{x}, \mathbf{s}) d\Omega = \int_{\theta=0}^{\pi} \int_{\phi=0}^{2\pi} L(t, \mathbf{x}, \mathbf{s}) \sin\theta d\theta d\phi$, for $\mathbf{s} = (\sin\theta \cos\phi, \sin\theta \sin\phi, \cos\theta)^{\top}$.

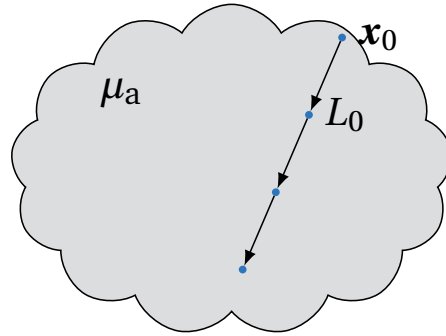


Figure 2.2.: Lambert–Beer states an exponential loss of radiance along the traveled path, characterized by the absorption parameter of the volume.

2.2. The Law of Lambert–Beer

Imagine an absorbing volume that gets illuminated by a pencil beam. The incident radiance at position x_0 with intensity L_0 then propagates through the volume as depicted in Figure 2.2 and attenuates accordingly to the traveled distance and the absorption coefficient μ_a . This RT model is known as the law of Lambert–Beer, that predicts an exponential attenuation with respect to the passed distance

$$L(\mathbf{x}) = L_0 \exp(\mu_a |\mathbf{x}_0 - \mathbf{x}|) . \quad (2.2)$$

This simple formula does not model scattering or any other phenomena than absorption and hence is not appropriate for general RT problems in volume. For example, the incident ray does not deviate its traveling direction and hence, does not contribute to ambient illumination. Scattering events become relevant for the light propagation in dense microalgae suspension and as such, the law of Lambert–Beer is a rudimentary model that is not known for its accuracy, as pointed out in more detail in Section 7.2.

However, for pure absorbing media the law of Lambert–Beer is an appropriate choice, which can be solved in many cases analytically or by numerical schemes. Both, the computational costs and the complexity of the algorithm, are manageable.

2.3. The Equation of Radiative Transfer in Participating Media

Radiance propagating through optically interacting volume, e. g. milk, biological tissue or clouds, is not only governed by the passed distance, but absorption and scattering behavior. Let us consider radiance that hits a single droplet or volume element from

2. Radiative Transport Modeling

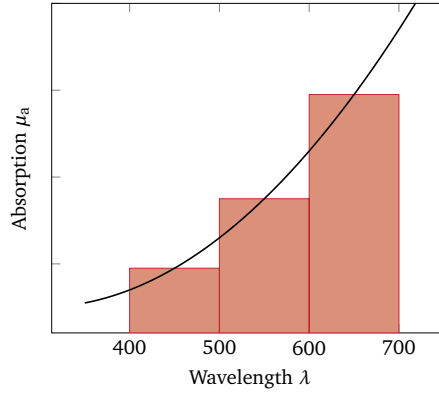


Figure 2.3.: Stair case approximation of the spectrum, also referred to as box model. The RTE is solved independently for every discrete spectrum. A weighted sum of the results is considered to be a good approximation.

direction \mathbf{s} . Then, the radiance diminishes due to out-scattering in an arbitrary direction and absorption. Conversely, there might be radiance associated to a traveling direction \mathbf{s}' , that equally gets out-scattered into direction \mathbf{s} , which then yields in a gain of the radiance in direction \mathbf{s} , named in-scattering. Taken together these phenomena, the RTE

$$\frac{1}{c} \partial_t L + \mathbf{s} \cdot \nabla L = -(\mu_a + \mu_s) L + \mu_s \int_{\Omega} p(\mathbf{s}', \mathbf{s}) L(t, \mathbf{x}, \mathbf{s}') d\Omega', \quad (2.3)$$

describes the evolution of radiance $L(t, \mathbf{x}, \mathbf{s})$ in a volume with specific absorption and scattering coefficients μ_a and μ_s and phase function p . The speed of radiation is given by c . Note, this formula is valid with respect to a specific wavelength λ , since the absorption and scattering coefficients are typically a function of the wavelength. In order to model the visible light spectrum from 400–700 nm, one approximates it by constant functions (staircase approximation or box model) and solves the RTE for every staircase independently. The staircase approximation of the spectrum is illustrated in Figure 2.3.

The first term on the right hand side of the RTE accounts for the linear loss of radiance propagating in direction \mathbf{s} , due to absorption and out-scattering. The second term models the gain of radiance due to in-scattering from all possible incident directions \mathbf{s}' , as indicated by the integral. The probability of incident radiance from \mathbf{s} being scattered into direction \mathbf{s}' , is denoted by $p(\mathbf{s}, \mathbf{s}')$. Unlike the constant phase function in isotropic scattering volume, anisotropic scattering behavior, such as Mie or Rayleigh scattering, can be covered by more sophisticated phase function. For further reading it is referred to textbooks [19, 28, 129, 89]. Solving the RTE is a numerical difficult task, mainly due to its integro-differential form, for which many numerical methods have been developed. This

2.3. The Equation of Radiative Transfer in Participating Media

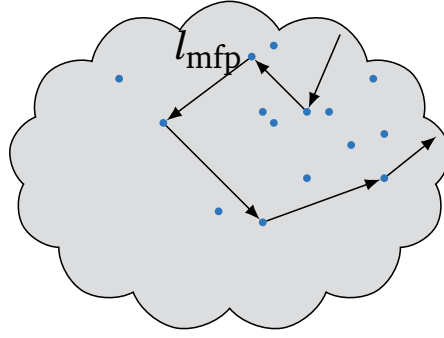


Figure 2.4.: Incident radiance changes its propagation direction due to scattering with the volume, e. g. water droplets. The average distance between a scattering or absorption event is denoted by the mean free path l_{mfp} .

thesis outlines the MC and Discrete-Ordinate Method (DOM) as the dominant stochastic, respectively deterministic, algorithm in Section 2.8.

The following introduces into the optical characterization of transport regimes. A characteristic length for the radiation transfer regime is the mean free path

$$l_{\text{mfp}} = (\mu_a + \mu_s)^{-1} ,$$

which accounts for the average distance between absorption or scattering events. Figure 2.4 illustrates a trajectory of an incident ray, that changes direction due to scattering events. This quantity is directly related to the optical thickness, sometimes referred to as optical depth, of the RT. The ratio of the mean free path and a characteristic length l_{phys} yields in the (non-dimensional) optical depth

$$b = (\mu_a + \mu_s) l_{\text{phys}} .$$

This quantity depicts the optical thickness of the volume considering a specific problem size l_{phys} . Further, the amount of scattering along a mean free path is measured by the (transport) scattering albedo

$$a = \frac{\mu_s}{\mu_a + \mu_s} .$$

Both, the optical depth and the scattering albedo, characterize the RT regime in the volume and allow to define RT regimes for which approximations of the RTE are known.

2. Radiative Transport Modeling

2.3.1. Radiative transport regimes

The difficulty in solving general RT problems in volume is mainly due to the (anisotropic) scattering, which results in the complex integro-differential form of the Boltzmann-type equation [24]. Fortunately, the RTE can be approximated by much simpler equations, either by the law of Lambert–Beer or a Helmholtz equation, depending on the portion of scattering along a mean free path. To this aim, the RT can be classified into a ballistic ($a \rightarrow 0$) or diffuse ($a \rightarrow 1$, $b > 1$) regimes. For both RT regimes, the radiance can be approximated in its steady-state¹. First, assuming a ballistic regime, the RTE reduces to the law of Lambert–Beer $\mathbf{s} \cdot \nabla L = -\mu_a L$ with the solution $L(\mathbf{x}) = L_0 \exp(-\mu_a |\mathbf{x} - \mathbf{x}_0|)$. This fallback shows not only the consistency to more basic model equations, but predicts the exponential decrease of radiance along the optical depth coordinate. Second, the Helmholtz equation $D\Delta L(\mathbf{x}) = \mu_a L(\mathbf{x})$ approximates the RTE in the diffuse transport regime, with diffusion coefficient Δ , for which a detailed survey and derivation is presented in Section 2.5. However, the prediction of general RT in volume is equally essential and challenging for general numerical RT solvers. It can only be attained by a precise implementation of the scattering and absorption behavior of the media. In addition, anisotropic scattering media requires the accurate treatment of the in-scattering integral.

2.3.2. Scattering events and phase functions

The phase function² is a conditional probability distribution function and accounts for the single scattering events of radiance and media. Given radiance arriving from direction \mathbf{s} , expression $p(\mathbf{s}, \mathbf{s}')$ denotes the probability of a post-scattering direction \mathbf{s}' , as shown in Figure 2.5. If the probability of such events depends on the location, such as in inhomogeneous media, the phase function is additionally formulated with respect to position \mathbf{x} . Thinking of (homogeneous) algae suspension, the phase function measures the probability of the deviation of an incident light beam into direction \mathbf{s}' inside an infinitesimal small control volume. From a physical standpoint, the phase function has to

¹RT is an instantaneous transport and the many applications focuses on the steady-state. This thesis does not emphasis on transient transport phenomena.

²Phase functions that depend only on directions are usually called bidirectional reflection distribution functions (BRDF). More sophisticated phase functions are able to model surfaces as skin or clothes, where light enters at a certain point, undergoes several subsurface scattering events and eventually leaves at another point.

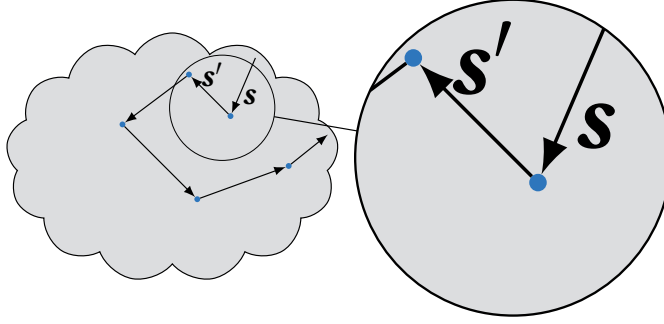


Figure 2.5.: Single scattering event from direction \mathbf{s} into \mathbf{s}' . The phase function denotes the probability of all such scattering events.

fulfill the following properties:

$$p(\mathbf{s}, \mathbf{s}') \geq 0, \quad (2.4a)$$

$$p(\mathbf{s}, \mathbf{s}') = p(\mathbf{s}', \mathbf{s}), \text{ for all } \mathbf{s}, \mathbf{s}' \in \mathbb{R}^3, \text{ Helmholtz reciprocity,} \quad (2.4b)$$

$$\int_{\Omega} p(\mathbf{s}, \mathbf{s}') d\Omega' = 1, \text{ Energy conservation.} \quad (2.4c)$$

Scattering events from \mathbf{s} to \mathbf{s}' or from \mathbf{s}' to \mathbf{s} happen with the same probability (Helmholtz reciprocity). The energy conservation guaranties that the scattering event does not consume radiance. However, the radiance might get reordered or distributed, hence change the propagation direction. In the literature there are many different notations for the phase function, e. g. $p(\mathbf{s} \cdot \mathbf{s}')$, $p(\mathbf{s} \rightarrow \mathbf{s}')$ or $p(\theta)$, where angle θ is given by $\cos(\theta) = \mathbf{s} \cdot \mathbf{s}'$.

In case of isotropic scattering, the phase function is constant. However, anisotropic scattering behaviour requires a general scattering model, e. g. Henyey–Greenstein phase function. A common characterization of anisotropy is the anisotropy factor or mean cosine defined by

$$g(\mathbf{s}) = \int_{\Omega} \mathbf{s} \cdot \mathbf{s}' p(\mathbf{s}, \mathbf{s}') d\Omega'. \quad (2.5)$$

This quantity averages the probability for all scattering events by measuring the amount anisotropy. In case of isotropic scattering the anisotropy factor equals 0 due to the symmetry. A negative anisotropy factor means that backward scattering is dominant. Otherwise, the considered media mainly scatters forward.

The following presents analytic phase function models that are common in literature and shows that the RTE is a very general equation that is able to model many different RT phenomena. The Phone model implements RT on surfaces, whereas the Henyey–Greenstein model accounts for RT in media.

2. Radiative Transport Modeling

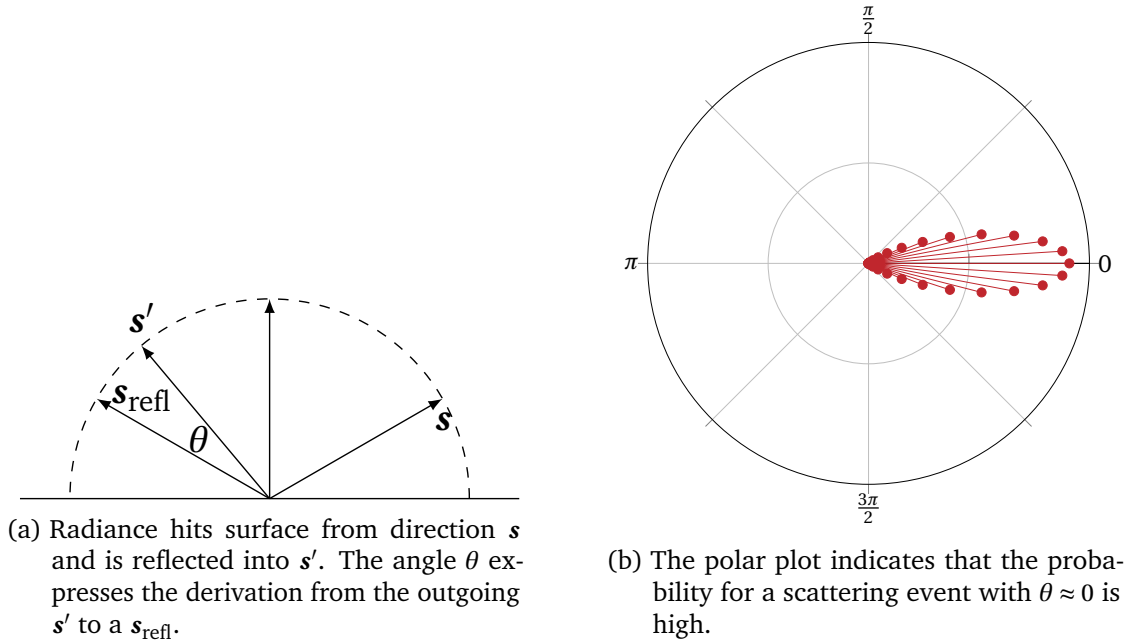


Figure 2.6.: Illustration of the Phong phase function and the modeled reflection on surfaces.

The Phong phase function

The Phong phase function models scattering behaviour on surfaces. Consider radiance hitting a surface with orientation \mathbf{n} from direction \mathbf{s} . For perfectly specular surfaces, the radiance is mirrored on \mathbf{n} in direction \mathbf{s}_{refl} . Other outgoing directions are not considered and hence this surface behaves like a mirror. Contrary holds for a diffuse surface, where the incident ray is scattered equally in every direction.

However, most surfaces are rough up to a certain level and the scattering is neither specular nor diffuse. The Phong phase function models exactly the mixture of specular and diffuse surfaces by a preferred scattering direction, see Figure 2.6. With the definition of θ as the angle defined by \mathbf{n} and \mathbf{s}_{refl} the Phong phase function is obtained as

$$p^{\text{phong}}(\theta) = \frac{N+1}{2\pi} \cos^N(\theta), \quad \theta \in [0, 2\pi],$$

for a positive integer N that accounts for the narrowness of the outpoint directions. For $N = 0$, the Phong phase function models diffuse surfaces, indicated by $p = \text{const.}$. The other limit of $N \rightarrow \infty$ models the specular surfaces. For moderate N the Phong phase function models specular surfaces with a diffuse portion, e. g. mirrors with a preferred scattering direction.

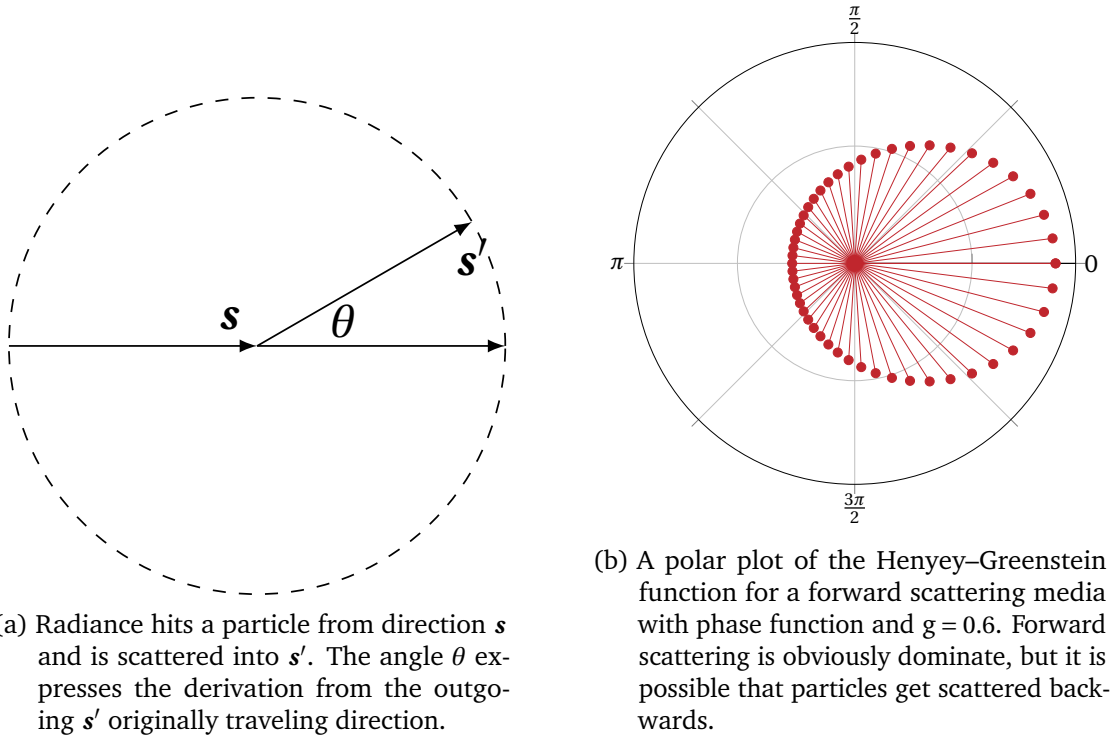


Figure 2.7.: Radiance hits particle from direction \mathbf{s} and is reflected into \mathbf{s}' . The angle θ expresses the deviation from the outgoing \mathbf{s}' to a \mathbf{s} .

The Henyey–Greenstein phase function

The Henyey–Greenstein phase function accounts for single particle scattering of radiance, which can be thought of as light getting scattered on droplets e. g. inside fog or milk. Such a scattering event with resulting deviation of the traveling direction by θ is associated to a probability by

$$p^{HG}(\theta) = \frac{1 - g^2}{2(1 + g^2 - 2g \cos \theta)^{3/2}}, \quad \theta \in [0, 2\pi]$$

where $g \in [-1, 1]$ is the anisotropy factor, that indicates forward or backward scattering behaviour of the volume (2.5). Figure 2.7 shows the Henyey–Greenstein phase function for a forward scattering media ($g > 0$). Note that particles may get scattered backwards. However, the probability for such an event is very low compared to the forward directions. For $g = 0$, the Henyey–Greenstein phase function is a constant function, thus represents isotropic scattering. That shows the consistence of the Henyey–Greenstein phase function to the trivial ones of isotropic scattering.

In order to apply this phase function to engineering applications, the model parameter g

2. Radiative Transport Modeling

has to be fitted to the measurements.

General scattering models

Radiation propagating through volume interacts and gets absorbed and scattered, according to RTE (2.3). Consider a scattering on a single spherical particle of diameter d by radiation with wavelength λ . Then, the elastic scattering regime can be classified into

$\lambda \ll d$ *Mie* scattering

$\lambda \gg d$ *Rayleigh* scattering

$\lambda \approx d$ The surface of the particle is fully resolved and treated as a normal surface with roughness and specular properties.

In dilute gases where mainly single scattering events occur, the phase function together with the RTE is a very accurate model. Such transport regimes are well suited to MC simulations. First, the few gas particles can be simulated in reasonable time. Second, the simulation as well as the model share the microscopic approach and which result in an intuitive numerical scheme.

However, in dense gases the scattering is overlapped multiple times and the RTE can be approximated by a technique called diffusion approximation, as is shown later in Section 2.5. In fact, after several scattering events the particle has lost the information about the original or incident direction and the recent propagation direction is totally independent. It can be said that after several scattering events the radiative regime is almost diffuse and as such, the phase function that models single scattering events gets less relevant.

2.4. Optical Characteristics of Algae Suspensions

The characterization of algae suspension with respect to scattering and absorption properties is a non trivial experimental task. Measurements depend on the wavelength and growth conditions, also the scattering must be analyzed within very thin suspensions, in order to avoid multiple scattering events that would blur the results.

Kandilian et al. investigated the radiation characteristics for *C. reinhardtii* and *C. vulgaris* grown under nitrogen-replete conditions [93, 94]. The authors present a simple experimental procedure for retrieving the averaged spectral absorption cross-section of concentrated microalgae suspensions, that was proven to predict the fluence rate and absorption. Including theoretical methods, based on the Mie theory treating microalgae

as polydisperse homogeneous spheres, the scattering cross-section and anisotropy factor was found to be in good agreement to measurements. An emphasis of their work is the impact of algae morphology and the inappropriate homogeneous spheres assumption for *C. vulgaris*. A summary of the experimental measurements of [93, 94] is given in Table 2.1. From the measurements it is seen, that algae suspension is a highly scattering media ($a \gg 0$) which will justify the diffusion approximation of the RTE in Section 2.5.

nm	$\hat{\mu}_a$ in $\text{m}^2 \text{kg}^{-1}$	$\hat{\mu}_s$ in $\text{m}^2 \text{kg}^{-1}$	$\hat{\mu}_t$ in $\text{m}^2 \text{kg}^{-1}$	a
470	400	800	1200	0.66
600	140	1700	1840	0.92
680	380	1300	1680	0.77

Table 2.1.: Experimentally obtained absorption, scattering and extinction cross-sections besides scattering albedo of *C. reinhardtii* for three wavelengths 470, 600 and 680 under optimal growth conditions [93].

For a biomass concentration of 1 gL^{-1} the extinction coefficient for light with wavelength 680 nm results in 1680 m^{-1} . Estimating the light attenuation briefly by Lambert–Beer, it is retrieved that after 1 mm the residual light holds 18% of the incident intensity. This example shows the steep light gradient inside algae cultures.

2.5. Diffusion Approximation

The present section focuses on the diffusion approximation of the RTE. As many other approximation techniques of describing RT it is designed to accomplish two goals. First, to make RT accessible to numerical investigations by developing simulation tools that solve the approximation. Second, to gain insight in the RT regime and the interaction of the scattering and absorption parameters. It is known, that in the limit of high scattering albedo, radiance propagates nearly isotropic and hence, the radiation transport is approximately diffusive. Under this *diffusion hypothesis*, the RTE can be approximated by a diffusion equation, here the Helmholtz equation. This technique is well-known in literature [89, 184] and summarized in the present Section.

Figure 2.8 illustrates the diffusion approximation, where a car is placed in a foggy environment. The car headlights emits the radiation, which travels from droplet to droplet and changes the traveling direction due to scattering. The further away the radiation travels the more the traveling direction becomes independent of the emitting direction and hence diffusive. However, close to the source the RT regime remains anisotropic. In this example, the quality of the diffusion approximation is characterized by the scattering

2. Radiative Transport Modeling

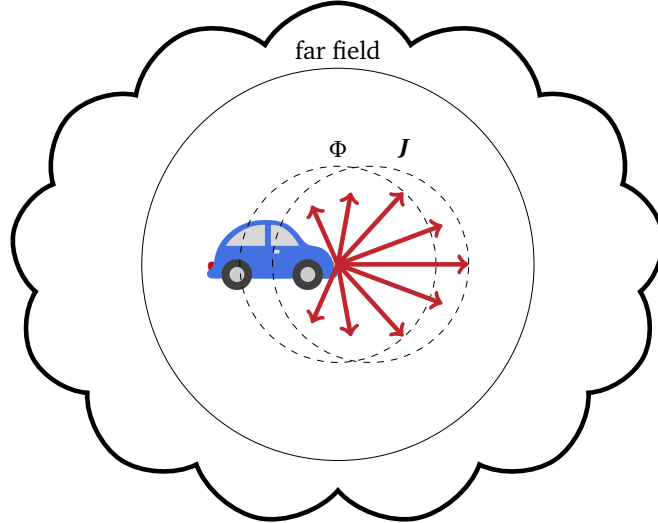


Figure 2.8.: The car headlights emit radiation that gets scattered on the droplets. The RT regime is diffusive in the far field. Close to the radiative source the regime is highly anisotropic.

property of the volume. To summarize the illustration it can be said, that the diffusion equation approximates the RT in the far field and that the higher the amount of scattering the better the diffusion approximation.

In the first step, the radiance is expanded in the basis of spherical harmonics

$$L(t, \mathbf{x}, \mathbf{s}) \approx \frac{1}{4\pi} \Phi(t, \mathbf{x}) + \frac{3}{4\pi} \mathbf{J}(t, \mathbf{x}) \cdot \mathbf{s}, \quad (2.6)$$

up to first order in \mathbf{s} . This expansion composes radiance as an isotropic and anisotropic part. For an almost isotropic radiance, this is a reasonable approximation. The second step is based on substituting the expansion (2.6) in (2.3) and integrating over the solid angle, which yields

$$\frac{1}{c} \frac{\partial}{\partial t} \Phi(t, \mathbf{x}) + \mu_a \Phi(t, \mathbf{x}) + \nabla \cdot \mathbf{J}(t, \mathbf{x}) = 0. \quad (2.7)$$

By repeating this procedure, but first multiplying (2.3) by \mathbf{s} , the integration yields in

$$\frac{1}{c} \frac{\partial}{\partial t} \mathbf{J}(t, \mathbf{x}) + (\mu_a + \mu_s) \mathbf{J}(t, \mathbf{x}) + \frac{1}{3} \nabla \Phi(t, \mathbf{x}) = 0. \quad (2.8)$$

The closure of these two equations assumes that the partial time derivative of \mathbf{J} can be neglected, which leads directly to Fick's law $\mathbf{J} = -D\nabla\Phi$, see (2.8) and

$$D = \frac{1}{3(\mu_a + \mu_s)}. \quad (2.9)$$

2.6. Approximated Solutions of Radiative Transfer in Volume

Note, that this diffusion coefficient is a result of the approximation hypothesis and might deviate from measured values [154, 50]. Since the radiation field reaches a steady state quasi instantaneously, this is a reasonable approximation. Substitution of this finding in (2.7) yields

$$\frac{1}{c} \frac{\partial}{\partial t} \Phi - \nabla \cdot \left(\frac{1}{3(\mu_a + \mu_s)} \nabla \Phi \right) + \mu_a \Phi = 0. \quad (2.10)$$

With the definition of an effective attenuation coefficient

$$\mu_{\text{eff}} = \sqrt{3\mu_a(\mu_a + \mu_s)} \quad (2.11)$$

the RTE is finally approximated in the steady state by the Helmholtz equation

$$\Delta \Phi = \mu_{\text{eff}}^2 \Phi. \quad (2.12)$$

To summarize the diffusion approximation, the complex RTE with independent parameters μ_a , μ_s and p can be approximated by a simple Helmholtz equation with a single parameter μ_{eff} . The diffusion approximation has been widely discussed in literature and predicts general RT in the diffuse regime accurately at distances from sources and boundaries greater than one mean free path [179, 50, 184]. When it comes to the numerical effort, it is clear that solving the approximated RT problem results in notable less numerical cost.

Where are the limits of the diffuse approximation? One shortcoming is the restriction to isotropic propagation. Close to boundaries and in particular close to radiative source where photons get injected, there is anisotropic RT. However, this directional character of RT vanishes after several mean free path lengths or equally in the far field and as such, the far field is still predicted properly. Both phenomena are also observed in the simulation part of this PhD thesis, see Section 4.2.2.

2.6. Approximated Solutions of Radiative Transfer in Volume

General solutions for RTE are barely known and hence approximated solutions come to the fore. On the one hand, they provide information about the RT regime and help to understand the modeling parameter better. On the other hand, they found the basis for the validation of numerical schemes for solving RTE. The derivation of the approximated solutions, given in the following, can be found in the textbooks [22, 89, 184].

In a large distance from the boundaries, inlet respectively outlet, and for some geometries the diffusion approximation can be solved in a closed form. The following presents

2. Radiative Transport Modeling

two examples for which approximated solutions are known. The case I considers an isotropic point source in an infinite media, see illustration in Figure 2.9. The solution is

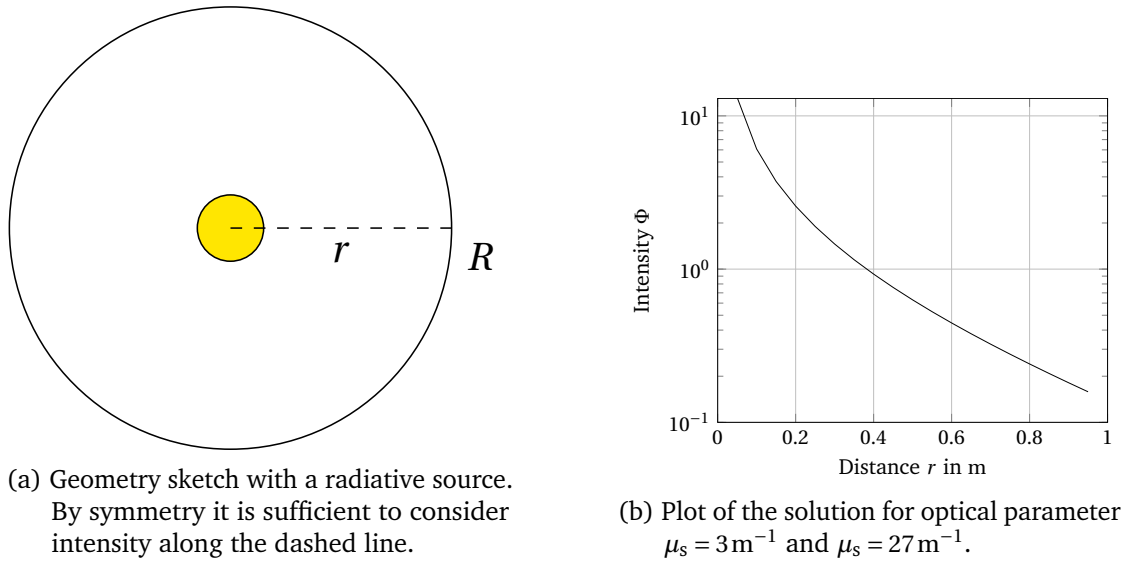


Figure 2.9.: Case I: Point source with infinitesimal small radius and outlet radius $R \rightarrow \infty$. By symmetry it is sufficient to consider intensity along the dashed line.

of exponential character and reads

$$\Phi(r) = \frac{3(\mu_a + \mu_s)}{4\pi r} \exp\left(-\sqrt{3\mu_a(\mu_a + \mu_s)} r\right) \quad (2.13)$$

$$= \frac{1}{4\pi D r} \exp(-\mu_{\text{eff}} r) \quad (2.14)$$

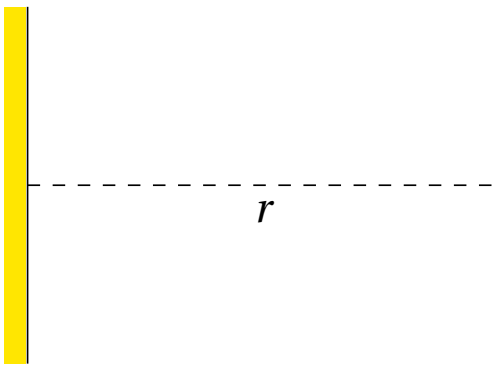
for distance $r = |\mathbf{x}|$ from an infinitesimal small light source at position $\mathbf{x} = \mathbf{0}$, diffusion parameter D (2.9) and effective attenuation coefficient μ_{eff} (2.11). In Section 5.1 this solutions enters a experimental order of convergence (EOC) study to determine the order of the numerical scheme.

Case II assumes an incident beam of infinite diameter, see Figure 2.10. In the simulation this is modeled by a source that extends over the entire wall. The approximated solution reads

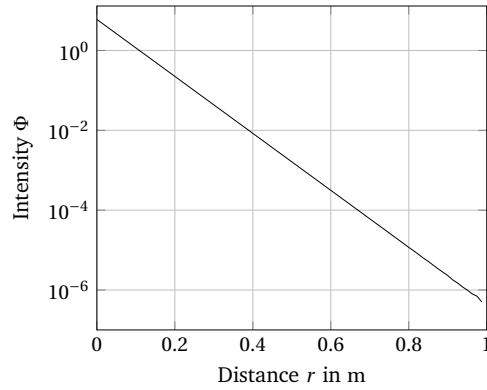
$$\Phi(r) = \Phi_0 \exp(-\mu_{\text{eff}} r), \quad (2.15)$$

for an effective attenuation coefficient μ_{eff} and r as above. Here, the decrease of radiance is described only by an exponential function with a proportional constant Φ_0 . As before this is a solution at large distance from the boundaries or simply far field. The slope of the solution in Figure 2.10, is determined by the effective attenuation coefficient or in

2.7. Boundary Conditions for the Radiative Transfer Equation



(a) The beam enters from the entire left hand side, hence is of infinite diameter. Approximated solutions are known along the dashed line.



(b) The plot shows the intensity of the solution. The y-log representation clearly indicates an exponential decay of intensity.

Figure 2.10.: Case II: The infinite beam illuminates the domain from the left. By construction the intensities along the dashed line are sufficient to determine the RT.

other words, by the absorption and scattering coefficient simultaneously. In fact, the solutions is no longer unique in terms of scattering and absorption. This behaviour shows the approximating character of the diffusion approximation.

2.7. Boundary Conditions for the Radiative Transfer Equation

The interaction of radiance with surfaces defines the boundary condition for general RT problems in volume. Some surfaces are transparent and the radiance just passes them. Others may absorb or reflect radiance or even a mixture of all three phenomena together. The main focus of the present work are boundary layers that are between two volumes. Usually every volume is characterized by refractive indices n_i and n_o , for the inner volume, respective outer volume. Depending whether there is a refractive indices match $n_i = n_o$ or not, the radiance passes the boundary strictly or not.

In the scope of LBM there are two main modeling aspects. At its simplest case, the radiance leaves the volume of interest or in other words, there is no radiance re-entering the volume. In the situation is expressed by the refractive index match $n_i = n_o$, where the boundary is completely transparent and all the radiance passes. Such a boundary can be written, for all boundary points \mathbf{x} with orientation \mathbf{n} , in the form $L(t, \mathbf{x}, \mathbf{s}) = 0$ for all \mathbf{s}

2. Radiative Transport Modeling

with $\mathbf{s} \cdot \mathbf{n} > 0$. The integral version reads

$$\int_{\mathbf{s} \cdot \mathbf{n} > 0} L(t, \mathbf{x}, \mathbf{s}) d\Omega = 0$$

where expression $\mathbf{s} \cdot \mathbf{n} > 0$ ensures that only the directions that pointing into the volume are taken into account. This phenomena is named transmission and can be observed for two volumes with the same refractive index.

In the general case, radiance is (partly) reflected on the interface and re-enters the volume. The portion of the re-entering radiance is described by *Fresnel's equation* and depends strongly on the direction \mathbf{s} that hits the boundary layer. Since the key part of LBM boundary modeling is to find appropriate incoming discrete particle density functions on the boundary, the present work discusses the partly reflected portion on the surface in detail.

For an in-depth understanding of the interaction of radiance with surfaces, it is provided a brief recall of Snell's law. Given a surface normal \mathbf{n} and volume specific refractive indices n_i, n_o with $n_i < n_o$, Snell's law states the change in the propagation direction by the *refraction angle*

$$\theta_r(\theta) = \arcsin\left(\frac{n_i}{n_o} \sin \theta\right),$$

for an incident angle θ . An illustration of Snell's law is presented in Figure 2.11. In the case of $n_i > n_o$, a critical angle is defined as $\theta_c = \arcsin\left(\frac{n_o}{n_i}\right)$, where total reflection is observed for $\theta > \theta_c$ and radiance is entirely reflected (mirrored at \mathbf{n}) back into medium.

The key modeling equation of the present work, the *Fresnel's equation*, reads

$$R_F(\theta) = \begin{cases} 1, & \text{for } \theta > \theta_c, \\ \frac{1}{2} \left(\frac{n_{\text{rel}} \cos \theta_r - \cos \theta}{n_{\text{rel}} \cos \theta_r + \cos \theta} \right)^2 + \frac{1}{2} \left(\frac{n_{\text{rel}} \cos \theta - \cos \theta_r}{n_{\text{rel}} \cos \theta + \cos \theta_r} \right)^2, & \text{for } 0 \leq \theta \leq \theta_c. \end{cases} \quad (2.16)$$

Given the boundary specific *relative refractive index* $n_{\text{rel}} = n_i/n_o$, the Fresnel's equation associates an incident angle to a certain reflectivity in the interval $[0,1]$. For the sake of compactness, it is written θ_r instead of $\theta_r(\theta)$. The special case of $R_F = 1$ models total reflection, e. g. mirrors, and $R_F = 0$ pure transmission, e. g. $n_i = n_o$. An illustration of the strong dependence of R_F on the incident direction is shown in Figure 2.12.

Assuming that radiance hits an interface at position \mathbf{x} from direction θ . Then the re-entering or partly reflected radiance can be stated informally by

$$L(t, \mathbf{x}, \theta') = L(t, \mathbf{x}, \theta) R_F(\theta), \quad (2.17)$$

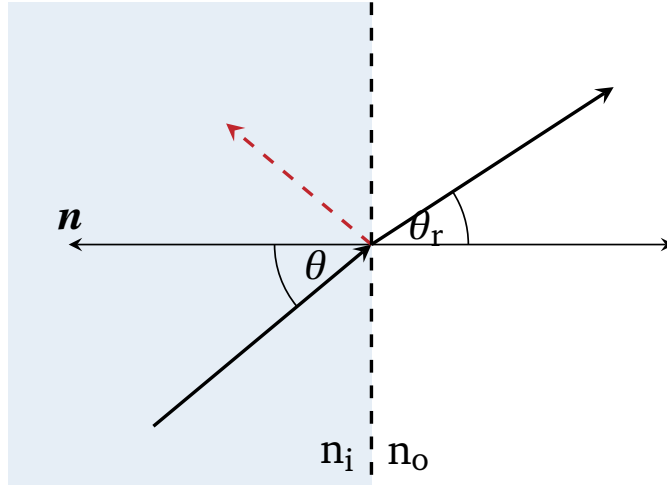


Figure 2.11.: Dashed line represents the interface of two volumes with refractive index n_i and n_o . Incident radiance from angle θ changes its direction to angle θ_r when passing the volumes. Dashed arrow (red) indicates the reflected portion governed by Fresnel's equation.

for an reflected angle θ' , compare Figure 2.11. According to this formula, the reflected radiance (left hand side) is the product of incident radiance and Fresnel's equation (right hand side). As a first guess, one could derive an LBM scheme from (2.17), by choosing a large set of discrete directions in order to reduce the discretization error. However, the regular grid of LBM implies to roll out this set of directions for the whole domain, which installs an undesired coupling of boundary discretization error and numerical cost for the whole domain.

This downside can be avoided by, first substituting (2.17) by a less direction-sensitive boundary formulation and second, deriving a discrete version. To this aim, there are introduced two quantities that average the direction of radiance. First, the *irradiance* is introduced

$$J_{\text{ir}}(t, \mathbf{x}) = \int_{\mathbf{n} \cdot \mathbf{s} > 0} L(\mathbf{s}) \mathbf{s} \cdot \mathbf{n} d\Omega \quad \text{in } \text{Js}^{-1} \times \frac{1}{\text{m}^2},$$

which accounts for the total incident radiance on a surface point with orientation \mathbf{n} . Accordingly, the average outgoing radiance is introduced by the *radiosity*

$$J_{\text{ra}}(t, \mathbf{x}) = \int_{\mathbf{n} \cdot \mathbf{s} < 0} L(\mathbf{s}) \mathbf{s} \cdot \mathbf{n} d\Omega \quad \text{in } \text{Js}^{-1} \times \frac{1}{\text{m}^2}.$$

Both quantities are associated to a position \mathbf{x} with the surface normal \mathbf{n} , where incident directions satisfy $\mathbf{n} \cdot \mathbf{s} > 0$ and outgoing directions satisfy $\mathbf{n} \cdot \mathbf{s} < 0$. By expanding the

2. Radiative Transport Modeling

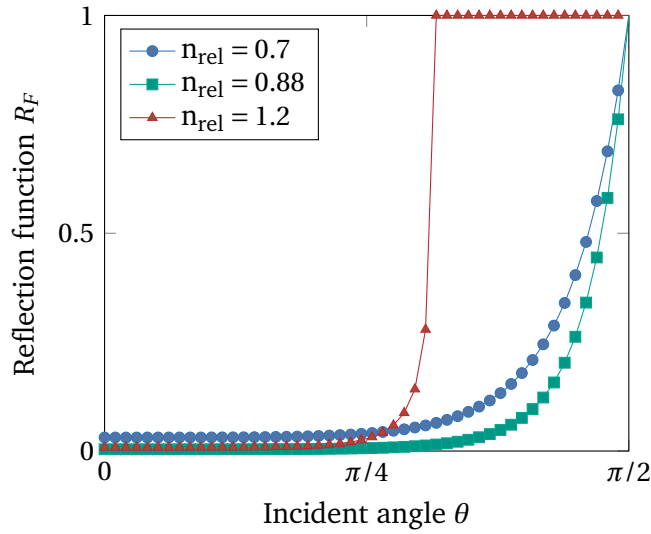


Figure 2.12.: Fresnel's equation R_F plotted over incident angle θ for varying relative refractive index n_{rel} . Total reflection is observed for a water-air interface ($n_{rel} = 1.2$) only for radiation that hits the interface almost parallel. Other directions are almost fully transmitted and pass the boundary interface.

radiance in the basis of spherical harmonics, up to first order, it yields

$$L(t, \mathbf{x}, \mathbf{s}) = \frac{1}{4\pi} \Phi(t, \mathbf{x}) + \frac{3}{4\pi} \mathbf{J}(t, \mathbf{x}) \cdot \mathbf{s},$$

and subsequently the irradiance is reformulated, by means of Φ and \mathbf{J} , to

$$\mathbf{J}_{ir} = \frac{1}{4} \Phi + \frac{1}{2} \mathbf{J} \cdot \mathbf{n}, \quad (2.18)$$

respectively the radiosity with a negative second term, due to the change of sign in direction \mathbf{n} . This is a reasonable approximation for the radiance, if there is considered a highly scattering media. With this findings, the averaged version of (2.17) is derived in Section 4.3.

2.8. Existing Numerical Methods

Many numerical tools are available to solve RT problems in participating media or volume. Most widely used are the MC and DOM, since they provide a reasonable compromise of accuracy and computation time. The following presents the predominant stochastic scheme, the MC, and also a deterministic representative, the DOM.

2.8.1. Monte–Carlo Methods

RT in volume can be simulated by the MC. This method traces single photon packages by resolving the persistent trajectory that is determined by scattering and absorption on the volume. The absorption reduces the energy of the photon packages and the scattering changes the propagation direction. After computing sufficient photon paths the physical quantity light distribution can be estimated.

A single path is a random walk that samples every scattering event and computes a single post-scattering direction. As such, anisotropic scattering events and even spectral scattering can be incorporated straight forward, through adequate phase functions. This equally outlines the importance of sampling of the phase function, which indeed is a key task for MC in general. A good quality of the sampling, referred to as variance, is achieved by keeping the statistical noise at a minimal level. Typically, the sampling of scattering events is responsible for the time consuming character and enormous numerical effort. Together with the slow numerical convergence rate, this method loses attraction for heavy scattering light regimes. Still, the straight forward implementation and the robustness are strong arguments in many computer graphic applications. For example, RT problems with few scattering events, such as RT on surfaces, are most often computed by the MC.

The development focuses more and more on sophisticated photon tracing methods, that are specialized to certain geometries and light regimes [181, 180, 192]. In particular the bidirectional and Metropolis light transport models are promising by reducing the path length and variance and hence the noise as well as the computation time.

2.8.2. Discrete Ordinate Method

The study of radiative (heat) transfer in isotropic and anisotropic scattering media with the DOM goes back to Fiveland [49] and Truelove [176]. By dividing the unit sphere of the scattering integral into discrete directions, according to an integration rule, the RTE can be transformed into a set of partial differential equations. The retrieved approximated equations represent the RT along discrete directions, which leads to the interpretation of the DOM as a simple finite differencing of the directional dependence of the RTE [44].

More recently, Mishra et al. proposed a novel quadrature scheme for the DOM that benefits from a very simple evaluation of ordinates and corresponding weights [128]. The validation of 1D and 2D square enclosures containing absorbing, emitting and scattering medium was found to provide accurate results. A recent review of the advances in DOM for the solution of radiative heat transfer problems in participating media was presented [31]. The development of grid structures, spatial discretization and angular

2. Radiative Transport Modeling

discretization schemes are presented along the progress in accuracy and alternative formulations. When simulation 3D RT, typically the angular discretization is critical. In order to prevent ray-effects in optical thin media, it is required a very fine spatial discretization that comes with high computation costs.

3. Lattice Boltzmann Methods

The LBM emerged from the lattice gas automata in the late 1980s. They become rapidly popular in the modeling of hydrodynamics by overcoming the limitation of statistical noise of the lattice gas automata [201]. By replacing the Boolean configuration by continuous distribution functions, the LBM, as we know them today, were derived in the early 1990s [119, 152, 12]. Almost ten years later, in 1998, Chen and Doolen outlined in their highly accepted work, that LBM is in particular successful in fluid flow applications involving interface dynamics and complex boundaries [30].

A first incubator for the rapid development is undoubtedly the intuitive modeling on the mesoscopic level, which allows to incorporate many physical phenomena in fluids and others with a clear physical understanding. From the very beginning, this attracted engineers from many disciplines, that then speed up the development and spreading the application scope of LBM in a remarkable way [3, 105, 69]. Compared to traditional CFD methods, they are easy to implement, easy parallelizable and, able to model complex multi-physics problems. In fact, pure mathematicians hardly can reproduce many of those contributions in their stringent formalism of asymptotic and convergence [9, 183, 160, 64]. The trend of highly parallel computer hardware can be named as a second crucial incubator, that favored the spreading of LBM as a benchmark application for high performance computers [191, 202, 194, 131]. Today, LBM are recognized as a reliable numerical tool in industry, where the pioneers companies getting bought up by big global players. The standard graduate textbooks [105, 69, 130] prove that the LBM has matured and is well-established along the traditional numerical solvers.

One characteristic for LBM is its microscopic modeling and the mesoscopic equations. Coming from the Navier–Stokes equation, people are familiar with the macroscopic scope and variables. However, the modeling scope for LBM is closer to the particle character or molecules and requires a brief introduction. Let's imagine a swarm of bees. From a macroscopic standpoint, the swarm is described through its moving direction and speed, or briefly the velocity. This scope however, does not consider individual bees and hence, does not know about the interaction of the bees or even the queen bee. As a result the swarm of bees, lacks crucial information in the macroscopic scope which could help to

3. Lattice Boltzmann Methods

understand the swarm of bees in greater detail.

A natural choice would then be to consider the individual bees. This corresponds to the microscopic modeling scope and allows to resolve the behaviour of individual bees, even the queen bee. Once, the evolution of the bees is computed, respecting the queen bee and the interactions, the information of the velocity of the swarm can be obtained by averaging the velocities of all bees. Keeping in mind, that the averaging is a rather trivial task compared the evolution of a single bee. The complexity depends directly on the amount of modeled individuals and might exceed rapidly the available memory or computing time. In particular for gases, this microscopic model is very challenging due to several hundreds of billion individuals.

A good workaround of those two classic scopes is an introduction of a third one, the mesoscopic scope, which lies in between. The goal is to be as close as possible to the microscopic scope such that the relevant behaviour is still represented. But on the other side, keeping the computational effort at a feasible level. This motivates the mesoscopic modeling scope of the LBM, which is introduced in the following.

3.1. Kinetic Theory

In kinetic theory the configuration of a system is described by distribution functions. This abstracts stochastic description is said to be on mesoscopic scope and sits right between the two classic micro- and macroscopic scopes. It claims to be close enough to the microscopic level preserving the particle character of the molecules and at the same time, it allows to express the relevant macroscopic phenomena [166, 110]. In particular, the latter is an asymptotic statement which must be proven carefully with either by Chapman–Enskog analysis or other multiscale expansions [195, 105].

Considering a gas occupying a volume \mathbf{X} with a single species of N molecules, then the particles in a control volume element $d\mathbf{x} \subset \mathbf{X}$ move with velocities \mathbf{v} . It is presumed that there is a sufficient large number of molecules in $d\mathbf{x}$, such that the population can be considered as a continuum. This hypothesis ensures that the mesoscopic scale is a reasonable approximation of a dense gas, accordingly to the *law of large numbers*. The expression

$$f(t, \mathbf{x}, \mathbf{v}) d\mathbf{x} d\mathbf{v}$$

denotes the average number of molecules in the control volume element $d\mathbf{x}$ around position \mathbf{x} that travel with velocities in the vicinity $d\mathbf{v}$ of velocity \mathbf{v} at time t . Distribution function f is the central quantity in the mesoscopic scale and also the main modeling

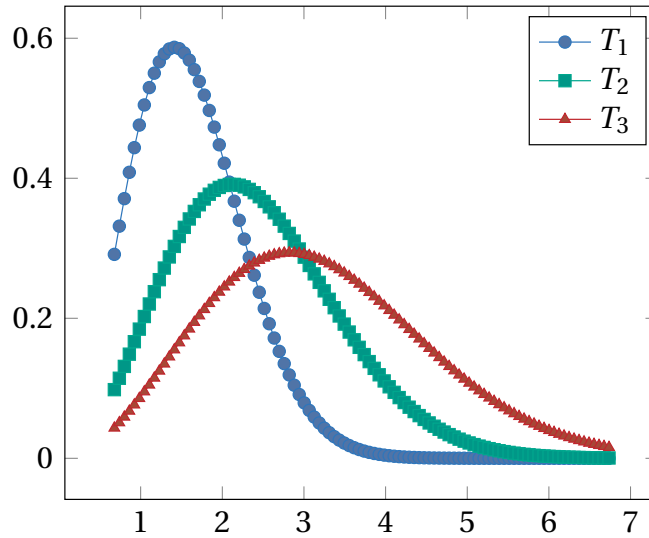


Figure 3.1.: Graph shows the Maxwell–Boltzmann distribution function plotted over velocity. The three different temperatures results in individual velocity distributions.

quantity of the present work. Sometime f is said to be the velocity distribution function or velocity density distribution function, depending on the personal favor. Finally, this function is defined on the phase space $[0, \infty) \times \mathbf{X} \times \mathbf{V}$

A common example of such a (velocity) distribution function is the Maxwell–Boltzmann¹ function

$$f(\mathbf{v}) = \left(\frac{m}{2\pi kT}\right)^{\frac{3}{2}} \exp\left(-\frac{m|\mathbf{v} - \mathbf{u}|^2}{2kT}\right) \quad (3.1)$$

that describes the velocity distribution of an idealized gas with particle mass m , for the Boltzmann constant k , temperature T and local mean average velocity \mathbf{u} . Such an ideal gas consists of randomly moving point particles, that undergo particle-particle collisions and their velocity distribution, in the equilibrium state, is described by the Maxwell–Boltzmann function shown in Figure 3.1. This function answers the question: How many particles have a certain velocity for a gas of temperature T ? Since the quantity of interest is velocity, the function is referred to as velocity (density) distribution function.

Famous other distribution function are the Bose–Einstein function that models ideal quantum Bose gas or the Fermi–Dirac function that models ideal quantum Fermi gas.

The connection from the mesoscopic modeling function f to macroscopic observable

¹Maxwell derived this function through a heuristic approach in 1870. It was Boltzmann that derived this function based on mechanics in 1872 .

3. Lattice Boltzmann Methods

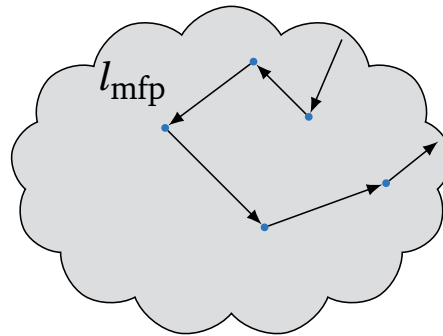


Figure 3.2.: A particle experiences several particle-particle collisions. The mean free path l_{mfp} is the average distance between such collisions and denotes the characteristic length on mesoscopic scale.

quantities is established by the moments of the distribution function, or simply by averaging. Note, that position and time are macroscopic variables but the \boldsymbol{v} is strictly a mesoscopic velocity and \boldsymbol{u} the macroscopic velocity. In the context of fluid flow application, the fluid characteristic quantities such as density ρ , velocity \boldsymbol{u} and total energy E are obtained by the following formula:

$$\rho(t, \boldsymbol{x}) = \int f(t, \boldsymbol{x}, \boldsymbol{v}) d\boldsymbol{v}, \quad (3.2a)$$

$$\rho \boldsymbol{u}(t, \boldsymbol{x}) = \int \boldsymbol{v} f(t, \boldsymbol{x}, \boldsymbol{v}) d\boldsymbol{v}, \quad (3.2b)$$

$$\rho E(t, \boldsymbol{x}) = \frac{1}{2} \int |\boldsymbol{v}|^2 f(t, \boldsymbol{x}, \boldsymbol{v}) d\boldsymbol{v}. \quad (3.2c)$$

Here, the integral considers all possible velocities in \mathbb{R}^d for $d \in \{2, 3\}$ and connects the kinetic scope to macroscopic observables.

Another linkage between the meso- and macroscopic level is the ratio of the length scales. Imagine a gas molecule that travels on a trajectory and hits other gas molecules as illustrated in Figure 3.2. The average distance between those particle-particle interactions is named *mean free path* l_{mfp} and serves as the characteristic length on the mesoscopic scale. With the latter the dimensionless *Knudsen number* Kn is defined as

$$\text{Kn} = \frac{l_{\text{mfp}}}{l_{\text{phys}}} \quad (3.3)$$

for a macroscopic reference length l_{phys} . Gas regimes that are characterized by a Knudsen number < 0.1 can be approximated properly by the Navier–Stokes equations. Flow regimes with a higher Knudsen number are typically based on very small macroscopic

length, e. g. flow in micro channels and are no longer described by the Navier–Stokes equations [166, 72].

3.2. Boltzmann Equation

The evolution of a system, described by a particle distribution function f , is governed by the *Boltzmann equation*. Assume there is a boundary condition or any other force, that forces the system away from the state of equilibrium. Then, the time evolution of the distribution function reads in its most general form

$$\frac{d}{dt}f(t, \mathbf{x}, \mathbf{v}) = Q(f)(t, \mathbf{x}, \mathbf{v}), \quad (3.4)$$

for a general collision operator Q . The magic part of this equation is the collision modeling, that typically models the particle-particle interaction [170, 24, 8] and is provided later. To be precise, for the specific Boltzmann collision operator [26], this simple yet powerful equation was formulated between 1872 and 1875 by its name giver Ludwig Eduard Boltzmann. Boltzmann met with many difficulties in making his theory understood by his contemporaries. Today it is difficult to imagine, that he was constantly attracted and criticized by his opponents for his visionary concept that relates the principles from mechanics to an irreversible statistical process [25].

The physics of the modeled system is solely determined by the collision operator, which is specified later in Section 3.3.1. Quantities such as viscosity, diffusivity and many more are hidden behind this versatile operator.

One of the major problems, when dealing with the Boltzmann equation, is the complicated nature of the collision integral. Instead of computing the original collision operator formulated by Boltzmann it is considered a simplified version that equally conserves and models the desired quantities. Wolf-Gladrow pointed out two constraints that all collision operators Q should respect [195]:

1. Preservation of mass, momentum and energy:

$$\int Q(f) d\mathbf{v} = 0, \quad \text{Mass conservation,} \quad (3.5a)$$

$$\int \mathbf{v} Q(f) d\mathbf{v} = \mathbf{0}, \quad \text{Momentum conservation,} \quad (3.5b)$$

$$\int |\mathbf{v}|^2 Q(f) d\mathbf{v} = 0, \quad \text{Energy conservation.} \quad (3.5c)$$

2. Collision expresses tendency to a Maxwell–Boltzmann distribution (H-Theorem)

3. Lattice Boltzmann Methods

These are the minimal requirements for a collision operator for e. g. fluid flow problems. Some author emphasis the strong connection to the Maxwell–Boltzmann distribution by naming the equilibrium function f^M . Both constraints are matched by the *BGK* collision operator, named after the authors of the original work [15]. The collision nature of the molecules is modeled by a collision time τ that relaxes the recent particle distribution function towards the equilibrium state

$$Q(f) = \frac{1}{\tau} (f^{eq} - f) .$$

Note, that the collision expresses the tendency to Maxwell–Boltzmann distribution locally.

3.3. Lattice Boltzmann Method Algorithm

A typical LBM simulation is based on a domain discretization into a structured uniform grid of cubes. Thus, the domain \mathbf{X} is divided into cubes¹ of equal size with edge length Δx . Every cube is equipped with a set of discrete directions, along which virtual particles travel to neighbouring cubes, see Figure 3.3. The grid together with the discrete directions

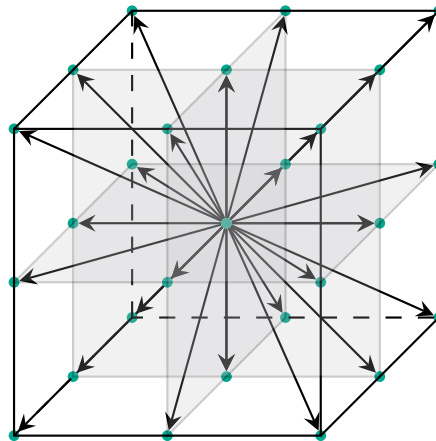


Figure 3.3.: Discrete cube equipped with 27 discrete directions, referred to as a *D3Q27* stencil. Every green dot represents virtual particles propagating along certain directions to a neighboring cube.

represents the discrete phase space. According to the distance to the neighboring cube, the discrete directions are associated to weights, which ensure an isotropic setting. In LBM such an arrangement is referred to as a stencil with nomenclature *DnQq* for dimension $n = 1, 2$ and 3 and number of directions q .

¹In the context of LBM the cubes are typically referred to as cells.

3.3. Lattice Boltzmann Method Algorithm

The iterative nature of LBM is due to the alternately performed collide-and-stream step. The first recomputes the particle distribution in the cells according to a collision rule that imposes the desired physics, e. g. viscosity, diffusivity and more. The second updates the domain with the particle configuration after the collision. Details on the LBM specific discretization can be found in the standard LBM literature [105, 69, 130].

According to the above discretization, the *discrete particle velocity function* reads

$$f_i(t, \mathbf{x}) = w_i f(t, \mathbf{x}, \mathbf{v}_i) ,$$

with respect to a cell at position \mathbf{x} and directions \mathbf{v}_i or directly i . In addition to the velocity discretization, there are q lattice weights w_i such that the moments, defined in (3.2), are computed exactly by a Gaussian quadrature formula

$$\int \mathbf{v}^k f(t, \mathbf{x}, \mathbf{v}) d\mathbf{v} = \sum_i \mathbf{v}_i^k f_i ,$$

for $k = 0, 1$ and 2 . It can be seen, that the lattice weights w_i are the integration weights of the Gaussian quadrature formula. According to the number of discrete directions q , the three dimensional LBM stencil is named $D3Qq$.

The collide-and-stream equation is then stated

$$f_i^*(t, \mathbf{x}) = f_i(t, \mathbf{x}) - Q(f_i)(t, \mathbf{x}) , \quad (3.6a)$$

$$f_i(t + \Delta t, \mathbf{x} + \mathbf{v}_i \Delta x) = f_i^*(t, \mathbf{x}) , \quad (3.6b)$$

in accordance to a collision operator Q , which has to be specified. The first equation is local in position \mathbf{x} , where the collision rule is applied for every direction i , whereas the second equation streams the updated discrete particle fluence f_i^* along direction \mathbf{v}_i to a neighbouring node. The essential difficulty in any application of LBM lies in verifying that the simple collide-and-stream step on the mesoscopic scale solves asymptotically a desired macroscopic partial differential equation. To clarify this issue, researchers examine a multi-scale analysis such as the Chapman–Enskog expansion and prove that the correct asymptotic behaviour is achieved. The central ingredient therefore is a small Knudsen number of the system (3.3).

With regard to high-performance computing and parallel efficiency, it is important that the collision is a purely local operation, which is responsible for the embarrassingly parallel algorithm. However, the streaming requires the neighbouring cube and causes the bandwidth limitation of LBM implementations. It is also noteworthy to emphasize on the simple domain discretization and decomposition, which is a major benefit of LBM

3. Lattice Boltzmann Methods

when it comes to mesh generation and load balancing in parallel execution.

3.3.1. Collision operators in LBM

The collision operator models the physics and is a crucial ingredient for every LBM. As derived above, one requirement to a typical collision operator is the conservation of mass, momentum and energy, see (3.5) along the (local) trend towards a Maxwell–Boltzmann distribution. The discrete analogs of the conservation equations read

$$\sum_{i=1}^q Q(f_i) = 0, \quad (3.7a)$$

$$\sum_{i=1}^q \mathbf{v}_i Q(f_i) = \mathbf{0}, \quad (3.7b)$$

$$\sum_{i=1}^q |\mathbf{v}_i|^2 Q(f_i) = 0. \quad (3.7c)$$

There are many formulations for such collision operators as the recent survey of Coreixas et al. [33] shows. For the sake of simplicity it is considered the *BGK* collision operator

$$Q_{BGK}(f_i) = \frac{1}{\tau} (f_i^{eq} - f_i), \quad (3.8)$$

for a relaxation time τ and a discrete representation of an equilibrium function f_i^{eq} . LBM that implement the *BGK* collision operator are often referred to as *BGK* LBM. This collision operator relaxes the recent particle distribution function towards an equilibrium state at the rate determined by relaxation time τ . The physics behind this rather synthetic *BGK* collision operator is based on two aspects, the relaxation time and the equilibrium function. Thinking of a fluid, the relaxation time is related to the viscosity and the equilibrium function to the fluid state at equilibrium.

Let's assume that the equilibrium state is reached by the particle distribution function f_i , then the Boltzmann equation vanishes $\frac{d}{dt}f = 0$ and hence the simulated system is at equilibrium. The magic happens when forcing the particle distribution away from equilibrium by imposing boundary conditions. Then the simulated 'forced away from equilibrium' state expresses a proper physical state of velocity field or pressure field through the moments. Depending on the relaxation time τ the viscosity of the fluid is adjusted.

3.3.2. Equilibrium functions in LBM

Considering *BGK* LBM and its application to hydrodynamics, the equilibrium function is chosen as a discrete Maxwell–Boltzmann distribution. The derivation of the discrete Maxwell–Boltzmann distribution is separated into two steps: a Taylor truncation of the continuous distribution and a Gauss–Hermite integration of the collision invariants (3.7). First, the local equilibrium state of the populations is formulated for ideal gases according to Maxwell–Boltzmann distribution

$$\begin{aligned} f(\mathbf{v}) &= \left(\frac{m}{2\pi RT}\right)^{\frac{3}{2}} \exp\left(-\frac{m|\mathbf{v}-\mathbf{u}|^2}{2RT}\right) \\ &= C \exp\left(-\frac{|\mathbf{v}|^2}{2RT}\right) \exp\left(\frac{|\mathbf{u}|^2}{2RT} - \frac{\mathbf{v}\cdot\mathbf{u}}{RT}\right) \\ &\approx C \exp\left(-\frac{|\mathbf{v}|^2}{2RT}\right) \left(1 + \frac{\mathbf{v}\cdot\mathbf{u}}{RT} + \frac{2(\mathbf{v}\cdot\mathbf{u})^2}{(2RT)^2} - \frac{|\mathbf{u}|^2}{2RT}\right), \end{aligned}$$

for the specific gas constant R , some constant C and Taylor expansion up to second order in \mathbf{u} . This trivial case proves the consistency of the modeling. This truncated Maxwell–Boltzmann equation is of form $f(\mathbf{u}) = \exp(-u^2)p(u)$ for a polynomial p of second order and can be integrated exactly by the Gauss–Hermite quadrature rule, for certain LBM weights w_i and velocity sets \mathbf{v}_i . The order of the Gauss–Hermite quadrature is chosen such that, the discrete collision invariants

$$\int \mathbf{v}^k f(\mathbf{v}) d\Omega = \int \mathbf{v}^k p(\mathbf{v}) \exp(-|\mathbf{v}|^2) d\Omega = \sum_i \mathbf{v}_i^k w_i p(\mathbf{v}_i), \text{ for } k=0, 1 \text{ and } 2$$

are preserved. This property is important and guaranties the mass, momentum and energy conservation of the collision operator, here *BGK* collision.

In more detail, the (discrete) equilibrium function is retrieved by

$$f_i^{eq}(\rho, \mathbf{u}) = w_i \rho \left(1 + \frac{\mathbf{v}_i \cdot \mathbf{u}}{c_s^2} + \frac{(\mathbf{v}_i \cdot \mathbf{u})^2 - c_s^2 |\mathbf{u}|^2}{2c_s^4}\right), \quad (3.9)$$

as a function of macroscopic density ρ and velocity \mathbf{u} . For 3D applications, the *D3Q19* stencil with its 19 directions (in favor of Gauss–Hermite quadrature: 19 grid points) and the lattice speed of sound $c_s = \sqrt{1/3}$ is a suitable discretization stencil. Details for the precise derivation is found in mathematics-style works [195, 101, 41].

The main characteristics of an equilibrium function is, that it is a function of macroscopic observables and needs only the information of the averaged population f_i .

3.3.3. LBM and target equations

The LBM are designed on mesoscopic scale to solve certain macroscopic target equations. Here, common LBM models for typical target equations, namely Navier–Stokes, advection–diffusion and diffusion equations, are presented briefly. The brief classification assigns the order of the Maxwell–Boltzmann equilibrium to the target equation and is adopted from the textbook of Mohamad [130] and can also be found in Krause et al. [103].

LBM for Navier–Stokes equation

The Navier–Stokes equation for incompressible fluids ($\nabla \cdot \mathbf{u} = 0$) reads

$$\partial_t \mathbf{u} + (\mathbf{u} \cdot \nabla) \mathbf{u} = -\frac{\nabla p}{\rho} + \nu \nabla^2 \mathbf{u},$$

for fluid velocity \mathbf{u} , density ρ , pressure p and kinematic viscosity ν .

The corresponding LBM deploys a 2nd order Maxwell–Boltzmann equation (3.9) and assigns the relaxation time τ to the viscosity by formula $\nu = c_s^2 (\tau - \frac{\Delta t}{2})$. According to the second-order non-linearity of the target equation, the Navier–Stokes equation, the LBM scheme relies also on a second order equilibrium expression. A suitable lattice stencil is the $D3Q19$ model. Such LBM methods are second order schemes for the velocity and first order schemes for the pressure, in the diffusive scaling ($\Delta t = (\Delta x)^2$), see theoretical analysis of the truncation and asymptotic behavior in [79, 92].

LBM for advection–diffusion equation

The general advection–diffusion equation, for a species of interest Φ in a fluid field of velocity \mathbf{u} , reads

$$\partial_t \Phi = \nabla \cdot D \nabla \Phi - \nabla \cdot \mathbf{u} \Phi.$$

Here, D is the diffusion coefficient or the (thermal) diffusivity. Combining both, the Navier–Stokes and advection–diffusion, a multi-physics Euler–Euler model for the simulation of dilute particulate fluid flows is achieved [177]. Another promising approach is to solve the conservative form of the energy equation in the framework of LBM, whose solution appears as a source term in the advection–diffusion equation. The source term formulations is suitable for conjugated heat transfer in general multiphase or multicomponent systems, being independent of the topology of the interface [174, 97].

The relaxation time for the simulation is defined by equation $D = c_s^2 (\tau - \frac{\Delta t}{2})$, see [106, 145]. It is sufficient to use the Maxwell–Boltzmann equation (3.9) up to first order

and $D3Q7$ lattice stencils.

LBM for diffusion–reaction equation

Diffusion–reaction equation (steady-state) or more general Poisson equation reads

$$\nabla \cdot D \nabla \Phi(\mathbf{x}) = S(\mathbf{x}) ,$$

for a right hand side S that models the reactive part. For a vanishing reactive term, the equation reduces to the Laplace equation and for a linear reactive term, the equation corresponds to the Helmholtz equation. The comparisons of LBM with analytical solutions and alternative numerical solutions is discussed with respect to solution accuracy, convergence and computational efficiency [140, 145, 27]. Ponce Dawson et al. [145] pointed out, that this LBM is most accurate for $\tau = 1$ (relative error of 0.04%) and of 2nd order considering diffusion without any reactive terms.

In summary, it can be said, that the LBM for diffusion processes is obtained through the LBM for advection–diffusion processes by fixing the fluid velocity \mathbf{u} to zero. Hence, the Maxwell–Boltzmann equation is of zeroth order and the diffusion parameter as above. Additional sinks or sources can be incorporate according to the procedure of external forces in fluid flow applications.

3.4. From Lattice Boltzmann Methods to Macroscopic Equations

A crucial difference of LBM compared to traditional numerical schemes such as Finite–Volume Method (FVM), is the modeling and simulation scope. LBM is not a discrete formulation of a macroscopic equation, e. g. Navier–Stokes and others. The typical collide-and-stream equations of the LBM can be obtained through discretization of the (continuous) Boltzmann equation equipped with the BGK collision operator, see the pioneer work of He and Luo [77]. However, without an evidence or linkage from the retrieved collide-and-stream equations to macroscopic observables, this procedure is of little interest. This task is typically completed by a multiscale expansion of the LBM followed by several courageous algebraic operations, researchers translate mesoscopic parameter and equations to their macroscopic counterparts [29, 66]. Despite the fact, that these methods are widely used, mathematicians often found the procedures to rely on sloppy grounds [183].

3. Lattice Boltzmann Methods

Surprisingly, the initial goal of this discretization is not to solve the Boltzmann equation but instead solve macroscopic target equations, e. g. Navier–Stokes equations and others. In other words, the LBM, as we know them today, are motivated by the particle character of the Boltzmann equation and applied to solve macroscopic equations, rather than the Boltzmann equation. The relation of the modeling scope and its typical equation is illustrated in Figure 3.4. It is also important to note, that the simplification of the collision

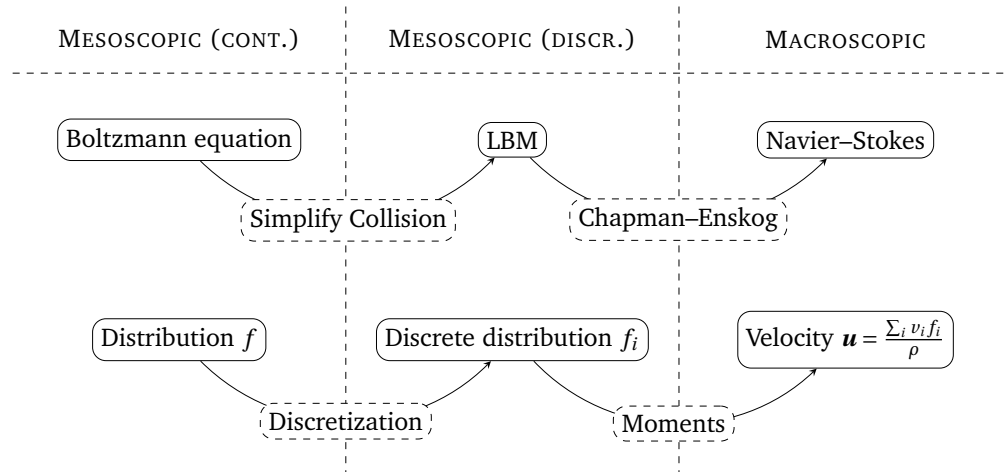


Figure 3.4.: Summary and relation of the micro-, meso- and macro level for application to fluid flows.

already assumes some physical behavior as the two constraints above demonstrates. As a consequence, the derivation of LBM beyond the common hydrodynamic discipline, might implement other constraints to retrieve collide-and-stream equations from their model equation, as discussed in [125] and Section 4.2. In fact, the first LBM are designed as lattice gas automata and were not related to macroscopic equations at all as pointed out in [195].

In the last two decades, the application of LBM towards solving multi-physics problems catalyzed and speeded-up the development in a tremendous way. Over the years, researches developed a zoo of collision operators, claiming diligently their collision operator outperforms others for a specific problem. An objective and theoretical comparison of collision models for hydrodynamic LBM was presented in Coreixas et al. [33].

To summarize the modeling and origin of LBM it can be said, they evolved as a bottom-up approach that originates in the Boltzmann equation. The numerical algorithm is derived for a simplified collision model and is known to solve the Navier–Stokes equations in the hydrodynamic limit [160, 9].

4. Radiative Transport with LBM

A relatively new technique for the simulation of radiation transfer are LBM, which are well-established tools in the context of fluid dynamics. Both, the radiation field and the fluid flow are modeled on mesoscopic scale, describing the evolution of the (velocity and photon) distribution function by a Boltzmann-type equation. Until now, LBM mainly are developed for hydrodynamics and with little focus on the radiation field, which is surprising since both phenomena are modeled by very similar Boltzmann equations. The main difference is referred to the particle-particle collision in the fluid flow context and particle-volume collision in the application to the RT. As a consequence, the application of LBM to RT is expected to differ on: (a) particle-volume collision operator and (b) equilibrium state for photon transport. Beyond those physical driven differences, the structure of the model equations is similar and deriving RTLBM is a very promising venture.

If the algorithm is equally parallel and intuitive than for LBM, RTLBM are a competitor for traditional numerical methods for RT. For instance, LBM have the great advantage that all computational operations are carried out locally in the numerical grid and no derivatives need to be approximated from adjacent grid points. This enables highly efficient implementations for parallel computing and super-computing [131, 45], which is particularly interest for computationally costly simulations of RT. Coupled heat transporting LBM benefit from the consistent scope of model equations as pointed out by [157, 52].

Analogously to the hydrodynamic LBM, a summary of the involved scopes in RTLBM is shown in Figure 4.1. There are two main strategies to develop general RTLBM. The bottom-up approach implements RTLBM as a discrete version of the RTE and aims to transport the particle character into the mesoscopic algorithm. Any kind of bottom-up motivated RTLBM, in this thesis, is name mesoscopic RTLBM. On the other side, the top-down approach relies on an indirection introduced by a target equation, here Helmholtz equation. For the latter, the technique of Chapman–Enskog provides evidence that the heuristically proposed RTLBM solves the target equation. The latter are designed to solve a macroscopic target equation and are hence named macroscopic RTLBM.

4. Radiative Transport with LBM

Being firstly suggested by Geist et al. [62], several mesoscopic RTLBM have been proposed over the last decade [16, 5, 115]. The majority of these models [115, 16, 5, 188] consider the RTE as a Boltzmann-type kinetic equation [148]. This class of models is based on a direct discretization of the RTE in the angular, spatial and temporal space. The numerical solution is obtained thereafter by an efficient collide-and-stream algorithm, which is a characteristic ingredient of general LBM. The target equation of the algorithm is the RTE itself, so that the physical model to be solved is still on the kinetic level. Mesoscopic models typically show first order convergence, anisotropic scattering can be incorporated intuitively and no assumption about the isotropy of radiance must be made [118].

An alternative approach presented in [111, 125] originates from the assumption that the solution of the RTE can be approximated by the solution of a macroscopic Helmholtz equation. Under the assumption, that the transport regime is scattering dominant, the diffusion approximation also known as P1-Approximation [184, 89] derives the Helmholtz equation from the RTE. This class of RTLBM aims to solve the RTE indirectly through the Helmholtz equation. The correct asymptotic behaviour of this scheme is analyzed by a Chapman–Enskog expansion, which connects the collision rule to the macroscopic diffusion coefficient what is in accordance to *classical* formulations of the LBM [125]. In a subsequent study, it was pointed out that the macroscopic model is numerically very efficient and accurate in optically thick media and that second order convergence is achieved due to the diffusive scaling of the transport coefficients [121].

Typically, for all general LBM, the flexibility and intuitiveness of RTLBM allows to extend the numerical algorithm to many related problems. For instance, the adaption of RTLBM to transient transport [208, 206, 188, 53], the polarized radiation [207] and to the visible light spectrum [116] have already been studied. Even adaptive mesh refinement and GPU implementation of RTLBM have been reported [187]. Recently, Cen et al. [23] reported an efficient RTLBM that is applied to optical tomography, emphasizing the performance improvements through RTLBM. The combination of volumetric radiation and natural convection has been simulated using the LBM, respectively RTLBM, in many publications [175, 114, 10]. By replacing the Maxwell–Boltzmann distribution by the Bose–Einstein distribution, researches developed a novel LBM for the transport of phonons [134, 68].

This chapter derives methodologically the general RTLBM as published by the authors Mink et al. [125, 121] and others [115]. Further, it is proposed for the first time a novel P1-RTLBM, that combines the benefits from macroscopic and mesoscopic RTLBM. Besides a clear development of the three RTLBM there is a precise categorization and

delineation to hydrodynamic LBM. Finally, the chapter closes with a comprehensive boundary modeling for general surfaces, based on the publication Mink et al. [123].

4.1. Discrete Radiative Transport Lattice Boltzmann Equation

The RTE describes the evolution of radiance due to scattering and absorption, through a Boltzmann-type equation. Except the formulation of the collision, that for RTE is a photon-volume collision, the mathematical structure is equal. Thus, applying similar discretization techniques as for fluid flow problems appears promising, when deriving an LBM for RTE phenomena.

Recall the RTE (2.3) is a balance equation that explains the change of radiance due to absorption μ_a and scattering μ_s by

$$\frac{1}{c} \partial_t L(t, \mathbf{x}, \mathbf{s}) + \mathbf{s} \cdot \nabla L(t, \mathbf{x}, \mathbf{s}) = -\mu_s \left(L(t, \mathbf{x}, \mathbf{s}) - \int_{4\pi} p(\mathbf{s}, \mathbf{s}') L(t, \mathbf{x}, \mathbf{s}') d\Omega' \right) - \mu_a L(t, \mathbf{x}, \mathbf{s}) \quad (4.1)$$

$$= -\mu_s (L(t, \mathbf{x}, \mathbf{s}) - L^{eq}(t, \mathbf{x}, \mathbf{s})) - \mu_a L(t, \mathbf{x}, \mathbf{s}) . \quad (4.2)$$

In addition the phase function p models the single scattering events. Black body radiation and other sources respectively sinks can be easily added to the above equation. The right hand side is separated according to the scattering and absorption contributions and yields already in a similar representation than the Boltzmann equation (3.1) equipped with the *BGK* collision operator (3.8). From this equation it can be seen how the radiative characteristics are represented as a *BGK*-Boltzmann equation in the context of LBM. The scattering corresponds to the collision and absorption plays the role of external forces or sinks. As LBM is a relaxation scheme, it is deduced, that RTLBM are suitable for RT regimes that scatter significantly. Media that is described by a dominant absorption parameter is expected to be critical.

Now, the goal is to apply the discretization known from hydrodynamic LBM to the above equation and obtain an explicit scheme that approximately solves RTE. It is expected that the retrieved numerical algorithm can be implemented as an LBM collide-and-stream equation and hence the computation of the radiation field and fluid flow is attained in a consistent framework of LBM. To start with the discretization of the phase space $[0, \infty) \times \mathbf{X} \times \mathbf{V}$, first the typical LBM stencils have to be specified. Consider a discrete phase space with a stencil that defines directions \mathbf{s}_i and weights w_i , then the radiance is expressed as a *photon fluence function*

$$f_i(t, \mathbf{x}) = w_i L(t, \mathbf{x}, \mathbf{s}_i) ,$$

4. Radiative Transport with LBM

where \mathbf{x} are discrete lattice points, also referred to as (lattice) cells, and vectors \mathbf{s}_i are pointing towards a neighbouring cell. A cell at position \mathbf{x} is equipped with q photon fluence functions f_i , for every direction as depicted in Figure 3.3. In the following the f_i are also referred to as *populations* to emphasis the numerous f_i for every cell.

Following the arguments of the discretization in space and time of the *BGK* Boltzmann equation from [105, Chapter 3.5] or the original work of He and Luo [77], the continuous equation (4.2) can be transferred to the discrete form

$$\frac{f_i(t + \Delta t, \mathbf{x} + c_i \mathbf{s}_i \Delta t) - f_i(t, \mathbf{x})}{\Delta t} = -\mu_s c_i (f_i(t, \mathbf{x}) - f_i^{eq}(t, \mathbf{x})) - \mu_a c_i f_i(t, \mathbf{x}). \quad (4.3)$$

Here, the equilibrium function f_i^{eq} is a discrete representation of L^{eq} , which will be presented in detail in Section 4.2. The contribution $c_i = |\mathbf{s}_i|$ is an additional term for RTLBM and accounts for the transport of radiance. For instance, the axis aligned directions are trivially $c_i = 1$, but the diagonal direction gets scaled.

In the last step (4.3) is rewritten in the collide-and-stream form

$$\begin{aligned} f_i^*(t, \mathbf{x}) &= f_i(t, \mathbf{x}) - \mu_s c_i \Delta t (f_i - f_i^{eq})(t, \mathbf{x}) - \mu_a c_i \Delta t f_i(t, \mathbf{x}), \\ f_i(t + \Delta t, \mathbf{x} + c_i \mathbf{s}_i \Delta t) &= f_i^*(t, \mathbf{x}), \end{aligned}$$

where in the first equation the population is rearranged according to the scattering and absorption characteristics of the volume. The second equation, then propagates the novel populations to the neighboring cells. More precise, after one time step Δt , every photon fluence function is transferred exactly to the neighboring cell located at $\mathbf{x} + c_i \mathbf{s}_i \Delta t$ or $\mathbf{x} + \mathbf{s}_i \Delta x$ for the definition $\Delta x_{(i)} = c_i \Delta t$. This collide-and-stream equation is the core of every RTLBM presented in the present thesis.

The following section presents three RTLBM with precise choice of stencils and equilibrium functions. All simulation models are given in a collide-and-stream form accompanied with the associated equilibrium expression.

4.2. Radiative Transport Lattice Boltzmann Methods

LBM are relaxation schemes in which populations tend toward a local equilibrium state (Maxwell–Boltzmann function (3.9)), typically a function of higher moments, e. g. 0th moment ρ and 1st moment \mathbf{v} . The speed of this relaxation process is determined by the relaxation time τ for general LBM or $\mu_s c_i$ in the context of RTLBM.

In fact, the equilibrium formulation is such a dominant ingredient for RTLBM, that can

be used to classify the RTLBM in literature. One category consists of the moment-based equilibrium formulations presented in Section 4.2.1, named macroscopic RTLBM and P1-RTLBM. The second category, referred to as mesoscopic RTLBM, contains the fully discretized scattering integral formulations, see Section 4.2.2. The latter strikes out a new path by considering a discrete version of the phase function and computing the scattering integral for all directions in an LBM stencil. A full theoretical discussion of the presented models is provided in Section 4.2.4. Finally, the Fresnel boundary is introduced in Section 4.3 to equip the RTLBM with physical boundary models.

All presented RTLBM, boundary models and normalization techniques are available to the public in OpenLB version 1.3 as referenced in more detail in Appendix E.

4.2.1. Macroscopic RTLBM

RT in highly scattering media can be approximated by a Helmholtz equation as presented in Section 2.5. From theory, it is known, that the approximation is accurate in RT regimes with scattering albedo $a > 0.9$, describing the RTE by the macroscopic Helmholtz equation

$$\Delta\Phi = \mu_{\text{eff}}^2\Phi,$$

for an effective attenuation coefficient μ_{eff} which is a function of absorption and scattering coefficients as depicted in (2.11). Instead of solving the RTE, the macroscopic RTLBM aims at first to approximately solve the macroscopic target equation. The gained insights are then applied to develop an enhanced version in Section 4.2.3, where additional information from the approximation are plugged in the equilibrium formula.

The first 3D RTLBM was proposed by Mink et al. [125] reporting a collide-and-stream equation

$$f_i(t + \Delta t, \mathbf{x} + \mathbf{s}_i\Delta x) = f_i(t, \mathbf{x}) - \frac{1}{\tau} (f_i(t, \mathbf{x}) - f_i^{\text{eq}}(t, \mathbf{x})) - \frac{\mu_{\text{eff}}^2}{8} (\Delta x)^2 f_i(t, \mathbf{x}), \quad (4.4)$$

with 0th order discrete Maxwell–Boltzmann equilibrium distribution (3.9) of

$$f_i^{\text{eq}} = w_i \sum_j f_j,$$

equipped with relaxation time $\tau = 1$ and $D3Q7$ stencils. Special attention is paid to the choice of the lattice stencil $D3Q7$ with axis aligned directions \mathbf{s}_i and weights w_i . They are chosen, such that the moments of f_i^{eq} can be computed by a Gauss–Hermite quadrature formula, e. g. $\int f^{\text{eq}}(t, \mathbf{x}, \mathbf{s}) d\Omega = \sum_i w_i f^{\text{eq}}(t, \mathbf{x}, \mathbf{s}_i) = \sum_i f_i^{\text{eq}}(t, \mathbf{x})$. As emphasized by Mink

4. Radiative Transport with LBM

et al. [125], this guaranties that the general conservation requirements of LBM collision in (3.7) and the energy conservation of the scattering integral in (2.4) are satisfied. For details on the Gauss–Hermite quadrature rule and common LBM stencils it is referred to [77, 195].

In agreement to the approximation, where absorption and scattering is bunched in the effective attenuation coefficient μ_{eff} , the above RTLBM is stated only in μ_{eff} . The authors reported that a small set of 7 discrete directions results in a very fast converging scheme (2nd order)[125], that in addition benefits from low memory requirements.

In contrast to general transient diffusion–reaction LBM, where the non-dimensional relaxation time τ is a function of the diffusivity D see [145, 27, 61, 137], this approach allows choosing $\tau = 1$. Since LBM for diffusion problems are in particular accurate for $\tau \approx 1$, this is an elemental step which is achieved by a suitable target equation that does not depend on the diffusion coefficient, but on the effective attenuation coefficient. Two assumptions justify this approach as pointed out in [184, 125, 121]. First, the RT happens instantaneously at the considered time scales, which allows to consider the steady representative. Second, the reformulation to the Helmholtz equation (diffusion–reaction equation with $D = 1$) leads to the choice of $\tau = 1$. This point is further discussed in Section 5.1.2 by means of numerical experiments.

The numerical validation against a spherical test geometry with known analytical solution is presented in Section 5.1 and the Chapman–Enskog analysis, that translates the kinetic algorithm to macroscopic target equations, is provided in Appendix A. The comprehensive validation against MC data is presented in Section 6.4.

Additional numerical test cases from [105, Section 8.6.1] and Chai and Shi [27, Example 2] have been implemented in OpenLB ¹. The results agree with the literature and suggest that the implementation is validated for diffusion problems.

4.2.2. Mesoscopic RTLBM

The mesoscopic RTLBM aim to approximate the scattering integral with the same set of discrete directions then imposed by the LBM as the discretization of the phase space. By using the same stencil, the computations can be executed on the same grid yielding a collide-and-stream equation in the framework of LBM.

The RTLBM with resolved scattering integral are in particular interesting for two reasons. First, they are designed to incorporate anisotropic scattering with volume through a discretization scheme for the phase function. Second, the stencil differs from

¹The implementation is found in the source code application `gaussianHill2D` and `helmholtz`.

the fluid flow stencils, as they are based on the Lebedev–Laikov quadrature rule as proposed originally by McHardy et al. [115].

Recall the scattering integral that accounts for the in-scattering from all \mathbf{s}' into propagation direction \mathbf{s} by

$$\int_{4\pi} p(\mathbf{s}, \mathbf{s}') L(t, \mathbf{x}, \mathbf{s}') d\Omega' = L^{eq}(t, \mathbf{x}, \mathbf{s}) . \quad (4.5)$$

The probability of a single scattering event at position \mathbf{x} from direction \mathbf{s} into \mathbf{s}' is denoted by the phase function $p(\mathbf{s}, \mathbf{s}')$, or the discrete analog $p(\mathbf{s}_i, \mathbf{s}_j) = p_{i,j}$. The straight forward discretization into q directions of (4.5) yields in an approximation error, that in particular violates the energy conservation property for anisotropic scattering events as reported in Kim and Lee [98] and Hunter and Guo [87]. Consequently, many techniques have been developed, to cure the discretization error with different normalization strategies [87, 86, 85, 88, 98]. All techniques are designed such that the two closures of the discrete phase function

$$\begin{aligned} \sum_i p_{i,j} &= 1, \\ \sum_i \mathbf{s}_i \cdot \mathbf{s}_j p_{i,j} &= g, \end{aligned}$$

for all $j = 1, \dots, q$ are fulfilled simultaneously, where g is the anisotropy factor (2.5). Both constraints have already been stated in its continuous counterparts, see (2.4c) and (2.5). Those $2q$ equations form an under determinate system of linear equations, since there are $q(q+1)/2$ unknown $p_{i,j}$. Note that the matrix with entries $p_{i,j}$ can be defined by $q(q+1)/2$ parameters, due to its symmetry. A unique solution that satisfies the two closures, from above, is obtained by means of Moore–Penrose inverse [167], solving a least square problem. The iterative nature of the normalization scheme makes this task time consuming for LBM stencils with many directions, e. g. $D3Q27$ stencils. However, this computation has to be carried out only once per simulation and takes less than 5 min due to the hardware optimized implementation of the least square algorithm in LAPACK. Further remarks and comments on the OpenLB implementation of the normalization technique proposed in Hunter and Guo [87] is provided in Appendix E.3.

Next, the construction of the equilibrium function is retrieved, starting from the discrete formula

$$f_i^{eq} = w_i L^{eq}(t, \mathbf{x}, \mathbf{s}_i) ,$$

for an intensity equilibrium (4.5). Consider the general matrix \mathbf{A} retrieved by the normalization strategy from above and with entries $\mathbf{a}_{\mu,\nu}$ which account for the probability

4. Radiative Transport with LBM

of a particle undergoing an scattering event $\mathbf{s}_\mu \rightarrow \mathbf{s}_\nu$. It is known that matrix \mathbf{A} is symmetric, since scattering event is symmetric, conserves energy and the anisotropy factor. The retrieved equilibrium function then reads

$$f_i^{eq} = w_i \sum_j \mathbf{a}_{i,j} f_j. \quad (4.6)$$

Together with the collide-and-stream equation

$$f_i(t + \Delta t, \mathbf{x} + c_i \mathbf{s}_i \Delta t) = f_i(t, \mathbf{x}) - \mu_s c_i \Delta t \left(f_i - w_i \sum_j \mathbf{a}_{i,j} f_j \right) (t, \mathbf{x}) - \mu_a c_i \Delta t f_i(t, \mathbf{x}), \quad (4.7)$$

this states the mesoscopic RTLBM with resolved scattering integral, proposed initially by [115] and with enhancements in [121]. The corresponding stencils are obtained from the Lebedev–Laikov quadrature rule, see Appendix E.2.

Recently, an enhancement of the present mesoscopic RTLBM was developed by applying a Runge–Kutta (RK) scheme to the collision step. The RK approximates collision at the time Δt through four several intermediate steps and it was found to foremost improve the ballistic RT [121, 118]. The method was co-authored and implemented in OpenLB, see Appendix E.2 by the author of the present thesis. The computational expensive method improves mainly the accuracy for absorbing media and was presented first and in full detail in the PhD thesis of McHardy [118]. The validation against MC data for various RT regimes is shown in Section 4.2.2.

4.2.3. P1-RTLBM

The P1-RTLBM combines the comprehensive modeling of radiative phenomena from the mesoscopic RTLBM with the computational efficiency of the macroscopic RTLBM. It is designed to overcome the limitations of both, the heavy computational cost and the poor modeling of radiative characteristics, and combine the strength to make general RT problems more accessible for LBM. To this goal, the complex equilibrium expression of the mesoscopic RTLBM in (4.6) is simplified according to the technique of spherical harmonics.

The derivation of the equilibrium expression is based on the expansion of radiance in the base of spherical harmonics. This expansion is an essential element in the P1-Approximation of the RTE and also in the present RTLBM. Hence, the resulting LBM

scheme is named P1-RTLBM. The truncated spherical harmonics expansion yields

$$L(t, \mathbf{x}, \mathbf{s}) = \int L(t, \mathbf{x}, \mathbf{s}) d\Omega + \mathbf{s} \cdot \int \mathbf{s}' L(t, \mathbf{x}, \mathbf{s}) d\Omega. \quad (4.8)$$

Higher order terms are found in the textbook of Wang and Wu [184]. This expansion can be interpreted as a decomposition of radiance into an isotropic (first term on the right hand side) and an anisotropic part (second term on the right hand side) compare Figure 2.8. By substituting the definition of the discrete particle fluence rate $f_i = w_i L(t, \mathbf{x}, \mathbf{s}_i)$ into (4.8) and applying the Lebedev–Laikov quadrature rule, then the radiance is retrieved as

$$\begin{aligned} L(t, \mathbf{x}, \mathbf{s}) &= w_i \left(\sum_j f_j + \mathbf{s}_i \cdot \sum_j \mathbf{s}_j f_j \right) \\ &= w_i (\Phi + \mathbf{s}_i \cdot \mathbf{J}). \end{aligned}$$

The second term on right hand side accounts for the directed (anisotropic) transport, e. g. close to boundary where the injected particles impose anisotropic transport which depends on direction \mathbf{s} . This formula connects the 0th and 1st moment (macroscopic variables) with the mesoscopic equilibrium populations and is chosen as the novel equilibrium expression

$$f_i^{eq}(\Phi, \mathbf{J}) = w_i (\Phi + \mathbf{s}_i \cdot \mathbf{J}). \quad (4.9)$$

It is clear, that for vanishing flux \mathbf{J} this construction simplifies to $f_i^{eq} = w_i \Phi$ which shows consistency to the macroscopic RTLBM in isotropic transport regimes. All together, the P1-RTLBM reads as a collide-and-stream equation

$$f_i(t + \Delta t, \mathbf{x} + c_i \mathbf{s}_i \Delta t) = f_i(t, \mathbf{x}) - \mu_s c_i \Delta t \left(f_i - w_i \left(\sum_j f_j + \mathbf{s}_i \cdot \sum_j \mathbf{s}_j f_j \right) \right) - \mu_a c_i \Delta t f_i(t, \mathbf{x}).$$

Models with higher order expansion in the basis of spherical harmonics can be implemented straight forward in the framework of P1-RTLBM. The P1-RTLBM is equipped with a moment based formula for the local equilibrium state and therefore follows the spirit of general LBM. Due to the local averaging through moments and integration of directed RT, this model is closer to the radiative characteristics, than the macroscopic RTLBM and requires notable less computations than the mesoscopic RTLBM with its resolved scattering integral. A detailed numerical validation is presented in Section 6.3.

4.2.4. Discussion of the RTLBM

The pioneer work of Geist et al. [62] developed a collide-and-stream equation where the particle-volume interaction is written as a matrix vector multiplication. This expression is a rather untypical in LBM literature, but the equilibrium contribution in (4.6) can also be written as a matrix multiplication of $\mathbf{A}\mathbf{f}$ where the populations f_i are written as a vector \mathbf{f} . Now, by adding the absorption term in (4.7) to the diagonal of the matrix \mathbf{A} the original matrix of Geist et al. is retrieved. A distinctive feature however is, that the constructed matrix in [62] is not symmetric, which contradicts the reciprocity of scattering events. However, this constraint has been cured by the methodological derivation of the mesoscopic RTLBM, where the computation of the scattering matrix is treated carefully. It is required to solve the least square problem to obtain the normalized discrete scattering matrix.

Another interpretation of this particular matrix is, that it states an equilibrium configuration towards which the population relaxes. Interestingly, this configuration deviates from the Maxwell–Boltzmann distribution (3.9). Due to its photon-particle collision, the concept of a photon distribution function at rest does not apply as for particle-particle collision of the ideal gas. The relaxation towards this equilibrium configuration is determined solely by the scattering behavior of the volume, compare relation of viscosity and relaxation time in hydrodynamic LBM. Since this equilibrium does not consider moments, it follows rather the spirit of DOM approach of a discretized Boltzmann equation, than standard LBM. As numerical experiments will show, the mesoscopic RTLBM shares even the ray-effects, known in DOM.

Wang et al. propose a novel FVM-based LBM to simulate RT problems, where the numerical integration of the scattering is based on an FVM [189]. In light of the philosophy of the multi-speed LBM, this method requires a vast number of discrete directions, for instance $q = 48$ directions for 2D problems. None of the numerical test cases treat 3D RT, which would be challenging keeping in mind the required directions. However, the FVM-based LBM was extended by the same group to many interesting topics such as transient and multi-group RT [188, 186] but also technical topics such as adaptive mesh refinement and unstructured meshes [187, 189].

The mesoscopic RTLBM installs a single stencil for computational grid and discrete scattering. Therefore, not only the accuracy of the discrete scattering events are governed by the Lebedev–Laikov stencils, but also the computational grid itself, which is necessary to implement RT in the framework of LBM. This coupling is strong and might limit the choice of stencils with many discrete directions, due to an increasing amount of

memory and computation time. Until now, the mesoscopic RTLBM cannot compute the scattering at a higher accuracy and then distributes the population to a stencil of fewer directions.

When considering isotropic RT, the macroscopic RTLBM is expected to be accurate. Its modeling relies on high scattering albedo which is equally to say isotropic RT, yielding a computational efficient RTLBM equipped with $D3Q7$ stencil, as shown later in Section 6.4. Its drawback of predicting anisotropic transport regimes, for instance close to radiative sources but also walls, is well understood from theory of the diffusion approximation [89, 184] and macroscopic solvers [51, 39]. Numerical investigations of the macroscopic RTLBM in Section 6.4 will show that this deficits apply also to this LBM scheme.

This deficit is cured by the mesoscopic RTLBM, that aim to resolve the anisotropic transport regimes. This is in particular relevant for regions close to any radiative source or wall, since after several mean free paths the transport regime becomes rapidly isotropic. However, the increased computational cost remains constant through the domain, unlike simpler models such as the macroscopic RTLBM are sufficient after the length of several mean free paths. Thus, a trade-off between computation time and the modeling of anisotropic transport has to be managed, when applying to any of the RTLBM models.

A hybrid model, that simplifies the anisotropic transport implementing a P1-Approximation motivated equilibrium expression, is then proposed to implement a precise and efficient RTLBM. The P1-RTLBM is based on a mesoscopic equilibrium that accounts additionally, to the flux, when compared to macroscopic RTLBM, and is shown in Section 5 to be valid for a greater set of optical parameters, beyond the highly scattering media.

4.3. Boundary Models for RTLBM

Boundaries for RT are typically non-permeable, which stands out from many fluid flow problems. The reason for that is, that radiation can either be transmitted, emitted or reflected on the boundary, even a combination of all microscopic phenomena. In terms of radiative sources, the main task for LBM boundary treatment is, the construction of populations f_i such that the imposed intensities are matched on macroscopic level, here by the relation (2.1). This is a non-trivial task since generally there are more populations to choose than there are conditions. The same situation holds for outgoing boundary treatment. Meaning, in most cases there is an under determined system of equations to solve on every boundary cell on every time step.

Boundaries for the application to RTLBM are rarely discussed and analyzed in the literature. Most often they are stated as a special collision rule that can be computed

4. Radiative Transport with LBM

rapidly with rather unspecific physical meaning [188, 186, 206, 208, 199, 23]. For instance, Wang et al. [188] applied a reflection scheme that is not further related to the physic of reflection on surfaces nor is it proven to be grid independent. This two points are treated with little interest in all above mentioned publications. To address the raised issues, a general approach of deriving a RTLBM boundary treatment for partly reflecting surfaces is proposed in Section 4.3.3. The developed mesoscopic model and its parameters are linked to surface properties described by Fresnel's equation.

A proper understanding of boundary interplay is needed since only the boundary effects forces the population away from the equilibrium state and as a result there is a non-trivial radiative distribution. Without providing boundaries with physical meaning, the RTLBM might not attract the attention they aim for and will be limited to the academic examples e. g. rectangular enclosures.

4.3.1. Source models

The source models are classified into collimated and diffuse sources. Both are described on macroscopic level by a fix intensity Φ_B at a boundary position \mathbf{x}_B . In the first scenario, the radiative source injects populations only orthogonal to the wall orientation, whereas the diffuse source injects photons into all inward pointing directions. These are simple boundary treatments and the construction on a suitable kinetic boundary population is straight forward.

In the scenario collimated source the boundary populations are constructed by

$$f_i(\mathbf{x}_B) = \begin{cases} \Phi_B(\mathbf{x}_B), & i \text{ inward pointing and orthogonal to the wall,} \\ 0, & \text{else,} \end{cases}$$

on a boundary element \mathbf{x}_B . For axis aligned boundaries, there is exactly one direction i that is orthogonal to the wall normal. It is clear, that the defined boundary populations yield in $\sum_i f_i = \Phi_B$, as imposed by macroscopic boundary condition.

Analogous to this, the diffuse source is modeled by

$$f_i(\mathbf{x}_B) = \begin{cases} \frac{w_i}{\bar{w}} \Phi_B(\mathbf{x}_B), & i \text{ inward pointing,} \\ 0, & \text{else.} \end{cases}$$

The variable \bar{w} is the sum of all weights w_i which are associated to an inward pointing direction i . There might be several inward pointing directions, such that a normalization by \bar{w} ensures the desired boundary intensity. Note, that both formula apply equally for sources and general emitting walls. This might also serve for the purpose of simulating

conjugated heat transfer and other multi-physics application.

By this construction the boundary populations recover the imposed constant macroscopic intensities, as the moments show for the collimated respectively diffuse source

$$\sum_i f_i(\mathbf{x}_B) = \Phi_B(\mathbf{x}_B),$$

shows. The physical interpretation for such boundaries is that they impose a fixed intensity or in other words a Dirichlet boundary [121]. Implementation details can be found in OpenLB as indicated in Appendix E.4. Note, that this source boundary models does define equally a flux, which is clearly seen by computing the 1st moment $\mathbf{J} = \sum_i s_i f_i$.

The presented source modeling is predominant in the RTLBM literature and to the best of the authors knowledge there is no ongoing discussion. Compared to general LBM boundary modeling, the development of powerful boundary treatments in RTLBM has still not started in great detail. For instance, up to now, the source models are formulated for axis aligned walls, which is a serious limitation to any application to more complex geometries.

4.3.2. Bounce-back wall

One of the most elementary and oldest boundary formulation in LBM is the bounce-back scheme, where the outgoing particle f_i re-enters¹ in the opposite direction \bar{i} . In the context of hydrodynamics, this boundary scheme models solid no-slip boundaries and imposes Dirichlet condition for the (macroscopic) fluid velocity at the wall. Despite its age, the bounce-back scheme is the most popular wall model which might be explained by its simplicity of implementation and intuitiveness in modeling.

One possible implementation consists of replacing the collide-and-stream equation (3.6) on the boundary by

$$f_{\bar{i}}(t + \Delta t, \mathbf{x}_B + c_i \mathbf{s}_i \Delta t) = f_i(t, \mathbf{x}_B),$$

where \bar{i} is the opposite direction of i , see Figure 4.2. A full review of its variants along a detailed analysis is presented in Krüger et al. [105, Paragraph 5.3.3.].

For RTLBM the bounce-back scheme corresponds to a zero Neumann boundary for the radiant energy density, since there is no change in radiance on a boundary cell. Throughout the present work, it is deployed the full way bounce-back scheme and subsequently the collision on the boundary is realized by a trivial swap of f_i by $f_{\bar{i}}$, see

¹In LBM literature bounce-back is commonly described by reflection of direction. In order to avoid abuse of language, the term *reflect* is used in microscopic modeling and *re-enter* in the mesoscopic context.

4. Radiative Transport with LBM

the original work on bounce-back for LBM [35, 210].

4.3.3. Partial bounce-back wall

This section first derives a macroscopic counterpart of the Fresnel's equation that models reflection on surfaces on the mesoscopic level. The applied technique originates from the P1-Approximation and can be found in the textbook of Wang and Wu [184]. After analyzing the macroscopic parameters that describe the surface properties, a novel RTLBM is proposed to solve the derived macroscopic equation. This indirect strategy of solving an approximated target equation has also been applied in the derivation of the macroscopic RTLBM, see Section 4.2.1.

On a boundary surface with orientation \mathbf{n} , the expression $\mathbf{n} \cdot \mathbf{s} < 0$ depicts all directions \mathbf{s} that hit the surface from within the volume. Radiance that hits surfaces from such directions is partly reflected according to Fresnel's equation (2.16). The integral formula for this boundary reflectance is

$$\int_{\mathbf{n} \cdot \mathbf{s} > 0} L(\mathbf{s}) \mathbf{s} \cdot \mathbf{n} d\Omega = \int_{\mathbf{n} \cdot \mathbf{s} < 0} R_F(\mathbf{s} \cdot \mathbf{n}) L(\mathbf{s}) \mathbf{s} \cdot \mathbf{n} d\Omega, \quad (4.10)$$

where the re-entering radiance (left hand side) equals the reflected part of the incident radiance, given by the right hand side. The argument (t, \mathbf{x}) has been dropped for the sake of compactness. A numerical integration of the above equation in the framework of LBM yield an uncertain discretization error, since the quadrature rules of Gauss–Hermite, respectively Lebedev–Laikov, do not compute this integral exactly. However, the following derives an approximated version of (4.10) which can be solved by well-known LBM techniques.

Approximation to macroscopic equation

In the following, the above boundary equation is approximated by a Robin boundary condition under the assumption of a highly scattering volume. More details of the purely algebraic operations can be found in [184]. The effective reflection coefficient is introduced by

$$R_{\text{eff}} = \frac{\int_{\mathbf{s} \cdot \mathbf{n} < 0} R_F(\mathbf{s} \cdot \mathbf{n}) L(\mathbf{s}) \mathbf{s} \cdot \mathbf{n} d\Omega}{\int_{\mathbf{s} \cdot \mathbf{n} < 0} L(\mathbf{s}) \mathbf{s} \cdot \mathbf{n} d\Omega}. \quad (4.11)$$

With the expansion of the irradiance (2.18) and the definitions

$$R_\Phi = \int_0^{\pi/2} 2 \sin \theta R_F(\theta) d\theta ,$$

$$R_J = \int_0^{\pi/2} 3 \sin \theta (\cos \theta)^2 R_F(\theta) d\theta ,$$

the effective reflection coefficient is retrieved

$$R_{\text{eff}} = \frac{R_\Phi + R_J}{2 - R_\Phi + R_J} . \quad (4.12)$$

By know, R_{eff} is no longer expressed in terms of the unknown radiance and the incident direction, but can be computed solely by means of R_F , which is equivalent to knowing n_{rel} , see definition (2.16).

Starting off with the substitution of (4.11) into the original boundary equation (4.10) yields

$$\int_{\mathbf{n} \cdot \mathbf{s} > 0} L(\mathbf{s}) \mathbf{s} \cdot \mathbf{n} d\Omega = R_{\text{eff}} \int_{\mathbf{n} \cdot \mathbf{s} < 0} L(\mathbf{s}) \mathbf{s} \cdot \mathbf{n} d\Omega .$$

Followed by plugging-in the expanded irradiance (2.18), it holds

$$\frac{1}{4} \Phi + \frac{1}{2} \mathbf{J} \cdot \mathbf{n} = R_{\text{eff}} \left(\frac{1}{4} \Phi - \frac{1}{2} \mathbf{J} \cdot \mathbf{n} \right) ,$$

and finally, with Fick's law ($\mathbf{J} = -D \nabla \Phi$) and the following definition

$$C_R = \frac{1 + R_{\text{eff}}}{1 - R_{\text{eff}}} , \quad (4.13)$$

the macroscopic Robin boundary condition is stated

$$\Phi(t, \mathbf{x}) - 2 C_R D \nabla \Phi(t, \mathbf{x}) \cdot \mathbf{n} = 0 . \quad (4.14)$$

Here, $D = 1/(3(\mu_a + \mu_s))$ is a diffusion coefficient as in (2.9) and C_R a constructively derived dimensionless parameter accounting for the surface reflection. Table 4.1 shows typical values for C_R (water-glass $n_{\text{rel}} = 0.88$). The computation of R_{eff} and C_R for given refractive indices is published in OpenLB version 1.3 and also outlined in Appendix E.1.

The Robin boundary condition is a sum of Dirichlet and Neumann boundary condition, where the product $C_R D$ indicates whether the Dirichlet or Neumann part dominates. For instance, the Neumann part $\nabla \Phi$ becomes dominant for $C_R D \rightarrow \infty$ and contrary for $C_R D \rightarrow 0$. However, the latter concludes $\Phi = 0$ and hence the Dirichlet boundary is imposed.

4. Radiative Transport with LBM

From a phenomenology perspective, the reflection parameter C_R depends on the relative refractive index n_{rel} through the definition of R_{eff} and hence is the boundary surface specific parameter. In addition, the volume is covered by the diffusion parameter D . The modeling predicts for refractive index match ($n_i = n_o$) no reflection on the wall, see the Fresnel's equation (2.16). This observation is matched on the macroscopic scale by the derived Robin equation that does not include reflection properties ($C_R = 1$). This concludes that the approximation is consistent with respect to refractive index match. The general situation is analyzed by a Chapman–Enskog expansion in Appendix B and investigated numerically in Section 5.2.

n_{rel}	1.0	0.88	0.7	0.5
C_R	1.0	1.0478	1.14	1.35

Table 4.1.: Refractive index match ($n_{\text{rel}} = 1$) is indicated by $C_R = 1$.

Mesoscopic algorithm

Fresnel's equation states that outgoing radiance is partially reflected and re-enters the computational domain. The corresponding Fresnel boundary equation is formulated in (2.17), respectively in its integral form (4.10). By following this microscopic picture, it is proposed a *partial bounce-back* scheme

$$f_{\bar{i}}(t + \Delta t, \mathbf{x}_B + c_i \mathbf{s}_i \Delta t) = r_F f_i(t, \mathbf{x}_B), \quad (4.15)$$

in order to solve the Fresnel boundary equation, for a wet boundary node \mathbf{x}_B , an outgoing direction i and its opposite direction \bar{i} . With the *mesoscopic reflection function*

$$r_F = 1 - \frac{2}{4C_R D + 1}, \quad (4.16)$$

for (non-dimensional) diffusion coefficient D and C_R as in (4.13), this scheme solves the Robin boundary condition derived previously (4.14). This formula indicates that the Fresnel's equation is reduced on mesoscopic scale to a sole reflectivity of the wall given by r_F . The latter is further related to its macroscopic counterpart of C_F , see Chapman–Enskog expansion in Appendix B. This formula simplifies the Fresnel's equation by averaging the direction of the re-emitted populations. By implementing specular reflection this deficit can be compensated.

The innovation of this boundary model lies in a precise and physically based description of the mesoscopic reflection function. Besides, it is equipped with a clear and simple

implementation of the relevant parameter, namely C_R that covers the Fresnel's boundary at the surface and additionally the volume properties that are represented by D . Finally, the mesoscopic scheme is almost as simple as a standard bounce-back scheme and therefore very well suited for high performance computing.

For the quantitative considerations, it should be noted that the mesoscopic reflection function r_F takes values in the interval $[-1, 1]$. In its most simple case, $r_F = 1$, the boundary scheme is equivalent to bounce-back, thus photon density $f_i(t, \mathbf{x}_B)$ re-enters totally at the opposite direction \bar{i} , see Figure 4.2. This is in excellent agreement to macroscopic considerations, where for $D^*C_R \rightarrow \infty$ the zero Neumann boundary for the density is obtained. In fact, the limit of $D^*C_R \rightarrow \infty$ result in $r_F \rightarrow 1$ and hence the partial bounce-back scheme fulfils the macroscopic prediction.

4.3.4. Specular wall

An interesting approach on mesoscopic scale to incorporate specular reflection are slip boundaries, already discussed in fluid flow LBM literature [169, 161, 7]. They are designed as bounce back rules that in addition respect the re-emitted directions depending on the incident angle. In the context of fluid flows, the velocity slip becomes noticeable for Knudsen number ≤ 0.01 where equally the continuum assumption for the Navier–Stokes equation is violated. Among the boundary models for such transport regimes are the diffuse reflection models, that assumes microscopically rough walls on which particles get reflected uncorrelated with their incident angle [4, 165, 104, 209]. Guo et al. [70] studied the discrete effects of slip boundaries in simulating microscale gas flows. Most boundary treatments are dedicated to 2D axis aligned rectangle enclosures which lack on generality. For instance, the extension to curved boundaries is non-trivial and 3D cases need to be studied, validated and investigated.

With regard to RTLBM, the slip boundary can model specular boundaries for axis aligned enclosures with straight walls. Also a mixture of diffuse and specular reflection might be considered to implement certain surface roughness. In fact, the implementations of such numerical schemes require only a little more effort and the knowledge of the wall orientation. However, these boundary treatments apply primarily to very dilute volume and ballistic RT regimes, where the usage of a relaxation scheme such as LBM is obsolete. The recommended simulation tool for this scenario would be MC and its rich (sub-) surface models.

4. Radiative Transport with LBM

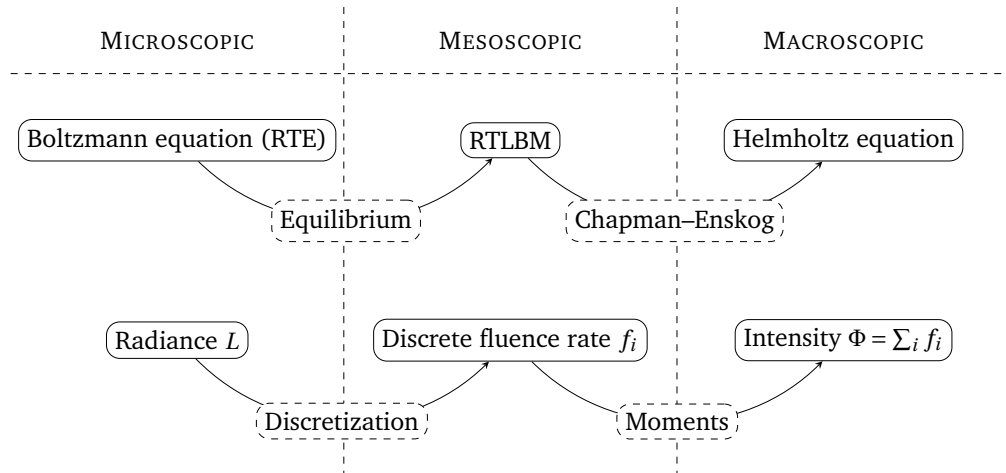


Figure 4.1.: Summary and relation of the micro-, meso- and macro level for RTLBM and the corresponding quantities. The macroscopic RTLBM focus on the Chapman-Enskog technique and the mesoscopic RTLBM emphasis the discretization of the RTE.

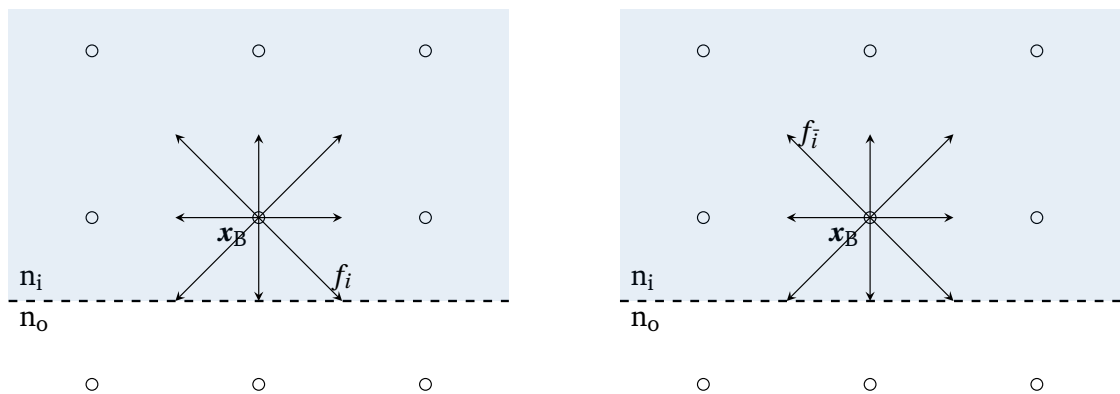


Figure 4.2.: Boundary region represented by the dashed line with a wet boundary node x_B . The pre-collision configuration is shown on the left side and the post-collision state on the right side. The population f_i hits the boundary surface and after collision, the population re-enters in the opposite direction \bar{i} .

5. Numerical Validation Against Analytical Solutions

Besides a careful derivation of RTLBM the methodological development of novel numerical algorithm requires numerical experiments. Only, the latter show whether sophisticated algorithms apply to real engineering problems and provide accurate predictions. Since the emergence of RTLBM over the last years, few investigations consider methodology numerical research. The majority of the proposed schemes are not investigated with respect to grid convergence/independence or validation against measurements for a rich parameter set, see for instance [111, 199, 188]. This shows the lack of general studies and limited insights of RTLBM and might explain the many variations of RTLBM in literature, suggesting distinct development approaches.

The author provides in the present and the following chapter a comprehensive and general validation study of the three RTLBM introduced in Section 4.2. The main focus of this chapter is the validation against analytical solutions, where the conducted numerical experiments comprise the convergence studies published by Mink et al. [125] and Mink et al. [123]. It is shown, that the macroscopic RTLBM approach is of 2nd order and the Fresnel boundary condition is a 1st order model.

5.1. Validation of Macroscopic RTLBM

The following validates the macroscopic RTLBM against analytical solutions that are known for a particular setup, based on a spherical domain and spherical radiative source. Considering numerical errors for different grid sizes, the EOC is conducted for non-absorbing and general participating media. The main outcome is a numerical study of grid convergence, which indicates that the macroscopic RTLBM is a 2nd order scheme.

5. Numerical Validation Against Analytical Solutions

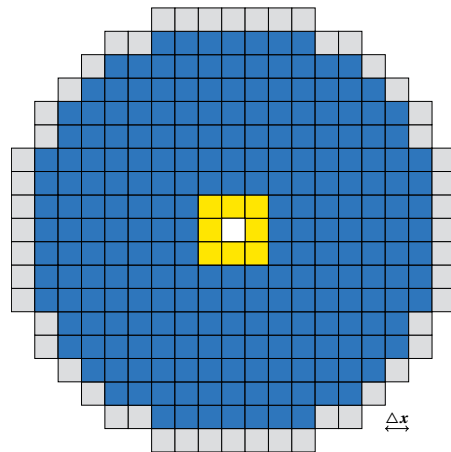


Figure 5.1.: Cross section of three dimensional discrete geometry, with cell size Δx . Yellow indicates radiative source, blue is participating volume and grey is the outgoing boundary.

5.1.1. Simulation setup and analytical solution

In Section 2.6 the analytical solutions of the Helmholtz equation (2.12) is presented. For an isotropic radiative source placed at position r_0 , the intensity in the domain reads

$$\Phi_{\mu_a, \mu_s}(r) = \frac{3(\mu_a + \mu_s)}{4\pi|r - r_0|} \exp\left(-|r - r_0| \sqrt{3\mu_a(\mu_a + \mu_s)}\right),$$

for constant coefficients $\mu_a, \mu_s > 0$ and $r > 0$, which denotes the distance of a considered point \mathbf{x} to the radiative source at $r = 0$. For the sake of simplicity, the absorption and scattering indices are dropped and the analytical solution is written as Φ .

The domain of interest is a sphere denoted by \mathbf{X} with radius L_0 , which is placed in the origin of a coordinate system. Equipped with Dirichlet boundaries for each, the radiative source at (an arbitrary) distance $r_i = 0.1L_0$ and the walls at $r_o = 1L_0$, the entire domain is defined, see Figure 5.1. Due to the singularity of the analytical solutions at the r_0 , the radiative source is placed arbitrarily at distance of $0.1L_0$. Here, L_0 denotes a characteristic length of the system in m. The fixed boundary values are given by the analytical solution and are projected to the discrete lattice nodes. This procedure guaranties that the source lattice nodes are initialized by the continuous value of Φ , which is important since the staircase approximation of the sphere does not guaranty that all source nodes are at the same distance to the origin, see Figure 5.1. For implementation details, it is referred to Appendix D and the documentation of OpenLB [103]. The knowledge of analytical solution makes this situation valuable for numerical error analysis.

For a stringent numerical analysis and validation, the relative error is introduced by

$$e_N = \frac{\|\Phi_N - \Phi\|_{L^2(\mathbf{x})}}{\|\Phi\|_{L^2(\mathbf{x})}}.$$

for an analytical solution Φ and a computed solution Φ_N , associated to a grid size N , e. g. $N = \frac{L_0}{\Delta x}$. However, the formula also includes averaging and might not account for the maximum deviation at a single cell.

When studying the asymptotic behaviour of the relative error for decreasing grid sizes, the analysis is based on the EOC. The EOC measures the convergence order of the numerical scheme experimentally and determines the rate of decrease of the relative error¹ subjected to the grid sizes N and M

$$EOC_{N,M} = \frac{\log(e_N) - \log(e_M)}{\log(M) - \log(N)}.$$

In the following, several EOC are computed for the above mentioned setup, in order to determine grid convergence of the numerical method.

5.1.2. Convergence study and discussion

This section provides studies of the non-absorbing and general RT regimes. A discussion on the retrieved results and its linkage to the relaxation time closes this section.

Radiative transport without absorption

The macroscopic RTLBM presented in Section 4.2.1 is applied to non-absorbing participating media ($\mu_a = 0$). Since both, the RTLBM and the target equation reduces to the standard configuration for diffusion problems, for which LBM literature provides studies [196], this is an appropriate setup for a fundamental evaluation.

For the non-absorption case the collide-and-stream equation reduces to a *BGK*-type equation, already presented in (4.4). In accordance to the target equation (2.12), the sink term vanishes. RTLBM presented in [5, 16] show the same behaviour for this particular case. Since both models are based on the direct discretization approach, it is hard to derive a meaningful relationship to the macroscopic target equation out of collide-and-stream equations. As a consequence, their LBM solutions are compared against FVM results, which makes convergence analysis or error estimation difficult. In contrast, the

¹The EOC is basically the slope in the log-log plot of the relative error over the grid size.

5. Numerical Validation Against Analytical Solutions

modeling of the macroscopic RTLBM is connected to target equations and hence, enables an error analysis based on analytical solutions.

The computed solutions depend equally on the grid size N and on the coefficient μ_s , through the Dirichlet boundary condition. For the configuration of $\mu_a = 1$ the relative errors of the macroscopic RTLBM for varying grid size N are shown in Figure 5.2a. The presented simulations are evaluated by grids up to size 401^3 and show good agreement with analytical solutions. It is shown that the grid refinement leads to more accurate computations. A refinement of the grid by factor of 2 reduces the relative error by factor of 4. This observation is summarized in an $EOC \approx 2$. and was also proven for other absorption parameters.

General RT

The macroscopic RTLBM presented in Section 4.2.1 is applied to general participating volume. Recall, the collide-and-stream equations reads

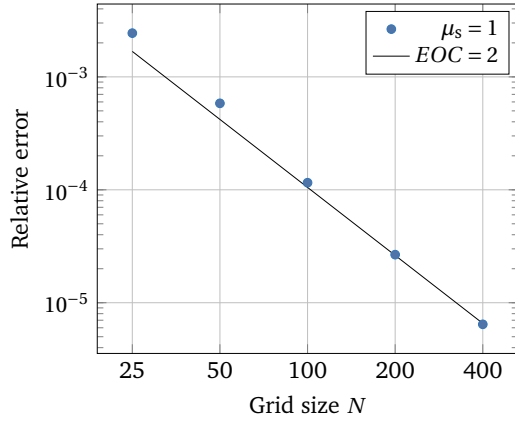
$$f_i(t + \Delta t, \mathbf{x} + \mathbf{s}_i \Delta x) = f_i(t, \mathbf{x}) - \frac{1}{\tau} (f_i(t, \mathbf{x}) - f_i^{eq}(t, \mathbf{x})) - \frac{\mu_{\text{eff}}^2}{8} (\Delta x)^2 f_i(t, \mathbf{x}),$$

for a mesoscopic sink term $\frac{\mu_{\text{eff}}^2}{8}$ as in (2.11) and the isotropic equilibrium $f_i^{eq} = w_i \Phi$, for $D3D7$ stencils. After reaching steady state¹ of the RTLBM, the relative error is computed for several optical parameters, see Figure 5.2b. Already for a resolution of 50 grid-points in every direction, the relative errors, over the entire domain, is $< 1\%$ for all considered participating media μ_i^2 . This is remarkable, taking into account, the staircase character of the regular grid and the spherical simulation domain.

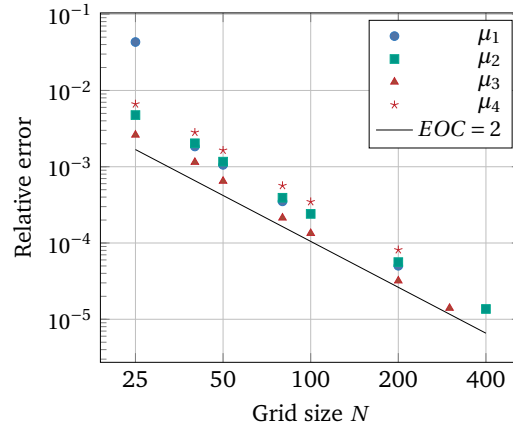
To determine numerical grid convergence, the trend of the relative error with an increased resolution is studied. To this aim, all participating media are simulation for resolutions up to 400 yielding an overall number of 250×10^6 cells. Figure 5.2b shows, that the relative error decreases for higher grid resolutions with an $EOC = 2$ for all participating media.

¹Steady state criteria for simulations is a density deviation in L^2 -norm of less than 1×10^{-5} during a period of N^2 iteration steps.

²Participating media are characterized by optical parameter sets $\mu_1 : \mu_a = 5/3, \mu_s = 1/3$, $\mu_2 : \mu_a = 3/2, \mu_s = 1/2$, $\mu_3 : \mu_a = 1, \mu_s = 1$ and $\mu_4 : \mu_a = 2, \mu_s = 1$.



(a) Relative error as a function of the grid size N for fixed $\mu_s = 1$ and $\mu_a = 0$. For relaxation coefficient $\tau = 1$ grid convergence of $EOC = 2$ is observed.



(b) Relative error as a function of the grid size N for relaxation coefficient $\tau = 1$ and several participating media μ_i .

Figure 5.2.: Left figure shows the EOC analysis for non-absorbing volume. Right figure depicts the EOC study for general volume.

Discussion of the relaxation time

Ponce Dawson et al. [145] pointed out that the LBM relaxation time is related to the diffusivity of the advection–diffusion equation through the formula given in 3.3.3 and determined the range of relaxation time τ for which the LBM is accurate. The findings of relative errors $\approx 0.04\%$ for $\tau = 1$ and $\approx 5\%$ for $\tau = 10$ lead to the conclusion that LBM is only a good approximation method for small relaxation times. From the computed relative errors of 3 and 1 % for grid sizes 256 and 512, indicate an EOC between 1–2. This observation was confirmed by A. A. Mohamad at the DSFD conference in Edinburgh 2015, where he reported an EOC of two, when choosing relaxation time τ wisely. Both surveys considered two dimensional pure diffusion problems.

The 3D numerical experiments in this section met the above observations and concluded that the macroscopic RTLBM is a 2nd order scheme for solving the Helmholtz equation. In this context, it is crucial that the macroscopic RTLBM allows to choose $\tau = 1$ and model the photon-media interaction solely by the mesoscopic sink term, see Section 4.2.1. It is remarkable, that even the extension by an additional mesoscopic sink term preserves the order of convergence as shown in the conducted simulations.

5.2. Validation of Fresnel Boundaries

The following validates the Fresnel boundary model against analytic data known from theory. Based on a spherical domain and spherical radiative source, the walls where radiation leaves the domain is investigated. The later is referred to as outlet of the simulation domain. The investigation concludes the numerical errors for different grid sizes and the hereby obtained EOC indicates, that the proposed boundary treatment is a 1st order scheme.

5.2.1. Simulation setup

The validation of the Fresnel boundary equation (4.15) is based on a spherical geometry setup, with a spherical radiative source inside, see Figure 5.1. Here, the isotropic radiative source is placed at a distance $0.1L_0$ from the center and the investigated outgoing boundary at a fixed distance $1L_0$, where L_0 is a characteristic length given in m. The regular grid is associated to a grid size N for which the cell size reads $\Delta x = \frac{L_0}{N}$. This simulation setup is a natural choice, since for Dirichlet boundaries at the radiative source and the novel boundary at the outlet, there are solutions form literature.

Unless otherwise stated, absorption and scattering is given by $\mu_a = 0.5\text{m}^{-1}$ and $\mu_s = 1.5\text{m}^{-1}$. Further, the refractive index for the participating volume is given by $n_i = 1.33$ (water) and for boundary by $n_o = 1.51$ (glass). Given the above parameters, the macroscopic refraction coefficient results in $C_R = 1.0478$, see Table 4.1 and diffusion coefficient in $D = \frac{1}{6}\text{m}$. The following considers the non-dimensional versions $D^* = D\Delta x^{-1}$, $\mu_a^* = \mu_a\Delta x$ and $\mu_s^* = \mu_s\Delta x$.

Steady state criteria for simulations is a density deviation in L^2 -norm of less than 1×10^{-5} during a period of N^2 iteration steps. The time scale is proportional to $(\Delta x)^2$ and thus diffusive scaling is deployed. Finally, the radiative source is defined as Dirichlet radiant energy density, accordingly to previous work [125].

5.2.2. Convergence study

First, numerical simulations have been carried out to prove that the model is stated grid independently and converges. For this purpose, the simulation data along the positive x-axis is investigated, which is a reasonable choice due to the symmetry of computational domain. In Figure 5.3 simulations for varying resolutions and fixed absorption and scattering coefficients are shown. It is seen, that a grid size of $N = 40$ or $\Delta x = 0.025L_0$ is sufficient to resolve the problem properly and higher resolutions do not result in a

substantially more accurate simulations. This observation suggests, that the algorithm is grid convergent, including the novel boundary formulation.

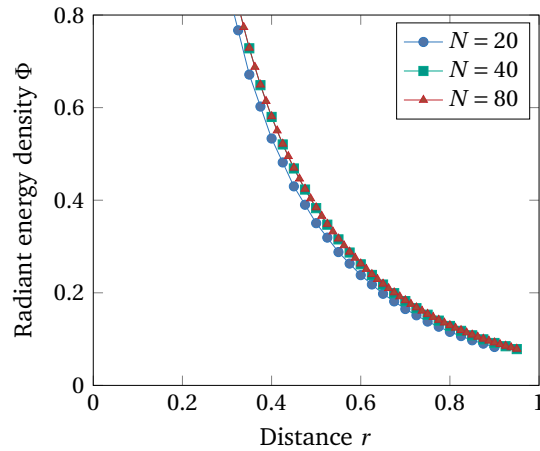
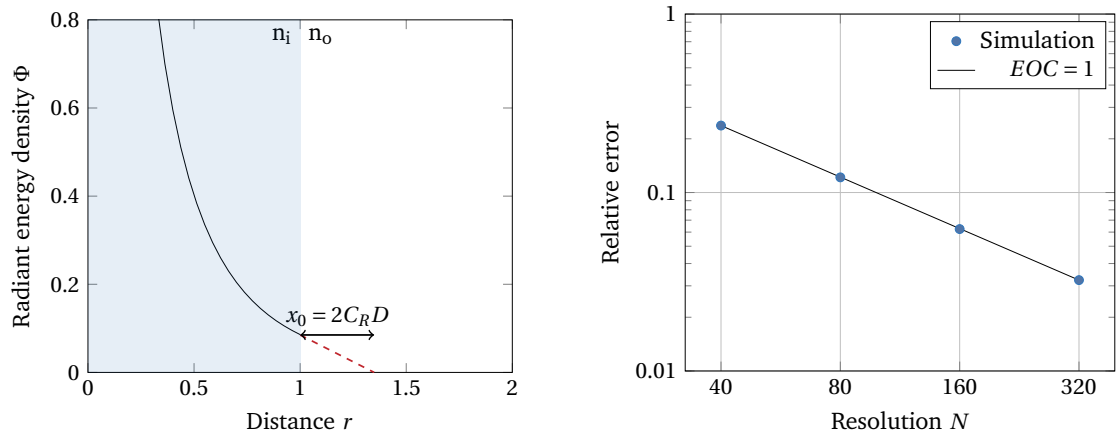


Figure 5.3.: Simulated radiant energy density over distance to origin $r = |x|$.

Second, the convergence rate is investigated, which is important to estimate the benefit of a finer grid. Together with the increase in necessary time steps (diffuse scaling), the computation time increase finally by a factor of 16. As a result, the available computing resources might exceed very fast. The validation against the extrapolated length x_0 , known from literature [184, 89], after which the tangent on the boundary density intersects with the x-axis, depicted in Figure 5.4a, is presented in the following. It is known from literature that the length is determined by $x_0 = 2DC_R$, see [74, 184]. Here, the simulation is validated by means of computing first the density gradient on the wall by a simple two-point form and second, determine the intersection with the x-axis. This procedure retrieve the length $x_{0,N}$ obtained from simulation data. Figure 5.4b depicts the relative errors for varying grid resolutions. Simulation data yields an $EOC_{40,320} = 0.9588$ and suggests that the proposed Fresnel boundary scheme is first order convergent. It is expected that the relative error can be reduced further by applying a halfway bounce-back scheme, as literature reports [205, 210].

Remarks on computational effort At the resolution of 40 the steady state is reached after about 10500 iterations for this particular configuration. The iterations can be reduced by initializing the domain with an appropriate guess, for example the solution known for Dirichlet boundary. A resolution of 320 results in more than 125×10^6 voxels and has been executed on a high performance cluster ForHLR II at the Karlsruhe Institute of Technology.

5. Numerical Validation Against Analytical Solutions



(a) Solid line represents simulated intensities in volume subjected to n_i . Predicted length x_0 is given by the intersection of the tangent (red dashed line) with the x-axis.

(b) Relative error plotted over resolution for parameter choice $\mu_a = 0.5$, $\mu_s = 1.5$ and $C_R = 1.0478$. The EOC indicates that the Fresnel boundary is a 1st order scheme.

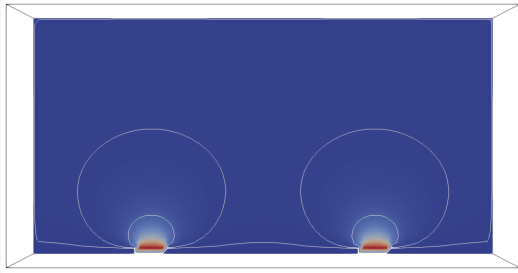
Figure 5.4.: Left side shows the validation setup with $x_0 = 0.3492$. Right side presents the data from the EOC study.

5.2.3. Application to multiple LED spots

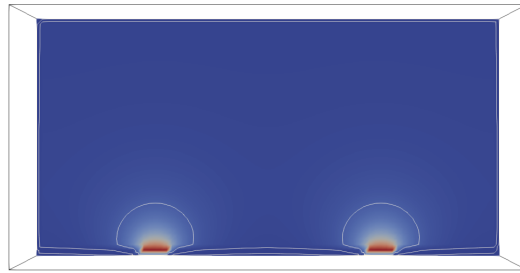
Simulating radiative sources and hence boundaries, can be realized by two Dirichlet boundaries. One implements the light source and another one the density on the outlet. Generally, the light intensity at the outlet is not known, thus it is often set to zero and hence, lacks on physical meaning. In addition, the simulation is very unstable due to the non-steady jump of densities close to source and outlet. However, the novel boundary model is capable of simulating general outlet boundaries, taking the reflectivity into account. Applications such as multiple LED spots demonstrate the need of such boundary schemes for RTLBM. The geometry setup in Figure 5.5 is based on a cuboid with extension of $0.2\text{ m} \times 0.1\text{ m} \times 0.1\text{ m}$. Except to two rectangular light sources ($0.01\text{ m} \times 0.01\text{ m}$), that are realized by a Dirichlet boundary condition at the bottom, the outgoing walls are either Fresnel or Dirichlet boundaries.

The comparison of the simulation results obtained from Dirichlet boundary and the novel Fresnel boundary is shown in Figure 5.5. The Fresnel boundary is imposed for a refractive index $n_{\text{rel}} = 0.88$, which corresponds to water-glass interface, and the volume specific parameters are $\mu_a = 3\text{ m}^{-1}$ and $\mu_s = 27\text{ m}^{-1}$. It is seen, that the Fresnel boundary predicts a remarkably higher light density in the volume. This can be explained by the partially reflected radiation that leaves the domain and gets reflected, instead of fixing the light density to almost zero by 1×10^{-6} in the case of Dirichlet boundaries. This

5.2. Validation of Fresnel Boundaries



(a) For Dirichlet boundary we observe a poor penetration depth of light into the media. Already after short distance, the light reduced by factor of 10.



(b) The novel Fresnel boundary leads to a significantly higher prediction of the intensity, since there is reflectivity at all walls except the light source.

Figure 5.5.: Cross section with contour lines for values 0.1, 0.01 and 0.001 of intensity Φ . Radiative source is initialized with intensity of 1.

simulation example emphasis the need of Fresnel reflection on surfaces to model general light source configurations of finite extend.

6. Numerical Validation Against Monte-Carlo

RTLBM emerged over the last decade and are relatively new numerical tools for the simulation of RT in volume. Therefore, it is hardly surprising that a systematic validation comparing existing models, is overdue. In addition, a comprehensive investigation of the range of validity, in terms of the optical parameters, is also still missing. As many derivations of RTLBM emphasize to a certain discipline, for instance thermal problems, its validation is limited to a narrow set of optical parameters relevant for thermal problems. However, this procedure does not only impede the acceptance of RTLBM, but also restricts artificially its application to other disciplines, such as photocatalytic reactors and photobioreactors. This might be due to a lack of guidance of the proper choice of a RTLBM model with respect to an RT regime, or due to the fact that the majority of existing RTLBM are restricted to one or two spatial dimensions. Until now, 3D RT was only considered in the pioneer work [62] and, more than a decade later, in [115] as well as by Mink et al. [125, 121, 123].

This chapter investigates the presented RTLBM models from Section 4.2 for a set of 35 different participating media applied to four benchmark scenarios, see Section 6.1. The comprehensive validation of the RTLBM against MC data reveals their strength and weakness, according to the modeling hypothesis and discretization strategies. In Section 3.3.1 it is concluded the overall quality and asymptotic trends for general RTLBM. Together with the analysis of simulation time, the validity range is depicted systematically. At the end, guidelines for the choice of RTLBM are formulated considering RT from ballistic to diffuse regimes. These efforts spread RTLBM to a much wider audience than before and establish them in LBM literature as an autonomous field of application. The presented results of the mesoscopic and macroscopic RTLBM can also be found in the author's publication Mink et al. [121]. However, the survey of the P1-RTLBM is shown for the first time in the present thesis. The chapter closes with a discussion on future model extension in Section 6.6.

6.1. Benchmark Design and Transport Regimes

The four numerical validation benchmarks, presented in the section, are based on a cubic domain with either a diffuse or collimated radiative source. For this setting, the steady-state RT is compared to MC simulations. First, the benchmark scenario is presented together with the validation criteria and error measure. Then, the 35 RT regimes are defined in order to validate the RTLBM in detail.

6.1.1. Benchmark design

The simulated geometry is based on a cubic domain with edge length L_0 , which is equipped with a rectangular radiation source at one of the walls, see Figure 6.1. The domain is discretized with a regular grid of equidistant nodes with fixed spacing $\Delta x = 0.01L_0$. For MC simulations, the spatial discretization consists of cubic volume elements with an edge length similar to the grid spacing of the RTLBM. Unless otherwise stated, the steady-state criterion for all simulations is a change of the dimensionless radiation intensity of less than 1×10^{-8} in the whole domain during 160 iterations. The radiative source emits radiance either diffusely or collimated and is implemented according to Section 4.3. Other boundary nodes are modeled as transmissive walls where radiation leave the domain and no radiation enters. In thermal applications those walls are referred to as black walls.

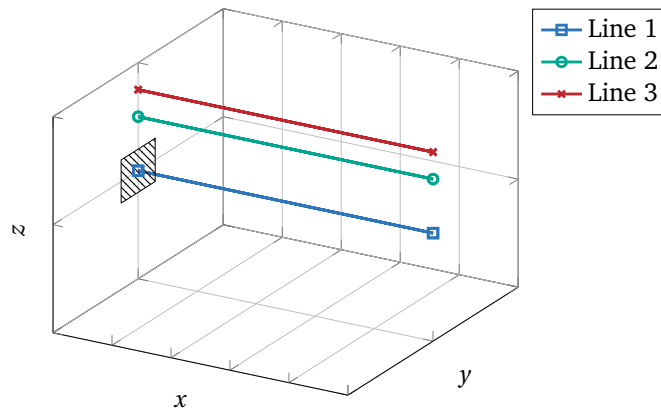
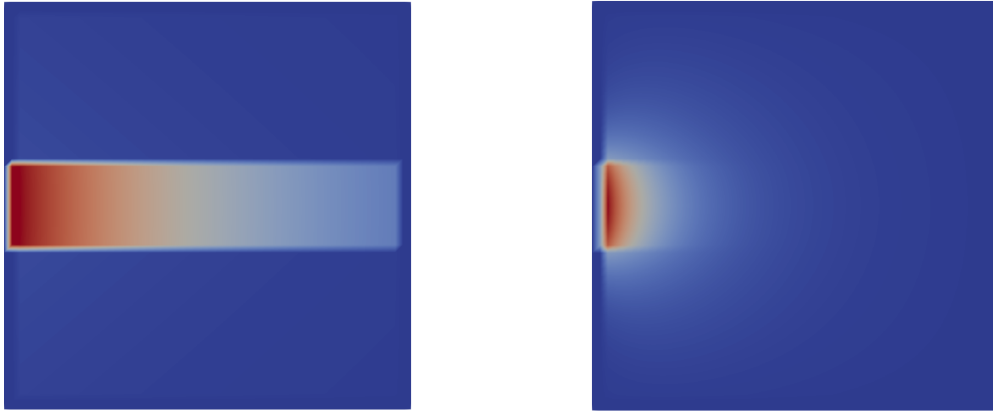


Figure 6.1.: Sketch of the cubical simulation geometry with the rectangular radiative source in the yz -plane. For validation the data along the lines is compared. Line 1 (green rectangles) goes through $z = 0.5L_0$, line 2 (orange circles) goes through $z = 0.75L_0$ and line 3 (yellow crosses) line goes through $z = 0.875L_0$. From red to blue the light intensity decreases.



(a) Ballistic RT regime with parameters $a = 0.7$, $b = 0.2$.

(b) Diffuse RT regime with parameters $a = 1$, $b = 20$.

Figure 6.2.: Cross section of intensity field for benchmark scenario *finite collimated beam*. Comparison of ballistic (left) and diffuse (right) RT regimes with finite source located on left wall.

Four benchmark scenarios are defined to survey the proposed RTLBM in great detail. The scenarios include a collimated as well as a diffuse beam on infinite extent. Those benchmarks are designed to minimize the influence of the radiative source and focus on the simulation of the domain. The other class of scenarios are a collimated as well as a diffuse beam on finite extent of edge length $0.2L_0$. These scenarios are designed to study not only the RT into ambient regions, that are not directly imposed to the radiation source, but also the boundary model itself.

Due to symmetry, the intensity inside the cube is validated along line 1, 2 and 3, where the first accounts for the direct RT and the others for the ambient RT. In non-scattering transport regimes (ballistic regime) the radiative intensity in the ambient regions vanishes, see Figure 6.2a. This changes as the scattering becomes more dominant (diffuse regime), by the diffusive effects of the photon-media scattering, see Figure 6.2b. Note, that approximating solutions, namely Lambert–Beer for ballistic RT and Diffusion–reaction equation for diffuse RT, are discussed briefly in Section 2.6. A cross section (xy -plane) of the simulated intensities inside a cube, with finite radiative source, is shown in Figure 6.2 to illustrate the two limiting cases of RT regimes.

Typically, radiative intensities vary over several orders or magnitudes, depending on the optical thickness of the media. Thus, the comparison of general transport regimes is hardly balanced. To this aim, the absolute L^2 -error is normalized by the total intensity along the considered line, to provide a reasonable measure for the validation of general

6. Numerical Validation Against Monte–Carlo

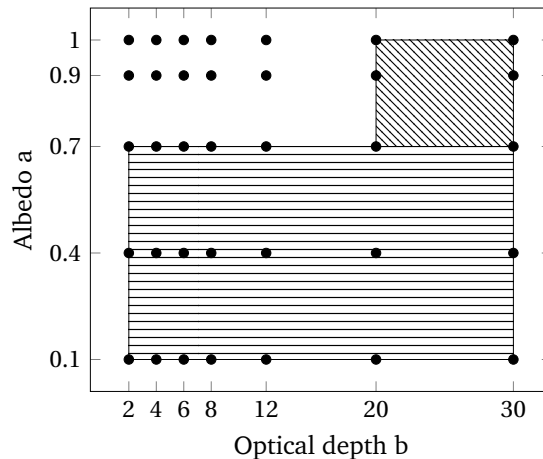


Figure 6.3.: The 35 parameter set is characterized by the optical depth and the scattering albedo. The diffusive regime is represented by the upper right region and the ballistic regime by the lower region.

RT regime. The error measure is defined for a simulated intensity Φ along line 1, 2 and 3 as

$$e = \frac{\|\Phi - \Phi^*\|_{L^2}}{\|\Phi^*\|_{L^1}},$$

with respect to the reference solution Φ^* from the MC simulation. Norm L^p is defined as follows $\|(\Phi_1, \Phi_2, \dots, \Phi_N)\|_{L^p} = \sqrt[p]{\frac{1}{N} \sum_{n=1}^N |\Phi_n|^p}$. The survey in the PhD thesis includes the analyze of intensities along line 1, 2 and 3. For the sake of completeness, the intensity profiles for every benchmark scenario and every optical parameter are found in the publication [121].

6.1.2. Transport regimes and optical parameter set

The limit of applicability of the RTLBM is studied by the help of a large set of optical parameters, that covers RT in principle from the ballistic to the diffuse regime. Following Van de Hulst [179], the parameter set is formulated with respect to scattering albedo and optical depth, see Figure 6.3. An isotropic single scattering phase function with $g = 0$ is assumed for the mesoscopic RTLBM and the MC in all simulations. The diffusive regime herein is represented by the upper right region and the ballistic regime by the lower region. In total, there are 35 different sets of optical parameter, which can be thought of certain participating media. Every benchmark scenario is executed for 35 different participating media to provide a comprehensive validation data.

The following discusses RTLBM models in ascending order with respect to their com-

putational effort and complexity. First, the mesoscopic RTLBM is analyzed followed by P1-RTLBM and the macroscopic RTLBM.

6.2. Numerical Experiments for Mesoscopic RTLBM

This section provides the validation of the mesoscopic RTLBM presented in Section 4.2.2. First, it is investigated the effects of angular discretization by the Lebedev–Laikov stencils, followed by a grid independence study. Both aspects were not included into the publication [121]. Then, the benchmark scenarios of infinite and finite radiative source, each considering diffuse and collimated source, are validated against MC data considering 35 different RT regimes.

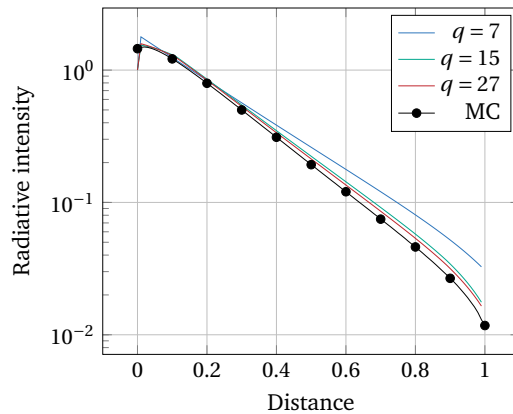
6.2.1. Angular discretization and grid independence

This section investigates the impact of the Lebedev–Laikov quadrature rule considering the 7, 15 and 27 directions. Then, the grid independence is shown for grids of resolution 50, 100 and 150. The analysis is based on a collimated radiative source and the diffuse RT regime given by $a = 1$ and $b = 6$.

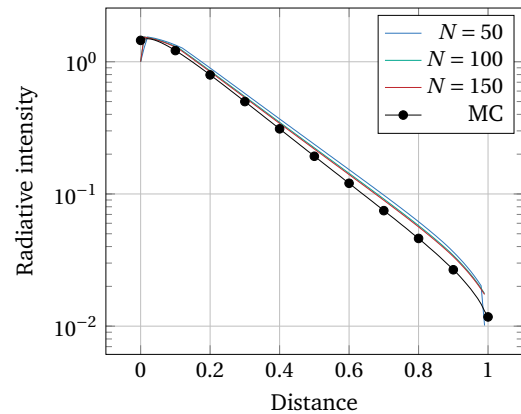
Angular discretization

The mesoscopic RTLBM aims for a precise computation of the scattering integral of the RTE. However, the discrete propagation directions from the LBM limit the angular discretization and hence, the precision of the discrete scattering integral, see (4.6). To understand the influence and importance of the angular discretization of the mesoscopic RTLBM the simulation results of the Lebedev–Laikov stencils with 7, 15 and 27 directions are plotted in Figure 6.4a. When considering diffuse radiative regimes, the discretization of the scattering integral is related directly to the Lebedev–Laikov quadrature rule and hence, the quality of the scattering phenomena. It is seen that 7 discrete directions are not able to predict the correct intensities at distances greater than 0.3 m or equivalently twice the mean free path length. The simulation is more accurate for an increased number of discrete directions. This trend is in good agreement to the theory of quadrature rules and is a notable difference compared to hydrodynamic LBM. Unlike for Navier–Stokes LBM, where considering more than 19 directions does not provide any information for the flow field, the mesoscopic RTLBM becomes more accurate for an increased number of directions.

6. Numerical Validation Against Monte–Carlo



(a) Impact of discretization stencil with 7, 15 and 27 directions.



(b) Grid independence study for Lebedev–Laikov quadrature with 15 directions.

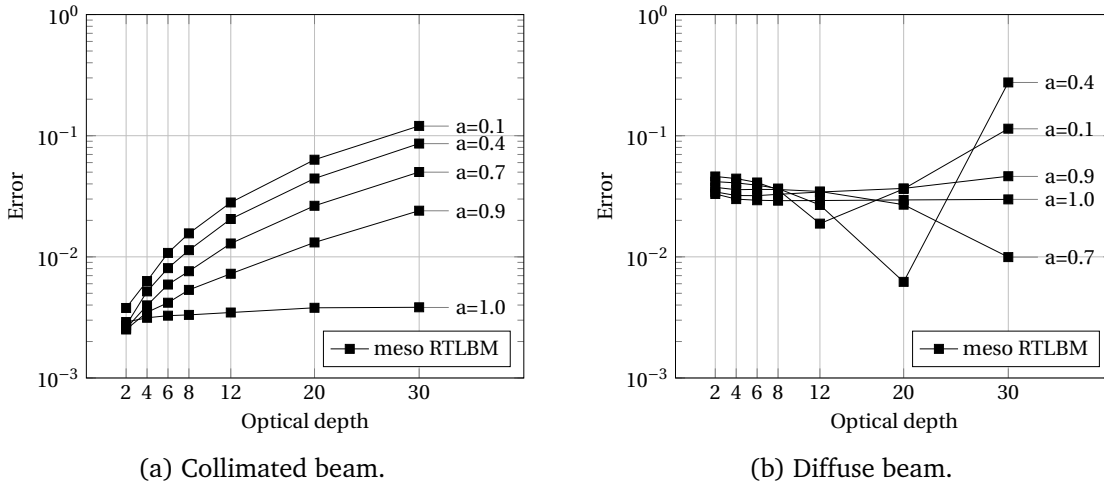
Figure 6.4.: Benchmark scenario of a *finite collimated source* and diffuse RT regime ($b = 6$, $a = 1$) simulated with the mesoscopic RTLBM.

A representative ballistic regime is predicted accurately and independently of the discrete directions (not shown). Due to the lack of scattering, there is only attenuation along the incident direction as predicted by Lambert–Beer. Hence, an increase of angular discretizations does not have any influence of the simulation.

Another aspect is the small jump in the intensity profile close to the radiative source at about 0.1 m. This jump is determined by the extent of the radiative source, where radiance is injected diffusely into the domain. Radiance emitted in diagonal direction at the very end of the source, crosses at distance 0.1 m into the simulation domain and results in this artificial jump. For more details it is referred to discussion in Figure 6.7.

Grid independence

Grids of resolution 50, 100 and 150 are simulated in order to identify grid independence. Figure 6.4b depicts the intensities along line 1 for the Lebedev–Laikov with 15 directions for varying grid resolutions. It is clearly seen, that the considered diffuse transport regimes is grid independent for the mesoscopic RTLBM. This observation is also valid for the entire parameter set in Figure 6.3 (not shown). Already a resolution of $\Delta x = 0.01L_0$ yields in a grid convergent method for this setup, independently of the considered transport regime. McHardy [118] pointed out in his PhD thesis that the method is a first order scheme.

Figure 6.5.: Errors for the benchmark scenario *infinite beam*.

6.2.2. Infinite radiative source

The mesoscopic RTLBM and MC simulations are examined to the two benchmark scenarios *infinite diffuse beam* and *infinite collimated beam*. Both scenarios implement a radiation source that extends to an entire wall. By analyzing the simulation errors along the central line 1, the accuracy of the simulated RT is addressed. However, it is difficult to clearly assign shortcomings to absorption, in- or out-scattering effects, due to the extent of the source.

The simulation errors for the 35 different participating media are presented in Figure 6.5 for collimated and diffuse sources. Media with equal transport scattering albedo are represented within a line, whereas the optical depth b ranges from 2–30.

Collimated beam

The mesoscopic RTLBM is generally and independently of the albedo in good agreement with the MC results ($\approx 10\%$), with the trend of performing better in optical thin media. The overall trend for an increased optical intensity however is a loss of precision independently of the scattering albedo. This result can be explained by the fact that all simulations were performed on the same numerical grid, so that the radiation-volume interaction between two points is less accurately resolved at high optical depth. Thus, the observed error of the mesoscopic RTLBM subjected to radiative source of infinite extent might not be determined by the validity range of the model, rather than by spacial discretization reasons.

Diffuse beam

The observed errors of the mesoscopic RTLBM are $\leq 10\%$ over almost all investigated RT regimes. Apparently, the optical depth of the media is not the major determinant of the method's accuracy and the shape of the error curves is not intuitively understandable. A closer evaluation of the simulated intensity distribution in the whole domain (not shown) indicated that the error is mostly caused by the radiation flux across the open boundaries of the domain. This can be explained by the coarse directional discretization of radiance in the mesoscopic model, which leads to an inaccurate representation of the angular irradiation pattern of the diffuse source. Consequently, the problem arises that too much energy is transported along single discrete directions and parts of the radiative energy do not leave the domain at the correct location what leads to the observed error. It seems plausible that the observed effect and its magnitude depends on the albedo. In case of a strongly scattering system ($a > 0.9$), the source characteristics do not play a role after a short distance apart from the source, what is also reflected in the smooth trend of the respective error curves. In other cases, the propagation of radiative energy along rays becomes more important and causes the described error. Additionally, if absorption is strong ($a \rightarrow 0$), the radiation intensity varies strongly in space so that small absolute deviations of the local intensity to the reference solution may cause large errors according to the applied normalized error measure. Therefore, the erratic shape of the error curves for ($a \leq 0.4$) and the case of an infinite diffuse beam result from a combination of the directional discretization and high absorption. It can be expected that the simulation error decreases in domains with larger width-to-length ratios, where fluxes across the open boundaries become less important for the simulation results. However, with regard to the current example of a cubic domain, it can be concluded that the mesoscopic RTLBM delivers reliable results since the error was $\leq 10\%$ for most participating media.

6.2.3. Finite radiative source

The results obtained for the scenario of an *infinite beam* cannot answer the question of how accurate the in- and out-scattering of radiation is treated. In addition, the transport of radiation to ambient regions, that are not exposed directly to the radiative source, cannot be validated properly. To this aim, this section is based upon a spatially restricted radiative source of extent $0.2 \times 0.2\text{m}$, which corresponds to the scenario of a *finite beam*, see benchmark design in Figure 6.1. The simulations are carried out again for all 35 participating media and the errors between the mesoscopic RTLBM and the MC simulation are depicted for diffuse and collimated beams in Figure 6.6.

Now, the errors along line 2 and 3 will be of particular interest, since they measure the accuracy of the simulation of the absorbed as well as the in- and out-scattered radiation. In particular, the transport of radiation to ambient regions, that are not exposed directly to the radiative source, is of interest since it was not accessible by benchmark scenario *infinite beam*.

Collimated beam

The observed errors of the mesoscopic RTLBM on line 1 are generally in good agreement to the MC data and less than 10%. With an increase in optical depth, the simulation is less accurate for the same reason as discussed in the benchmark of *infinite collimated beam*. Considering lines 2 and 3, the errors remain equal or increase slightly, compared to those measured on line 1. However, the accuracy in diffuse transport regimes ($a \geq 0.9$) is almost constant over lines 1, 2 and 3. This indicates that the RT to ambient regions is computed exactly for highly scattering media. Such transport regimes are almost diffuse and the angular discretization must cover isotropic transport, that is achieved. However, the more the transport regimes becomes ballistic the less accurate are the simulations of the ambient RT. Optical thick regimes enhance this model deficit.

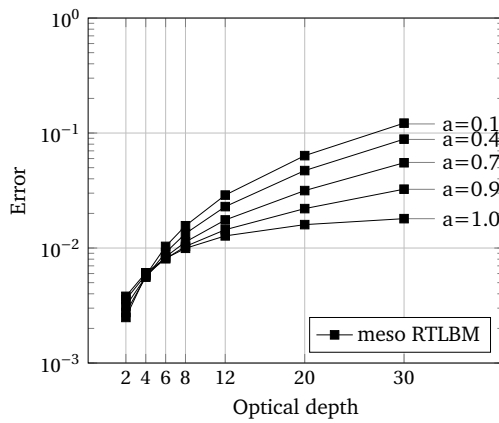
Diffuse beam

The general trends of the error of the mesoscopic RTLBM along line 1 follow similar patterns as it was already discussed for the scenario of an infinite collimated beam. It is seen that the error in purely scattering systems ($a = 1$) remains constant at high optical depths $b \geq 12$. Under these conditions, radiation transfer is diffusive and the solutions of the RTE are more or less similar and independent of the optical depth. This behavior explains the observed constant deviation from the MC reference solution.

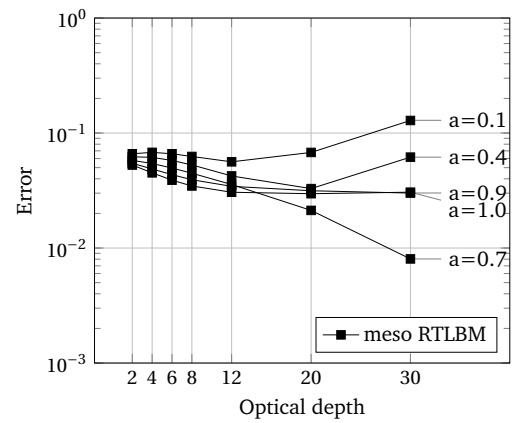
Regarding the errors along line 2 and 3, the crossing of the curves for $a = 0.9$ and $a = 1$ at $b > 12$ seems to be related to the observation of a constant error in purely scattering systems because in case of ($a < 1$) the solution is no longer approximately independent of the optical depth. In the limiting case of $a \rightarrow 0$ and $b \rightarrow 0$ the accuracy of the method decreases. Similar to the scenario of a collimated finite beam, this behaviour is related to the directional discretization of the governing equation, thus the RTE. In fact, the finite diffuse source is the most challenging setup, because the number of discrete directions not only affects the computation of scattering but also the accuracy with which the diffuse source can be modeled.

In order to illustrate the impact of the finite diffuse beam, it is referred to Figure 6.7a

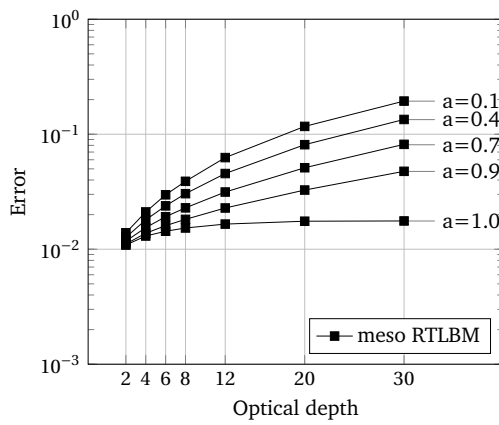
6. Numerical Validation Against Monte-Carlo



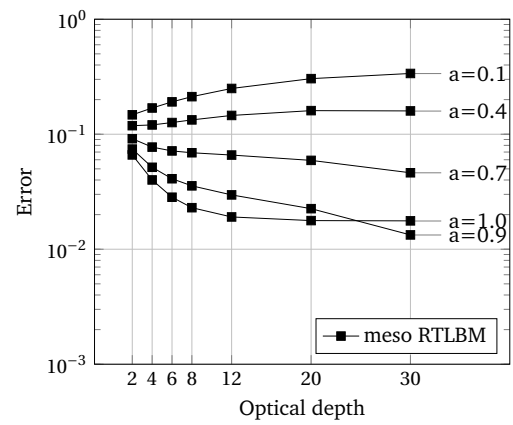
(a) Collimated beam along line 1.



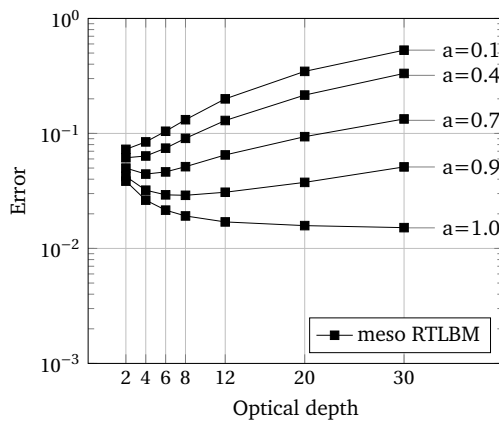
(b) Diffuse beam along line 1.



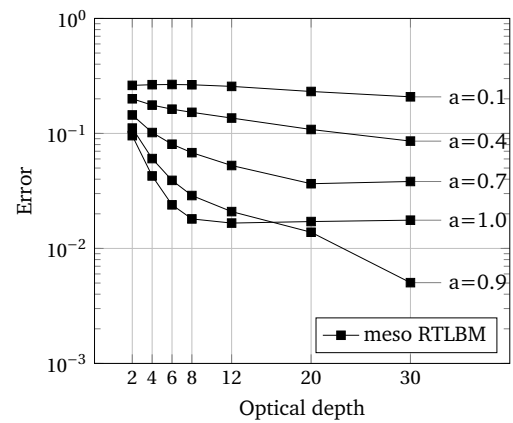
(c) Collimated beam along line 2.



(d) Diffuse beam along line 2.



(e) Collimated beam line 3.



(f) Diffuse beam line 3.

Figure 6.6.: Errors for the benchmark scenario *finite beam*.

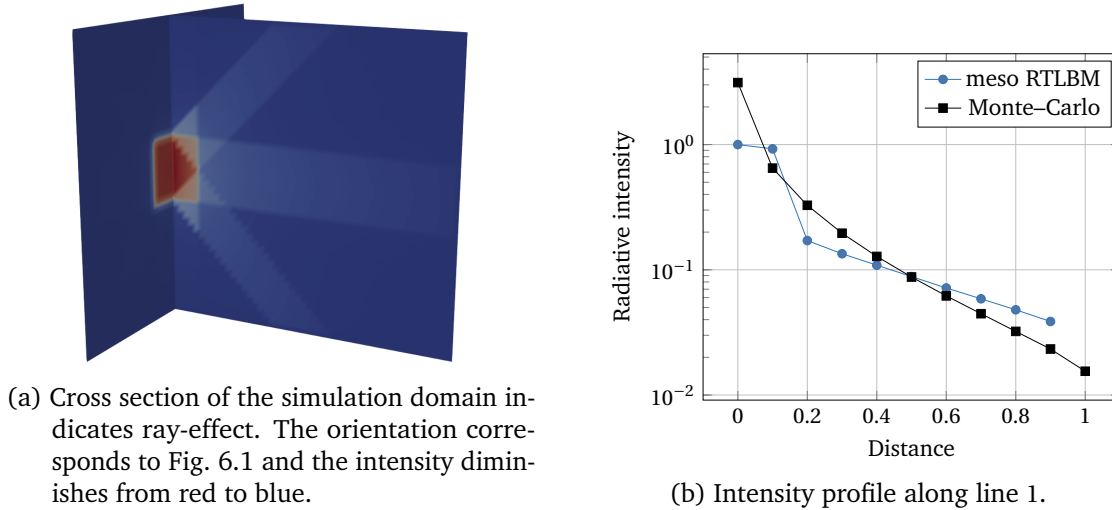


Figure 6.7.: *Finite diffuse source* and optical thin media ($b = 2$, $a = 0.9$).

where the intensity cross section for optical thin media is depicted. From the contour of the radiation intensity it is seen that the diffuse emission of photons applies foremost to the discrete directions yielding in rays. Close to the radiative source the diagonal emitted photons lead to an overlay and form an artificial intensity pyramid. The intensity along line 1 is subsequently subjected to a jump, see Figure 6.7b. Similar observations hold for line 2 and 3. The diffuse radiative source leads to ray-effects that originates from angular discretization errors, similar to the smearing ray-effect observed in DOM. In summary, it can be stated that the finite diffuse beam is a very challenging case for the mesoscopic RTLBM and very sensitive to the discrete directions of the stencil. In case of high optical depth and high albedo, this ray-effect diminishes and the mesoscopic RTLBM is accurate as discussed here. Other optical media might be predicted wrong close due to the occurrence of rays in the simulation.

6.3. Numerical Experiments for P1-RTLBM

This section provides the validation of the novel P1-RTLBM presented in Section 4.2.3. First, it is investigated the effects of angular discretization by the Lebedev–Laikov stencils, followed by a grid independence study. Then, the benchmark scenarios of infinite and finite radiative source, each considering diffuse and collimated source, are validated against MC data considering 35 different RT regimes.

6.3.1. Angular discretization and grid independence

This section investigates the impact of the Lebedev–Laikov quadrature rule for $q = 7, 15$ and 27 directions and the grid size to the computed intensities along line 1. The considered scenario includes a finite collimated radiative source and a highly scattering volume that is characterized by optical parameters $a = 1$ and $b = 6$.

Similar to the mesoscopic RTLBM the present numerical model is based on a Lebedev–Laikov quadrature rule to compute the equilibrium expression (4.9) for the collide-and-stream equation. From theory, it is expected that a higher integration order yields in a more accurate computation of the scattering integral. To verify this forecast, a diffuse RT regimes is computed for the benchmark scenario of a finite and collimated beam for Lebedev–Laikov stencils with $7, 15$ and 27 directions. The simulation results along line 1 are depicted in Figure 6.8a and show that the intensity profile for the stencil with 27 is the most accurate one. The stencils with 7 and 15 directions lose in precision. This observation meets the expectation from the theory of quadrature rules and suggests that increased integration order enhances accuracy of the numerical algorithm.

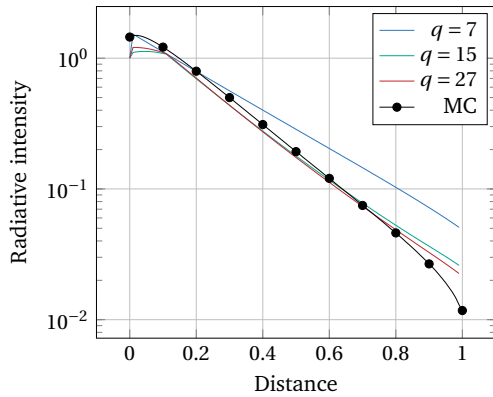
Various grids of resolution $50, 100$ and 150 are simulated in order to identify grid independence of the P1-RTLBM. Figure 6.8b depicts the intensities along line 1 for the Lebedev–Laikov stencil with 15 directions and varying grid sizes. The simulated intensities for the diffuse transport regime are in good agreement and already a resolution of $\Delta x = 0.01L_0$ lead to precise data. A further increase in the grid resolution does not provide significant improvements on the accuracy. The following analysis is subsequently based on grid size $N = 100$ or equivalently $\Delta x = 0.01L_0$.

6.3.2. Infinite radiative source

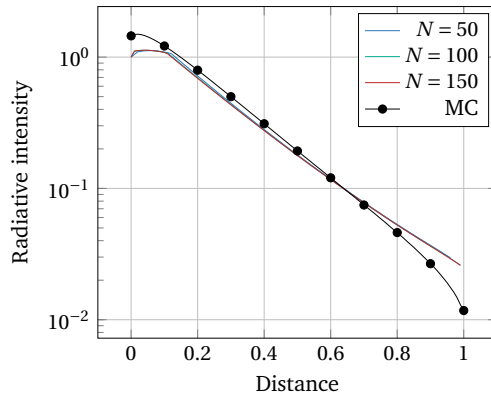
The P1-RTLBM and MC simulations are examined to the benchmark scenario *infinite collimated beam* and *infinite diffuse beam*, where the radiation source extends to an entire wall. By analyzing the simulation errors along the central line, the overall quality of the simulated RT can be specified. However, it is difficult to clearly assign shortcomings due to absorption, in- or out-scattering.

The simulation errors for the 35 different participating media are presented in Figure 6.9 for collimated and diffuse sources. Media with equal transport scattering albedo are represented within a line, whereas the optical depth b ranges from 2 – 30 . The general trends and also the simulation error are similar to the ones reported for the mesoscopic RTLBM reported in Section 6.2.

6.3. Numerical Experiments for P1-RTLBM

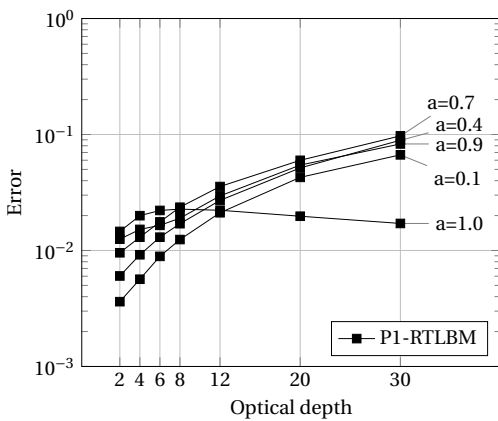


(a) Impact of discretization stencil with 7, 15 and 27 directions.

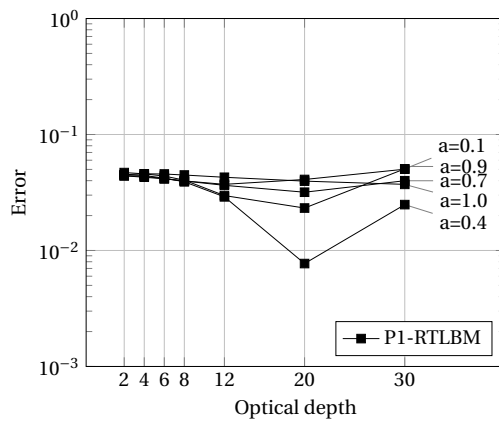


(b) Grid independence study for Lebedev-Laikov quadrature with 15 directions.

Figure 6.8.: *Finite collimated source* and diffuse RT regime ($b = 6, a = 1$) simulated with the P1-RTLBM. Depicted intensity profiles represent line 1 in the cubical simulation geometry.



(a) Collimated beam.



(b) Diffuse beam.

Figure 6.9.: Errors for the benchmark scenario *infinite beam*.

6. Numerical Validation Against Monte–Carlo

Collimated beam

The precision of the P1-RTLBM is over all optical parameters good and the measured error is smaller than 10%. Except for volumes that are characterized by scattering albedo $a = 1$, there is a clear trend of better performance for optical thin media. This is explained in analogy to the mesoscopic RTLBM. Considering for instance the volumes of $a = 0.4$ and varying optical depth. Then the increase in optical depth leads to more photon-volume interaction per grid point. However, the fixed numerical grid size does not account for the increased interaction and resolves the optical thick media not as precise as the optical thin media.

Non-absorbing media ($a = 1$) are predicted with an error of 1–2% independently of the optical depth. This shows the consistency to the diffusion approximation of the P1-RTLBM and is explained by the vanishing flux in the equilibrium expression (4.9) due to the diffuse RT.

Diffuse beam

The measured errors of the P1-RTLBM are smaller than 10% for all 35 optical parameter sets. Despite the outliers of $a = 0.4$ and optical depth 20 all simulations are of very similar quality with no remarkable trends. The lack of a clear tendency over the large optical parameter set, that including distinct transport regimes, assumes that the error measurement of this benchmark scenario is not able to point out the strength and weaknesses of the numerical algorithm. As a consequence this survey can not provide a valid and comprehensive validation of the P1-RTLBM for diffuse radiative sources of infinite extent. Further investigations including different boundary models, such as equilibrium boundaries, might help to understand the simulation error.

6.3.3. Finite radiative source

The results obtained for the scenario of an infinite beam cannot answer the question of how accurate the in- and out-scattering of radiation is treated. In particular, the transport of radiation to ambient regions, that are not exposed directly to the radiative source, cannot be validated properly. To this aim, this Section is based upon a spatially restricted radiative source, which corresponds to the scenario of a *finite beam*, see Figure 6.1. The P1-RTLBM simulations are carried out again for all 35 participating media and the errors between the macroscopic RTLBM and the MC simulation are depicted in Figure 6.10.

Now, the errors along line 2 and 3 will be of particular interest, since they measure the accuracy of the simulation of the absorbed as well as the in- and out-scattered radiation.

In particular, the transport of radiation to ambient regions, that are not exposed directly to the radiative source, is of interest since it was not accessible by benchmark scenario *infinite beam*.

Collimated beam

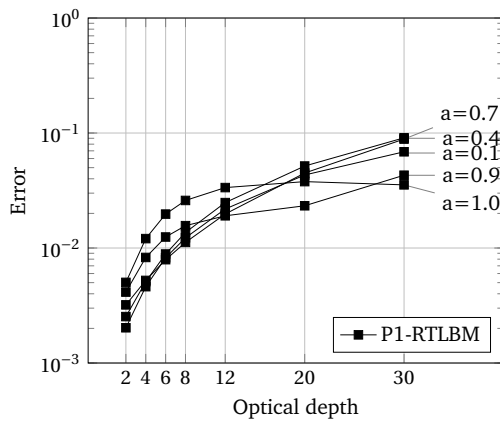
In this benchmark scenario the P1-RTLBM shows very good results along line 1 for optical thin media with an error $\leq 1\%$, almost independently of the scattering albedo. For higher optical depths, the error diverges, except for $a = 1$, for the same reasons as for the benchmark scenario of a collimated finite beam, pointed out above. Diffuse transport ($a = 1$) in contrast is predicted more accurately for an increased optical depth, which is also observed for the above referred benchmark scenario.

When considering the RT to ambient regions by computing errors for line 2 and 3, the general tendency of a great prediction of diffuse RT is conserved and even more striking. The latter is depicted in Figure 6.10c and 6.10e for $a = 1$. More precisely, while the error on line 2 still decreases and seems to converge for an increased optical depth, the error depicted on line 3 stagnates for optical depths ≥ 12 and remains at a low level about 1%. Other transport regimes are predicted on line 2 and 3 with an error $\geq 10\%$ and are not considered to be reliable. This is confirmed by the lack of a plausible trend considering the scattering albedo. Instead, the error levels are crossing of the errors for $a = 0.4$ and $a = 0.9$ and others.

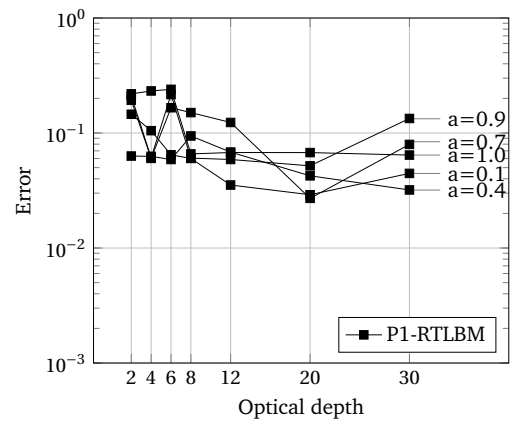
Diffuse beam

The results of this benchmark scenario are depicted in Figure 6.10 (right column). RT along line 1 is predicted with an error $\approx 8\%$, independently of the optical depth and scattering albedo. As in the scenario of a diffuse infinite beams, there is no remarkable trend among the 35 different volumes. The reasons therefore might be manifold and need additional analysis. The diffuse characteristic of the radiative source does lead to a pyramid effect as for the mesoscopic RTLBM and falsify the prediction. Better boundary conditions might prevent the ray-effect for general diffuse sources. Interestingly, diffuse RT into ambient regions is predicted with the same quality as the collimated infinite beam scenario. This observation might be due to the smoothing character of the P1-equilibrium term (4.9).

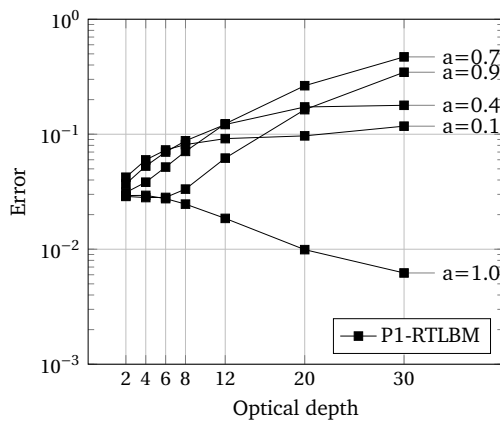
6. Numerical Validation Against Monte-Carlo



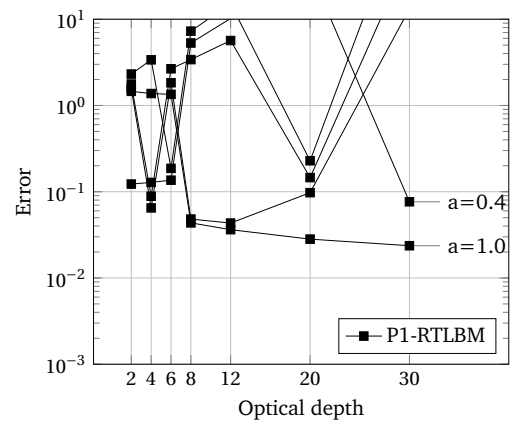
(a) Collimated beam along line 1.



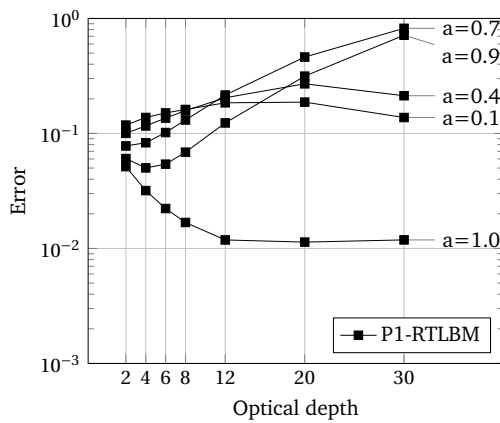
(b) Diffuse beam along line 1.



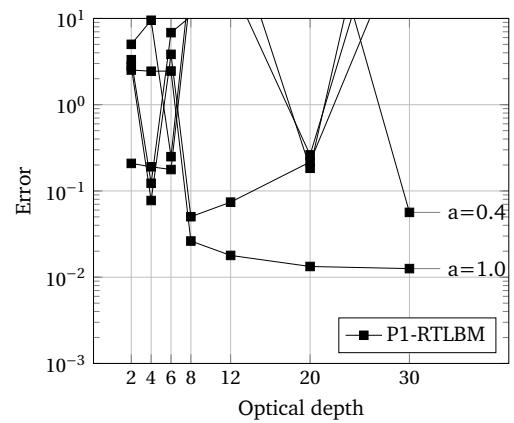
(c) Collimated beam along line 2.



(d) Diffuse beam along line 2.



(e) Collimated beam line 3.



(f) Diffuse beam line 3.

Figure 6.10.: Errors for the benchmark scenario *finite beam*.

6.4. Numerical Experiments for Macroscopic RTLBM

This section provides the validation of the macroscopic RTLBM presented in Section 4.2.1 that is based on an indirect strategy of solving the diffusion approximation presented in Section 2.5. An essential requirement for the accuracy of the diffusion approximation is that the transport regime is characterized by a high scattering albedo. After a short radiative path, the photons undergo numerous scattering events that deviates the incident direction and leads to diffuse propagation in the far field. In such situations literature reports an error at predicting the magnitude of radiance intensity of $< 10\%$ for media with $a > 0.95$, see [50]. RT regimes with a strong anisotropic tendency, typically close to boundaries and sources, violate the diffusion hypothesis and can not properly be described by the Helmholtz equation (2.12), which is pointed out in the course of this section.

To start with, it is introduced to the methodological drawback of the diffusion approximation at boundaries and the good prediction of the far field. Figure 6.11 illustrates an exemplary profile for a diffuse transport regime with optical parameters $a = 0.9$ and $b = 30$. The observed inaccuracy close to the boundary is due to the modeling hypothesis of isotropic scattering (isotropic equilibrium state), that fails to predict anisotropic transport by associating every direction the same portion of radiance through the formula $f_i^{eq} = w_i \Phi$. However, after a penetration depth of about $2l_{\text{mfp}}$ the radiation transport is almost diffuse and the results are very close to the MC data. This behaviour is further confirmed by computing the flux according to (3.2), which vanishes after some mean free path length, indicating isotropic transport. The latter is often referred to as the far field and is simulated in remarkable agreement to MC data.

6.4.1. Angular discretization and grid independence

The macroscopic RTLBM was validated in Mink et al. [125] concerning standard $D3Q7$ stencils and shown to be grid independent. It has also been pointed out, that the macroscopic RTLBM is a second order scheme subjected to Dirichlet boundary conditions. Since the model assumes isotropic scattering behaviour of the volume, the angular resolution of the axis aligned direction is sufficient. This is also suggested by the spherical geometry and diffuse source of the investigated geometry in Mink et al. [125].

6. Numerical Validation Against Monte–Carlo

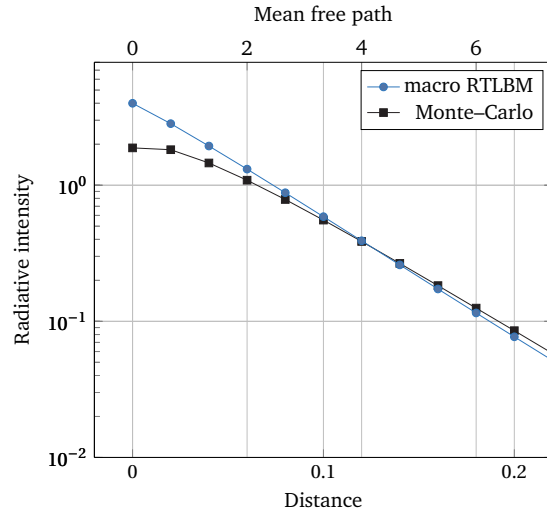


Figure 6.11.: Radiance intensity profiles along line 1 for $a = 0.9$ and $b = 30$. Radiance close to boundary is not predicted accurately due to the isotropic equilibrium of the macroscopic RTLBM.

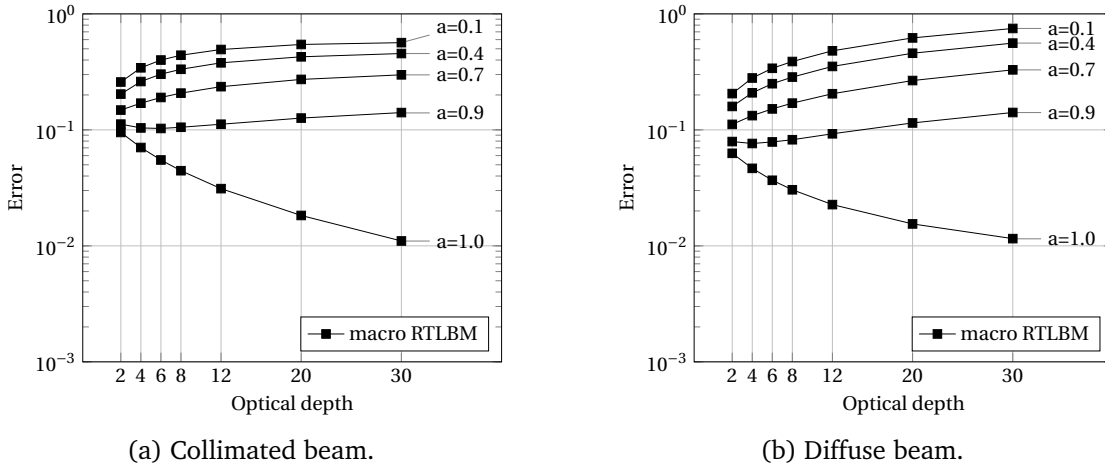
6.4.2. Infinite radiative source

The macroscopic RTLBM and MC simulations are examined to the benchmark scenario *infinite collimated beam* and *infinite diffuse beam*, where the radiation source extends to an entire wall. By analyzing the simulation errors along the central line, the overall quality of the simulated RT can be specified. However, it is difficult to clearly assign shortcomings due to absorption, in- or out-scattering.

The simulation errors for the 35 different participating media are presented in Figure 6.12 for collimated and diffuse sources. Media with equal transport scattering albedo are represented within a line, whereas the optical depth is in the range of 2–30.

Collimated beam

The errors along line 1 of the macroscopic RTLBM are accurate for highly scattering media of $a \geq 0.9$, which is also claimed from theory. For such transport regimes the method even converges fast towards the MC solution for high optical depths and is already appropriate for $b \geq 12$. This observation shows the quality of the diffusion approximation in diffuse transport regimes. On the other hand, for media with $a \leq 0.7$, the macroscopic RTLBM stagnates independently of the optical depth. This can be explained by the violation of the diffusion approximation requirements, which is a scattering albedo of $a > 0.9$. For such RT regimes the diffusion approximation is no longer accurate and the macroscopic

Figure 6.12.: Errors for the benchmark scenario *infinite beam*.

RTLBM cannot provide reliable simulation data.

The sampling of scattering albedo into 0.1, 0.4, 0.7, 0.9 and 1 is not sufficient fine to determine the exact break point of the diffusion hypothesis. According to the simulation errors, an additional sampling in the range of 0.9–1 might determine the validity range of the diffusion approximation in greater detail. In general, it is clear, that the transport regimes with scattering albedo > 0.9 are suitable for the simulation with the macroscopic RTLBM. Compared to the mesoscopic RTLBM, this is a small range of optical parameters.

Diffuse beam

The macroscopic RTLBM is applied to $D3Q7$ stencils that are equipped with axis aligned directions. Due to the lack of diagonal directions, diffuse boundaries cannot be modeled by this $D3Q7$ LBM stencil. Hence, the macroscopic RTLBM simulation results are very similar to the collimated source data. As such, the distribution of radiation in optically thin media and absorption dominated media is predicted poorly. This deficit is due the violation of the diffusion hypothesis, similar as for the case of a collimated infinite beam. However, the simulation matches the reference MC in highly scattering media, resulting in a precise prediction for diffuse transport regimes. A strong dependency of the accuracy on the scattering albedo is also observed. Therefore, the method requires $a > 0.9$ for an error of $\leq 10\%$.

6.4.3. Finite radiative source

The results obtained for the scenario of an infinite beam cannot answer the question of how accurate the in- and out-scattering of radiation is treated. In particular, the transport of radiation to ambient regions, that are not exposed directly to the radiative source, cannot be validated properly. To this aim, this Section is based upon a spatially restricted radiative source, which corresponds to the scenario of a *finite beam*, see Figure 6.1. The simulations are carried out again for all 35 participating media and the errors between the macroscopic RTLBM and the MC simulation are depicted in Figure 6.13.

Now, the errors along line 2 and 3 will be of particular interest, since they measure the accuracy of the simulation of the absorbed as well as the in- and out-scattered radiation. In particular, the transport of radiation to ambient regions, that are not exposed directly to the radiative source, is of interest since it was not accessible by benchmark scenario *infinite beam*.

Collimated beam

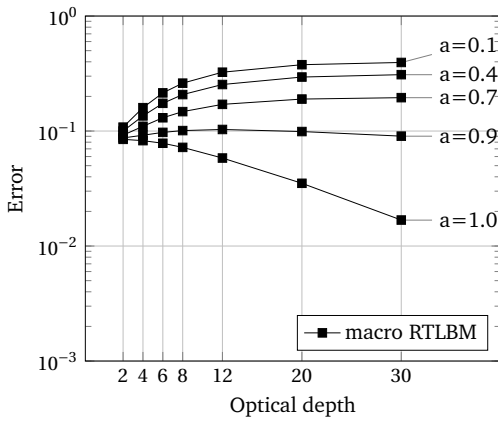
Considering the errors of the macroscopic RTLBM along line 1, 2 and 3, the scheme is accurate for a high scattering albedo and converges in the limit of a high optical depth. This means that diffuse RT is simulated accurately by the macroscopic RTLBM, also in the ambient regions of the domain, see Figure 6.13c and 6.13e for $a = 1$. These results coincide with the findings in Mink et al. [125], where it is showed that the macroscopic RTLBM is a very accurate and suitable scheme for highly scattering media. Compared to the diffuse RT, the ballistic and other RT regimes are predicted with a loss of precision up to an error of $\geq 1\%$. This observation follows the trend of an increased error, the more the RT becomes ballistic.

The minimum error along line 3 for the $b = 20$ and $a = 0.4$ (see Figure 6.13e), is explained by the definition of the error measurement. Here, the intensity profiles are not only aligned to the MC data but even intersect. This yields in an artificially small error which is also observed later in the scenario of a finite diffuse beam. Nevertheless, this phenomenon is observed only for transport regimes of $a = 0.1, 0.4$ and 0.7 , which are not of particular interest due to the violation of the diffusion approximation hypothesis.

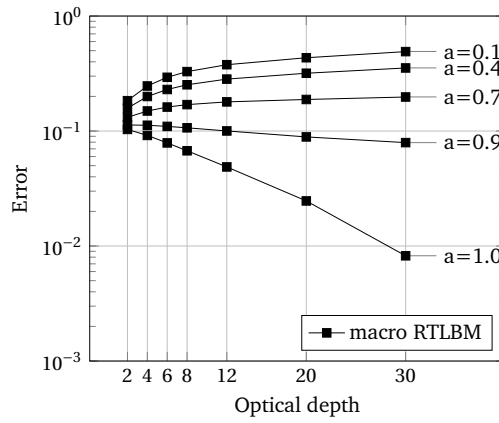
Diffuse beam

With regard to the diffuse transport regime, the macroscopic RTLBM predicts the radiation intensity accurately along all three lines. This verifies that the simple isotropic equilibrium is able to predict complex radiative sources of finite extent and diffuse characteristic. By

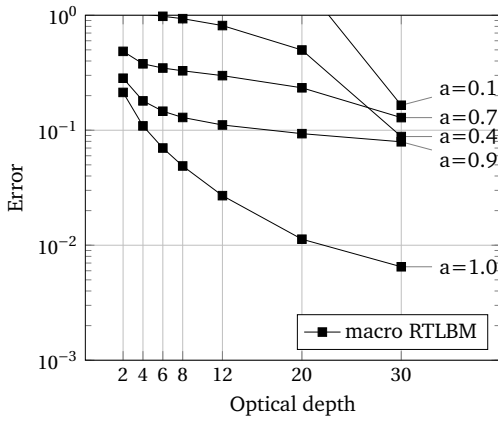
6.4. Numerical Experiments for Macroscopic RTLBM



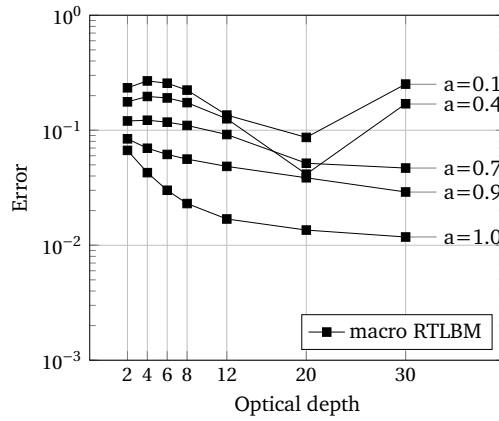
(a) Collimated beam along line 1.



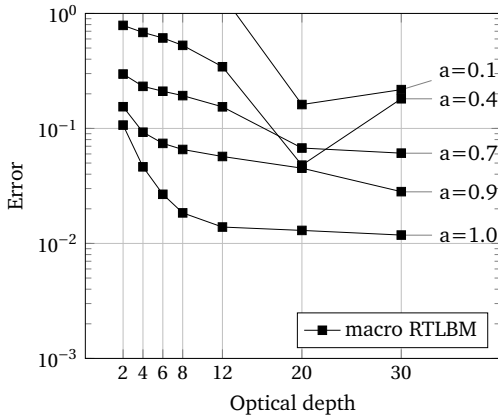
(b) Diffuse beam along line 1.



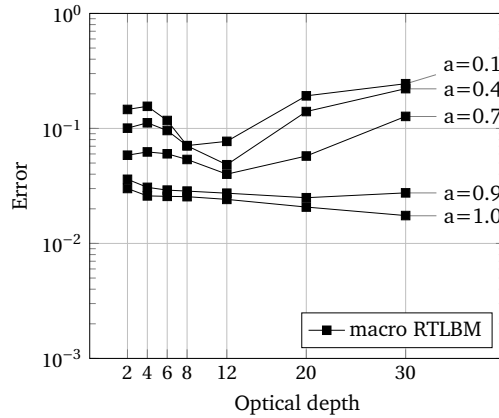
(c) Collimated beam along line 2.



(d) Diffuse beam along line 2.



(e) Collimated beam line 3.



(f) Diffuse beam line 3.

Figure 6.13.: Errors for the benchmark scenario *finite beam*.

6. Numerical Validation Against Monte–Carlo

running simulations for 35 different participating media, the scope of validity for the diffuse transport regimes is indicated numerically. Taking all lines 1, 2 and 3 into account, it can be said that the macroscopic RTLBM performs excellent for a ≥ 0.9 . As expected, a smaller scattering albedo violates the assumptions behind the diffusion approximation and as a result the numerical scheme is not an adequate choice for such media. This tendency of poor numerical results the more the transport regime becomes ballistic is suggested by the data and expected by the theory of the diffusion approximation.

6.5. Performance of RTLBM

This section provides a discussion and comparison of the conducted numerical experiments for the mesoscopic, the P1 and the macroscopic RTLBM. Aspects as validity range in Section 6.5.1 and computation time in Section 6.5.2 are discussed and as a conclusion the guidelines for a good choice of RTLBM in Section 6.5.3 are proposed. The main effort of this concentration of the simulation data¹ is to clearly assign the strength of the specific RTLBM to finally guide application engineers to a proper choice of the numerical scheme.

6.5.1. Validity range of RTLBM

Depending on the transport regime, the conceptual strengths and weaknesses for both RTLBM have been validated in detail. Most of the discussed phenomena can be reduced and explained by the equilibrium function, which imposes the physics by defining a local target configuration for the photon populations. Commonly, the equilibrium function is a function of higher moments, e. g. intensity Φ and flux J , meaning that the equilibrium is based on the averaged photon populations. At this point, the mesoscopic RTLBM differs from the macroscopic RTLBM and its moment–based equilibrium function, in the spirit of the common LBM. The first strikes out a new path by considering a discrete version of the phase function and computing the scattering integral for all directions in an LBM stencil. A combination of both approaches is introduced by the P1-RTLBM and its spherical harmonics based equilibrium construction. The mesoscopic algorithm relaxes for this RTLBM scheme towards an equilibrium stated defined by the intensity (isotropic) and the flux (anisotropic). It can be considered as an extension of the macroscopic RTLBM by a higher order equilibrium function in the base of spherical harmonics.

¹Four benchmarks scenario considering three lines, executed to 35 optical parameter sets and simulated by three different algorithm are about 1200 data sets.

The simulation results of the benchmark scenario *infinite collimated beam* are summarized in Figure 6.14, where the contour lines account for the simulation error in the set of optical parameters, defined in Figure 6.3. In terms of asymptotic, it can be said that the macroscopic RTLBM converges in the limit of optical thick media ($b \gg 0$) under the constraint of a high scattering albedo. Otherwise, the underlying P1-Approximation hypothesis is violated and the derived macroscopic RTLBM suffers from inaccurate simulation results. A contrary results holds for the mesoscopic RTLBM, that converges for optical thin media. Higher grid resolutions are expected to resolve optical thick media better and reduce the error. The coupling of resolution and optical parameter might constrain the method in real engineering application as well as the limitation to light sources of finite extend. In addition, the sensitivity to diffuse boundaries and the integration stencil, with regards to ray-effects might limit the application. Both methods have been reviewed in terms of convergence order [125, 121, 118], where the macroscopic RTLBM was found to be a 2nd order scheme and the mesoscopic RTLBM is a 1st order scheme. The novel P1-RTLBM combines both asymptotic behaviour being generally accurate in optical thin media and converging for optical thick media under the constraint of high scattering albedo.

6.5.2. Comparison of computation time

The application to complex three dimensional geometries might be time critical or even bounded by the memory. A comparison of the computation time for meso- and macroscopic RTLBM and the 35 different optical media is found in Figure 6.15. The simulations were performed on a single core (Intel Xeon Silver 4114) for the purpose of a consistent comparison. In applications, the RTLBM is typically executed on parallel computers to benefit from the outstanding parallel performance of the LBM algorithm and reducing the computation time drastically [131]. Here, the grid is discretized in every direction by 100 nodes ($\Delta x = 0.01L_0$) and the simulation was terminated after a deviation of 1×10^{-8} in the light intensity during 160 iterations. The overall computation time is mostly smaller than 50 min and both RTLBM take similar time to reach the steady state RT. It is remarkable, that this observation changes for an increase in optical depth. Already for $b \geq 12$, the computation time for the mesoscopic RTLBM is superior and this trend increases the thicker the media, independently of the scattering albedo. Media with optical depth of 20 and higher is computed about three times faster by the macroscopic RTLBM. This comparison does not include exact numbers of the P1-RTLBM. However, the absolute numerical cost is a little higher than the macroscopic RTLBM, as the flux has to

6. Numerical Validation Against Monte-Carlo

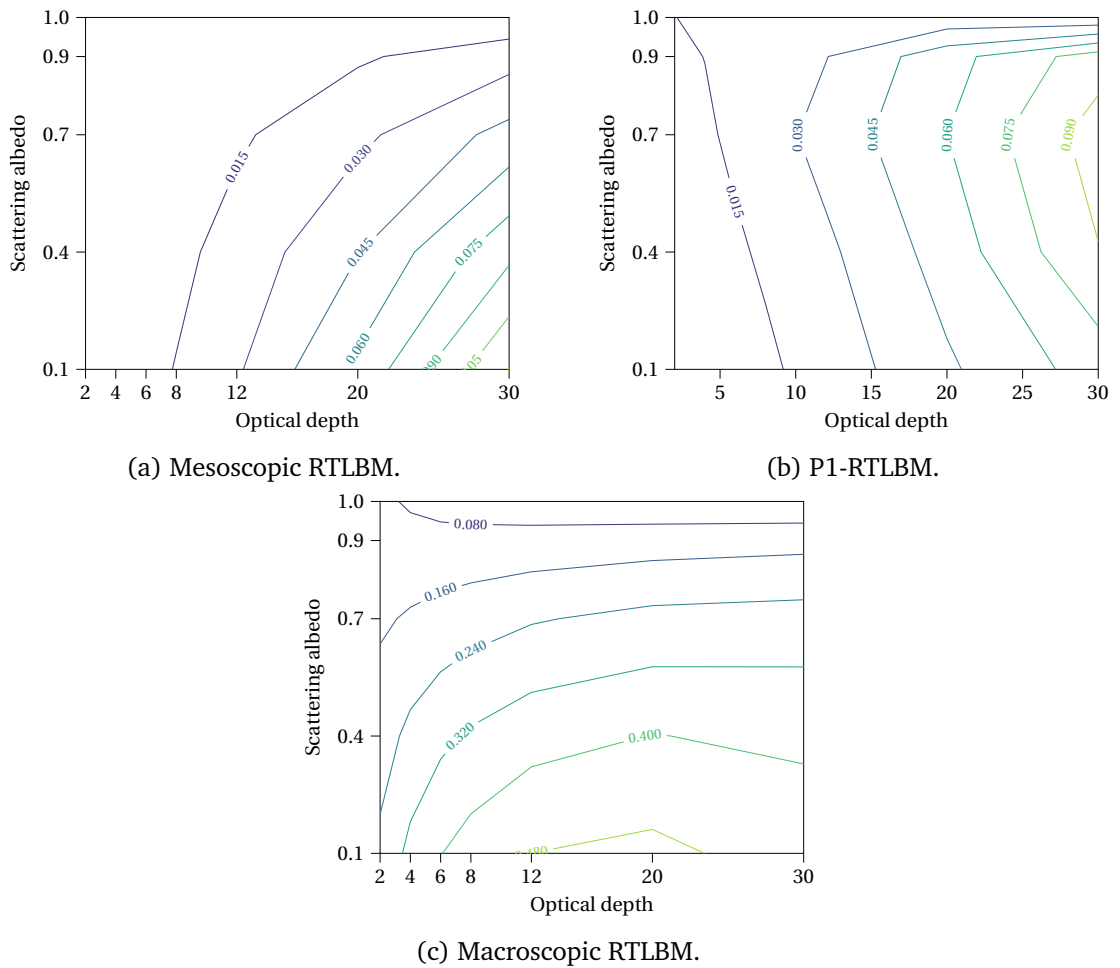


Figure 6.14.: Contour plots of the determined error over the total optical parameter set.

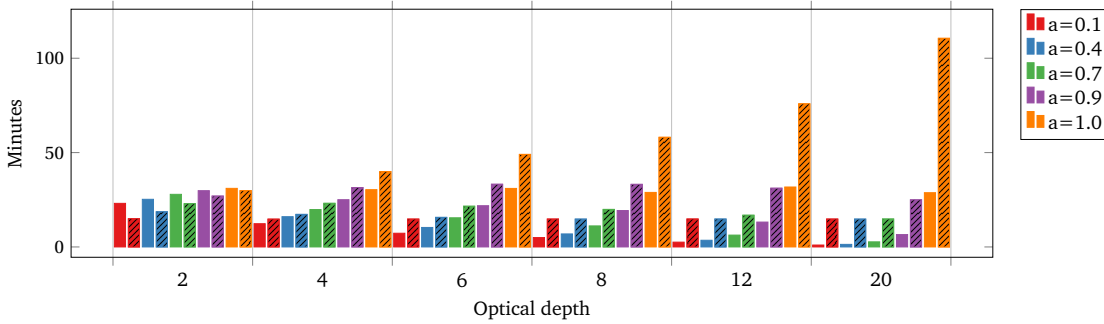


Figure 6.15.: Comparison of computation time in minutes plotted over the optical depth and scattering albedo (color). E. g. the green bar in the optical depth of 12 corresponds to the simulation time of macroscopic RTLBM for participating media with $a = 0.7$ and $b = 12$, where the mesoscopic RTLBM is additionally plotted with a pattern.

be computed additionally, but does not reaches the mesoscopic time effort. Considering the tendency over the parameter set, the P1-RTLBM as both other methods comes with an increase of computation time for diffuse transport regimes.

The strict convergence criteria of the present investigation, regardless of the total intensity in the domain, might bias the comparison of media of the upper and lower bound of the optical depth. Whilst the simulation with high optical depth and hence, high extinction reaches for almost all nodes rapidly very low radiative intensities, the simulation of thinner media takes generally more time to converge. Similar phenomena was taken into account by the normalization of the absolute error in the validation against MC data in Section 6.1.1 and could be applied to the time aspect as well. Still, the analysis allows drawing conclusion when comparing the RTLBM for a specific parameter set, as presented in the above discussion.

6.5.3. The choice of suitable RTLBM

To summarize, it is presented guidelines and recommendations for the choice of the RTLBM, that is based on the desired illumination by finite or infinite radiative sources of either diffuse or collimated character and the desired error tolerance. Starting with the infinite collimated light sources, it is recommended to simulate optical thin media < 20 with either the mesoscopic or P1-RTLBM. Both achieve an accuracy of $< 6\%$ and while the computation time of the P1-RTLBM is smaller (not showed) due to the much simpler equilibrium function, the mesoscopic RTLBM is more accurate by a factor of two. In the limit case of scattering albedo ≈ 1 the macroscopic RTLBM produces accurate results and

6. Numerical Validation Against Monte–Carlo

is recommended over the others, since the computational effort and memory requirements is the smallest. This situation changes dramatically when the radiative source becomes diffuse and small, for instance general LED spots. Then, the diffuse emission of the source leads to ray-effects that extends over the entire computational domain, for both the mesoscopic and P1-RTLBM. Even though this phenomenon becomes less significant with increased scattering albedo, it does not vanish and as a consequence both RTLBM should be avoided. However, the macroscopic RTLBM has shown its advantage for this radiative configurations and is recommended due to its fast and precise simulation.

6.6. Future Model Extensions

The numerical experiments showed that the macroscopic RTLBM lacks of precision for ballistic transfer regimes, while the performance of the mesoscopic RTLBM depends strongly on the configuration of the radiation source. According to the investigation, both RTLBM differ greatly in their computation time and precision for the different RT regimes. A possible performance improvement of RTLBM is a hybrid model that computes anisotropic transport by the mesoscopic method, whereas the diffuse transport is simulated by the fast efficient macroscopic RTLBM. Such a hybrid model should speed-up the simulations significantly while the error is kept at the same level. In order to avoid numerical interpolation, both methods should run on the same LBM stencil and in dependence of the flux J and hence, anisotropic transport, the hybrid RTLBM chooses the suitable collision rule. A first step, towards such hybrid models has been proposed with the P1-RTLBM, where the anisotropic transport is resolved by a higher order diffusion approximation. Similar approaches for connecting solvers, even solvers from different disciplines, to compute the RTE exist in the literature [184, 91]. However, the unique feature of an LBM based model is, that RTLBM benefit from a consistent methodological approach, which promises advantages in terms of computational efficiency and avoids additional complexity of interpolation.

Extensions of the presented models are also desirable in view of thermal radiation transport. In each of the investigated benchmark simulations non-thermal gray radiation transfer in non-emitting and homogeneous media was considered. To account for thermal radiation transfer, emission of radiation must be incorporated into the models in addition. For both presented models, this extension can be easily realized by another source term accounting for the emission of thermal radiation. In fact, most of the previous scientific applications of RTLBM focused on heat transfer problems and emitting materials have been considered in different 1D and 2D models [126, 127, 114, 14]. In these works

isotropic emission was modeled with respect to the local temperature and a similar implementation in the here presented 3D RTLBM is straightforward.

A further extension to heterogeneous thermal problems and conjugated heat transfer can be achieved by a source term [97, 114, 109]. This is remarkably intrinsic compared to the conventional CFD solvers treatment, where Dirichlet or Neumann conditions are imposed on the interface, which need to be solved by iterative schemes and adds further complexity, for instance in porous structures.

Another open point is the spectral nature of radiation, which has been rarely considered in applications of RTLBM [116], although the underlying concept of tracing a population of pseudo-particles offers interesting opportunities of doing so. In addition to the fluence function f that accounts for radiation at a certain wavelength, it is straightforward to add a second fluence function g representing radiation at another wavelength in a medium with different radiation characteristics and so forth. Every fluence function is associated to a discrete RT regime for a specific wavelength and is simulated simultaneously on the same mesh and hence the total intensity, the local temperature and emission can be computed accordingly to the simulated wavelengths in a non-gray medium. This procedure is widely adopted in multi-physics LBM, for instance conjugated heat transport or multi-phase and -component applications [164, 71, 177, 112]. With regard to non-gray applications, the collision kernels of the RTLBM should be selected accordingly to the radiation property of the participating media, as shown by the computations in the present thesis. By doing so, both models can be solved in parallel on the same mesh, accounting for RT at certain wavelengths, whereby the number of simulated wavelengths might be limited to the order of 10 under the current constraints of computational power, which however seems sufficient for applications of non-gray radiation transfer [172].

7. Comprehensive Kinetic Model of PBR

The design and optimization of PBR can benefit from the development of robust and yet quantitatively accurate computational models, that incorporate the complex interplay of fundamental phenomena. At a minimum, the simulation model requires at least three submodels for hydrodynamic, light supply and biomass kinetics as pointed out by various review articles on CFD models for PBR design [17, 59, 143]. By modeling the hydrodynamics, the LD-cycles can be detected and the mixing characteristic of the flow besides its mass transport is analyzed. The underlying modeling equations and simulation algorithm are discussed in Section 7.1. The RT model is deployed to predict the local light intensities according to wavelength of the light and scattering characteristic of the culture, to which Section 7.2 is dedicated. The third submodel implements the biomass growth kinetic, by coupling the local light intensities to hydrodynamic information of CO₂ concentration, to predict the algal growth as pointed out in Section 7.3. Figure 7.1 depicts the three (sub-) models and its coupling, indicated by the arrows. All presented models are formulated and computed by an LBM, yielding a consistent simulation scope and simple yet efficient coupling.

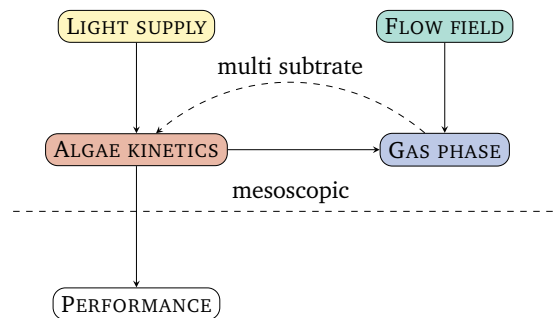


Figure 7.1.: Interplay between light supply, fluid flow, gas transport and algae kinetics. The arrows indicate the implemented coupling in the present work. The coupling indicated by the dashed line is discussed in the outlook and requires a multi substrate model for the growth kinetic.

The developed mesoscopic simulation model is then applied to three real PBR. The first reactor is based on a traditional flat plate geometry and is simulated in Section 7.4. Its

7. Comprehensive Kinetic Model of PBR

simple hydrodynamics and light setup allows to discuss the coupling comprehensively and emphasize the prototype character, by quantitative identification of coupling parameters. Whereas the next PBR is internally-illuminated and has complex light sources and boundaries, see Section 7.5. Light simulations for two wavelengths provide insights in the local light intensities and demonstrate the need of light models that account for spectral light composition in the reactor illumination. Finally, a tubular PBR with transparent walls and internal sponge structure is investigated in Section 7.6. The complex hydrodynamics and the homogeneous illumination in such reactors is very promising for CFD based optimization.

7.1. Fluid, Particle and Gas Transport Models

A crucial feature in the cultivation of microalgae is the mixing, that reduces nutrients, temperature and pH gradients in PBR as well as mechanically prevents the cell sedimentation, dead zones and cell attachment to reactor walls. Another important aspect of mixing is the increased gas transport between the gas-liquid phase and finally the homogenization of the irradiance through cell movement, also referred to as LD-cycles. The reason why the mixing cannot be maximized without any constraint is twofold. First, an increase in mixing intensity can apply high shear stress to the microalgae and finally deals damage to the cell. For instance, *P. tricornutum* is reported to decline in specific growth rate when the micro-eddies become smaller than $45\ \mu\text{m}$ [32, 47]. As a rule of thumb fluid velocities around $0.2\text{--}0.5\ \text{ms}^{-1}$ are recommended for tubular reactors [147]. Second, extensive mixing undoubtedly increases the operating costs and hence is a key parameter for the efficient operating of PBR.

7.1.1. State-of-the-art

Recent progress in closed PBR design focus intensely on passive turbulence promoters to implement a proper mixing while reducing the energy uptake significantly. Numerical investigation of tubular reactors with diameter of 0.05 m presented by Gómez-Pérez et al. [65] compared algae trajectories in the flow field for different wall turbulence installations. They concluded that the flow velocity can be halved while retaining or even improving the mixing. The hydrodynamics in a tubular reactor with diameter of 0.04–0.08 m equipped with helical installations were analyzed using CFD in several publications [142, 204, 153]. It was found that (helical) static mixer enhance the mixing, mass transfer and homogenize the irradiance to the algae culture. This findings were

confirmed by cultivation experiments, that showed an increase of biomass productivity of *Chlorella sp.* by 37.26% in such tubular PBR. Similar approaches for flat plate PBR are found in literature, where the arrangement of risers is analyzed by CFD [81, 141] and analogously, the bubble column reactors are analyzed by CFD [136, 117].

Recently, ultra-thin flat plate PBR gained attraction by the reported increase of biomass concentration and hence biomass productivity, due to very short light paths [63]. The experimental study conducted extremely high microalgal concentration with up to 24 kg m^{-3} for *Chlorella sorokiniana* in 3 mm thick reactors illuminated by light intensity of $1000 \mu\text{mol m}^{-2} \text{ s}^{-1}$. A more complex Taylor vortex PBR was survey in a sequence of publications [56, 57, 55, 54], where the gap with of 12.7 mm indicates also an ultra-thin reactor geometry. The particular study [55] focused on the CFD based investigation of Euler–Euler mass transfer model. However, the findings are specific to the Taylor vortex design and do not apply to general reactor designs.

7.1.2. Fluid flow equation and Lagrangian particle tracking

Numerical investigation of general fluid fields are based on the Navier–Stokes equation for incompressible fluids

$$\partial_t \mathbf{u} + (\mathbf{u} \cdot \nabla) \mathbf{u} = -\frac{\nabla p}{\rho} + \nu \nabla^2 \mathbf{u}.$$

For the fluid density ρ , pressure p and kinematic viscosity ν , they determine the fluid velocity \mathbf{u} . This macroscopic equation is solved according to the LBM algorithm showed in Section 3.3.3 and is computed by the open-source LBM solver *OpenLB* [103, 100]. Typically, the inlet of the PBR is imposed to a constant velocity condition, where the outlet is subjected to a pressure boundary condition. Other boundaries are implemented as a no-slip walls, according to the model of Bouzidi et al. [21]. Instead of simulating the no-slip wall by a standard bounce-back method, this algorithm is an interpolated bounce-back method and reduces the staircase error of the aforementioned on the curved walls. To account for the turbulence, it is applied a large-eddy simulation that replaces the viscosity with an (local) effective viscosity that models the non-resolved scales [135, 75]. Basically, the turbulence in the flow regime is either modeled or resolved depending on the eddy-size, yielding a computational efficient and comprehensive CFD tool for complex fluid flows. The deployed LBM simulation model has been presented in [78] and is available to the public through the solver *OpenLB*.

The individual algae cells are tracked in the flow field inside the PBR by an Euler–Lagrange approach, to determine their trajectory. After computing the fluid velocity according to the above scheme, a representative set of point particles are added to the

7. Comprehensive Kinetic Model of PBR

flow field. Those algae cells are modeled as spherical Lagrangian point particles of mass m_p and tracked according to Newton's second law of motion

$$m_p \partial_t \mathbf{u}_p = \mathbf{F}_p,$$

for a general force \mathbf{F}_p and fluid velocity \mathbf{u} . Unlike Euler–Euler models, that consider the algae cells as a continuum phase, the Lagrangian approach resolves single particles, typically spherical shaped, in the flow field ¹. Due to the small characteristic size of microalgae (2–10 μm) the Stokes drag force

$$\mathbf{F}_p = \frac{\pi r_p^2}{2} \rho_p C_D (\mathbf{u}_F - \mathbf{u}_p),$$

for a drag coefficient C_D applies, with particle radius r_p and density ρ_p [107]. The model assumption behind this formula is that the algae does not affect the fluid flow. Instead, the algae particle experiments a general force \mathbf{F}_p from the fluid that can be easily extended to gravity, buoyancy, virtual mass and lift forces if desired. Some authors add a noise or fluctuation components to the computation of the trajectory to account for the turbulence in the flow field [57, 65, 149]. This might be explained by the smoothing behaviour of their fluid turbulence models, namely $k-\epsilon$ or Reynolds-averaged Navier–Stokes (RANS) models, that might require a supplemented artificial noise to retrieve non-laminar trajectories. The deployed LBM simulation model for both, the large-eddy simulation and Euler–Lagrange model, has been presented in [78, 75] and is available to the public through the solver OpenLB.

In summary, it can be said, that the Euler–Lagrange model is a comprehensive tool to study the time evolution of a representative population of algae cells in the fluid flow and to draw conclusion of trapped algae in eddies, the quality of mixing and the induced shear strain stress [107, 58].

7.1.3. Gaseous transport equation

Mass transport of a species or concentration c in a flow field \mathbf{u}_F is modeled by the advection–diffusion equation

$$\partial_t c + \nabla \cdot \mathbf{u}_F c = D \Delta c + R, \quad (7.1)$$

¹Since particle-particle interaction is neglected, particles of different size can be simulated straight forward by multiple Lagrange particles of different mass and radius.

also known as Euler–Euler model. Here, the evolution of the CO₂ concentration c is due to diffusivity D and advection by fluid velocity \mathbf{u}_F , which has to be computed in advance, and a sink term R . The latter accounts for the CO₂ consumption depicted by the photosynthetic conversion and is modeled as a linear function of the photo-conversion rate. Note, that diffusion is an isotropic phenomenon that transports the concentration in all directions equally. In contrast, the advection term transports accordingly to the fluid velocity and in its non-trivial cases it is anisotropic transport. The ratio of both transport regimes is denoted by the *Peclet number* and is a critical number for stability of the numerical scheme.

The simulation of the present work implements a corresponding Euler–Euler model in the framework of LBM presented and validated in [177].

7.2. Light Model

Light supply is the predominant factor in cost efficient cultivation of microalgae in PBR, which is fundamental to achieve economic feasibility and large-scale demand of general biomass production. For the measurements of the efficiency of light conversion to products such as lipids, carbohydrates and proteins, it is introduced the photoconversion efficiency (PCE) as the fraction of irradiance that is converted to chemical energy in a photo-bioprocess. Outdoor microalgal production attain theoretically a maximum PCE of 8–12% depending on the total spectrum of the irradiance [193], while experimental data of a closed indoor PBR showed a PCE of 5.6%. Interestingly, industrial-scale microalgal production hardly attain a PCE of 2%, even at optimal growth conditions. The great loss is due to three phenomena as emphasized in the review article of Nwoba et al. [138]. First, the total solar energy is diminished in the atmosphere by a factor of about 17%. Then, the latitudinal position on the earth yields in about a loss of 30%, depending on where the PBR is placed. Followed by clouds and other participating media in the troposphere that accounts for a further 65% of attenuation. This list applies foremost to outdoor PBR and could be extended to the horizontal reactor orientation and many more. But it shows also, that the few variables, in PCE and light supply considerations, that can be addressed by a proper reactor design, should be optimized with emphasis. For indoor installations the importance of a clever strategy is unaffected and becomes even more eminent, due to the increased control of light guidance and an almost free choice of reactor geometry.

Generally, the light regimes inside a reactor can be categorized into three domains. Close to the light source, algae are exposed to high intensities that might favor photo-inhibition that reduces the PCE. The second regime is the culture that is subjected to

7. Comprehensive Kinetic Model of PBR

photo-limitation. Both volumes are not desired due to their contribution to mixing costs and others, but not to photo-conversion to biomass, for instance lipids, proteins and more. The remaining reactor volume is subjected to photo-saturation and represents the ideal cultivation scenario with respect to light supply. Considering algae concentration of $\approx 2\text{gL}^{-1}$ inside a flat plate PBR that gets illuminated from one direction, then the photo-limitation starts after some few cm [147]. Subjecting the great majority for the reactor volume to photo-saturation is one of the major tasks in successful PBR design and decides whether a PBR can be operated efficiently or not.

From an engineering perspective, the light management to increase the PBR efficiency is manifold and a difficult task. The strategy of cultivation thin biomass concentrations can increase the portion of adequately illuminated microalgae cells, since the light paths are longer before getting absorbed by cells. In other words, the penetration depths of light is greater and equally the light gradient is less strong, which both are desired when cultivating algae. However, the downside of a lower productivity, compared to thick suspensions, is eminent and poses a dilemma for microalgae cultivation in PBR that is being subject of many investigations [171, 46, 139]. On the other side, the approach of an increased surface to volume ratio achieved by either ultra-thin flat plate [63] or capillary reactors [155] or internal-installations diluting the irradiance [90, 43] attain a homogeneous light supply. The trade-off between both strategies can be managed by numerical studies and prediction of local light intensities. To this goal, the following section introduces to the modeling and simulation techniques of light in PBR and discusses the interplay with hydrodynamic simulation with regard to improve light supply.

7.2.1. State-of-the-art

A basic model equation of RT in volume is formulated by the law of Lambert–Beer (2.2), accounting for absorption of the microalgae. The error introduced by Lambert–Beer’s law increases for high biomass concentrations [46], due to the lack of scattering in the model equation. For nearly any configurations that does not involve orthogonal illumination through flat surfaces, this model is a poor approximation. This deficit is well-known and therefore a modified Lambert–Beer model was proposed by Pruvost et al. [150] to predict light in tubular reactors, illuminated by the reactor walls. Still, this empirical model was fitted to predict light in tubular reactors and might not be reliable for general light transport in PBR. General RT in volume is governed by the RTE, which accounts additionally for the scattering characteristic of microalgae. Based on cell size and pigment concentrations, the local light intensities are predicted by the RTE for the

desired wavelength.

Over the last decade, researches applied FVM, MC, RTLBM, DOM and other numerical tools to solve the general RTE and predict local light intensities in microalgal suspension [38, 99, 83, 36, 121]. All of these methods can be used for the prediction and a subsequent quantitative analysis of the light supply. Although the MC is an intuitive and widely used algorithm, that suits complex light constellations, it is computational expensive and compared to the FVM or DOM, the coupling to hydrodynamic solvers is difficult. To this aim, the choice of the numerical algorithm for the computation of light must take carefully by avoiding additional complexity by different scopes of modeling equations and algorithm, as outlined in review articles [17, 143, 59]. Many authors claimed the numerical solvers of RTE to be time consuming and difficult to include in the CFD framework due to different grid sizes and other coupling reasons [57, 143, 17]. Due to the complex 3D geometries, including many light sources, precise numerical investigations of light supply on the basis of RTE are rare in PBR literature [99]. Instead, the light model complexity is often reduced using Lambert–Beer’s law and most importantly, meanwhile, it is emphasized on the interplay to hydrodynamics [57, 1, 48]. This gap is closed by the present thesis and its proposed RTLBM model for solving the RTE in the framework of LBM, which is a well established hydrodynamic solver.

For the optimization based on the above prediction of local light intensities, there are various engineering strategies and approaches. An effective strategy of homogenizing the irradiance in the culture is the intense mixing along the light gradient. Photo-conversion is known to extend over a very short time period and alternating LD-cycles enhance the biomass growth, known as flashing-light effect [182, 163]. This light memory or buffering effect is taken as a basis of many CFD optimization studies that focus on flow control through inner structures in PBR [81, 185, 198, 200]. General numerical studies of hydrodynamics based on an Euler–Lagrange particle tracking in PBR are presented in [151, 113, 57].

An additional technique of homogenizing the light supply is attained by clever light guidance strategies, summarized as the internally-illuminated PBR [178]. They share the idea of guiding (artificial or sun) light through an increased surface into the culture. Experiments demonstrate that the biomass production is increased by 23.42% for flat plate PBR equipped with hollow light guides [43]. Similar results are obtained in PBR with helical structures of photo-translucent material, that enhance additionally the mixing, showing an increase of 25% in growth rate and a higher biomass productivity of 35.26% [90, 204]. Both studies were accompanied by CFD studies to additionally gain insights on the effect of the helix height and screw pitch.

7.2.2. Light model equation

In spatially homogeneous medium, light transport is governed by the following RTE, which models the loss or radiance L due to absorption μ_a and the redistribution of radiance by scattering μ_s

$$\frac{1}{c} \partial_t L + \mathbf{s} \cdot \nabla L = -(\mu_a + \mu_s) L + \mu_s \int_{\Omega} p(\mathbf{s}', \mathbf{s}) L(t, \mathbf{x}, \mathbf{s}') d\Omega'.$$

This equation models the change of light intensity traveling in time t with speed c along a path element \mathbf{s} , through algae suspension characterized by absorption and scattering coefficients and scattering integral with phase function p [129, 28]. Inside a small control volume at position \mathbf{x} the local light intensity Φ is obtained by formula

$$\Phi(t, \mathbf{x}) = \int L(t, \mathbf{x}, \mathbf{s}) d\Omega.$$

Note, that the RTE is formulated with respect to a certain wavelength λ , which is dropped for the sake of simplicity as mentioned earlier in Section 2.3. Bubbles in the suspension are not considered, since they do not influence the light supply as shown in the experimental and numerical works [117, 13].

Spectral light regimes are typically approximated by the Box model, where RTE is solved for several wavelengths and the computed intensities are averaged [84, 116]. This extension might be of interest when improving the light utilization efficiency, since not all absorbed light in the visible spectrum contributes equally to the conversion to valuable bioproducts. Inhomogeneous suspensions are modeled by spacial varying optical parameters μ_a and μ_s . In addition, light sources of arbitrary shape and number can be added by introducing corresponding source terms. The extension to incorporate thermal phenomenon was recently investigated in the framework of RTLBM and is technically achieved by adding a source term [114, 14, 52]. This model extension can contribute to design the cooling of reactors, that is necessary for most internally-illuminated setups.

In previous work, Mink et al. [125, 121] established the RTLBM as a numerical tool to solve the general RTE by the following collide-and-stream equation

$$f_i(t + \Delta t, \mathbf{x} + \mathbf{s}_i \Delta x) = f_i(t, \mathbf{x}) - \frac{1}{\tau} (f_i(t, \mathbf{x}) - f_i^{eq}(t, \mathbf{x})) - \frac{\mu_{\text{eff}}^2}{8} (\Delta x)^2 f_i(t, \mathbf{x}),$$

with 0th order discrete Maxwell–Boltzmann equilibrium $f_i^{eq} = w_i \sum_j f_j$ equipped with relaxation time $\tau = 1$ and $D3Q7$ stencils. The computed populations f_i represent in its

λ in nm	$\hat{\mu}_t$ in $\text{m}^2 \text{kg}^{-1}$	a
470	1200	0.66
600	1840	0.92
680	1680	0.77

Figure 7.2.: Extinction cross-section and scattering albedo for three wavelengths [93].

steady-state the light intensities in PBR by local averaging

$$\Phi(\mathbf{x}) = \sum_i f_i(\mathbf{x}) .$$

As this LBM scheme is executed on the same numerical grid as the fluid flow simulation, they share the data design and data interfaces, which facilitates the coupling. For details about this RTLBM and the definition of the effective attenuation μ_{eff} ¹ it is referred to Section 4.2.1 where the method was introduced.

7.2.3. Optical characteristic of microalgae suspension

As pointed out in Section 6.5.3, the choice of an appropriate RTLBM has to be taken carefully, depending on the optical properties of the media, numerical tolerance and computational conditions. For a modeling organism *C. reinhardtii*, an extract of spectral measurements are shown previously in Table 2.1 and are recalled in Table 7.2. Needless to say, that the extinction coefficient μ_t is retrieved by multiplying the extinction cross-section $\hat{\mu}_t$ by the culture density c_x . This relation explains the increase of culture density in a PBR by an increased light extinction and hence steeper light gradients. Dimensionless characteristic parameters are the scattering albedo a and the optical depth b. The optical depth is linked to the reactor geometry by $b = \mu_t L_0$, for a characteristic length L_0 of the PBR.

Figure 7.3 links the optical properties of the algae to the application guidelines and validity range of general RTLBM shown in Section 6.5. The axis span the optical parameter field, defined by scattering albedo and optical depth, and form a map for which the performance of RTLBM is validated. Orange and red light is recommended to simulate with the macroscopic RTLBM whereas the blue light might be simulated with the mesoscopic or P1-RTLBM, according to the discussion in Section 6.5.3.

¹The effective attenuation parameter was previously defined in (2.11) as $\mu_{\text{eff}} = \sqrt{3\mu_a(\mu_a + \mu_s)}$.

7. Comprehensive Kinetic Model of PBR

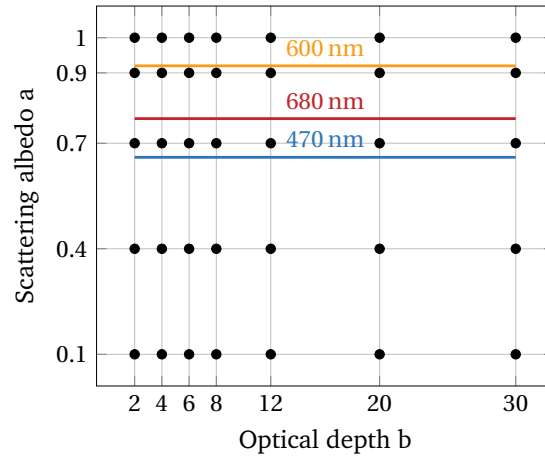


Figure 7.3.: Colored lines indicate the transport regime of the three wavelength. The optical depths increase according to the culture density.

7.2.4. Boundary treatment

The Fresnel's and Snell's law model the reflection and transmission of radiance on surfaces, yielding the following boundary condition. Radiance that hits the boundary surface from angle θ is reflected back and attenuates according to Fresnel's equation

$$R_F(\theta) = \begin{cases} \frac{1}{2} \left(\frac{n_{\text{rel}} \cos \theta_r - \cos \theta}{n_{\text{rel}} \cos \theta_r + \cos \theta} \right)^2 + \frac{1}{2} \left(\frac{n_{\text{rel}} \cos \theta - \cos \theta_r}{n_{\text{rel}} \cos \theta + \cos \theta_r} \right)^2, & \text{for } 0 \leq \theta \leq \theta_c, \\ 1, & \text{for } \theta > \theta_c. \end{cases}$$

Only if the incident angle is greater than the critical angle θ_c , the radiance is totally reflected and there is no transmission. Otherwise, the incident radiation gets multiplied by Fresnel's equation R_F that results in an attenuation factor due to reflection and transmission. Parameter n_{rel} accounts for the reflection properties of the surface. In the framework of LBM, this boundary condition translates into a partial bounce-back scheme, as shown in previous work [123].

Simulating a light source embedded in a boundary, can be realized by two Dirichlet boundaries. One for the light source and another density on the outlet. Generally, the light density at the outlet is not known but much lower than the source, thus it is often set to zero. This lacks on physical meaning but in addition, the simulation is very unstable due to the jump of density. This deficit can be fixed by the Fresnel boundary presented in Section 4.3.

7.3. Algal Growth Models

The assessment of productivity of microalgal cultivation is heavily based on the biomass accumulation. Therefore, the main focus here is on theoretical modeling of photo-conversion due to light supply, assuming nutrient saturation. Microalgae attain the maximum growth rate at specific light intensities, referred to as photo-saturated light level. Below and above this level, the growth is limited either by photo-limitation or photo-inhibition. Due to the strong light gradient in PBR all three light regimes has to be taken into account by any growth kinetic model. Even if the general PBR design aims for prevailing photo-saturation and photo-limitation or in other words, aims for a homogeneous light supply.

The recent review articles of Béchet et al. [11], Lee et al. [108], and Darvehei et al. [37] present theoretic models for algae growth, that focus on the supply of light, nutrient and temperature or even its combination. Apparently, there is a great variety of models that have been proposed in algal research and when choosing one, the trade-off between model complexity and usability must be taken into account. One aspect are undoubtedly the numerous empiric parameters, that are expected to be a function of the specific algae, temperature and many more cultivation parameters. This might be a time consuming process of fitting or calibrating the model to experimental data.

General growth kinetic models, that consider light supply, are approximating the growth by a descriptive approach. Rather than explaining the kinetics, these models are developed for the prediction, which can be observed by the many empiric parameters. One representative, that describe the relationship between light supply and rate of photosynthesis is the PI relationship (photosynthetic rate and light intensity). It is based on a characterization of light supply into three distinct regimes (a) The rate of photosynthesis in *photo-limited regimes* is governed by the photon capture rate and is of linear nature, (b) At *photo-saturated regimes* the photosynthetic rate reaches its maxima and is hardly dependent on the light intensity, represented by the plateau, (c) When the light intensity is increased further the cells are subjected to *photo-inhibited regimes* and the photosynthetic rate decreases. To increase the PCE, it is clear that the reactors design stresses on *photo-limited regimes*, where the light conversion efficiency is the highest.

This classification into three light regimes considers photosynthetic rate as a function of light assuming saturation of nutrients, e. g. temperature, nutrient supply and others. In such situations, the light supply is a critical factor of photosynthetic activity. This descriptive modeling is widely represented in algal research, see the review articles [11,

7. Comprehensive Kinetic Model of PBR

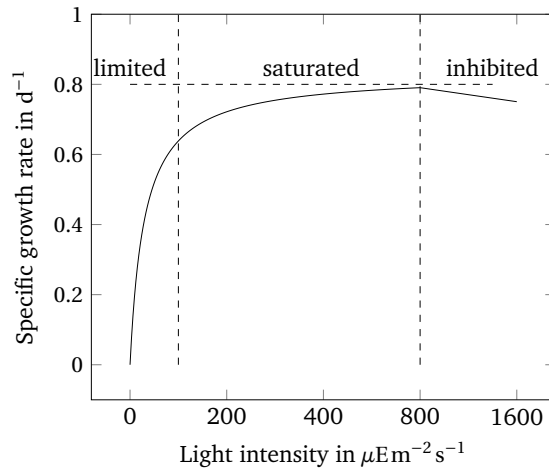


Figure 7.4.: Growth kinetics and the three light regimes of *Porphyridium purpureum* [156].

108, 37] and a possible model formula is the *Monod equation*

$$P(L) = P_{\max} \frac{L}{L_K + L}, \quad (7.2)$$

for local light intensity L , specific maximum photosynthetic rate P_{\max} and constant L_K . Note, that this single substrate model has already two parameters that has to be determined through calibration, which has been performed in the pioneer work of Tamiya et al. [173]. An illustration of the PI relationship is shown in Figure 7.4. Further, the specific rate of photosynthesis is proportional to the specific growth rate μ . This basic (yet general) population model can be applied to other relevant scenarios in microalgal cultivation, e. g. to describe growth under low and moderate nutrient concentrations, considering the limitation by a single nutrient [6, 80, 146], not to forget the pioneer work Monod [132].

As pointed out by Lee et al. [108], the Monod model cannot explain growth under nutrient absence or inhibition caused by high nutrient concentration. It also fails to implement internal nutrient storage behavior. Over the years, model improvements that addressed the better fitting to experimental results have been presented [2, 67, 40, 150]. Modifications that consider the photosynthetically usable radiation (PUR) instead of the photosynthetically active radiation (PAR) have just recently been proposed [18]. A even more precise modeling makes usage of the mechanical abstraction of the cell and its photosynthetic unit (PSU) and is designed to account for photo-adaption, photo-inhibition and the LD-cycles [158, 60]. This 3-state model, proposed originally by Eilers and Peeters [42], assumes that PSU consists of a resting x_1 , an active x_2 and an inhibited fraction x_3 ,

with the closure of $x_1 + x_2 + x_3 = 1$. Accordingly to Wu and Merchuk [197], the evolution of the PSU is given by

$$\begin{aligned}\frac{dx_1}{dt} &= -\alpha J x_1 + \gamma x_2 + \delta x_3 \\ \frac{dx_2}{dt} &= \alpha J x_1 - \gamma x_2 - \beta J x_2 \\ \frac{dx_3}{dt} &= \beta J x_2 - \delta x_3,\end{aligned}$$

predicting finally the specific growth rate by

$$\mu = k\gamma x_2 - M.$$

The parameters α, β, γ and k depend on temperature and the specific species, whereas the algae maintenance coefficient is denoted by M [120]. The irradiance is accounted for by light flux J . A comparative study of six PSU models from literature is presented in [159], including a sensitivity analysis of the parameters.

Following the growth model classification into three types, see Béchet et al. [11], it is deduced that the strategy of PSU is related to the Type III models. Compared to Type I or II models, this model implements cell maintenance and respiration and accounts for LD-cycles. For complex flow regimes, the algae experiences a very heterogeneous illumination yielding an alternating light exposure history. Only, Type II models account for the local light-history and hence are recommended for PBR with complex fluid flows.

Model Type I assumes that the culture is a continuum that gets illuminated. Hence, there are no individual cells or fluid vortices that trap cells, which is a common assumption for ideally mixed PBR. The rate of photosynthesis is modeled by the Monod equation or its variants with light intensity L to be the averaged or modeled by Lambert–Beer. Both kinetic parameters, constant L_K and maximum rate of photosynthesis P_{\max} have to be fitted empirically as a function of the culture density, temperature and nutrient supply.

7.4. Application to Flat Plate PBR

In flat plat reactors the algae are cultivated in rectangular enclosures, that are either illuminated from one or both sides. They are one of the most robust reactors designs, not only for the flexibility in implementing any desired illumination by varying the reactor depth. The mixing is implemented by the sparging with CO₂-enriched air at the bottom, that has been reported to be the most gentle way to keep shear stress the algae cells at a

7. Comprehensive Kinetic Model of PBR

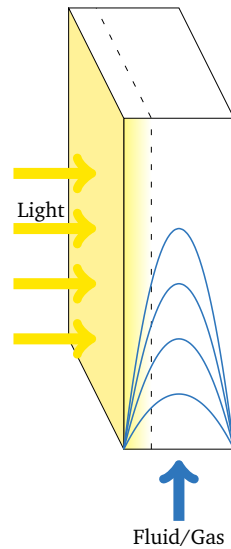


Figure 7.5.: Model of the flat plate PBR with fluid inflow at the bottom that additionally transports the gas phase. The reactor is illuminated over the entire left wall. Dashed reactor volume is subjected to light-saturation and consumes the gas due to photosynthetic activity.

low level [147].

7.4.1. Modeling of the reactor dynamics

The PBR geometry is given by two panels ($0.3 \times 0.1\text{m}$) at distance 0.05 m as illustrated in Figure 7.5. The irradiance is modeled as an infinite beam that enters orthogonally on the left reactor wall. Note, that such illumination setup has been validated in Chapter 6, called benchmark scenario *infinite collimated beam*. The intensity of the light source is normalized and the biomass concentration of approximately 1 gL^{-1} at $\lambda = 600\text{ nm}$ of *C. reinhardtii* [93] is modeled by scattering albedo $a = 0.9$ and optical depth $b = 12$.

Concerning the hydrodynamics, the flow enters at the bottom with velocity 0.001 m s^{-1} in a Poiseuille profile. The pressure boundary at the top ensures the outflow, whereas the walls are modeled as no-slip walls by the LBM bounce-back scheme. In addition, the reactor bottom is subjected to a fixed gas concentration that is transported upwards by the fluid flow, according to the Euler–Lagrange model presented in Section 7.1. The ratio of both transport phenomena, gas diffusivity and advection by fluid, is denoted by the Peclet number indicating which transport regime dominates. With regard to numeric, the Peclet number is a critical parameter since the numerical model becomes less stable for decreasing diffusion. The present thesis deployed for the flat plate PBR gas transport

a Peclet number of 400. A closer match to typical parameters from application was not considered for various reasons. First, the laminar flow regime allows studying the interplay of diffusion of the gas and its advection by the flow field without adding further complexity (e. g. turbulence models) or numerical artifacts. This simplifies the methodical development of a coupled simulation in general and speed-up the implementation process. Second, the performance can be retrieved by simple algae growth kinetics, that consider a continuum algae culture, instead of light exposure history of single cells, and averaged light intensities, known as Type I models in [11].

The reactor thickness of 0.05 m is discretized by 30 discrete nodes, yielding an overall number of about 300000 fluid cells for the LBM simulation. The program simulates first the light intensities by the macroscopic RTLBM and then the Euler–Euler gas transport. Both information are subsequently coupled by the computed photosynthetic rate, depending on the local light supply, that enters the sink term gas transport model equation. Most of the total simulation time (parallel execution on Intel i7-6700) of about 20 min is spent in solving the gas transport in the flow field. The solver for the light transport takes less than 3 min.

This model focus on understanding the interplay of the modeling parameters and lacks on precise description of the typical experimental design. First, the air gets injected as bubbles at to bottom and as they rise, the induce the fluid flow. Second, the described gradient in gas concentration cannot be observed in experiments. The gas consumption and gas transport happens on different time scales.

7.4.2. Simulation results

Figure 7.6 shows the light and gas supply in the flat plate PBR. The light simulation, based on the macroscopic RTLBM, indicates that only a small reactor volume close to the light source is subjected to photo-saturation, see Figure 7.6a. After the distance of about 0.01–0.02 m the light attenuates already about two orders of magnitude, which is in good agreement to experimental data [147]. This is explained by the relatively high algal concentration of 1 gL^{-1} yielding steep light gradients, such that most of the algae suspension is cultivated in photo-limitation. The latter is not desired and the simulation concludes to construct thinner reactors and simultaneously illuminated from both walls. Both strategies favor an increase in homogeneous light supply and enhance PBR performance.

A normalized gas concentration enters the reactor at the bottom and is transported upwards by the implemented fluid flow. While being transported, the gas concentration

7. Comprehensive Kinetic Model of PBR

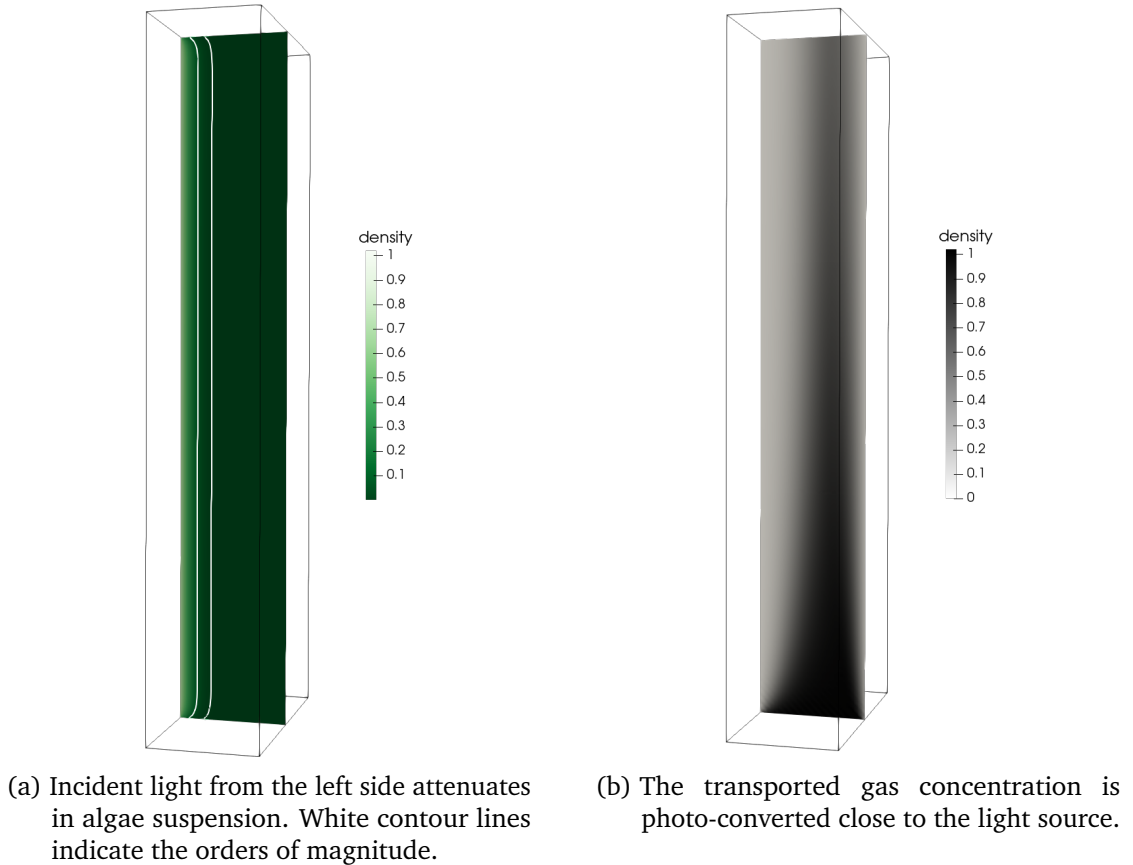


Figure 7.6.: Cross section of light and gas supply simulation in a 3D flat plate PBR of width 0.05 m and biomass concentration of 1 gL^{-1} .

is converted by photo-conversion, accordingly to the local light intensities, which results in a loss of gas close to the left wall, see Figure 7.6b. Without the coupling of gas to the light field, the gas phase would follow the fluid flow and develop a Poiseuille profile. The consistent simulation scope applies in particular to this gas-light coupling by a simple sink term in the advection–diffusion equation (7.1). At every grid node the information of light intensity and CO_2 concentration are available and are coupled as follows: First, the (local) photosynthetic rate is computed, accordingly to Monod (7.2). The modularity allows to easily switch for most other growth models. Second, the gas concentration is reduced linearly with respect to the determined photosynthetic rate, determined for instance by a Monod model. This work identifies the coupling parameters in the simulation model and its interplay to the models. However, its calibration to experimental data might determine the precise proportional constant for the sink expression.

A closer look to the time evolution of the gas transport is shown in Figure 7.7. At

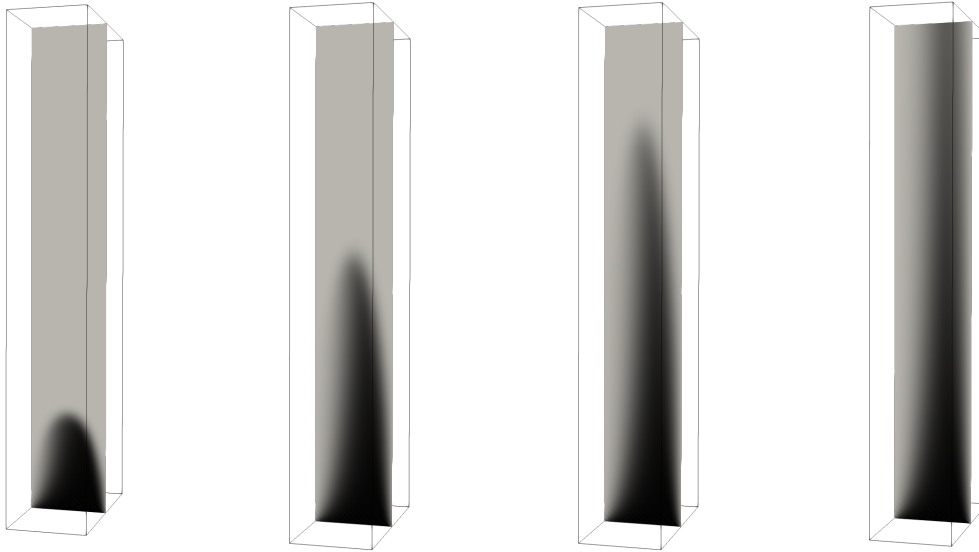


Figure 7.7.: Time evolution of the gas phase in the fluid flow, till steady-state is reached. Black color indicates high CO_2 concentration. The coupling to light supply yields in a consumption of CO_2 close to the left reactor wall.

the beginning (left side) of the parabolic Poiseuille fluid flow profile transports the gas concentration upwards, by means of advection. Needless to say, that the shown cross section indicates also a parabolic profile of the gas concentration in the bottom. While the fluid field transports the gas towards the top, this changes due to two aspects. The longer the gas remains in the flow, the more it gets diluted by diffusion processes. This concludes the first observation of a blurred gas-liquid interface towards the top of the flat plate PBR. On the other side, the coupling to light intensities simulates the consumption of CO_2 in the photo-saturated volume, mainly observed close to the left reactor wall. This consumption results in a biased Poiseuille profile of the gas transport and depicts the second phenomena.

An appropriate model for algae growth kinetics in such laminar fluid flows and simple illumination scenarios, is the Type I model in [11]. By volumetric considerations, based on the amount of culture volume that experience photo-saturation, the growth kinetics are formulated. This assessment assumes that the fluid flow is a continuum and that there is not mixing along the light gradient. As a summary, the performance evaluation of flat plate PBR with laminar flow field does not require the tracking of algae particles and is based solely on the light supply inside the culture. Calibrated models for the CO_2 consumption can identify a maximum plate height, till the suspension suffers CO_2 limitation. This height might be optimized for various reactor depths and fluid flow

regimes to meet the design demands.

7.5. Application to Algine – An internally-illuminated PBR

Internally-illuminated PBR benefit from additional light sources inside the algae culture, contributing to a potentially homogeneous light supply by the increase irradiance surfaces. On the assumption of cultivating a microalgal concentration of 2 gL^{-1} and more, the light supply of the present reactor is designed. For such suspensions it is known, that after a short light path of 0.01–0.02 m the light intensity is no longer sufficient and the volume is subjected to photo-limitation. As a consequence, the goal of the immense constructional effort for this reactor is to attain a homogeneous light supply inside a compact cylindrical reactor by means of a minimal distance from any algae cell to its next light source of less than 0.02 m.

7.5.1. Reactor dimensions

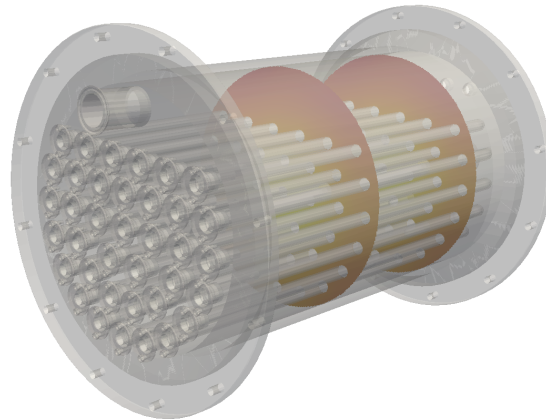
The geometry of the reactor is based on a horizontally mounted tubular reactor of diameter 0.3 m and length 0.5 m equipped with 37 internal cylindrical installations of diameter 0.016 m, see Figure 7.8a. The radial distance between the cylindrical internal installations vary from 0.03–0.05 m. Each of them is equipped with 72 LED spots that are mounted helical, resulting in a horizontal distance between the LED spots of about 0.05 m as depicted in Figure 7.8b. This construction attains a minimal distance from any algae cell to the closest light source of about 0.02 m, as concluded from previous considerations.

When discretizing the reactor into a regular grid, it is clear that the small inner cylinders determine the choice of the grid size. Without grid refinement, the regular grid in LBM can be a constraint for such scenarios. A possibly high number of grid nodes is avoided by exploiting the axial symmetry of the Algine reactor by considering shorter cylinders. For instance of length 0.1 m instead the original 0.5 m. Then, the reactor discretization with 30 nodes resolving the diameter of inner cylinders, results already in a total node number of 10×10^6 . This makes the visualization by the software *ParaView* on desktop machines (Intel i7-6700, 32 GB RAM) just feasible, more nodes might exceed the memory.

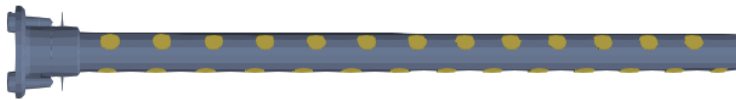
Another relevant LBM issue for its application to real engineering problems is the decomposition of the computational domain into small sub-blocks, for the execution on massive parallel computer hardware¹. Those sub-blocks than can be computed almost

¹The outstanding parallel performance of LBM is often based on clever domain composition.

7.5. Application to Algine – An internally-illuminated PBR



- (a) Reactor diameter of 0.3 m and length 0.5 m equipped with 37 cylindrical light installations of diameter 0.016 m.



- (b) Internal light cylinder equipped with 72 LED spots mounted in a helical arrangement. Horizontal distance between LED spots is 0.05 m.

Figure 7.8.: The Algine PBR with complex internal illumination based on 37×72 single LED spots. The LED arrangement ensure a homogeneous light supply in the suspension.

7. Comprehensive Kinetic Model of PBR

independently and are a key element in the parallelization strategy. For cuboid based geometries the block decomposition is a simple and yet powerful tool. However, the internal-illumination structure of the Algine PBR is less appropriate. Consider a Algine simulation ¹ that is executed on 2000 cores and hence requires at least the same amount of sub-blocks. Then, the decomposition results in a sub-block size of about the size of the diameter of an inner cylinder. This is critical for the parallel performance, since the blocks might contain an extremely varying amount of nodes that actually has to be computed (e. g. algae suspension) and not (e. g. hollow inner cylinders). This is an unbalanced decomposition into sub-block of uneven computational time.

In the experiments, the CO₂ supply is attained by a sparger at the bottom of the reactor. The fluid flow inside the present Algine PBR will not be simulated, mostly due to the lack of a boundary condition of a flow field that is imposed by raising bubbles. Since the reactor is not entirely filled with suspension, the gas escapes from the fluid phase on the upper surface in the cylinder.

7.5.2. Simulation results

The illumination of the reactor is attained by many internal light sources of finite extent. This LED spots emit light almost diffusely and hence the macroscopic RTLBM is chosen for the simulation of the light supply. As pointed out in Section 6.5.3, the macroscopic RTLBM is able to predict diffuse light sources of finite extent. Besides the vast number of LED spots, the present reactor has foremost curved walls, which in total makes light prediction a challenging task. With respect to the reactor walls, the simulation models the light source as a Dirichlet (constant) source, where other boundaries are partly reflecting, accounting for the water-glass interface, as discussed in Section 4.3. Figure 7.9 shows the light simulation setup with resolved LED spots besides the predicted illumination of the culture suspension. As indicated above, the simulation considers a representative part of the reactor with length 0.1 m. It is clearly seen, that the internally-illumination setting benefits from an increased surface to volume ratio in comparison to the flat plate PBR in Section 7.4 and can hardly be modeled by Lambert–Beer’s law.

As emphasized by Nwoba et al. [138], the light management in PBR might include the spectral selection and filtration to deliver a more useful amount of PAR to the culture. In addition, the tailoring to specific wavelengths should also lead to substantially reduction of heat, which is an actual issue for this reactor. In order to understand the light supply better, the following study investigates the light transport for two red wavelengths 600 nm

¹For the Algine reactor of length 0.1 m and a sub-block size of 0.016 m, there are about 2000 sub-blocks.

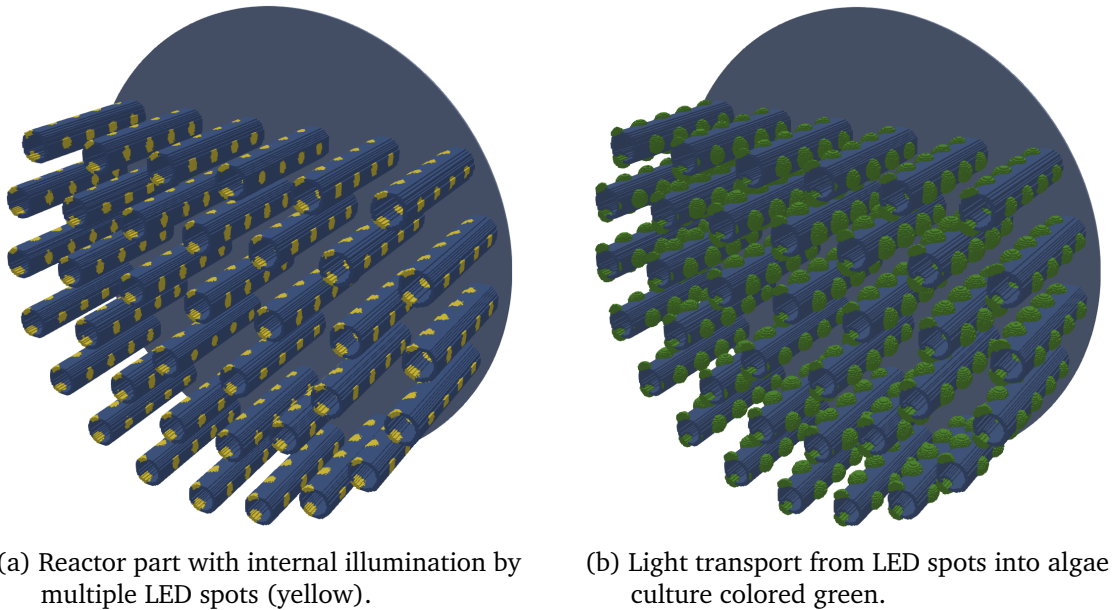


Figure 7.9.: The complex geometry and the multiple LED spots require a carefully modeling of the boundary. Here, the blue part are outlet boundaries that are modeled by the novel reflection boundary. The radiation field is computed according to the macroscopic RTLBM.

and 680 nm, according to the optical parameters presented in [94]. Both transport regimes are characterized by very similar extinction coefficient¹ of 736 m^{-1} and 672 m^{-1} ². However, the scattering albedo varies from 0.9 at 600 nm to 0.77 at 680 nm, which allows to study the penetration depth into the algae suspension of light with varying wavelength, as depicted in Figures 7.10 and 7.11. Both cross sections show the 37 internal cylinders on which multiple LED spots are helically mounted, seen by its non-symmetric light intensities. The simulation shows, that an increased scattering albedo (600 nm)³ results in an enhanced penetration depth of the light, compared to data obtained for 680 nm. The modeling error, considering only extinction parameters, is significant as it predicts very similar light supplies for the distinct wavelengths. However, the independent modeling of absorption and scattering by the RTLBM clearly accounts for the high absorption at 680 nm, as it leads to a significantly higher light attenuation and hence a very steep light gradient, compared to the results at 600 nm. This concludes, that a spectral filtration and selection of the light sources is crucial in dense algal cultivation process to establish a

¹The extinction coefficient is defined as the sum of absorption and scattering by $\mu_t = \mu_s + \mu_a$

²Interestingly to note, the Lambert–Beer model predicts the light supply only be means of extinction, hence the light intensities are expected to be very similar.

³The amount of scattering on the extinction is called scattering albedo and is defined by $a = \mu_s (\mu_a + \mu_s)^{-1}$.

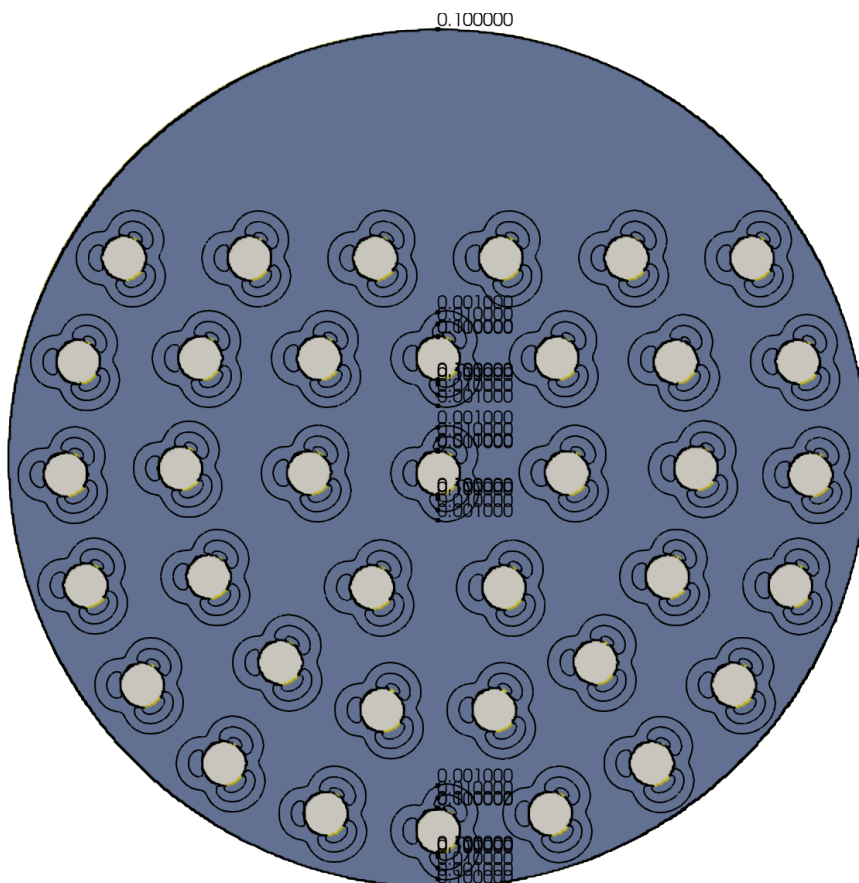


Figure 7.11.: Light supply by 680 nm in an algae suspension of 0.4 gL^{-1} - scattering albedo $a = 0.77$ ($\mu_a = 152 \text{ m}^{-1}$ and $\mu_s = 520 \text{ m}^{-1}$). Contour lines are drawn at intensities 0.1, 0.01 and 0.001.

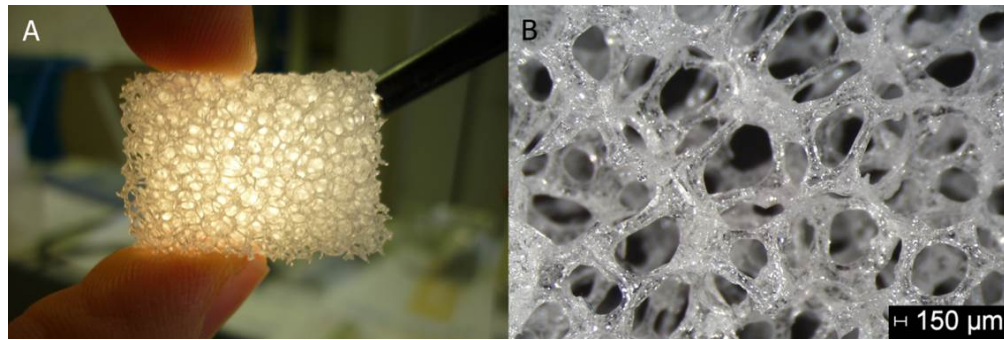


Figure 7.12.: Idealized foam of equal-sized bubbles.

tubes are known [178]. Its large illumination surface attains a reasonable homogeneous light supply in the culture. However, the mass transfer concerning supply of CO₂ and removal of dissolved oxygen is known to be a major challenge in efficient microalgae cultivation in large tubular reactors.

The present tubular reactor increases the illumination surface through an internal installation of a photo-translucent sponge structure. Figure 7.12 depicts the sponge structure based on an idealized foam of equal-sized bubbles [190], named *Weaire–Phelan structure*. It is expected that the photo-translucent material acts similar to light guides and increases the irradiance surface. In addition, the passive sponge structure induces complex hydrodynamics that might improve the mixing and even implement LD-cycles. The experimental work of Jacobi et al. [90] reviewed the PCE for such reactors and suggested the improvement in efficiency of biomass build-up to be more apparent in high cell densities.

7.6.1. Modeling of reactor dynamics

The simulation of the reactor covers the light supply and the tracking of algae cells in the flow field in the framework of LBM. Special attention is paid to the discretization of the fine sponge structure and the coupling of the submodels.

The simulated tube is of diameter 0.05 m, where the sponge structure is placed at 0.5 m from the inlet. Since the hydrodynamics develop after the inlet boundary and requires to settled, the tube is extended to a total length of 1 m to allow the development of the flow pattern. First, the light simulation is carried out, where the photo-translucent sponge together with the tubing acts as a radiative source of constant light intensity. Afterwards, the fluid field is simulated for a Poiseuille inflow profile and no-slip walls with vanishing fluid velocity on the sponge surface and tube walls. Since the entire geometry is provided

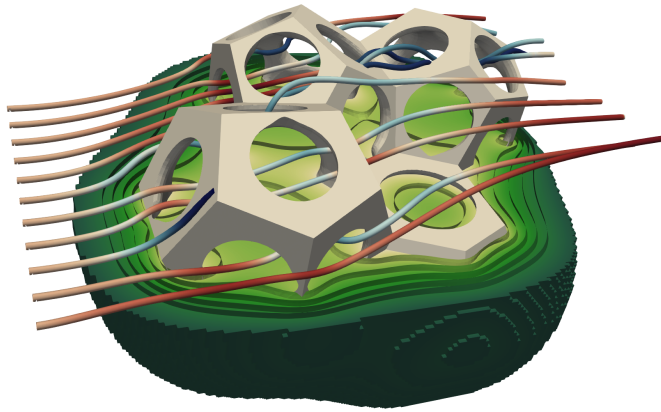


Figure 7.13.: Simulation of light supply (green) and algae trajectory inside the sponge-structured PBR.

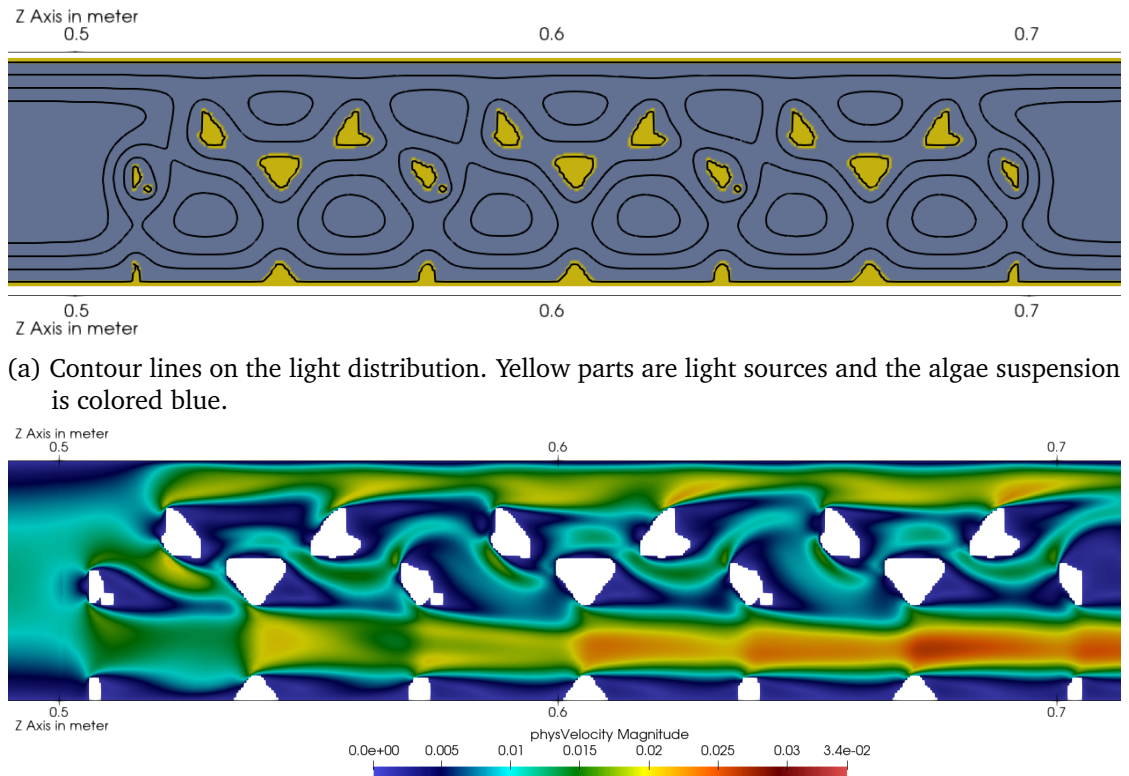
by a Stereolithography (STL) file, the interpolated bounce-back model of Bouzidi et al. [21] is deployed for the no-slip walls. It is observed to be more stable for the staircase approximation of the sponge structure, by the regular grid. After the full flow pattern is developed for an inflow velocity of 0.01 ms^{-1} , the algae cells are added and tracked accordingly to the Euler–Lagrange approach, as shown in Section 7.1.2. An illustration of the simulation data is given in Figure 7.13.

The discretization into a regular grid, comes with a trade-off of maximum possible grid nodes or lattice cells and the quality of the staircase approximation of the fine sponge structure. Due to memory and computation time constraints, the pore sizes of $0.002\text{--}0.004 \text{ m}$ from the original experiments [90] can not be resolved by the regular grid. Instead, the present work considers a pore size of 0.02 m , that is resolved by 20 grid nodes, of size 0.0005 m , yielding an overall number of approximately 15×10^6 grid cells. Compared to the original pore size, the present pore size is increased about factor 10.

7.6.2. Simulation results

Light simulation results are depicted on the contour plot in Figure 7.14a. It is seen that the sponge structure extends over $0.5\text{--}0.7 \text{ m}$ in the axial direction and clearly enlarges the inner surface of the reactor. This cross section representation allows studying two characteristic light supply regimes. The first regimes is a classic tube reactor, illuminated only by its transparent walls, see both ends of the tube. Herein, the algae culture is subjected to steep radial gradients, shadowing most of the suspension, which is undesired and leads to a dominant photo-limited reactor volume. The strategy of increasing the light intensity on the walls might reduce the photo-limited volume. However, this approach

7. Comprehensive Kinetic Model of PBR



(a) Contour lines on the light distribution. Yellow parts are light sources and the algae suspension is colored blue.

(b) Local velocities for an inflow of 0.01 ms^{-1} entering from the left side. White regions are the sponge structure modeled as no-slip walls.

Figure 7.14.: Cross section of the sponge structure installations inside the tubular PBR.

exposes simultaneously suspension close to the reactor walls to a photo-inhibitory light intensity, that might even damage the algae cells. Thus, the strategy of increasing the light intensities translates the deficit to other reactor regions and barely solve the issue of heterogeneous light supply.

Much better homogenization of the light supply is achieved in the second light regimes, observed in the sponge structure. Here, the large irradiance surfaces dilutes the light into the deeper part of the reactor, by the photo-translucent sponge structure. As a summary it can be said, that the implementation of a sponge structure inside the tubular reactor is a promising strategy to homogenizes the light distribution by increasing the surface of irradiance. It further allows to lower the intensity of the light source, while implementing a homogeneous light distribution inside the reactor.

At the same time, the sponge structure attains a complex flow pattern that enhances the radial mixing. While the fluid passes the sponge, the local constrictions leads to high velocities and a complex flow pattern develops already for very slow inlet velocity

7.6. Application to Sponge-Structured PBR

of 0.01 ms^{-1} , see Figure 7.14b. Typically, for the implemented flow obstacle, the fluid flow develops a preferred path, that is indicated in the present figure by the increased velocities in red.

After the flow field is fully developed, the particles are seeded randomly at the inlet and are tracked through the reactor. Figure 7.15 depicts the radial position of such tracked algae cells, computed by the Euler–Lagrange model. The color gradient indicates the time evolution in the flow field from the beginning (dark) to the end (light). Along its trajectory the algae is subjected to significant radial movements that indicates non-laminar flow pattern and proves the mixing characteristic of this particular reactor design. The information of the spacial positions is further analyzed by coupling to the light intensity and recording the local light exposure history, as depicted in Figure 7.16 for the same particles. When considering the computational effort of this light-particle coupling, the consistent simulation scope of the algae tracking and light supply pays off. Analyzing the algae light history along the z-direction (axial), it is clearly seen that the sponge structure increases the general light supply through homogenization as pointed out earlier. Before and after the sponge the subjected light decreases and remains at a constant level. The latter shows also the laminar character of the flow field and how algae cells are not mixed and remain therefore at a certain light regime. A survey that considers the light history over time, might indicate the presence of LD-cycles and its precise frequency. However, the present data only indicates the tendency to LD-cycles given the alternating light exposure history in Figure 7.16.

The modeling of trajectory and its coupling to the light model, allows studying the light history of individual algae cells. From the simulation data it can be concluded that tubular reactors of diameter 0.05 m have poor radial mixing properties for fluid velocities 0.01 ms^{-1} and lower. Further improvements have been confirmed by placing a photo-translucent sponge structure inside the flow field. The simulation shows a homogenization of the light supply while enhancing at the same time the radial mixing.

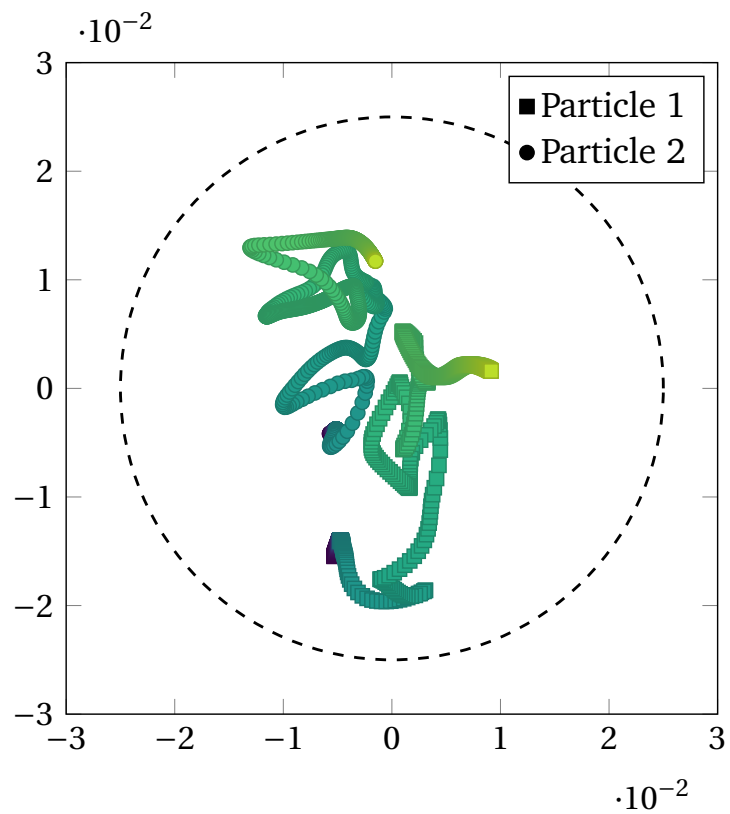


Figure 7.15.: Cross section of tubular reactor shows the time evolution of two algae in the axial position. The trajectory begin is indicated by the dark blue and the end by light green colors.

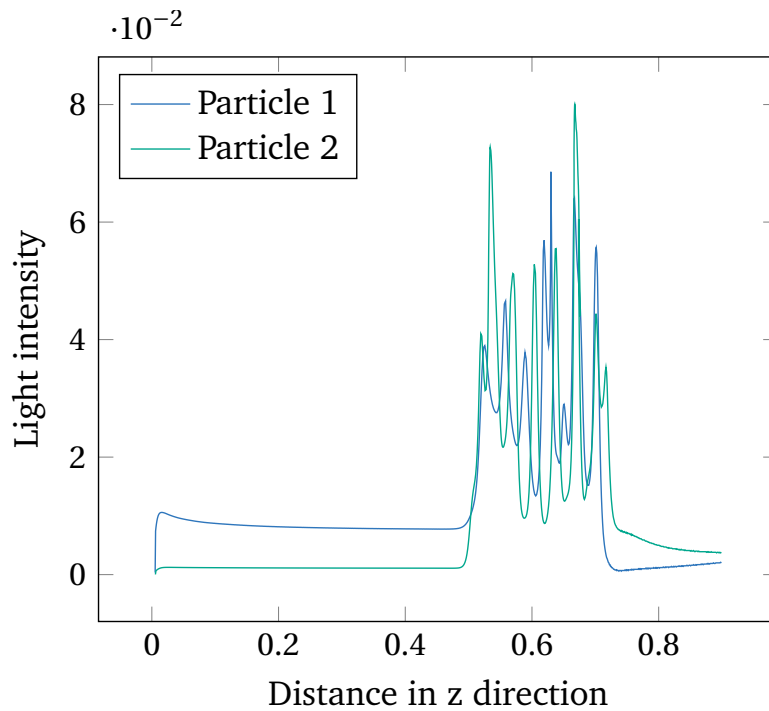


Figure 7.16.: Experienced light intensity plotted over traveled axial distance. The increase of subjected light intensity at axial position 0.5 m is due to the sponge structure. Before and after the sponge structure, the subjected light is constant.

8. Conclusion and Outlook

8.1. Conclusion

The objective of this work was the development of a consistent simulation framework for the prediction of light supply, hydrodynamic mixing and biomass growth kinetics in Photobioreactors (PBR). By studying the interplay of the tree simulation submodels, reactor designs can be improved by quantitative predictions of PBR performance and the process scale-up can be supported as well. It was chosen a mesoscopic modeling scope and the algorithm has been implemented in the framework of Lattice Boltzmann Methods (LBM), best known for their parallel performance and multi-physics models. For this background, it was derived, tested and validated a novel mesoscopic submodel, based on LBM, to simulate the light supply inside reactors, accordingly the model of the radiative transport equation (RTE). Additional LBM for the fluid flow, mass transport and microalgae tracking has been implemented, to gain insights in complex flow patterns and to better understand the mixing. Due to the consistent scope of model equation and numerical algorithm of light and hydrodynamic, the coupling was achieved in a numerical efficient way and did not add significant complexity, through a biomass growth kinetic model.

The mesoscopic simulation framework was successfully applied to three PBR to quantitatively analyze and propose design improvements of the reactors. Thereby, the initially formulated questions could have been answered in detail:

1. Can we predict the spacial light distribution inside general PBR geometries?

The developed Radiative Transport Lattice Boltzmann Methods (RTLBM) have been validated beyond the optical parameter set of typical algae suspension in closed PBR. It has been shown that the light supply in PBR can be predicted robustly and accurately in complex 3D geometries and for the entire photosynthetically active radiation (PAR).

2. What is the impact of the coupled process parameters such as light intensity, flow rate and CO₂ concentration in a reactor?

8. Conclusion and Outlook

The consistent modeling scope of the key factors such as local light supply, algae trajectories and gas supply is a major benefit of the developed LBM based simulation framework. It has been performed quantitative studies of a simple algae growth model, that revealed the great ability, of the transparent model formulation, in deriving the impact of the modeling parameters, without the conversion into different scopes. Further qualitative studies regarding experimental data, might determine the coupling coefficients.

3. What recommendations can be derived for PBR operating parameters, with respect to existing reactor and also novel reactor types?

For a non-laminar fluid flow, it is essential to take the algae trajectory into account to derive the performance of PBR. The performed simulation indicate that the mixing quality can be enhanced by passive turbulence promoters, such as a sponge-structured inlet for tubular PBR. An increase of fluid velocity can damage individual algae cells due to shear stress and a high reactor surface combined with few cultivation volume can lead to an undesired raise of temperature in the reactor. Both phenomena can be addressed by further simulation work, since there are already LBM based simulation models for them.

Special attention was paid to complex reactor geometries and light settings, for which sophisticated simulation models are needed due to the absence of known analytical solutions (e. g. Lambert–Beer for flat plate PBR) or correlations of mass transport and hydrodynamics (e. g. tubular PBR). Additionally, the robustness and numerical efficiency of the simulation framework was demonstrated on a complex sponge-structured tubular PBR with internal illumination. Its complex flow patterns and light setup emphasized the need of a consistent and yet highly efficient algorithm to solve and predict real 3D PBR. This survey suggested that the proposed framework is also suitable for the support of process scale-up of PBR, that requires efficient 3D predictions.

General radiative transport (RT) in participating volume is a popular topic and gains importance for the light prediction in the computer aided design of PBR. Its governing equation, the RTE, accounts for the absorption and scattering and is easily extendable to heat transfer as well. The gap in LBM literature, concerning 3D RT models, has been closed successfully by deriving novel RTLBM, to solve an-/isotropic RTE within the framework of LBM. Validation against analytical solution and Monte–Carlo Methods (MC) data showed, that the RTLBM is suitable for the prediction of light supply in PBR. Further, the multiscale expansion of Chapman–Enskog demonstrated the correct asymptotic behavior of the mesoscopic algorithm. For the first time, the RTLBM have

been review with respect of a great optical parameter set, to identify its validity range and provide general guidelines for the application to engineering problems. Additionally, novel boundary models have been developed to incorporate the reflection of radiance on surfaces. This completed the development of RTLBM, as a submodel for the prediction of light supply in general PBR. Since the algorithm was implemented in the open-source LBM library OpenLB, the source files are available to the public in the release 1.3 of OpenLB. As a bonus, the generic derivation of RTLBM allows reusing or extend the developed numerical tool to many engineering problems as the comprehensive validation and the application guidelines revealed.

In a further step, the work addressed the submodels for the simulation of hydrodynamic, including Lagrangian particle trajectories of microalgae cells in the flow field, and mass transport in PBR with LBM. This procedure was catalyzed by existing Euler–Lagrange and Euler–Euler models in LBM literature and corresponding simulation modules, available in the LBM solver OpenLB. Additionally, the present work implemented the consumption of CO₂ by means of the photosynthetic-rate, determined by the local light intensities, based on a single substrate (light) limited Monod model. This coupling scheme completed the design of the novel mesoscopic simulation framework for the prediction of PBR performance and support of process scale-up. Since all submodels were based on LBM, by means of mesoscopic equations and algorithm, the simulation model has been formulated on a consistent scope. With respect to numeric, this persistent concept facilitated intuitive and efficient coupling, based on common data structures, and equally avoided complex data interfaces and time consuming interpolation between different numerical grids.

The developed numerical framework was then applied to three distinct PBR to demonstrate and analyze the interplay of the submodels and finally answer the above questions. While the first reactor was a standard flat plate PBR, the second one already increased the complexity of the light setting by internal-illumination by more than 2000 single LED spots. However, the demands to the framework were further increased by the tubular reactor with sponge structure installations, that dilute the light supply by its photo-translucent material. The simulation of the flat plate PBR showed, that the coupling of the light and mass transport model allows to predict the evolution of gas supply and identify a maximum reactor height, till the algal growth is CO₂ limited. Although the internally-illuminated PBR lacks on a precise fluid flow model, the complex artificial light setting was simulated for different wavelengths. This survey emphasized the impact of polychromatic light and the importance of spectral filtration to attain a homogeneous light supply in high biomass concentration, by the concept of composing a clever spectral composition with varying penetration depth and photosynthetic response inside the algae

8. Conclusion and Outlook

culture. The last study stressed on the algae tracking in complex flow fields and the history of the light exposure of individual microalgae cells. It was found that the sponge structure acts similar to turbulence promoters by enhancing the radial mixing and at the same time achieved a homogenization of light supply. This finding was observed by studying the light exposure history of representative cells, that in addition indicated a high frequency light/dark cycles (LD-cycles) along trajectories.

8.2. Outlook

The outlook contains aspects in the recent development of reactor designs and new simulation strategies, that turned out to be very promising during the course of the present doctoral thesis and might be considered in further works. Ultra-thin PBR with very short light paths are designed to address a high surface to volume ratio and subject most of the algae culture to photo-saturation, which enhances the performance of PBR, as conducted in the experimental work [63]. The almost homogeneous light supply, on the one hand, has a highly sensitive demand on a proper irradiance intensity and requires careful treatment. On the other side, the fluid flow simulation simplifies, since particle tracking might not even be necessary, due to the lack of significant light gradients. However, ultra-thin reactors suffer on small culture volume and absolute biomass growth and are consequently mounted on racks or are enlarged for process scale-up. Such arrangement might subject them to a much more complex irradiance constellation and in particular, the enlargement is critical due to the limitation in mass transfer due to the long holding times. Both phenomena have to be incorporated in future investigations of the ultra-thin PBR, based on computational models.

Another design strategy are turbulence promoters, that overcome the poor radial mixing of traditional tubular reactors. While the mass transfer can be significantly enhanced, the induced shear stress to the algae cells might cause cell damage. Small eddies of the size of an algae cell are transferring energy which will be dissipated by a cell, yielding a potentially damaged cell, as addressed by computational fluid dynamics (CFD) investigation in [58]. Explicit studies based on CFD are still missing and might require the development of specific submodels that account for the shear stress to algae cells.

The increase in reactor surface comes typically with a rapid heating, such that the appropriate culture medium temperatures need to be controlled [133]. In particular, outdoor PBR are subjected to a much wider spectrum than the PAR and the infrared radiation could be filtered, to manage the temperature more easily by heat exchangers

and other technical concepts. Due to existing and very comprehensive radiative heat surveys in the discipline of LBM [52, 97], future simulation frameworks of LBM might be extended to account for these phenomena.

Another important design aspect, is the limited performance of large systems of tubular PBR, due to the dissolved oxygen, that inhibits the photosynthetic conversion rate at high concentrations. Simulation wise, it is straight forward to run LBM simulation simultaneously for multiple concentrations and adopt for dissolved oxygen. The so called multi-phase models have improved significantly over the original versions, but much remains to be done to increase accuracy further [168, 170].

The raise of complexity in multi-physics simulation data requires at the same time adequate biomass growth models that can cope the new insights. Biomass growth models that account for multiple substrate and environment factors, presented in [108], are able to address available CO₂ and dissolved oxygen concentration as well as temperature effects. Future computational models might consider such biomass growth models and equally emphasis on the calibration to experimental data, since the many model parameter have to be adjusted.

Bibliography

- [1] F. Acién Fernández, J. Fernández Sevilla, and E. Molina Grima. “Photobioreactors for the production of microalgae”. In: *Reviews in Environmental Science and Bio/Technology* 12.2 (2013), pp. 131–151. DOI: 10.1007/s11157-012-9307-6.
- [2] S. Aiba. “Growth kinetics of photosynthetic microorganisms”. In: *Microbial reactions*. Springer, 1982, pp. 85–156.
- [3] C. K. Aidun and J. R. Clausen. “Lattice-Boltzmann method for complex flows”. In: *Annual review of fluid mechanics* 42 (2010), pp. 439–472. DOI: 10.1146/annurev-fluid-121108-145519.
- [4] S. Ansumali and I. V. Karlin. “Kinetic boundary conditions in the lattice Boltzmann method”. In: *Physical Review E* 66.2 (2002). DOI: 10.1103/physreve.66.026311.
- [5] P. Asinari, S. C. Mishra, and R. Borchiellini. “A lattice Boltzmann formulation for the analysis of radiative heat transfer problems in a participating medium”. In: *Numerical Heat Transfer, Part B: Fundamentals* 57.2 (2010), pp. 126–146. DOI: 10.1080/10407791003613769.
- [6] S. Aslan and I. K. Kapdan. “Batch kinetics of nitrogen and phosphorus removal from synthetic wastewater by algae”. In: *Ecological engineering* 28.1 (2006), pp. 64–70. DOI: 10.1016/j.ecoleng.2006.04.003.
- [7] L. d. L. X. Augusto, J. Ross-Jones, G. C. Lopes, P. Tronville, J. A. S. Gonçalves, M. Rädle, and M. J. Krause. “Microfiber filter performance prediction using a lattice Boltzmann method”. In: *Commun Comput Phys* 23 (2018), pp. 910–931. DOI: 10.4208/cicp.0A-2016-0180.
- [8] H. Babovsky. *Die Boltzmann-Gleichung: Modellbildung – Numerik – Anwendungen*. Leitfäden der angewandten Mathematik und Mechanik. Vieweg+Teubner Verlag, 2013.
- [9] C. Bardos, F. Golse, and D. Levermore. “Fluid dynamic limits of kinetic equations. I. Formal derivations”. In: *Journal of Statistical Physics* 63.1-2 (1991), pp. 323–344. DOI: 10.1007/BF01026608.
- [10] S. Bavly-Hadida, O. Weinstein, and S. Brandon. “A MODIFIED APPROACH TO THE LATTICE BOLTZMANN MODEL (LBM) BASED ANALYSIS OF RADIATIVE HEAT TRANSPORT”. In: *International Heat Transfer Conference Digital Library*. Begel House Inc. 2018. DOI: 10.1615/IHTC16.rti.023868.

Bibliography

- [11] Q. Béchet, A. Shilton, and B. Guieysse. “Modeling the effects of light and temperature on algae growth: State of the art and critical assessment for productivity prediction during outdoor cultivation”. In: *Biotechnology Advances* 31.8 (2013), pp. 1648–1663. DOI: 10.1016/j.biotechadv.2013.08.014.
- [12] R. Benzi, S. Succi, and M. Vergassola. “The lattice Boltzmann equation: theory and applications”. In: *Physics Reports* 222.3 (1992), pp. 145–197. DOI: 10.1016/0370-1573(92)90090-M.
- [13] H. Berberoglu, J. Yin, and L. Pilon. “Light transfer in bubble sparged photobioreactors for H₂ production and CO₂ mitigation”. In: *International Journal of Hydrogen Energy* 32.13 (2007). ICHS-2005, pp. 2273–2285. DOI: 10.1016/j.ijhydene.2007.02.018.
- [14] S. Bettaibi, E. Sediki, F. Kuznik, and S. Succi. “Lattice Boltzmann simulation of mixed convection heat transfer in a driven cavity with non-uniform heating of the bottom wall”. In: *Communications in Theoretical Physics* 63.1 (2015), p. 91. DOI: 10.1088/0253-6102/63/1/15.
- [15] P. L. Bhatnagar, E. P. Gross, and M. Krook. “A model for collision processes in gases. I. Small amplitude processes in charged and neutral one-component systems”. In: *Phys. Rev.* 94 (3 1954), pp. 511–525. DOI: 10.1103/PhysRev.94.511.
- [16] H. Bindra and D. V. Patil. “Radiative or neutron transport modeling using a lattice Boltzmann equation framework”. In: *Phys. Rev. E* 86 (1 2012), p. 016706. DOI: 10.1103/PhysRevE.86.016706.
- [17] J. Bitog, I.-B. Lee, C.-G. Lee, K.-S. Kim, H.-S. Hwang, S.-W. Hong, I.-H. Seo, K.-S. Kwon, and E. Mostafa. “Application of computational fluid dynamics for modeling and designing photobioreactors for microalgae production: A review”. In: *Computers and Electronics in Agriculture* 76.2 (2011), pp. 131–147. DOI: 10.1016/j.compag.2011.01.015.
- [18] W. Blanken, P. R. Postma, L. de Winter, R. H. Wijffels, and M. Janssen. “Predicting microalgae growth”. In: *Algal Research* 14 (2016), pp. 28–38. DOI: 10.1016/j.algal.2015.12.020.
- [19] P. Bodenheimer, G. Laughlin, M. Rozyczka, T. Plewa, H. Yorke, and H. Yorke. *Numerical Methods in Astrophysics: An Introduction*. Series in Astronomy and Astrophysics. Taylor & Francis, 2006.
- [20] M. A. Borowitzka. “Commercial production of microalgae: ponds, tanks, and fermenters”. In: *Progress in industrial microbiology*. Vol. 35. Elsevier, 1999, pp. 313–321. DOI: 10.1016/S0079-6352(99)80123-4.
- [21] M. Bouzidi, M. Firdaouss, and P. Lallemand. “Momentum transfer of a Boltzmann-lattice fluid with boundaries”. In: *Physics of Fluids* 13.11 (2001), pp. 3452–3459. DOI: 10.1063/1.1399290.
- [22] K. M. Case and P. F. Zweifel. “Linear transport theory”. In: (1967).

- [23] X. Cen, Z. Yan, J. Jiang, and H. Wu. “An efficient forward model based on the Lattice Boltzmann method for optical tomography”. In: *Optik* 200 (2020), p. 163457. DOI: 10.1016/j.ijleo.2019.163457.
- [24] C. Cercignani. *The Boltzmann Equation and Its Applications*. Applied Mathematical Sciences. Springer New York, 1987.
- [25] C. Cercignani and R. Penrose. *Ludwig Boltzmann: The Man Who Trusted Atoms*. Ludwig Boltzmann: the man who trusted atoms v. 10. OUP Oxford, 2006.
- [26] C. Cercignani. “Boltzmann Equation and Rarefied Gas Dynamics”. In: *Recent Advances in the Aerospace Sciences*. Springer, 1985, pp. 75–89.
- [27] Z. Chai and B. Shi. “A novel lattice Boltzmann model for the Poisson equation”. In: *Applied Mathematical Modelling* 32.10 (2008), pp. 2050–2058. DOI: 10.1016/j.apm.2007.06.033.
- [28] S. Chandrasekhar. *Radiative Transfer*. reprinted by Dover Publications, 1960. Oxford, UK: Clarendon Press, 1950.
- [29] S. Chapman, T. G. Cowling, and D. Burnett. *The mathematical theory of non-uniform gases: an account of the kinetic theory of viscosity, thermal conduction and diffusion in gases*. Cambridge university press, 1990.
- [30] S. Chen and G. D. Doolen. “Lattice Boltzmann Method for Fluid Flows”. In: *Ann. Rev. Fluid Mech.* 30 (1998), pp. 329–364. DOI: 10.1146/annurev.fluid.30.1.329.
- [31] P. J. Coelho. “Advances in the discrete ordinates and finite volume methods for the solution of radiative heat transfer problems in participating media”. In: *Journal of Quantitative Spectroscopy and Radiative Transfer* 145 (2014), pp. 121–146. DOI: 10.1016/j.jqsrt.2014.04.021.
- [32] A. Contreras, F. García, E. Molina, and J. Merchuk. “Interaction between CO₂-mass transfer, light availability, and hydrodynamic stress in the growth of *Phaeodactylum tricornutum* in a concentric tube airlift photobioreactor”. In: *Biotechnology and Bioengineering* 60.3 (1998), pp. 317–325.
- [33] C. Coreixas, B. Chopard, and J. Latt. “Comprehensive comparison of collision models in the lattice Boltzmann framework: Theoretical investigations”. In: *Physical Review E* 100.3 (2019), p. 033305. DOI: 10.1103/PhysRevE.100.033305.
- [34] J.-F. Cornet. “Calculation of optimal design and ideal productivities of volumetrically lightened photobioreactors using the constructal approach”. In: *Chemical Engineering Science* 65.2 (2010), pp. 985–998. DOI: 10.1016/j.ces.2009.09.052.
- [35] R. Cornubert, D. d’Humières, and D. Levermore. “A Knudsen layer theory for lattice gases”. In: *Physica D: Nonlinear Phenomena* 47.1 (1991), pp. 241–259. DOI: 10.1016/0167-2789(91)90295-K.
- [36] Z. Csörgör, M. Herrenbauer, K. Schmidt, and C. Posten. “Light distribution in a novel photobioreactor – modelling for optimization”. In: *Journal of Applied Phycology* 13.4 (2001), pp. 325–333. DOI: 10.1023/A:1017974232510.

Bibliography

- [37] P. Darvehei, P. A. Bahri, and N. R. Moheimani. “Model development for the growth of microalgae: A review”. In: *Renewable and Sustainable Energy Reviews* 97 (2018), pp. 233–258. DOI: 10.1016/j.rser.2018.08.027.
- [38] J. Dauchet, S. Blanco, J.-F. Cornet, M. E. Hafi, V. Eymet, and R. Fournier. “The practice of recent radiative transfer Monte Carlo advances and its contribution to the field of microorganisms cultivation in photobioreactors”. In: *Journal of Quantitative Spectroscopy and Radiative Transfer* 128.0 (2013). Eurotherm Seminar on Computational Thermal Radiation in Participating Media IV, pp. 52–59. DOI: 10.1016/j.jqsrt.2012.07.004.
- [39] A. B. Davis and A. Marshak. “Solar radiation transport in the cloudy atmosphere: a 3D perspective on observations and climate impacts”. In: *Reports on Progress in Physics* 73.2 (2010), p. 026801. DOI: 10.1088/0034-4885/73/2/026801.
- [40] M. R. Droop. “25 years of algal growth kinetics a personal view”. In: *Botanica marina* 26.3 (1983), pp. 99–112. DOI: 10.1515/botm.1983.26.3.99.
- [41] M. Ehrhardt. *Progress in Computational Physics Volume 3: Novel Trends in Lattice-Boltzmann Methods*. Vol. 3. Bentham Science Publishers, 2013.
- [42] P. Eilers and J. Peeters. “A model for the relationship between light intensity and the rate of photosynthesis in phytoplankton”. In: *Ecological modelling* 42.3-4 (1988), pp. 199–215. DOI: 10.1016/0304-3800(88)90057-9.
- [43] “Enhancement of microalgae production by embedding hollow light guides to a flat-plate photobioreactor”. In: *Bioresource Technology* 207 (2016), pp. 31–38. DOI: 10.1016/j.biortech.2016.01.136.
- [44] K. F. Evans. “The spherical harmonics discrete ordinate method for three-dimensional atmospheric radiative transfer”. In: *Journal of the Atmospheric Sciences* 55.3 (1998), pp. 429–446. DOI: 10.1175/1520-0469.
- [45] C. Feichtinger, J. Habich, H. Köstler, U. Rüde, and T. Aoki. “Performance modeling and analysis of heterogeneous lattice Boltzmann simulations on CPU–GPU clusters”. In: *Parallel Computing* 46 (2015), pp. 1–13. DOI: 10.1016/j.parco.2014.12.003.
- [46] F. G. A. Fernández, F. G. Camacho, J. A. S. Pérez, J. M. F. Sevilla, and E. M. Grima. “A model for light distribution and average solar irradiance inside outdoor tubular photobioreactors for the microalgal mass culture”. In: *Biotechnology and Bioengineering* 55.5 (1997), pp. 701–714.
- [47] F. A. Fernández, J. F. Sevilla, J. S. Pérez, E. M. Grima, and Y. Chisti. “Airlift-driven external-loop tubular photobioreactors for outdoor production of microalgae: assessment of design and performance”. In: *Chemical Engineering Science* 56.8 (2001), pp. 2721–2732. DOI: 10.1016/S0009-2509(00)00521-2.
- [48] I. Fernández, F. G. Ación, M. Berenguel, and J. L. Guzmán. “First principles model of a tubular photobioreactor for microalgal production”. In: *Industrial & Engineering Chemistry Research* 53.27 (2014), pp. 11121–11136.

- [49] W. Fiveland. “Discrete ordinate methods for radiative heat transfer in isotropically and anisotropically scattering media”. In: *Journal of Heat Transfer (Transactions of the ASME (American Society of Mechanical Engineers), Series C);(United States)* 109.3 (1987). DOI: 10.1115/1.3248167.
- [50] S. T. Flock, M. S. Patterson, B. C. Wilson, and D. R. Wyman. “Monte Carlo modeling of light propagation in highly scattering tissues. I. Model predictions and comparison with diffusion theory”. In: *IEEE Transactions on Biomedical Engineering* 36.12 (1989), pp. 1162–1168. DOI: 10.1109/TBME.1989.1173624.
- [51] T. S. Flock. “The optical properties of tissues and light dosimetry at 633 nanometers”. PhD thesis. McMaster Universtiy, 1988.
- [52] M. Gaedtke, T. Hoffmann, V. Reinhardt, G. Thäter, H. Nirschl, and M. Krause. “Flow and heat transfer simulation with a thermal large eddy lattice Boltzmann method in an annular gap with an inner rotating cylinder”. In: *International Journal of Modern Physics C* 30.02n03 (2019), p. 1950013. DOI: 10.1142/S012918311950013X.
- [53] A. Gairola and H. Bindra. “Lattice Boltzmann method for solving non-equilibrium radiative transport problems”. In: *Annals of Nuclear Energy* 99 (2017), pp. 151–156. DOI: 10.1016/j.anucene.2016.08.011.
- [54] X. Gao, B. Kong, M. Ramezani, M. G. Olsen, and R. D. Vigil. “An adaptive model for gas–liquid mass transfer in a Taylor vortex reactor”. In: *International Journal of Heat and Mass Transfer* 91 (2015), pp. 433–445. DOI: 10.1016/j.ijheatmasstransfer.2015.07.125.
- [55] X. Gao, B. Kong, and R. D. Vigil. “CFD investigation of bubble effects on Taylor–Couette flow patterns in the weakly turbulent vortex regime”. In: *Chemical Engineering Journal* 270 (2015), pp. 508–518. DOI: 10.1016/j.cej.2015.02.061.
- [56] X. Gao, B. Kong, and R. D. Vigil. “Characteristic time scales of mixing, mass transfer and biomass growth in a Taylor vortex algal photobioreactor”. In: *Bioresource Technology* 198 (2015), pp. 283–291. DOI: 10.1016/j.biortech.2015.09.013.
- [57] X. Gao, B. Kong, and R. D. Vigil. “Comprehensive computational model for combining fluid hydrodynamics, light transport and biomass growth in a Taylor vortex algal photobioreactor: Lagrangian approach”. In: *Bioresource Technology* 224 (2017), pp. 523–530. DOI: 10.1016/j.biortech.2016.10.080.
- [58] X. Gao, B. Kong, and R. D. Vigil. “Multiphysics simulation of algal growth in an airlift photobioreactor: Effects of fluid mixing and shear stress”. In: *Bioresource Technology* 251 (2018), pp. 75–83. DOI: 10.1016/j.biortech.2017.12.014.
- [59] X. Gao, B. Kong, and R. D. Vigil. “Simulation of algal photobioreactors: recent developments and challenges”. In: *Biotechnology Letters* 40.9-10 (2018), pp. 1311–1327. DOI: 10.1007/s10529-018-2595-3.

Bibliography

- [60] F. García-Camacho, A. Sánchez-Mirón, E. Molina-Grima, F. Camacho-Rubio, and J. Merchuck. “A mechanistic model of photosynthesis in microalgae including photoacclimation dynamics”. In: *Journal of Theoretical Biology* 304 (2012), pp. 1–15. DOI: 10.1016/j.jtbi.2012.03.021.
- [61] T. Gebäck and A. Heintz. “A Lattice Boltzmann Method for the Advection-Diffusion Equation with Neumann Boundary Conditions”. In: *Communications in Computational Physics* 15.2 (2014), pp. 487–505. DOI: 10.4208/cicp.161112.230713a.
- [62] R. Geist, K. Rasche, J. Westall, and R. Schalkoff. “Lattice-Boltzmann Lighting”. In: *Eurographics Workshop on Rendering*. Ed. by A. Keller and H. W. Jensen. The Eurographics Association, 2004, pp. 355–362. DOI: 10.2312/EGWR/EGSR04/355-362.
- [63] I. Gifuni, A. Pollio, A. Marzocchella, and G. Olivieri. “New ultra-flat photobioreactor for intensive microalgal production: The effect of light irradiance”. In: *Algal Research* 34 (2018), pp. 134–142. DOI: 10.1016/j.algal.2018.07.014.
- [64] F. Golse. “From the Kinetic Theory of Gases to Continuum Mechanics”. In: *AIP Conference Proceedings* 1333.1 (2011), pp. 15–27. DOI: 10.1063/1.3562621.
- [65] C. Gómez-Pérez, J. Espinosa, L. M. Ruiz, and A. van Boxtel. “CFD simulation for reduced energy costs in tubular photobioreactors using wall turbulence promoters”. In: *Algal Research* 12 (2015), pp. 1–9. DOI: 10.1016/j.algal.2015.07.011.
- [66] H. Grad. “On the kinetic theory of rarefied gases”. In: *Communications on pure and applied mathematics* 2.4 (1949), pp. 331–407. DOI: 10.1002/cpa.3160020403.
- [67] E. M. Grima, J. F. Sevilla, J. S. Pérez, and F. G. Camacho. “A study on simultaneous photolimitation and photoinhibition in dense microalgal cultures taking into account incident and averaged irradiances”. In: *Journal of Biotechnology* 45.1 (1996), pp. 59–69.
- [68] Y. Guo and M. Wang. “Lattice Boltzmann modeling of phonon transport”. In: *Journal of Computational Physics* 315 (2016), pp. 1–15. DOI: 10.1016/j.jcp.2016.03.041.
- [69] Z. Guo and C. Shu. *Lattice Boltzmann Method and Its Applications in Engineering*. Advances in computational fluid dynamics. World Scientific, 2013.
- [70] Z. Guo, B. Shi, T. S. Zhao, and C. Zheng. “Discrete effects on boundary conditions for the lattice Boltzmann equation in simulating microscale gas flows”. In: *Phys. Rev. E* 76 (5 2007), p. 056704. DOI: 10.1103/PhysRevE.76.056704.
- [71] Z. Guo, B. Shi, and C. Zheng. “A coupled lattice BGK model for the Boussinesq equations”. In: *International Journal for Numerical Methods in Fluids* 39.4 (2002), pp. 325–342.
- [72] D. Hänel. *Molekulare Gasdynamik*: Springer, 2004.

- [73] I. Hariskos and C. Posten. “Biorefinery of microalgae—opportunities and constraints for different production scenarios”. In: *Biotechnology Journal* 9.6 (2014), pp. 739–752. DOI: 10.1002/biot.201300142.
- [74] R. C. Haskell, L. O. Svaasand, T.-T. Tsay, T.-C. Feng, M. S. McAdams, and B. J. Tromberg. “Boundary conditions for the diffusion equation in radiative transfer”. In: *J. Opt. Soc. Am. A* 11.10 (1994), pp. 2727–2741. DOI: 10.1364/JOSAA.11.002727.
- [75] M. Haussmann, A. C. BARRETO, G. L. KOUYI, N. Rivière, H. Nirschl, and M. J. Krause. “Large-eddy simulation coupled with wall models for turbulent channel flows at high Reynolds numbers with a lattice Boltzmann method – Application to Coriolis mass flowmeter”. In: *Computers & Mathematics with Applications* 78.10 (2019), pp. 3285–3302. DOI: 10.1016/j.camwa.2019.04.033.
- [76] X. He, N. Li, and B. Goldstein. “Lattice Boltzmann Simulation of Diffusion-Convection Systems with Surface Chemical Reaction”. In: *Molecular Simulation* 25.3-4 (2000), pp. 145–156. DOI: 10.1080/08927020008044120.
- [77] X. He and L.-S. Luo. “Theory of the lattice Boltzmann method : From the Boltzmann equation to the lattice Boltzmann equation”. In: *Phys. Rev. E* 56 (1997), pp. 6811–6818. DOI: 10.1103/PhysRevE.56.6811.
- [78] T. Henn, G. Thäter, W. Dörfler, H. Nirschl, and M. J. Krause. “Parallel dilute particulate flow simulations in the human nasal cavity”. In: *Computers & Fluids* 124 (2016). Special Issue for ICMME-2014, pp. 197–207. DOI: 10.1016/j.compfluid.2015.08.002.
- [79] D. J. Holdych, D. R. Noble, J. G. Georgiadis, and R. O. Buckius. “Truncation error analysis of lattice Boltzmann methods”. In: *Journal of Computational Physics* 193.2 (2004), pp. 595–619. DOI: 10.1016/j.jcp.2003.08.012.
- [80] H. Hsueh, W. Li, H. Chen, and H. Chu. “Carbon bio-fixation by photosynthesis of *Thermosynechococcus* sp. CL-1 and *Nannochloropsis oculata*”. In: *Journal of Photochemistry and Photobiology B: Biology* 95.1 (2009), pp. 33–39. DOI: 10.1016/j.jphotobiol.2008.11.010.
- [81] J. Huang, F. Feng, M. Wan, J. Ying, Y. Li, X. Qu, R. Pan, G. Shen, and W. Li. “Improving performance of flat-plate photobioreactors by installation of novel internal mixers optimized with computational fluid dynamics”. In: *Bioresource Technology* 182 (2015), pp. 151–159. DOI: 10.1016/j.biortech.2015.01.067.
- [82] Q. Huang, F. Jiang, L. Wang, and C. Yang. “Design of photobioreactors for mass cultivation of photosynthetic organisms”. In: *Engineering* 3.3 (2017), pp. 318–329. DOI: 10.1016/J.ENG.2017.03.020.
- [83] Q. Huang, T. Liu, J. Yang, L. Yao, and L. Gao. “Evaluation of radiative transfer using the finite volume method in cylindrical photoreactors”. In: *Chemical Engineering Science* 66.17 (2011), pp. 3930–3940. DOI: 10.1016/j.ces.2011.05.032.

Bibliography

- [84] Q. Huang, L. Yao, T. Liu, and J. Yang. “Simulation of the light evolution in an annular photobioreactor for the cultivation of *Porphyridium cruentum*”. In: *Chemical Engineering Science* 84.0 (2012), pp. 718–726. DOI: 10.1016/j.ces.2012.09.017.
- [85] B. Hunter and Z. Guo. “A New and Simple Technique to Normalize the HG Phase Function for Conserving Scattered Energy and Asymmetry Factor”. In: *Numerical Heat Transfer, Part B: Fundamentals* 65.3 (2014), pp. 195–217. DOI: 10.1080/10407790.2013.849992.
- [86] B. Hunter and Z. Guo. “Comparison of quadrature schemes in DOM for anisotropic scattering radiative transfer analysis”. In: *Numerical Heat Transfer, Part B: Fundamentals* 63.6 (2013), pp. 485–507. DOI: 10.1080/10407790.2013.777644.
- [87] B. Hunter and Z. Guo. “Conservation of asymmetry factor in phase function discretization for radiative transfer analysis in anisotropic scattering media”. In: *International Journal of Heat and Mass Transfer* 55.5-6 (2012), pp. 1544–1552. DOI: 10.1016/j.ijheatmasstransfer.2011.11.009.
- [88] B. Hunter and Z. Guo. “Numerical smearing, ray effect, and angular false scattering in radiation transfer computation”. In: *International Journal of Heat and Mass Transfer* 81 (2015), pp. 63–74. DOI: 10.1016/j.ijheatmasstransfer.2014.10.014.
- [89] A. Ishimaru. *Wave Propagation and Scattering in Random Media*. IEEE/OUP series on electromagnetic wave theory v. 2. Academic Press, 1978.
- [90] A. Jacobi, E. C. Bucharsky, K. G. Schell, P. Habisreuther, R. Oberacker, M. J. Hoffmann, N. Zarzalis, and C. Posten. “The Application of Transparent Glass Sponge for Improvement of Light Distribution in Photobioreactors”. In: *Journal of Bioprocessing & Biotechniques* 2.1 (2012). DOI: 10.4172/2155-9821.1000113.
- [91] S. L. Jacques and B. W. Pogue. “Tutorial on diffuse light transport”. In: *Journal of Biomedical Optics* 13.4 (2008), p. 041302. DOI: 10.1117/1.2967535.
- [92] M. Junk, A. Klar, and L.-S. Luo. “Asymptotic analysis of the lattice Boltzmann equation”. In: *Journal of Computational Physics* 210.2 (2005), pp. 676–704. DOI: 10.1016/j.jcp.2005.05.003.
- [93] R. Kandilian, J. Pruvost, A. Artu, C. Lemasson, J. Legrand, and L. Pilon. “Comparison of experimentally and theoretically determined radiation characteristics of photosynthetic microorganisms”. In: *Journal of Quantitative Spectroscopy and Radiative Transfer* 175 (2016), pp. 30–45. DOI: 10.1016/j.jqsrt.2016.01.031.
- [94] R. Kandilian, A. Soulies, J. Pruvost, B. Rousseau, J. Legrand, and L. Pilon. “Simple method for measuring the spectral absorption cross-section of microalgae”. In: *Chemical Engineering Science* 146 (2016), pp. 357–368. DOI: 10.1016/j.ces.2016.02.039.
- [95] Q. Kang, P. C. Lichtner, and D. Zhang. “An improved lattice Boltzmann model for multicomponent reactive transport in porous media at the pore scale”. In: *Water Resources Research* 43.12 (2007). DOI: 10.1029/2006WR005551.

- [96] R. Karande, A. Schmid, and K. Buehler. “Applications of Multiphasic Microreactors for Biocatalytic Reactions”. In: *Organic Process Research & Development* 20.2 (2016), pp. 361–370. DOI: 10.1021/acs.oprd.5b00352.
- [97] H. Karani and C. Huber. “Lattice Boltzmann formulation for conjugate heat transfer in heterogeneous media”. In: *Phys. Rev. E* 91 (2 2015), p. 023304. DOI: 10.1103/PhysRevE.91.023304.
- [98] T.-K. Kim and H. Lee. “Effect of anisotropic scattering on radiative heat transfer in two-dimensional rectangular enclosures”. In: *International Journal of Heat and Mass Transfer* 31.8 (1988), pp. 1711–1721. DOI: 10.1016/0017-9310(88)90283-9.
- [99] B. Kong and R. D. Vigil. “Simulation of photosynthetically active radiation distribution in algal photobioreactors using a multidimensional spectral radiation model”. In: *Bioresource Technology* 158.0 (2014), pp. 141–148. DOI: 10.1016/j.biortech.2014.01.052.
- [100] M. Krause, A. Mink, R. Trunk, F. Klemens, M.-L. Maier, M. Mohrhard, A. Claro Barreto, M. Haußmann, M. Gaedtke, and J. Ross-Jones. *OpenLB Release 1.2: Open Source Lattice Boltzmann Code*. online. 2018.
- [101] M. J. Krause. “Fluid Flow Simulation and Optimisation with Lattice Boltzmann Methods on High Performance Computers - Application to the Human Respiratory System”. PhD thesis. Karlsruhe Institute of Technology (KIT), 2010.
- [102] M. J. Krause, B. Förster, A. Mink, and H. Nirschl. “Towards Solving Fluid Flow Domain Identification Problems with Adjoint Lattice Boltzmann Methods”. In: *High Performance Computing in Science and Engineering '16*. Cham: Springer International Publishing, 2016, pp. 337–353. DOI: 10.1007/978-3-319-47066-5_23.
- [103] M. J. Krause, A. Kummerländer, S. J. Avis, H. Kusumaatmaja, D. Dapelo, F. Klemens, M. Gaedtke, N. Hafen, A. Mink, R. Trunk, J. E. Marquardt, M.-L. Maier, M. Hausmann, and S. Simonis. “OpenLB—Open source lattice Boltzmann code”. In: *Computers & Mathematics with Applications* (2020). DOI: 10.1016/j.camwa.2020.04.033.
- [104] S. Krithivasan, S. Wahal, and S. Ansumali. “Diffused bounce-back condition and refill algorithm for the lattice Boltzmann method”. In: *Physical Review E* 89.3 (2014). DOI: 10.1103/physreve.89.033313.
- [105] T. Krüger, H. Kusumaatmaja, A. Kuzmin, O. Shardt, G. Silva, and E. M. Viggen. *The Lattice Boltzmann Method*. Springer, 2017.
- [106] A. Kuzmin, I. Ginzburg, and A. Mohamad. “The role of the kinetic parameter in the stability of two-relaxation-time advection–diffusion lattice Boltzmann schemes”. In: *Computers & Mathematics with Applications* 61.12 (2011), pp. 3417–3442. DOI: 10.1016/j.camwa.2010.07.036.

Bibliography

- [107] A. Lapin, D. Müller, and M. Reuss. “Dynamic Behavior of Microbial Populations in Stirred Bioreactors Simulated with Euler–Lagrange Methods: Traveling along the Lifelines of Single Cells”. In: *Industrial & Engineering Chemistry Research* 43.16 (2004), pp. 4647–4656. DOI: 10.1021/ie030786k.
- [108] E. Lee, M. Jalalizadeh, and Q. Zhang. “Growth kinetic models for microalgae cultivation: A review”. In: *Algal Research* 12 (2015), pp. 497–512. DOI: 10.1016/j.algal.2015.10.004.
- [109] M. Li, D. Hu, and H. Liu. “Photobioreactor with ideal light–dark cycle designed and built from mathematical modeling and CFD simulation”. In: *Ecological Engineering* 73 (2014), pp. 162–167. DOI: 10.1016/j.ecoleng.2014.09.010.
- [110] R. L. Liboff. *Kinetic theory: classical, quantum, and relativistic descriptions*. Springer Science & Business Media, 2003.
- [111] Y. Ma, S. Dong, and H. Tan. “Lattice Boltzmann method for one-dimensional radiation transfer”. In: *Phys. Rev. E* 84 (1 2011), p. 016704. DOI: 10.1103/PhysRevE.84.016704.
- [112] M.-L. Maier, S. Milles, S. Schuhmann, G. Guthausen, H. Nirschl, and M. J. Krause. “Fluid flow simulations verified by measurements to investigate adsorption processes in a static mixer”. In: *Computers & Mathematics with Applications* 76.11 (2018), pp. 2744–2757. DOI: 10.1016/j.camwa.2018.08.066.
- [113] A. Massart, A. Mirisola, D. Lupant, D. Thomas, and A.-L. Hantson. “Experimental characterization and numerical simulation of the hydrodynamics in an airlift photobioreactor for microalgae cultures”. In: *Algal Research* 6, Part B (2014), pp. 210–217. DOI: 10.1016/j.algal.2014.07.003.
- [114] R. McCulloch and H. Bindra. “Coupled radiative and conjugate heat transfer in participating media using lattice Boltzmann methods”. In: *Computers & Fluids* 124 (2016). Special Issue for ICMMS-2014, pp. 261–269. DOI: 10.1016/j.compfluid.2015.05.024.
- [115] C. McHardy, T. Horneber, and C. Rauh. “New lattice Boltzmann method for the simulation of three-dimensional radiation transfer in turbid media”. In: *Opt. Express* 24.15 (2016), pp. 16999–17017. DOI: 10.1364/OE.24.016999.
- [116] C. McHardy, T. Horneber, and C. Rauh. “Spectral simulation of light propagation in participating media by using a lattice Boltzmann method for photons”. In: *Applied Mathematics and Computation* 319 (2018). Recent Advances in Computing, pp. 59–70. DOI: 10.1016/j.amc.2017.01.045.
- [117] C. McHardy, G. Luzi, C. Lindenberger, J. R. Agudo, A. Delgado, and C. Rauh. “Numerical analysis of the effects of air on light distribution in a bubble column photobioreactor”. In: *Algal Research* 31 (2018), pp. 311–325. DOI: 10.1016/j.algal.2018.02.016.

- [118] C. B. McHardy. “A Lattice Boltzmann Method for the simulation of light transfer in turbid media and its application in computational studies on microalgae growth kinetics”. Doctoral Thesis. Berlin: Technische Universität Berlin, 2019. DOI: 10.14279/depositonce-9096.
- [119] G. R. McNamara and G. Zanetti. “Use of the Boltzmann Equation to Simulate Lattice-Gas Automata”. In: *Phys. Rev. Lett.* 61 (1988), pp. 2332–2335. DOI: 10.1103/PhysRevLett.61.2332.
- [120] J. Merchuk, F. Garcia-Camacho, and E. Molina-Grima. “Photobioreactors – Models of Photosynthesis and Related Effects”. In: *Comprehensive Biotechnology* (2011), pp. 227–247. DOI: 10.1016/b978-0-08-088504-9.00103-3.
- [121] A. Mink, C. McHardy, L. Bressel, C. Rauh, and M. J. Krause. “Radiative transfer lattice Boltzmann methods: 3D models and their performance in different regimes of radiative transfer”. In: *Journal of Quantitative Spectroscopy and Radiative Transfer* 243 (2020), p. 106810. DOI: 10.1016/j.jqsrt.2019.106810.
- [122] A. Mink, C. Posten, H. Nirschl, and M. J. Krause. “Lattice Boltzmann Method for Light and Algae Simulations in Photobioreactors”. In: *International Congress on Particle Technology (PARTEC)*. Nürnberg, 2016.
- [123] A. Mink, K. Schediwy, M. Haussmann, C. Posten, H. Nirschl, and M. J. Krause. *Fresnel reflection boundary for radiative transport lattice Boltzmann methods in highly scattering volume*. 2021. arXiv: 2107.09411 [physics.comp-ph].
- [124] A. Mink, K. Schediwy, C. Posten, H. Nirschl, S. Simonis, and M. J. Krause. *Comprehensive computational model for coupled fluid flow, mass transfer and light supply in tubular photobioreactors equipped with glass sponges*. 2021. arXiv: 2107.12210 [physics.flu-dyn].
- [125] A. Mink, G. Thäter, H. Nirschl, and M. J. Krause. “A 3D Lattice Boltzmann method for light simulation in participating media”. In: *Journal of Computational Science* 17.Part 2 (2016). Discrete Simulation of Fluid Dynamics 2015, pp. 431–437. DOI: 10.1016/j.jocs.2016.03.014.
- [126] S. C. Mishra, N. Gullipalli, A. Jain, A. Barurah, and A. Mukherjee. “Analysis of hyperbolic heat conduction in 1-D planar, cylindrical, and spherical geometry using the lattice Boltzmann method”. In: *International Communications in Heat and Mass Transfer* 74 (2016), pp. 48–54. DOI: 10.1016/j.icheatmasstransfer.2016.02.015.
- [127] S. C. Mishra, H. Poonia, A. K. Das, P. Asinari, and R. Borchiellini. “Analysis of conduction-radiation heat transfer in a 2D enclosure using the lattice Boltzmann method”. In: *Numerical Heat Transfer, Part A: Applications* 66.6 (2014), pp. 669–688. DOI: 10.1080/10407782.2014.894376.
- [128] S. C. Mishra, H. K. Roy, and N. Misra. “Discrete ordinate method with a new and a simple quadrature scheme”. In: *Journal of Quantitative Spectroscopy and Radiative Transfer* 101.2 (2006), pp. 249–262. DOI: 10.1016/j.jqsrt.2005.11.018.

Bibliography

- [129] M. F. Modest. *Radiative heat transfer*. Academic press, 2013.
- [130] A. Mohamad. *Lattice Boltzmann Method: Fundamentals and Engineering Applications with Computer Codes*. SpringerLink : Bücher. Springer, 2011.
- [131] M. Mohrhard, G. Thäter, J. Bludau, B. Horvat, and M. J. Krause. “Auto-vectorization friendly parallel lattice Boltzmann streaming scheme for direct addressing”. In: *Computers & Fluids* 181 (2019), pp. 1–7. DOI: 10.1016/j.compfluid.2019.01.001.
- [132] J. Monod. “THE GROWTH OF BACTERIAL CULTURES”. In: *Annual Review of Microbiology* 3.1 (1949), pp. 371–394. DOI: 10.1146/annurev.mi.03.100149.002103.
- [133] M. Morita, Y. Watanabe, and H. Saiki. “Evaluation of photobioreactor heat balance for predicting changes in culture medium temperature due to light irradiation”. In: *Biotechnology and Bioengineering* 74.6 (2001), pp. 466–475. DOI: 10.1002/bit.1137.
- [134] A. Nabovati, D. P. Sellan, and C. H. Amon. “On the lattice Boltzmann method for phonon transport”. In: *Journal of Computational Physics* 230.15 (2011), pp. 5864–5876. DOI: 10.1016/j.jcp.2011.03.061.
- [135] P. Nathen, D. Gaudlitz, M. Krause, and J. Kratzke. “An extension of the Lattice Boltzmann Method for simulating turbulent flows around rotating geometries of arbitrary shape”. In: *21st AIAA Computational Fluid Dynamics Conference. American Institute of Aeronautics and Astronautics*. 2013.
- [136] E. K. Nauha and V. Alopaeus. “Modeling method for combining fluid dynamics and algal growth in a bubble column photobioreactor”. In: *Chemical Engineering Journal* 229 (2013), pp. 559–568. DOI: 10.1016/j.cej.2013.06.065.
- [137] M. Nazari, H. Shokri, and A. A. Mohamad. “Lattice Boltzmann simulation of natural convection in open end cavity with inclined hot wall”. In: *Applied Mathematics and Mechanics* 36.4 (2015), pp. 523–540. DOI: 10.1007/s10483-015-1928-9.
- [138] E. G. Nwoba, D. A. Parlevliet, D. W. Laird, K. Alameh, and N. R. Moheimani. “Light management technologies for increasing algal photobioreactor efficiency”. In: *Algal research* 39 (2019), p. 101433. DOI: 10.1016/j.algal.2019.101433.
- [139] G. Olivieri, P. Salatino, and A. Marzocchella. “Advances in photobioreactors for intensive microalgal production: configurations, operating strategies and applications”. In: *Journal of Chemical Technology & Biotechnology* 89.2 (2014), pp. 178–195. DOI: 10.1002/jctb.4218.
- [140] D. V. Patil, K. N. Premnath, and S. Banerjee. “Multigrid lattice Boltzmann method for accelerated solution of elliptic equations”. In: *Journal of Computational Physics* 265 (2014), pp. 172–194. DOI: 10.1016/j.jcp.2014.01.049.
- [141] I. Perner, C. Posten, and J. Broneske. “CFD Optimization of a Plate Photobioreactor Used for Cultivation of Microalgae”. In: *Engineering in Life Sciences* 3.7 (2003), pp. 287–291. DOI: 10.1002/elsc.200302964.

- [142] I. Perner-Nochta and C. Posten. “Simulations of light intensity variation in photobioreactors”. In: *Journal of Biotechnology* 131.3 (2007), pp. 276–285. DOI: 10.1016/j.jbiotec.2007.05.024.
- [143] J. C. Pires, M. C. Alvim-Ferraz, and F. G. Martins. “Photobioreactor design for microalgae production through computational fluid dynamics: a review”. In: *Renewable and Sustainable Energy Reviews* 79 (2017), pp. 248–254. DOI: 10.1016/j.rser.2017.05.064.
- [144] B. Podola, T. Li, and M. Melkonian. “Porous Substrate Bioreactors: A Paradigm Shift in Microalgal Biotechnology?” In: *Trends in Biotechnology* 35.2 (2017), pp. 121–132. DOI: 10.1016/j.tibtech.2016.06.004.
- [145] S. Ponce Dawson, S. Chen, and G. D. Doolen. “Lattice Boltzmann computations for reaction-diffusion equations”. In: *The Journal of Chemical Physics* 98.2 (1993), pp. 1514–1523. DOI: 10.1063/1.464316.
- [146] P. Popova and C. Boyadjiev. “About microalgae growth kinetics modeling”. In: *Chemical and biochemical engineering quarterly* 22.4 (2008), pp. 491–497.
- [147] C. Posten. “Design principles of photo-bioreactors for cultivation of microalgae”. In: *Engineering in Life Sciences* 9.3 (2009), pp. 165–177. DOI: 10.1002/elsc.200900003.
- [148] N. Pottier. *Nonequilibrium Statistical Physics: Linear Irreversible Processes*. Oxford University Press, 2010.
- [149] J. Pruvost, J.-F. Cornet, and J. Legrand. “Hydrodynamics influence on light conversion in photobioreactors: An energetically consistent analysis”. In: *Chemical Engineering Science* 63.14 (2008), pp. 3679–3694. DOI: 10.1016/j.ces.2008.04.026.
- [150] J. Pruvost, J. Legrand, P. Legentilhomme, and A. Muller-Feuga. “Simulation of microalgae growth in limiting light conditions: Flow effect”. In: *AIChE Journal* 48.5 (2002), pp. 1109–1120. DOI: 10.1002/aic.690480520.
- [151] J. Pruvost, L. Pottier, and J. Legrand. “Numerical investigation of hydrodynamic and mixing conditions in a torus photobioreactor”. In: *Chemical Engineering Science* 61.14 (2006), pp. 4476–4489. DOI: 10.1016/j.ces.2006.02.027.
- [152] Y. H. Qian, D. D’Humières, and P. Lallemand. “Lattice BGK Models for Navier–Stokes Equation”. In: *Europhysics Letters (EPL)* 17.6 (1992), pp. 479–484. DOI: 10.1209/0295-5075/17/6/001.
- [153] C. Qin, J. Wu, and J. Wang. “Synergy between flow and light fields and its applications to the design of mixers in microalgal photobioreactors”. In: *Biotechnology for biofuels* 12.1 (2019), p. 93. DOI: 10.1186/s13068-019-1430-y.
- [154] L. Reynolds, C. Johnson, and A. Ishimaru. “Diffuse reflectance from a finite blood medium: applications to the modeling of fiber optic catheters”. In: *Applied Optics* 15.9 (1976), p. 2059. DOI: 10.1364/ao.15.002059.

Bibliography

- [155] J. Rocha-Rios, N. Kraakman, R. Kleerebezem, S. Revah, M. Kreutzer, and M. van Loosdrecht. “A capillary bioreactor to increase methane transfer and oxidation through Taylor flow formation and transfer vector addition”. In: *Chemical Engineering Journal* 217 (2013), pp. 91–98. DOI: 10.1016/j.cej.2012.11.065.
- [156] R. M. Rosello Sastre. “Kopplung physiologischer und verfahrenstechnischer Parameter beim Wachstum und bei der Produktbildung der Rotalge *Porphyridium purpureum*”. German. PhD thesis. 2010. 154 pp. DOI: 10.5445/KSP/1000015569.
- [157] J. Ross-Jones, M. Gaedtke, S. Sonnicks, M. Rädle, H. Nirschl, and M. Krause. “Conjugate heat transfer through nano scale porous media to optimize vacuum insulation panels with lattice Boltzmann methods”. In: *Computers & Mathematics with Applications* 77 (2019), pp. 209–221. DOI: 10.1016/j.camwa.2018.09.023.
- [158] F. C. Rubio, F. García-Camacho, J. M. F. Sevilla, Y. Chisti, and E. M. Grima. “A mechanistic model of photosynthesis in microalgae”. In: *Biotechnology and Bioengineering* 81.4 (2002), pp. 459–473. DOI: 10.1002/bit.10492.
- [159] P. Rudnicki, X. Gao, B. Kong, and R. D. Vigil. “A comparative study of photosynthetic unit models for algal growth rate and fluorescence prediction under light/dark cycles”. In: *Algal Research* 24 (2017), pp. 227–236. DOI: 10.1016/j.algal.2017.03.028.
- [160] L. Saint-Raymond. *Hydrodynamic Limits of the Boltzmann Equation*. Hydrodynamic Limits of the Boltzmann Equation Nr. 1971. Springer, 2009.
- [161] M. Sbragaglia and S. Succi. “Analytical calculation of slip flow in lattice Boltzmann models with kinetic boundary conditions”. In: *Physics of Fluids* 17.9 (2005), p. 093602. DOI: 10.1063/1.2044829.
- [162] L. K. Schultze, M.-V. Simon, T. Li, D. Langenbach, B. Podola, and M. Melkonian. “High light and carbon dioxide optimize surface productivity in a Twin-Layer biofilm photobioreactor”. In: *Algal Research* 8 (2015), pp. 37–44. DOI: 10.1016/j.algal.2015.01.007.
- [163] E. Sforza, D. Simionato, G. M. Giacometti, A. Bertuccio, and T. Morosinotto. “Adjusted Light and Dark Cycles Can Optimize Photosynthetic Efficiency in Algae Growing in Photobioreactors”. In: *PLoS ONE* 7.6 (2012). Ed. by A. Webber, e38975. DOI: 10.1371/journal.pone.0038975.
- [164] X. Shan and H. Chen. “Lattice Boltzmann model for simulating flows with multiple phases and components”. In: *Phys. Rev. E* 47 (3 1993), pp. 1815–1819. DOI: 10.1103/PhysRevE.47.1815.
- [165] V. Sofonea and R. F. Sekerka. “Diffuse-reflection boundary conditions for a thermal lattice Boltzmann model in two dimensions: Evidence of temperature jump and slip velocity in microchannels”. In: *Physical Review E* 71.6 (2005). DOI: 10.1103/physreve.71.066709.
- [166] R. Soto. *Kinetic theory and transport phenomena*. Vol. 25. Oxford University Press, 2016.

- [167] G. Strang. *Introduction to linear algebra*. Vol. 3. Wellesley-Cambridge Press Wellesley, MA, 1993.
- [168] S. Succi. “Lattice Boltzmann 2038”. In: *EPL (Europhysics Letters)* 109.5 (2015), p. 50001. DOI: 10.1209/0295-5075/109/50001.
- [169] S. Succi. “Mesoscopic Modeling of Slip Motion at Fluid-Solid Interfaces with Heterogeneous Catalysis”. In: *Phys. Rev. Lett.* 89 (6 2002), p. 064502. DOI: 10.1103/PhysRevLett.89.064502.
- [170] S. Succi and S. Succi. *The lattice Boltzmann equation: for complex states of flowing matter*. Oxford University Press, 2018.
- [171] I. Suh and C.-G. Lee. “Photobioreactor engineering: Design and performance”. In: *Biotechnology and Bioprocess Engineering* 8.6 (2003), pp. 313–321. DOI: 10.1007/BF02949274.
- [172] Y. Sun, X. Zhang, and J. R. Howell. “Non-gray combined conduction and radiation heat transfer by using FVM and SLW”. In: *Journal of Quantitative Spectroscopy and Radiative Transfer* 197 (2017). The Eight International Symposium on Radiative Transfer, pp. 51–59. DOI: doi.org/10.1016/j.jqsrt.2016.10.022.
- [173] H. Tamiya, T. Iwamura, K. Shibata, E. Hase, and T. Nihei. “Correlation between photosynthesis and light-independent metabolism in the growth of *Chlorella*”. In: *Biochimica et Biophysica Acta* 12.1 (1953), pp. 23–40. DOI: 10.1016/0006-3002(53)90120-6.
- [174] A. Tarokh, A. A. Mohamad, and L. Jiang. “Simulation of Conjugate Heat Transfer Using the Lattice Boltzmann Method”. In: *Numerical Heat Transfer, Part A: Applications* 63.3 (2013), pp. 159–178. DOI: 10.1080/10407782.2012.725009.
- [175] H. A. Tighchi, M. Sobhani, and J. A. Esfahani. “Lattice Boltzmann simulation of combined volumetric radiation/natural convection to consider optical properties of nanoparticles”. In: *Radiation Physics and Chemistry* 159 (2019), pp. 238–251. DOI: 10.1016/j.radphyschem.2019.02.052.
- [176] J. Truelove. “Discrete-ordinate solutions of the radiation transport equation”. In: *Journal of Heat Transfer (Transactions of the ASME (American Society of Mechanical Engineers), Series C);(United States)* 109.4 (1987). DOI: 10.1115/1.3248182.
- [177] R. Trunk, T. Henn, W. Dörfler, H. Nirschl, and M. J. Krause. “Inertial dilute particulate fluid flow simulations with an Euler–Euler lattice Boltzmann method”. In: *Journal of Computational Science* 17.Part 2 (2016). Discrete Simulation of Fluid Dynamics 2015, pp. 438–445. DOI: 10.1016/j.jocs.2016.03.013.
- [178] C. Ugwu, H. Aoyagi, and H. Uchiyama. “Photobioreactors for mass cultivation of algae”. In: *Bioresource Technology* 99.10 (2008), pp. 4021–4028. DOI: 10.1016/j.biortech.2007.01.046.
- [179] H. C. Van de Hulst. *Multiple light scattering: tables, formulas, and applications*. Elsevier, 2012.

Bibliography

- [180] E. Veach. “Robust Monte Carlo Methods for Light Transport Simulation”. PhD thesis. Stanford, CA, USA, 1998.
- [181] E. Veach and L. J. Guibas. “Metropolis Light Transport”. In: *Proceedings of the 24th Annual Conference on Computer Graphics and Interactive Techniques*. SIGGRAPH '97. New York, NY, USA: ACM Press/Addison-Wesley Publishing Co., 1997, pp. 65–76. DOI: 10.1145/258734.258775.
- [182] C. Vejrazka, M. Janssen, M. Streefland, and R. H. Wijffels. “Photosynthetic efficiency of *Chlamydomonas reinhardtii* in flashing light”. In: *Biotechnology and Bioengineering* 108.12 (2011), pp. 2905–2913. DOI: 10.1002/bit.23270.
- [183] C. Villani. “A review of mathematical topics in collisional kinetic theory”. In: *Handbook of mathematical fluid dynamics, Vol. I*. Amsterdam: North-Holland, 2002, pp. 71–305. DOI: 10.1016/S1874-5792(02)80004-0.
- [184] L. Wang and H. Wu. *Biomedical Optics: Principles and Imaging*. Wiley, 2007.
- [185] L.-l. Wang, Y. Tao, and X.-z. Mao. “A novel flat plate algal bioreactor with horizontal baffles: Structural optimization and cultivation performance”. In: *Bioresour. Technol.* 164 (2014), pp. 20–27. DOI: 10.1016/j.biortech.2014.04.100.
- [186] Y. Wang, Y. Ma, and M. Xie. “High-order lattice Boltzmann method for multi-group neutron diffusion solution”. In: *Progress in Nuclear Energy* 110 (2019), pp. 341–353. DOI: 10.1016/j.pnucene.2018.10.014.
- [187] Y. Wang, M. Xie, and Y. Ma. “Neutron transport solution of lattice Boltzmann method and streaming-based block-structured adaptive mesh refinement”. In: *Annals of Nuclear Energy* 118 (2018), pp. 249–259. DOI: 10.1016/j.anucene.2018.04.013.
- [188] Y. Wang, L. Yan, and Y. Ma. “Lattice Boltzmann solution of the transient Boltzmann transport equation in radiative and neutron transport”. In: *Phys. Rev. E* 95.6 (2017), p. 063313. DOI: 10.1103/PhysRevE.95.063313.
- [189] Y. Wang, L. Yan, Y. Ma, and W. Li. “Finite volume lattice Boltzmann scheme for neutron/radiative transfer on unstructured mesh”. In: *Annals of Nuclear Energy* 109 (2017), pp. 227–236. DOI: 10.1016/j.anucene.2017.05.022.
- [190] D. Weaire and R. Phelan. “A counter-example to Kelvin’s conjecture on minimal surfaces”. In: *Philosophical Magazine Letters* 69.2 (1994), pp. 107–110. DOI: 10.1080/09500839408241577.
- [191] G. Wellein, T. Zeiser, G. Hager, and S. Donath. “On the single processor performance of simple lattice Boltzmann kernels”. In: *Computers & Fluids* 35.8-9 (2006), pp. 910–919. DOI: 10.1016/j.compfluid.2005.02.008.
- [192] J. Wenzel. “Light Transport on Path-Space Manifolds”. PhD thesis. Cornell University, 2013.
- [193] K. M. Weyer, D. R. Bush, A. Darzins, and B. D. Willson. “Theoretical maximum algal oil production”. In: *Bioenergy Research* 3.2 (2010), pp. 204–213. DOI: 10.1007/s12155-009-9046-x.

- [194] M. Wittmann, G. Hager, T. Zeiser, J. Treibig, and G. Wellein. “Chip-level and multi-node analysis of energy-optimized lattice Boltzmann CFD simulations”. In: *Concurrency and Computation: Practice and Experience* 28.7 (2015), pp. 2295–2315. DOI: 10.1002/cpe.3489.
- [195] D. Wolf-Gladrow. *Lattice-Gas Cellular Automata and Lattice Boltzmann Models: An Introduction*. Lattice-gas Cellular Automata and Lattice Boltzmann Models: An Introduction Nr. 1725. Springer, 2000.
- [196] D. Wolf-Gladrow. “A lattice Boltzmann equation for diffusion”. In: *Journal of Statistical Physics* 79.5-6 (1995), pp. 1023–1032. DOI: 10.1007/BF02181215.
- [197] X. Wu and J. C. Merchuk. “A model integrating fluid dynamics in photosynthesis and photoinhibition processes”. In: *Chemical Engineering Science* 56.11 (2001), pp. 3527–3538. DOI: 10.1016/S0009-2509(01)00048-3.
- [198] L. Xu, R. Liu, F. Wang, and C.-Z. Liu. “Development of a draft-tube airlift bioreactor for *Botryococcus braunii* with an optimized inner structure using computational fluid dynamics”. In: *Bioresource Technology* 119 (2012), pp. 300–305. DOI: 10.1016/j.biortech.2012.05.123.
- [199] H.-L. Yi, F.-J. Yao, and H.-P. Tan. “Lattice Boltzmann model for a steady radiative transfer equation”. In: *Phys. Rev. E* 94 (2 2016), p. 023312. DOI: 10.1103/PhysRevE.94.023312.
- [200] G. Yu, Y. Li, G. Shen, W. Wang, C. Lin, H. Wu, and Z. Chen. “A novel method using CFD to optimize the inner structure parameters of flat photobioreactors”. In: *Journal of Applied Phycology* 21.6 (2009), p. 719. DOI: 10.1007/s10811-009-9407-z.
- [201] G. Zanetti. “Hydrodynamics of lattice-gas automata”. In: *Phys. Rev. A* 40 (3 1989), pp. 1539–1548. DOI: 10.1103/PhysRevA.40.1539.
- [202] T. Zeiser, G. Hager, and G. Wellein. “Benchmark analysis and application results for lattice Boltzmann simulations on NEC SX vector and Intel Nehalem systems”. In: *Parallel Processing Letters* 19.04 (2009), pp. 491–511. DOI: 10.1142/s0129626409000389.
- [203] L. Zhang, L. Chen, J. Wang, Y. Chen, X. Gao, Z. Zhang, and T. Liu. “Attached cultivation for improving the biomass productivity of *Spirulina platensis*”. In: *Bioresource Technology* 181 (2015), pp. 136–142. DOI: 10.1016/j.biortech.2015.01.025.
- [204] Q. Zhang, X. Wu, S. Xue, K. Liang, and W. Cong. “Study of hydrodynamic characteristics in tubular photobioreactors”. In: *Bioprocess and biosystems engineering* 36.2 (2013), pp. 143–150. DOI: 10.1007/s00449-012-0769-2.
- [205] T. Zhang, B. Shi, Z. Guo, Z. Chai, and J. Lu. “General bounce-back scheme for concentration boundary condition in the lattice-Boltzmann method”. In: *Phys. Rev. E* 85 (1 2012), p. 016701. DOI: 10.1103/PhysRevE.85.016701.

Bibliography

- [206] Y. Zhang, H.-L. Yi, and H.-P. Tan. “Lattice Boltzmann method for short-pulsed laser transport in a multi-layered medium”. In: *Journal of Quantitative Spectroscopy and Radiative Transfer* 155 (2015), pp. 75–89. DOI: 10.1016/j.jqsrt.2015.01.008.
- [207] Y. Zhang, H. Yi, and H. Tan. “Lattice Boltzmann method for one-dimensional vector radiative transfer”. In: *Opt. Express* 24.3 (2016), pp. 2027–2046. DOI: 10.1364/OE.24.002027.
- [208] Y. Zhang, H. Yi, and H. Tan. “One-dimensional transient radiative transfer by lattice Boltzmann method”. In: *Opt. Express* 21.21 (2013), pp. 24532–24549. DOI: 10.1364/OE.21.024532.
- [209] Y. Zhang, R. Qin, and D. R. Emerson. “Lattice Boltzmann simulation of rarefied gas flows in microchannels”. In: *Physical Review E* 71.4 (2005). DOI: 10.1103/physreve.71.047702.
- [210] D. P. Ziegler. “Boundary conditions for lattice Boltzmann simulations”. In: *Journal of Statistical Physics* 71.5 (1993), pp. 1171–1177. DOI: 10.1007/BF01049965.

Publications and Contributions

Articles

- A. Mink, G. Thäter, H. Nirschl, and M. J. Krause. “A 3D Lattice Boltzmann method for light simulation in participating media”. In: *Journal of Computational Science* 17.Part 2 (2016). Discrete Simulation of Fluid Dynamics 2015, pp. 431–437. DOI: 10.1016/j.jocs.2016.03.014
- A. Mink, K. Schediwy, M. Haussmann, C. Posten, H. Nirschl, and M. J. Krause. *Fresnel reflection boundary for radiative transport lattice Boltzmann methods in highly scattering volume*. 2021. arXiv: 2107.09411 [physics.comp-ph]
- A. Mink, C. McHardy, L. Bressel, C. Rauh, and M. J. Krause. “Radiative transfer lattice Boltzmann methods: 3D models and their performance in different regimes of radiative transfer”. In: *Journal of Quantitative Spectroscopy and Radiative Transfer* 243 (2020), p. 106810. DOI: 10.1016/j.jqsrt.2019.106810
- A. Mink, K. Schediwy, C. Posten, H. Nirschl, S. Simonis, and M. J. Krause. *Comprehensive computational model for coupled fluid flow, mass transfer and light supply in tubular photobioreactors equipped with glass sponges*. 2021. arXiv: 2107.12210 [physics.flu-dyn]
- M. J. Krause, A. Kummerländer, S. J. Avis, H. Kusumaatmaja, D. Dapelo, F. Klemens, M. Gaedtke, N. Hafen, A. Mink, R. Trunk, J. E. Marquardt, M.-L. Maier, M. Haussmann, and S. Simonis. “OpenLB—Open source lattice Boltzmann code”. In: *Computers & Mathematics with Applications* (2020). DOI: 10.1016/j.camwa.2020.04.033

Congress proceedings

- M. J. Krause, B. Förster, A. Mink, and H. Nirschl. “Towards Solving Fluid Flow Domain Identification Problems with Adjoint Lattice Boltzmann Methods”. In: *High Performance Computing in Science and Engineering '16*. Cham: Springer International Publishing, 2016, pp. 337–353. DOI: 10.1007/978-3-319-47066-5_23
- A. Mink, C. Posten, H. Nirschl, and M. J. Krause. “Lattice Boltzmann Method for Light and Algae Simulations in Photobioreactors”. In: *International Congress on Particle Technology (PARTEC)*. Nürnberg, 2016

Conference talks and posters

- 1) Albert Mink, Hermann Nirschl, Mathias J. Krause; *Anisotropy modeling for the radiative transport lattice Boltzmann method* 16th International Conference for Mesoscopic Methods in Engineering and Science, July 22-26, 2019, Edinburgh, Scotland
- 2) Albert Mink, Hermann Nirschl, Mathias J. Krause; *Simulation der CO₂ Velleinage im durchströmten Photobioreaktor basierend auf Lattice-Boltzmann Methoden* ProcessNet 2019 Jahrestreffen Reaktionstechnik und Mehrphasenströmungen, May 27-29, 2019, Würzburg, Germany **Poster**
- 3) Albert Mink, Kira Schediwy, Clemens Posten, Nirschl, Mathias J. Krause; *Simulation von Licht und Gas im druchströmten Photobioreaktor basierend auf einem mesoskopischen Modellansatz*, 11. Bundesalgenstammtisch, September 27-28, 2018, Karlsruhe, Germany **Poster**
- 4) Albert Mink, Hermann Nirschl, Mathias J. Krause; *Mesoscopic modeling of Fresnel surfaces for the radiative transport lattice Boltzmann method*, 27th International Conference on Discrete Simulation of Fluid Dynamics, June 25-29, 2018, Worcester, U.S.A.
- 5) Albert Mink, Hermann Nirschl, Mathias J. Krause; *Boundary Modeling for Radiative Transport Lattice Boltzmann Methods*, ProcessNet 2018 Computational Fluid Dynamics und Mehrphasenströmungen, March 06-09, 2018, Bremen, Germany
- 6) Albert Mink, Mathias J. Krause; *Lattice Boltzmann Method for Radiative Transport Problems in Participating Media: Robin Boundary Condition*, 14th International Conference for Mesoscopic Methods in Engineering and Science, July 17-21, 2017, Nantes, France
- 7) Albert Mink, Hermann Nirschl, Mathias J. Krause; *Lattice Boltzmann Method for Radiative Transport Problems in Participating Media: Application to Photobioreactors*, ProcessNet 2017 Computational Fluid Dynamics und Mischvorgänge, March 16-17, 2017, Dresden, Germany
- 8) Albert Mink, Mathias J. Krause; *Collision Operator: Radiative Transport Lattice Boltzmann Methods (RTLBM)*, 1st Spring School: Lattice Boltzmann Methods with OpenLB Software Lab. March 06-10 2017, Hammamet, Tunisia
- 9) Albert Mink, Mathias J. Krause; *Mesoscopic Modeling and Simulation of Algal Growth in Photobioreactors*, 13th International Conference for Mesoscopic Methods in Engineering and Science, July 18-22, 2016, Hamburg, Germany
- 10) Albert Mink, Mathias J. Krause; *A Lattice Boltzmann Method for Light and Algae Simulations in Photobioreactors*, PARTEC 2016 International Congress on Particle Technology, April 19-21, 2016, Nürnberg, Germany
- 11) Albert Mink, Mathias J. Krause; *A 3D Lattice Boltzmann Method for Light Simulation in Participating Media*, 24th International Conference on Discrete Simulation of Fluid Dynamics, July 13-17, 2015, Edinburgh, Scotland

Curriculum Vitae

Albert Mink

Born 18-June-1989 in Ravensburg, Germany



Work

- 2020** SAP SE, T&I ABAP Platform Developer Tools
- 2012** ZF-Friedrichshafen AG (Friedrichshafen, Germany), 5 month Internship in FEM-post-processing with FORTRAN

Education

- 2015-2020** PhD thesis at Karlsruhe Institute of Technology
- 2013-2015** Master of Mathematics at the Karlsruhe Institute of Technology, "Lattice Boltzmann Method for Light Simulation in Participating Media" advisor Gudrun Thäter and Hermann Nirschl
- 2010-2011** Studies at Université de Bordeaux
- 2008-2013** Bachelor of Mathematics at Ulm University, "Operatorenideale auf Hilberträumen" advisor Wolfgang Arendt
- 2008** Secondary School Gymnasium Edith-Stein Schule Ravensburg

Acronyms

Notation	Description
CFD	computational fluid dynamics. 2, 128
DOM	Discrete–Ordinate Method. 11
EOC	experimental order of convergence. 20
FVM	Finite–Volume Method. 37
LBM	Lattice Boltzmann Methods. v, 3, 125
LD-cycles	light/dark cycles. 2, 128
MC	Monte–Carlo Methods. 4, 126
PAR	photosynthetically active radiation. 106, 125
PBR	Photobioreactors. v, 1, 125
PCE	photoconversion efficiency. 99
PSU	photosynthetic unit. 106
PUR	photosynthetically usable radiation. 106
PVD	ParaView Data. 160
PVTI	Parallel vtkImageData. 160
RK	Runge–Kutta. 46
RT	radiative transport. 3, 126
RTE	radiative transport equation. v, 3, 125
RTLBM	Radiative Transport Lattice Boltzmann Methods. 3, 125
STL	Stereolithography. 119, 167
TMP	template metaprogramming. 172
VTI	Serial vtkImageData. 159
VTK	Visualization Toolkit. 159
VTM	MultiBlock VTK. 163
VTU	Serial vtkUnstructuredGrid. 162
XML	Extensible Markup Language. 159

Acronyms

Notation **Description**

A. Chapman–Enskog Analysis of the RTLBM in Volume

The following is an extract of the publication Mink et al. [125] and repeated for the sake of completeness. The Chapman–Enskog expansion is a vehicle to derive macroscopic equations from collide-and-stream equations at the mesoscopic scale. This is a crucial part of the LBM development, since it is not guaranteed or even clear whether the computations on mesoscopic scale lead to suitable solutions of macroscopic target equations or not [195]. By showing that the proposed collide-and-stream equation of the macroscopic RTLBM presented in Section 4.2.1 solves the target diffusion equation with additional sink term (2.10), analytical evidence of the present approach is provided. Recall, that the collide-and-stream equation is given by

$$f_i(t + \Delta t, \mathbf{x} + \mathbf{v}_i \Delta t) = f_i(t, \mathbf{x}) - \frac{\Delta t}{\tau} (f_i - f_i^{eq})(t, \mathbf{x}) - \Delta t^2 \eta f_i(t, \mathbf{x}),$$

for $\eta = \frac{3\mu_a(\mu_a + \mu_s)}{8}$ and discretization parameter Δt .

Firstly, a Taylor series expansion up to second order of the left hand side reads

$$f_i(t + \Delta t, \mathbf{x} + \mathbf{v}_i \Delta t) = f_i(t, \mathbf{x}) + \Delta t (\partial_t + \mathbf{v}_i \cdot \nabla) f_i(t, \mathbf{x}) + \frac{\Delta t^2}{2} (\partial_t + \mathbf{v}_i \cdot \nabla)^2 f_i(t, \mathbf{x}).$$

Substituting this expression into the collide-and-stream equation, it holds

$$(\partial_t + \mathbf{v}_i \cdot \nabla) f_i + \frac{\Delta t}{2} (\partial_t + \mathbf{v}_i \cdot \nabla)^2 f_i = \frac{1}{\tau} (f_i - f_i^{eq}) - \Delta t \eta f_i, \quad (\text{A.1})$$

for $\hat{\eta} = \Delta t \eta$. By introducing a small, positive scaling parameter $\varepsilon^2 = \Delta t$, the time and space derivation can be rewritten according to the diffusive limit [130, 160]

$$\partial_t \rightsquigarrow \varepsilon^2 \partial_t, \quad \nabla \rightsquigarrow \varepsilon \nabla. \quad (\text{A.2})$$

A. Chapman–Enskog Analysis of the RTLBM in Volume

Then, the particle density function f_i is expanded by

$$f_i = f_i^{(0)} + \varepsilon f_i^{(1)} + \varepsilon^2 f_i^{(2)} + \dots . \quad (\text{A.3})$$

Deploying the scaling (A.2) and the expansion (A.3), the reformulated equation (A.1) can be rewritten in the consecutive orders of parameter ε as

$$\varepsilon^0 : f_i^{(0)} = f_i^{eq} , \quad (\text{A.4})$$

$$\varepsilon^1 : \mathbf{v}_i \cdot \nabla f_i^{(0)} = -\frac{1}{\tau} f_i^{(1)} , \quad (\text{A.5})$$

$$\varepsilon^2 : \partial_t f_i^{(0)} + \mathbf{v}_i \cdot \nabla f_i^{(1)} = -\frac{1}{\tau} f_i^{(2)} - \eta f_i^{(0)} . \quad (\text{A.6})$$

Inserting (A.4) and (A.5) in (A.6), it holds

$$\partial_t f_i^{eq} - \tau |\mathbf{v}_i|^2 |\nabla|^2 f_i^{eq} = -\frac{1}{\tau} f_i^{(2)} - \eta f_i^{eq} .$$

By two considerations, namely that the macroscopic density (irradiance) Φ can be recovered through the 0^{th} moment and due to the $D3Q7$ grid it yields $|\mathbf{v}_i|^2 = 1$, for $i = 1, \dots, 6$, the above equation can be rewritten

$$\partial_t \Phi - D \nabla^2 \Phi = -\eta \Phi ,$$

for relaxation time $\tau = D$, as defined in (2.9).

Considering the radiative diffusion which is reached immediately, the time evolution is obviously not relevant. As a result the partial time derivative on the left hand side vanishes and the macroscopic target diffusion equation with additional sink term (2.12) is recovered. Also the mesoscopic sink parameter η have been linked to corresponding macroscopic sink term μ_a and μ_s . This Chapman–Enskog expansion points out, that the proposed RTLBM solves the macroscopic target equation.

B. Chapman–Enskog Analysis of the RTLBM on Boundaries

The following is an extract of the work under review Mink et al. [123] and repeated for the sake of completeness. Based on the Chapman–Enskog expansion, the mesoscopic boundary formulation is related to the target Robin equation. This approach ensures that the simulation parameter on mesoscopic level are properly linked to the macroscopic parameters in the Robin equation. Recall, that the collide-and-stream equation in Section 4.2.1 for the highly scattering volume is given by

$$f_i(t + \Delta t, \mathbf{x} + \mathbf{s}_i \Delta t) = f_i(t, \mathbf{x}) - \frac{\Delta t}{\tau} (f_i - f_i^{eq})(t, \mathbf{x}) - \Delta t^2 \eta f_i(t, \mathbf{x}),$$

for $\eta = \frac{3\mu_a(\mu_a + \mu_s)}{8}$ and discretization parameter Δt . Firstly, a Taylor series expansion up to second order in Δt of the left hand side reads

$$f_i(t + \Delta t, \mathbf{x} + \mathbf{s}_i \Delta t) = f_i(t, \mathbf{x}) + \Delta t (\partial_t + \mathbf{s}_i \cdot \nabla) f_i(t, \mathbf{x}) + \frac{\Delta t^2}{2} (\partial_t + \mathbf{s}_i \cdot \nabla)^2 f_i(t, \mathbf{x}) \quad .$$

Substituting this expression into the collide-and-stream equation, it holds

$$(\partial_t + \mathbf{s}_i \cdot \nabla) f_i + \frac{\Delta t}{2} (\partial_t + \mathbf{s}_i \cdot \nabla)^2 f_i = \frac{1}{\tau} (f_i - f_i^{eq}) - \Delta t \eta f_i. \quad (\text{B.1})$$

By introducing a small, positive scaling parameter $\varepsilon^2 = \Delta t$, the time and space derivation can be rewritten

$$\partial_t \rightsquigarrow \varepsilon^2 \partial_t, \quad \nabla \rightsquigarrow \varepsilon \nabla. \quad (\text{B.2})$$

In addition the particle density function f_i is expanded by

$$f_i = f_i^{(0)} + \varepsilon f_i^{(1)} + \varepsilon^2 f_i^{(2)} + \dots. \quad (\text{B.3})$$

Using the scaling (B.2) and the expansion (B.3), equation (B.1) can be rewritten in the

B. Chapman–Enskog Analysis of the RTLBM on Boundaries

consecutive orders of parameter ε as

$$\varepsilon^0 : f_i^{(0)} = f_i^{eq}, \quad (\text{B.4})$$

$$\varepsilon^1 : \mathbf{s}_i \cdot \nabla f_i^{(0)} = -\frac{1}{\tau} f_i^{(1)}, \quad (\text{B.5})$$

$$\varepsilon^2 : \partial_t f_i^{(0)} + \mathbf{s}_i \cdot \nabla f_i^{(1)} = -\frac{1}{\tau} f_i^{(2)} - \eta f_i^{(0)}. \quad (\text{B.6})$$

From (B.3) and (B.5), it follows

$$\mathbf{s}_i \cdot \nabla f_i^{eq} = -\frac{1}{\tau \varepsilon} (f_i - f_i^{eq}),$$

or equivalently

$$w_i \mathbf{s}_i \cdot \nabla \Phi = -\frac{1}{\tau \varepsilon} (f_i - w_i \Phi), \quad (\text{B.7})$$

according to the definition of the equilibrium function $f_i^{eq} = w_i \Phi$.

To find a closure for the system (B.4), (B.5) and (B.6), the discrete version of the Robin boundary condition (4.14)

$$w_i \mathbf{s}_i \cdot \nabla \Phi = -\frac{w_i}{2C_{RD}} \Phi$$

is substituted by (B.7) leading to

$$w_i \Phi = \frac{f_i}{1 + \frac{\tau \varepsilon}{2C_{RD}}}.$$

For diffusion coefficient D in meter and diffusive scaling $\Delta t \propto \Delta x^2$. Further, the closure assumes that the incoming non-equilibrium parts equal the outgoing ones in the opposite direction [76, 95]. This relation reads

$$f_{\bar{i}} - f_{\bar{i}}^{eq} = -(f_i - f_i^{eq})$$

and is rewritten to

$$f_{\bar{i}} = \left(\frac{2}{1 + \frac{\varepsilon}{2C_{RD}}} - 1 \right) f_i. \quad (\text{B.8})$$

Note, in RTLBM it is common to set τ equals one [125, 27]. The definition of f_i^{eq} and the underlying stencil $D3Q7$ yields in $f_i^{eq} = f_j^{eq}$ for all $i, j \neq 0$. The derived equation can be interpreted as the discrete version of the boundary equation (4.10). Equation (B.8) is a general partial bounce-back formula and is derived through the performed Chapman–Enskog expansion.

C. Parallel Efficient Data Output in OpenLB

In the field of high performance computing the overall simulation domain of LBM contains typically more than 1×10^{12} grid points. The demand is met by strategies of sharing the work load and distributing the tasks among thousands of threads. As a matter of fact, the computed data is also distributed on the compute cluster and the process of data writing should adopt this paradigm of distributed data. If not, the data is written sequentially, which means one thread will write the data and the others have to wait. This increases the costly communication of data to this specific thread, but potentially more significant: All threads except of one are waiting till the data is written.

A possible workaround is to write data rarely and hence keep the sequential part small. However, this is not feasible for neither the development of simulations methods nor for the post-processing of simulation data for visualization purpose. To avoid this technical drawback every thread writes its data, which is a perfectly parallel task. By this approach the communication between the threads is kept at a minimum and ideally, the writing itself takes the same time for all threads. Only the master thread has to create an additional file that reference all files written by the threads.

The following introduces to the file format used by OpenLB and the parallel writing concept. The author of the present PhD thesis started working on this topic as a working student about the end of 2014 and then maintained and implemented the zLib compression in the following years.

C.1. VTK-Data Format

The Visualization Toolkit (VTK) provides a number of popular file format definition that are based on Extensible Markup Language (XML). Most relevant for the regular grid characteristics of LBM are the structured data formats named Serial vtkImageData (VTI). Such a VTI file starts with details to the extension, placement and spacing of the structured data. The latter depicts the distance between the point data on the regular grid

C. Parallel Efficient Data Output in OpenLB

and corresponds to the Δx in the OpenLB implementation of LBM. Next, the raw data is provided either as ASCII code, binary (base64) or zLib compressed. An example VTI file is given in Listing C.1. Its parallel version Parallel vtkImageData (PVTI) is designed to be a partition of the sequential VTI and suits parallel execution on several processors. However, the PVTI format requires that the assembled piece must be a cuboid. In general, OpenLB violates this assumption, by shrinking individual blocks to their necessary size and removing empty blocks. This requires a more general format the ParaView Data (PVD) that reference loosely any kind of data that can be loaded in ParaView the single VTI without further assumptions as in the case of PVTI.

C.2. Data Size

When comparing the file size of a CFD simulation with respect to the three raw data formats above (ASCII, binary, zLib) a typical simulation of the velocity and pressure of the fluid field is considered. In this scenario every grid point is associated to 3+1 floating-point data types that are stored in the structured data format. Unlike unstructured data sets, for regular grids it is sufficient to store the extension, the grid spacing and the raw data. There is no need to store the raw data along with its actual position, which in total results in more complex structures and bigger file sizes. Figure C.1 shows the data size for ASCII, binary and zLib VTK data for a simulation made up of 60×10^6 grid points. In the beginning the simulation is initialized with zero velocity and constant pressure and the compression of the zLib reduces the size to its minimum. During the simulation the flow pattern develops and the flow field together with the pressure takes many different values that cannot be compressed as efficient as the many zeros in the beginning. Yielding in a file size of 1000 MB. The same trend of an increase in file size as the flow field develops over time is observed for the ASCII format, however starting at bigger file size and ending at 2500 MB. The data stored in base64 binary format remains constant since it writes every floating-point in a binary representation. However, compared to the ASCII format it requires 60% of the storage with its 1600 MB.

To summarize it can be said that the binary type compared to ASCII type requires roughly half of the memory. The compression works excellent for monotone data of equal value and for general floating-point data it requires about a third compared to the ASCII type.

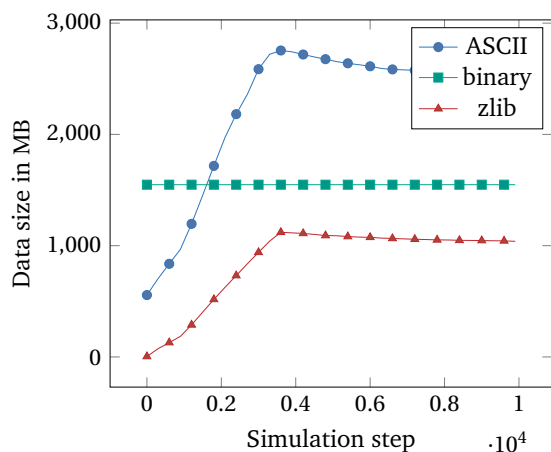


Figure C.1.: A comparison of the VTK data size during a simulation of 3D velocity field and pressure. The dynamic is due to the development of the flow field starting with a constant initialized field of size 60×10^6 .

C.3. Sequential Data Output

The sequential data format in OpenLB is the structured data format VTI. In contrast to unstructured data, there are no coordinates for the data values, but the extension and spacing of the uniform grid. This reduces the data size essentially and is a native choice for LBM in general. A minimal example for a structured data set is provided in Listing C.1 and is described in the following three steps:

1. The file begins with a line that describes the VTK file type and version.
2. The second line defines the extent, origin and spacing of the structured set.
3. Next, the plain data is stored with associated attributes of type, name, format and optionally the number of components. There might be several elements of *DataArray*, one for the velocity and a second for pressure.

A typically VTI data file of CFD application is given in Listing C.2. It is seen, that the velocity and pressure data are separate *DataArrays*, allowing different data types and number of components, that are compressed and hence require less memory. Sequential simulations that are based on a decomposed domain into several block write as many pieces as blocks.

Listing C.1: Minimal example of a structured data set.

```
<VTKFile type="ImageData" version="1.0">
<ImageData WholeExtent="0 1 0 1 0 1" Origin="0 0 0" Spacing="1 1 1
">
```

C. Parallel Efficient Data Output in OpenLB

```
<Piece Extent="0 1 0 1 0 1">
<PointData>
<DataArray type="Int32" Name="color" format="ascii">
0 0 0 0 0 0 0 0
</DataArray>
</PointData>
</Piece>
</ImageData>
</VTKFile>
```

Listing C.2: Structured data set.

```
<VTKFile type="ImageData" version="0.1" byte_order="LittleEndian"
compressor="vtkZLibDataCompressor">
<ImageData WholeExtent="-1 19 -1 13 -1 14" Origin="120 36 51"
Spacing="1 1 1">
<Piece Extent="-1 19 -1 13 -1 14">
<PointData>
<DataArray type="Float32" Name="physVelocity" NumberOfComponents="
3" format="binary" encoding="base64">
AQAAAEDsAABA7AAAtlYAAA==eJzsuXlUT...
</DataArray>
<DataArray type="Float32" Name="physPressure" NumberOfComponents="
1" format="binary" encoding="base64">
AQAAAAMBOAADATgAAESMAAA==eJztm3dX...
</DataArray>
</PointData>
</Piece>
</ImageData>
</VTKFile>
```

OpenLB writes the Lagrange particle simulations data to unstructured data sets of the type Serial `vtkUnstructuredGrid` (VTU). Every position and attributes e. g. mass and velocity are written to the file.

C.4. Parallel Data Output

The parallelization strategy for data structures in OpenLB is based on a domain partition into blocks. Every block consists of several cells and all blocks together represent the entire simulation domain. An exemplary simulation geometry in its block representation is shown in Figure C.2. Note that the blocks are only as big as necessary and not necessarily of equal size. By this blockification the simulation data is divided into small blocks which are further distributed to the threads. Here, *thread one* might simulated blockID of 0 and 1, and *thread two* might simulate blockID of 3 and 4. Obviously, this process is relevant for a much larger number of threads and blocks and total automatized

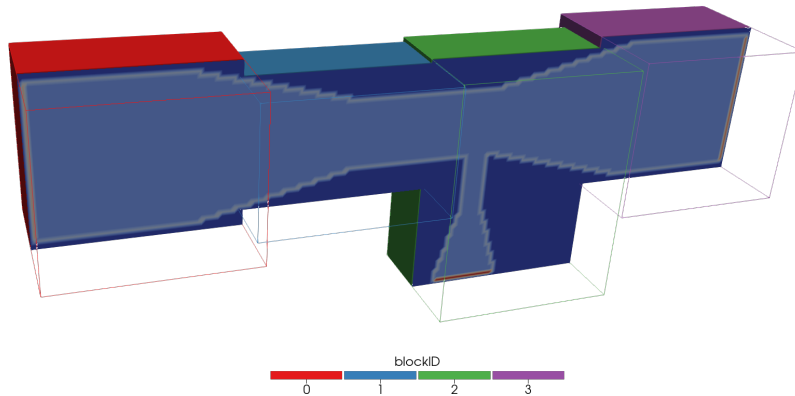


Figure C.2.: Cross section with colored block identification number. The domain is divided into four blocks of individual size. The more blocks the better the masking of the simulation domain.

in OpenLB. Note, that the simulation size is only limited by the available memory of all threads together and not by the memory of an individual thread. This brief sketch of the parallelization strategy is important to understand the parallel data output.

In a multi thread simulation every thread simulated blocks and also writes the data of those blocks. This results in a parallel writing to individual VTI files. In the above illustration thread one writes a VTI file for block 0 and a VTI file for block 1, analogously thread two writes block 2 and 3. Fortunately, the OpenLB parallel data structure can be matched closely with the VTK-Data format definition. There remains to create a file that references to all VTI files in order to bunch and collect the data. This is achieved by a MultiBlock VTK (VTM) file that references the simulation data of a single time step, see Listing C.3. The many VTM files for the individual simulation steps are further bunched in a PVD file, see Listing C.4. This format is the most general collection format in VTK and acts in OpenLB as the reference file for the simulation data.

Listing C.3: Multiblock data set – VTM.

```
<VTKFile type="vtkMultiBlockDataSet" version="1.0">
<vtkMultiBlockDataSet>
<Block index="0" >
<DataSet index="0" file="venturi3d_iT0000100iC00000.vti"/>
</Block>
```

C. Parallel Efficient Data Output in OpenLB

```
<Block index="1" >
<DataSet index= "0" file="venturi3d_iT0000100iC00001.vti"/>
</Block>
<Block index="2" >
<DataSet index= "0" file="venturi3d_iT0000100iC00002.vti"/>
</Block>
<Block index="3" >
<DataSet index= "0" file="venturi3d_iT0000100iC00003.vti"/>
</Block>
</vtkMultiBlockDataSet>
</VTKFile>
```

At the end the data writing routine is closely matched by the VTK format. The simulated data on the grid is stored to VTI files in parallel and multiple VTI files are referenced in VTM and PVD, in such a way that the files are assembled. Compared to sequential writing, this approach allows a parallel handling and execution of writing simulation data to the memory. This is crucial for simulations that are required to write frequently data for debugging purpose or video rendering. To minimize the file size up to a factor of 3, the data is stored either as binary or zLib compressed.

Listing C.4: Collection of data set – PVD.

```
<VTKFile type="Collection" version="1.0">
<Collection>
<DataSet timestep="0" part="" file="venturi3d_iT0000.vtm"/>
<DataSet timestep="100" part="" file="venturi3d_iT0100.vtm"/>
<DataSet timestep="200" part="" file="venturi3d_iT0200.vtm"/>
<DataSet timestep="300" part="" file="venturi3d_iT0300.vtm"/>
<DataSet timestep="400" part="" file="venturi3d_iT0400.vtm"/>
</Collection>
</VTKFile>
```

D. Functors in OpenLB

The general functor concept is motivated by the need to process the data provided in OpenLB. Might it be the goal to compute shear stress or drag data by the help of populations f_i or might it be the design of the computational grid and boundary conditions, all these tasks are heavily based on the omnipresent functor concept.

Knowing the population on the computational grid, the velocity can be computed easily through moments. This changes if additional information are needed, such as conversion factors to compute the physical velocity or geometry data for wall shear stress or drag coefficients. In OpenLB those tasks are defined in classes, that typically have attributes that provide conversion factors and geometry information. Then, the *operator()* executes the computation of e. g. velocity and others. The following section present show-cases for the arithmetic operations, modularity and geometry creation by functors. A short sketch of the implementation is shown in the end.

The author implemented and designed the very first version of the functors and its arithmetic in OpenLB version 0.8 back in 2013 in collaboration with Lukas Baron and Mathias J. Krause. Over the years the concept has been improved and also extended to `std::shared_ptr` for the memory management.

D.1. Calculations with Functors

By introducing arithmetic operations, the functors behave like general functions in mathematics and can be added, subtracted and many more. For example, the deviation of a simulated velocity field \mathbf{u} to a reference solution \mathbf{u}^* can be expressed as

$$\frac{\|\mathbf{u} - \mathbf{u}^*\|}{\|\mathbf{u}^*\|},$$

where the norm evaluates to $\|(\cdot)\| = n^{-1} \sum_{v=1}^n |(\cdot)|(\mathbf{x}_v)$ for n simulation grid point \mathbf{x}_v . The according implementation is shown in Listing D.1.

Listing D.1: Step by step computation of the relative error.

D. Functors in OpenLB

```
// typedef double T;
// typedef D3Q19<> DESCRIPTOR;
SuperLatticePhysVelocity3D<T,DESCRIPTOR> u(lattice,converter);
SuperLatticePhysVelocity3D<T,DESCRIPTOR> ustar(lattice,converter);
// |u-u^star|
SuperL2Norm3D<T> absoluteError( u - ustar, superGeometry, 1 );
// |u^star|
SuperL2Norm3D<T> norm( ustar, superGeometry, 1 );
// evaluate numerator and denominator
absoluteError( numerator, input );
norm( denominator, input );
// print relative error to terminal
std::cout << "rel error: " << numerator[0]/denominator[0] << std::
endl;
```

D.2. Application to Data Processing

Knowledge about maximum values of data fields such as velocity are important for CFD simulation. Often the diverging of simulation start in regions of extreme velocities and can be easily observed by functors. The present example computes first the velocity field for the entire domain with the `SuperLatticeVelocity3D` functor. Then the maximum x, y and z component are obtained by the `SuperMax3D` functor and available in variable `maxVelocity`, see Listing D.2.

Listing D.2: Compute maximum velocity components in flow field

```
// typedef double T;
// typedef D3Q19<> DESCRIPTOR;
SuperLatticeVelocity3D<T,DESCRIPTOR> u(superLattice);
SuperMax3D<T> maxVelocity( u, superGeometry, 1 );
int input[0];
T maxVelocity[3];
maxVelocityFunctor(maxVelocity, input);
std::cout << "maximum velocity components in domain" << std::endl;
std::cout << maxVelocity[0] << "; "
          << maxVelocity[1] << "; "
          << maxVelocity[2] << std::endl;
```

In case the local maximum velocity is desired, there is added an additional functor `SuperEuklidNorm3D` that computes the magnitude of the velocities, see Listing D.3. Then, the maximum value is determined for this functor and demonstrated the modularity of the general functor concept.

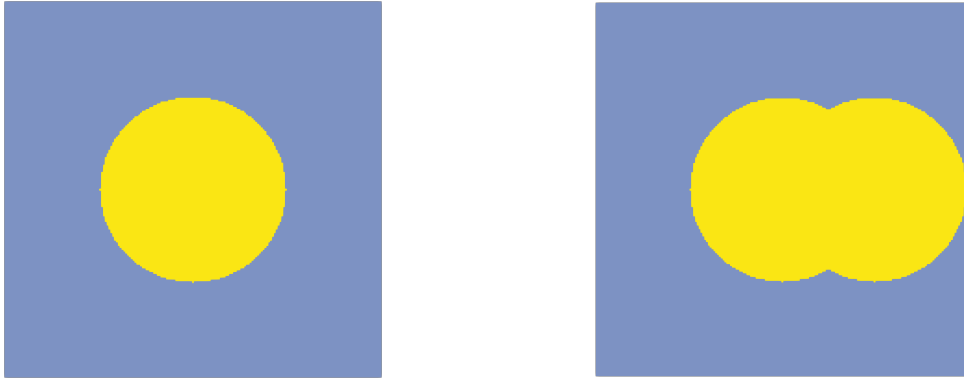


Figure D.1.: Two show-cases of arithmetic operations of indicator functors for geometry creation.

Listing D.3: Compute maximum local velocity of flow field

```
// typedef double T;
// typedef D3Q19<> DESCRIPTOR;
SuperLatticeVelocity3D<T,DESCRIPTOR> u(superLattice);
SuperEuklidNorm3D<T,DESCRIPTOR> normVel(u);
SuperMax3D<T> maxVelocity( normVel, superGeometry, 1 );
int input[0];
T maxVelocity[1];
maxVelocityFunctor(maxVelocity, input);
std::cout << "maximum velocity in domain" << std::endl;
std::cout << maxVelocity[0] << std::endl;
```

D.3. Facilitate Geometry Creation

OpenLB provides indicator functors that define geometric primitives, e. g. circles, cuboids, cones, spheres and many more. Simulation domains can be build out of this geometric primitives and the arithmetic allows to construct more complex geometries by means of unions and intersections of the indicators. An example of a rectangular simulation domain with circular obstacles is shown in Listing D.4 and illustrated in Figure D.1. For such basic simulation domains, the shipped indicator functors allows creating the simulation geometry without any external definition, for instance Stereolithography (STL) files.

Listing D.4: Geometric primitives as functors

```
// rectangle centered in (0,0) of given extent
IndicatorCuboid2D<T> rectangle(xExtent,yExtent,Vector<T,2>{0,0});
// circle placed in (0,0)
IndicatorCircle2D<T> circle(Vector<T,2>{0,0}, radius);
```

D. Functors in OpenLB

```
// circle placed in (0.5,0)
IndicatorCircle2D<T> circleShifted(Vector<T,2>{0.5,0}, radius);
// informally arithmetic operation -- std::shared_ptr are missing
IndicatorIdentity2D<T> ident1(rectangle-circle);
IndicatorIdentity2D<T> ident2(rectangle-(circle+circleShifted));
```

The typical geometry creation of a cylinder with an inner installation is shown in Listing D.5. This is productive code from the shown example of the sponge PBR in Section 7.6. Here, the Weaire–Phelan sponge structure is defined in an external STL file and loaded by the `STLReader`, that is a functor object itself. Since the STL defines only a periodic part, the indicator is shifted accordingly to obtain a large sponge structure in the cylinder. The translated parts are then added to one piece by arithmetic operations.

Listing D.5: Loading and assembling of a periodic sponge element defined by a STL file.

```
auto spongePart = std::make_shared<STLReader<T>>
    ("./periodicElement.stl", voxelSizeSI, convFactorSTL, 1);
auto domain = std::make_shared<IndicatorCylinder3D<T>>
    (center1, center2, channelLength);
auto stlTranslate1 = std::make_shared<IndicatorTranslate3D<T>>
    (std::array<T,3>{xShift,yShift, zShift}, *spongePart);
auto stlTranslate2 = std::make_shared<IndicatorTranslate3D<T>>
    (std::array<T,3>{xShift,yShift, zShift*2}, *spongePart);
auto stlTranslate3 = std::make_shared<IndicatorTranslate3D<T>>
    (std::array<T,3>{xShift,yShift, zShift*3}, *spongePart);
SuperGeometry3D<T> sGeometry(cuboidGeometry, loadBalancer, 2);
sGeometry.rename(0,2,*domain);
sGeometry.rename(2,1,1,1,1);
sGeometry.rename(1,3,stlTranslate1+stlTranslate2+stlTranslate3);
```

D.4. Functor Design

Here, the technical details of the arithmetic operations and how they unfold are presented. An overview of the available functor categories is also given.

D.4.1. Expression templates

For general functors $F1$ and $F2$ the expression $F1 + F2$ results in a new object, called `PlusFunctor`, that implements the addition by evaluating both functors and adding its values. The operations minus, multiplication and division have the same behaviour. This results in a hierarchy of classes for more complex expressions as $F1 + F2 + F3 + F4$ that only define the evaluation of the data. Technically, the general c++ operator precedence applies,

saying first $/$ and \star , then $+$ and $-$ and by equality from left to the right. This is exactly what we are used to from mathematics. Now, for functors $F1$, $F2$ and $F3$ the expression $F1 - F2/F3$ is capsuled into $F1 - (F2/F3)$ are class-wise `MinusFunctor(F1,DivisionFunctor(F2,F3))`. The memory management of the temporal arithmetic objects is based on `std::shared_ptr` and hidden from the user.

D.4.2. Class hierarchy

Functors are applications that operate either on the lattice \mathbb{N}^3 or more generally on \mathbb{R}^3 and might take values in \mathbb{R}^3 for instance velocity.

$$\text{Functor: } \Omega \rightarrow \mathbb{R}^d, \quad d \in \mathbb{N}$$

This very general concept of an application that associates data from Ω to \mathbb{R}^d is represented by the class `GenericF` that defines the data types and dimension of the spaces, see Listing D.6.

Listing D.6: Implementation of the base class of all functors.

```

/** Please take care about the data types and dimensions
 *   F: S^m -> T^n (S=source, T=target)
 */
template <typename T, typename S>
class GenericF {
protected:
    GenericF(int targetDim, int sourceDim);
private:
    int _n;
    int _m;
    // ...
public:
    // memory management
    std::shared_ptr< GenericF<T,S> > _ptrCalcC;
    bool operator() (T output[], S input);
    // ...
};

```

Depending on the data types of the domain and image of the functor, OpenLB implements a linear class hierarchy that is classified into the following categories.

$\mathbb{R}^3 \rightarrow \mathbb{R}^d$ `AnalyticalF3D`
 $\mathbb{R}^3 \rightarrow \{0,1\}$ `IndicatorF3D`
 $\mathbb{R}^3 \rightarrow [0,1]$ `SmoothIndicatorF3D`

D. Functors in OpenLB

$\mathbb{N}^3 \rightarrow \mathbb{R}^d$ LatticeF3D

LatticeF3D \rightarrow AnalyticalF3D Interpolation

AnalyticalF3D \rightarrow LatticeF3D Projection

Any implementation of an `IndicatorF3D`, for instance `IndicatorCuboid3D`, inherits from its base class. Functors that share the same base class can be added, subtracted and more. Of particular interest are the interpolation functors, that allow to access data in between grid nodes through interpolation. This is useful for general post-processing routines. Its counterpart are the projection functors that restrict functors defined on a continuous domain to the discrete grid nodes.

E. Radiative Transport LBM Implementation in OpenLB

The presented features are fully available to the public with the release of version 1.3 of OpenLB¹. The classes and functions discussed in this section are fully tested by the unit-test framework (non-public) in OpenLB, to facilitate the development and guaranty consistency during the substantial work on the OpenLB kernel. Note, that the flag/feature *OPENBLAS* must be added to the config.mk file. Otherwise, OpenBLAS is not available inside OpenLB.

List of publications and the associated implementation of benchmark cases:

Mink et al. (125) is based on simulation application *apps/albert/pbr3d*.

Mink et al. (123) is based on simulation application *apps/albert/robinBC*.

Mink et al. (121) is based on simulation application *apps/albert/ansioSB*.

The git commit hash in the GITLAB developer repository *e08084ff76fa7ebd* provides the above simulation applications in its most recent way and provides comprehensive insights in the implementation of the publications.

E.1. Conversion Factors and Refraction Parameter C_R

Conversion from physical to lattice units for RT specific parameters is implemented in class `RadiativeUnitConverter`, see Listing E.1. Once the object is created, the spacial discretization is retrieved by the method `getConversionFactorLength()`, the absorption in lattice dimensions through `getLatticeAbsorption()` and many more. See the online DoxyGen documentation <https://www.openlb.net/DoxyGen/html/index.html>.

Listing E.1: Constructor and documentation of `RadiativeUnitConverter`.

```
| template <typename T, template<typename U> class DESCRIPTOR >
```

¹Download link <https://www.openlb.net/download/>

E. Radiative Transport LBM Implementation in OpenLB

```
class RadiativeUnitConverter : public
    UnitConverterFromResolutionAndRelaxationTime<T, DESCRIPTOR> {
public:
    /** Documentation of constructor:
     *  \param resolution    is number of voxel per 1 meter
     *  \param latticeRelaxationTime    see class
     *  \param physAbsorption    physical absorption in 1/meter
     *  \param physScattering    physical scattering in 1/meter
     */
    constexpr RadiativeUnitConverter(
        int resolution,
        T latticeRelaxationTime,
        T physAbsorption,
        T physScattering,
        T anisotropyFactor=0,
        T charPhysLength=1,
        T refractiveMedia=1,
        T refractiveAmbient=1 )
}
```

Additionally, the computation of refraction parameter (4.13) and the partial bounce-back parameter (4.16) is implemented as free functions in file `src/core/radiativeUnitConverter.cpp`.

E.2. Collision Kernels and Integration Stencils

List of RTLBM collision models with OpenLB specific nomenclature:

macroscopic RTLBM PoissonDynamics in `src/dynamics/dynamics.h`

P1-RTLBM P1Dynamics in `src/dynamics/dynamics.h`

mesoscopic RTLBM RTLBMdynamicsMcHardyRK in `src/dynamics/rtlbmDynamics.h`

The Lebedev–Laikov integration stencils $D3Q7$, $D3Q15$ and $D3Q27$ are implemented in `src/dynamics/rtlbmDescriptors.h` and available in the namespace `descriptors` through `D3Q27DescriptorLebedev`. Note, that the introduction of compile time constant descriptors in OpenLB version 1.3 and later requires all stencil properties to be available at compile-time. The Lebedev–Laikov stencils store additionally the c_i that is the distance of discrete direction s_i , for instance diagonal s_i with $c_i = \sqrt{3}$. Unfortunately, function `std::sqrt` is according to the standard not computed at compile-time. As a workaround, the decimal numbers are hard-coded and might be replaced by template metaprogramming (TMP) or a `constexpr` function for c++-14 and later.

E.3. Discrete Phase Function

The routine for the discretization of the phase function accordingly to [87], called `computeAnisotropyMatrix`, is implemented in `src/utilities/anisoDiscr.h`. The LBM stencil is provided as a template argument and the least square problem is solved by LAPACK with function `dgels`. This iterative normalization scheme has to be computed only once for every simulation and is not time critical. The implementation in OpenLB was adopted from a Matlab script originally written by Christopher McHardy.

A second implementation of the discrete phase function, according to Kim and Lee [98], called `computeAnisotropyMatrixKimAndLee`, is implemented in `src/utilities/anisoDiscr.h`. Tests for the conservation of energy and anisotropy factor are implemented in the same file.

E.4. Boundary Conditions

The source boundary for diffuse and collimated incident radiance are implemented in the file `src/boundary/rtlbmBoundaryDynamics.h` with associated creator functions in `src/boundary/rtlbmBoundary.h`. The Fresnel boundary is implemented in the file `src/dynamics/dynamics.h` and class `PartialBounceBack`.

F. Factory Functions for XML-based Geometry Creation in OpenLB

OpenLB simulations are a c++ programs that set up the geometry, characteristic parameters, the collide-and-stream equation and many more. Changing one of these steps requires the modification of at least one c++ file, followed by a compilation of the program. To avoid editing source code files and achieve a robust encapsulation it is added an XML file that stores, independently to the c++ program, the desired parameters. During the runtime the program load the XML file and access the data. For example, simple variables such as spacial discretization or Reynolds number can be stored and loaded by this strategy. Even classes might be constructed by the variables loaded from the XML file. Most common there is the `createConverter` or `createGeometry` function that create general objects from given data. However, it is also possible to provide the definition of geometric primitives on which the simulation domain is based on.

The following provides an example of the definition of geometric primitives in XML files for the `createGeometry` function. Consider a geometry that is based on geometric primitives such as cylinders and cones, such as in Figure C.2. Then, the associated definition in an XML file format is a union of cylinders and cones as provided in Listing F.1.

Listing F.1: Definition of a simulation domain consisting of cylinders and cones.

```
<IndicatorUnion3D>
<IndicatorCylinder3D center1="5 50 50" center2="40 50 50" radius="20"/>
<IndicatorCone3D center1="40 50 50" center2="80 50 50" radius1="20"
  radius2="10"/>
<IndicatorCylinder3D center1="80 50 50" center2="120 50 50" radius="10"/>
<IndicatorCone3D center1="120 50 50" center2="160 50 50" radius1="10"
  radius2="20"/>
<IndicatorCylinder3D center1="160 50 50" center2="195 50 50" radius="20"/
>
<IndicatorCylinder3D center1="115 50 50" center2="115 25 50" radius="4"/>
<IndicatorCone3D center1="115 25 50" center2="115 5 50" radius1="4"
  radius2="10"/>
</IndicatorUnion3D>
```

Now, the modification of the inlet size or other dimensions is achieved by modifying the

F. Factory Functions for XML-based Geometry Creation in OpenLB

XML based primitive definitions. The absence of editing c++ files reduces the development time, by reduction of compilation process. Another aspect is the encapsulation of geometry and simulation information. For small simulations this might not be relevant, however the simulation domain of the Algfine reactor in Section 7.5 with several thousands of LED spots, is very demanding and could be scripted. Hence, the XML is a reasonable format that is also supported by many other tools, which is important when scripting the geometry definition. Finally, the separation facilitates the tracing down of errors in the development process, since changes in XML are less error prone than editing c++ files.

Finally, it is concluded that the added complexity of an XML based geometry definition outweighs the benefit of faster and more comprehensive development and simulation design.

F.1. Showcase: Algfine

An application show-case is the Algfine reactor with its 37 cylinders, which each of them is equipped with 72 LED spots. In total there are 37 of such cylinders, see Listing F.2, which together with the 72 LED spots on every cylinder results in an XML file with more than 2500 lines. The definition of a single cylinder with its LED spots is given in Listing F.3.

Listing F.2: The 37 cylinders of the Algfine reactor.

```
<Geometry>
<IndicatorUnion3D>
<IndicatorCylinder3D center1=" 0 -0.13 0 " center2=" 0 -0.13 0.5 " radius=" 0.008 "/>
<IndicatorCylinder3D center1=" -0.03912 -0.12397 0 " center2=" -0.03912 -0.12397 0.5 " radius=" 0.008 "/>
<IndicatorCylinder3D center1=" 0.03912 -0.12397 0 " center2=" 0.03912 -0.12397 0.5 " radius=" 0.008 "/>
<IndicatorCylinder3D center1=" -0.07461 -0.10646 0 " center2=" -0.07461 -0.10646 0.5 " radius=" 0.008 "/>
<IndicatorCylinder3D center1=" 0.07461 -0.10646 0 " center2=" 0.07461 -0.10646 0.5 " radius=" 0.008 "/>
<IndicatorCylinder3D center1=" 0.01954 -0.08785 0 " center2=" 0.01954 -0.08785 0.5 " radius=" 0.008 "/>
<IndicatorCylinder3D center1=" -0.01954 -0.08785 0 " center2=" -0.01954 -0.08785 0.5 " radius=" 0.008 "/>
<IndicatorCylinder3D center1=" -0.10318 -0.07908 0 " center2=" -0.10318 -0.07908 0.5 " radius=" 0.008 "/>
<IndicatorCylinder3D center1=" 0.10318 -0.07908 0 " center2=" 0.10318 -0.07908 0.5 " radius=" 0.008 "/>
<IndicatorCylinder3D center1=" 0.05495 -0.0712 0 " center2=" 0.05495 -0.0712 0.5 " radius=" 0.008 "/>
<IndicatorCylinder3D center1=" -0.05495 -0.0712 0 " center2=" -0.05495 -0.0712 0.5 " radius=" 0.008 "/>
<IndicatorCylinder3D center1=" -0.023 -0.045 0 " center2=" -0.023 -0.045 0.5 " radius=" 0.008 "/>
<IndicatorCylinder3D center1=" 0.023 -0.045 0 " center2=" 0.023 -0.045 0.5 " radius=" 0.008 "/>
<IndicatorCylinder3D center1=" -0.12291 -0.04437 0 " center2=" -0.12291 -0.04437 0.5 " radius=" 0.008 "/>
<IndicatorCylinder3D center1=" 0.12292 -0.04436 0 " center2=" 0.12292 -0.04436 0.5 " radius=" 0.008 "/>
<IndicatorCylinder3D center1=" 0.07999 -0.04126 0 " center2=" 0.07999 -0.04126 0.5 " radius=" 0.008 "/>
<IndicatorCylinder3D center1=" -0.07999 -0.04126 0 " center2=" -0.07999 -0.04126 0.5 " radius=" 0.008 "/>
<IndicatorCylinder3D center1=" -0.12988 -0.00554 0 " center2=" -0.12988 -0.00554 0.5 " radius=" 0.008 "/>
<IndicatorCylinder3D center1=" 0.12988 -0.00554 0 " center2=" 0.12988 -0.00554 0.5 " radius=" 0.008 "/>
<IndicatorCylinder3D center1=" -0.045 -0.005 0 " center2=" -0.045 -0.005 0.5 " radius=" 0.008 "/>
<IndicatorCylinder3D center1=" 0 -0.005 0 " center2=" 0 -0.005 0.5 " radius=" 0.008 "/>
<IndicatorCylinder3D center1=" 0.045 -0.005 0 " center2=" 0.045 -0.005 0.5 " radius=" 0.008 "/>
<IndicatorCylinder3D center1=" -0.08993 -0.00346 0 " center2=" -0.08993 -0.00346 0.5 " radius=" 0.008 "/>
<IndicatorCylinder3D center1=" 0.08993 -0.00346 0 " center2=" 0.08993 -0.00346 0.5 " radius=" 0.008 "/>
<IndicatorCylinder3D center1=" -0.12553 0.03379 0 " center2=" -0.12553 0.03379 0.5 " radius=" 0.008 "/>
<IndicatorCylinder3D center1=" 0.12553 0.0338 0 " center2=" 0.12553 0.0338 0.5 " radius=" 0.008 "/>
<IndicatorCylinder3D center1=" -0.08292 0.0338 0 " center2=" -0.08292 0.0338 0.5 " radius=" 0.008 "/>
<IndicatorCylinder3D center1=" -0.04146 0.035 0 " center2=" -0.04146 0.035 0.5 " radius=" 0.008 "/>
<IndicatorCylinder3D center1=" 0 0.035 0 " center2=" 0 0.035 0.5 " radius=" 0.008 "/>
<IndicatorCylinder3D center1=" 0.04146 0.035 0 " center2=" 0.04146 0.035 0.5 " radius=" 0.008 "/>
<IndicatorCylinder3D center1=" 0.08292 0.035 0 " center2=" 0.08292 0.035 0.5 " radius=" 0.008 "/>
<IndicatorCylinder3D center1=" -0.10954 0.07 0 " center2=" -0.10954 0.07 0.5 " radius=" 0.008 "/>
<IndicatorCylinder3D center1=" -0.065724 0.07 0 " center2=" -0.065724 0.07 0.5 " radius=" 0.008 "/>
<IndicatorCylinder3D center1=" -0.021908 0.07 0 " center2=" -0.021908 0.07 0.5 " radius=" 0.008 "/>
<IndicatorCylinder3D center1=" 0.021908 0.07 0 " center2=" 0.021908 0.07 0.5 " radius=" 0.008 "/>

```

```

<IndicatorCylinder3D center1=" 0.065724 0.07 0 " center2=" 0.065724 0.07 0.5 " radius=" 0.008 "/>
<IndicatorCylinder3D center1=" 0.10954 0.07 0 " center2=" 0.10954 0.07 0.5 " radius=" 0.008 "/>
</IndicatorUnion3D>
</Geometry>

```

For such an extensive geometry, the separation of c++ code and geometry definition is very comfortable. On the one hand, the geometry definition is based on a script, that then writes a general XML file. This routine avoids copy and paste errors, that might happen by such huge amount of data. On the other hand, the check-pointing and encapsulation achieved by clear separation enhances the user experience while developing.

Listing F.3: The 72 LED spots on a single cylinder.

```

<IndicatorUnion3D>
<IndicatorCone3D center1=" 0.01 -0.13 0.013 " center2=" 0 -0.13 0.013 " radius1=".005" radius2=".0"/>
<IndicatorCone3D center1=" -0.005 -0.12134 0.013 " center2=" 0 -0.13 0.013 " radius1=".005" radius2=".0"/>
<IndicatorCone3D center1=" -0.005 -0.13866 0.013 " center2=" 0 -0.13 0.013 " radius1=".005" radius2=".0"/>
<IndicatorCone3D center1=" 0.01 -0.13 0.0345 " center2=" 0 -0.13 0.0345 " radius1=".005" radius2=".0"/>
<IndicatorCone3D center1=" -0.005 -0.12134 0.0335 " center2=" 0 -0.13 0.0335 " radius1=".005" radius2=".0"/>
<IndicatorCone3D center1=" -0.005 -0.13866 0.0325 " center2=" 0 -0.13 0.0325 " radius1=".005" radius2=".0"/>
<IndicatorCone3D center1=" 0.01 -0.13 0.056 " center2=" 0 -0.13 0.056 " radius1=".005" radius2=".0"/>
<IndicatorCone3D center1=" -0.005 -0.12134 0.054 " center2=" 0 -0.13 0.054 " radius1=".005" radius2=".0"/>
<IndicatorCone3D center1=" -0.005 -0.13866 0.052 " center2=" 0 -0.13 0.052 " radius1=".005" radius2=".0"/>
<IndicatorCone3D center1=" 0.01 -0.13 0.0775 " center2=" 0 -0.13 0.0775 " radius1=".005" radius2=".0"/>
<IndicatorCone3D center1=" -0.005 -0.12134 0.0745 " center2=" 0 -0.13 0.0745 " radius1=".005" radius2=".0"/>
<IndicatorCone3D center1=" -0.005 -0.13866 0.0715 " center2=" 0 -0.13 0.0715 " radius1=".005" radius2=".0"/>
<IndicatorCone3D center1=" 0.01 -0.13 0.099 " center2=" 0 -0.13 0.099 " radius1=".005" radius2=".0"/>
<IndicatorCone3D center1=" -0.005 -0.12134 0.095 " center2=" 0 -0.13 0.095 " radius1=".005" radius2=".0"/>
<IndicatorCone3D center1=" -0.005 -0.13866 0.091 " center2=" 0 -0.13 0.091 " radius1=".005" radius2=".0"/>
<IndicatorCone3D center1=" 0.01 -0.13 0.1205 " center2=" 0 -0.13 0.1205 " radius1=".005" radius2=".0"/>
<IndicatorCone3D center1=" -0.005 -0.12134 0.1155 " center2=" 0 -0.13 0.1155 " radius1=".005" radius2=".0"/>
<IndicatorCone3D center1=" -0.005 -0.13866 0.1105 " center2=" 0 -0.13 0.1105 " radius1=".005" radius2=".0"/>
<IndicatorCone3D center1=" 0.01 -0.13 0.142 " center2=" 0 -0.13 0.142 " radius1=".005" radius2=".0"/>
<IndicatorCone3D center1=" -0.005 -0.12134 0.136 " center2=" 0 -0.13 0.136 " radius1=".005" radius2=".0"/>
<IndicatorCone3D center1=" -0.005 -0.13866 0.13 " center2=" 0 -0.13 0.13 " radius1=".005" radius2=".0"/>
<IndicatorCone3D center1=" 0.01 -0.13 0.1635 " center2=" 0 -0.13 0.1635 " radius1=".005" radius2=".0"/>
<IndicatorCone3D center1=" -0.005 -0.12134 0.1565 " center2=" 0 -0.13 0.1565 " radius1=".005" radius2=".0"/>
<IndicatorCone3D center1=" -0.005 -0.13866 0.1495 " center2=" 0 -0.13 0.1495 " radius1=".005" radius2=".0"/>
<IndicatorCone3D center1=" 0.01 -0.13 0.184 " center2=" 0 -0.13 0.184 " radius1=".005" radius2=".0"/>
<IndicatorCone3D center1=" -0.005 -0.12134 0.177 " center2=" 0 -0.13 0.177 " radius1=".005" radius2=".0"/>
<IndicatorCone3D center1=" -0.005 -0.13866 0.17 " center2=" 0 -0.13 0.17 " radius1=".005" radius2=".0"/>
<IndicatorCone3D center1=" 0.01 -0.13 0.204 " center2=" 0 -0.13 0.204 " radius1=".005" radius2=".0"/>
<IndicatorCone3D center1=" -0.005 -0.12134 0.197 " center2=" 0 -0.13 0.197 " radius1=".005" radius2=".0"/>
<IndicatorCone3D center1=" -0.005 -0.13866 0.19 " center2=" 0 -0.13 0.19 " radius1=".005" radius2=".0"/>
<IndicatorCone3D center1=" 0.01 -0.13 0.224 " center2=" 0 -0.13 0.224 " radius1=".005" radius2=".0"/>
<IndicatorCone3D center1=" -0.005 -0.12134 0.217 " center2=" 0 -0.13 0.217 " radius1=".005" radius2=".0"/>
<IndicatorCone3D center1=" -0.005 -0.13866 0.21 " center2=" 0 -0.13 0.21 " radius1=".005" radius2=".0"/>
<IndicatorCone3D center1=" 0.01 -0.13 0.244 " center2=" 0 -0.13 0.244 " radius1=".005" radius2=".0"/>
<IndicatorCone3D center1=" -0.005 -0.12134 0.237 " center2=" 0 -0.13 0.237 " radius1=".005" radius2=".0"/>
<IndicatorCone3D center1=" -0.005 -0.13866 0.23 " center2=" 0 -0.13 0.23 " radius1=".005" radius2=".0"/>
<IndicatorCone3D center1=" 0.01 -0.13 0.264 " center2=" 0 -0.13 0.264 " radius1=".005" radius2=".0"/>
<IndicatorCone3D center1=" -0.005 -0.12134 0.257 " center2=" 0 -0.13 0.257 " radius1=".005" radius2=".0"/>
<IndicatorCone3D center1=" -0.005 -0.13866 0.25 " center2=" 0 -0.13 0.25 " radius1=".005" radius2=".0"/>
<IndicatorCone3D center1=" 0.01 -0.13 0.284 " center2=" 0 -0.13 0.284 " radius1=".005" radius2=".0"/>
<IndicatorCone3D center1=" -0.005 -0.12134 0.277 " center2=" 0 -0.13 0.277 " radius1=".005" radius2=".0"/>
<IndicatorCone3D center1=" -0.005 -0.13866 0.27 " center2=" 0 -0.13 0.27 " radius1=".005" radius2=".0"/>
<IndicatorCone3D center1=" 0.01 -0.13 0.3045 " center2=" 0 -0.13 0.3045 " radius1=".005" radius2=".0"/>
<IndicatorCone3D center1=" -0.005 -0.12134 0.2975 " center2=" 0 -0.13 0.2975 " radius1=".005" radius2=".0"/>
<IndicatorCone3D center1=" -0.005 -0.13866 0.2905 " center2=" 0 -0.13 0.2905 " radius1=".005" radius2=".0"/>
<IndicatorCone3D center1=" 0.01 -0.13 0.325 " center2=" 0 -0.13 0.325 " radius1=".005" radius2=".0"/>
<IndicatorCone3D center1=" -0.005 -0.12134 0.318 " center2=" 0 -0.13 0.318 " radius1=".005" radius2=".0"/>
<IndicatorCone3D center1=" -0.005 -0.13866 0.311 " center2=" 0 -0.13 0.311 " radius1=".005" radius2=".0"/>
<IndicatorCone3D center1=" 0.01 -0.13 0.3455 " center2=" 0 -0.13 0.3455 " radius1=".005" radius2=".0"/>
<IndicatorCone3D center1=" -0.005 -0.12134 0.3385 " center2=" 0 -0.13 0.3385 " radius1=".005" radius2=".0"/>
<IndicatorCone3D center1=" -0.005 -0.13866 0.3315 " center2=" 0 -0.13 0.3315 " radius1=".005" radius2=".0"/>
<IndicatorCone3D center1=" 0.01 -0.13 0.365 " center2=" 0 -0.13 0.365 " radius1=".005" radius2=".0"/>
<IndicatorCone3D center1=" -0.005 -0.12134 0.359 " center2=" 0 -0.13 0.359 " radius1=".005" radius2=".0"/>
<IndicatorCone3D center1=" -0.005 -0.13866 0.353 " center2=" 0 -0.13 0.353 " radius1=".005" radius2=".0"/>
<IndicatorCone3D center1=" 0.01 -0.13 0.3845 " center2=" 0 -0.13 0.3845 " radius1=".005" radius2=".0"/>
<IndicatorCone3D center1=" -0.005 -0.12134 0.3795 " center2=" 0 -0.13 0.3795 " radius1=".005" radius2=".0"/>
<IndicatorCone3D center1=" -0.005 -0.13866 0.3745 " center2=" 0 -0.13 0.3745 " radius1=".005" radius2=".0"/>
<IndicatorCone3D center1=" 0.01 -0.13 0.404 " center2=" 0 -0.13 0.404 " radius1=".005" radius2=".0"/>
<IndicatorCone3D center1=" -0.005 -0.12134 0.4 " center2=" 0 -0.13 0.4 " radius1=".005" radius2=".0"/>
<IndicatorCone3D center1=" -0.005 -0.13866 0.396 " center2=" 0 -0.13 0.396 " radius1=".005" radius2=".0"/>
<IndicatorCone3D center1=" 0.01 -0.13 0.4235 " center2=" 0 -0.13 0.4235 " radius1=".005" radius2=".0"/>
<IndicatorCone3D center1=" -0.005 -0.12134 0.4205 " center2=" 0 -0.13 0.4205 " radius1=".005" radius2=".0"/>
<IndicatorCone3D center1=" -0.005 -0.13866 0.4175 " center2=" 0 -0.13 0.4175 " radius1=".005" radius2=".0"/>

```

F. Factory Functions for XML-based Geometry Creation in OpenLB

```
<IndicatorCone3D center1=" 0.01 -0.13 0.443 " center2=" 0 -0.13 0.443 " radius1=".005" radius2=".0"/>
<IndicatorCone3D center1=" -0.005 -0.12134 0.441 " center2=" 0 -0.13 0.441 " radius1=".005" radius2=".0"/>
<IndicatorCone3D center1=" -0.005 -0.13866 0.439 " center2=" 0 -0.13 0.439 " radius1=".005" radius2=".0"/>
<IndicatorCone3D center1=" 0.01 -0.13 0.4625 " center2=" 0 -0.13 0.4625 " radius1=".005" radius2=".0"/>
<IndicatorCone3D center1=" -0.005 -0.12134 0.4615 " center2=" 0 -0.13 0.4615 " radius1=".005" radius2=".0"/>
<IndicatorCone3D center1=" -0.005 -0.13866 0.4605 " center2=" 0 -0.13 0.4605 " radius1=".005" radius2=".0"/>
<IndicatorCone3D center1=" 0.01 -0.13 0.482 " center2=" 0 -0.13 0.482 " radius1=".005" radius2=".0"/>
<IndicatorCone3D center1=" -0.005 -0.12134 0.482 " center2=" 0 -0.13 0.482 " radius1=".005" radius2=".0"/>
<IndicatorCone3D center1=" -0.005 -0.13866 0.482 " center2=" 0 -0.13 0.482 " radius1=".005" radius2=".0"/>
</IndicatorUnion3D>
```